12-1-2017 11:37 AM

Investigating the mechanism of deep-focus earthquakes via in-situ acoustic emission experiments on Fe2SiO4 at high temperature and pressure

Timothy Officer
The University of Western Ontario

Supervisor
Dr. Richard Secco
The University of Western Ontario

Graduate Program in Geophysics
A thesis submitted in partial fulfillment of the requirements for the degree in Doctor of Philosophy

Abstract

In subduction zones, earthquakes are thought to be associated with faulting that arises from phase transformations. In order to test the viability of this mechanism experimentally, it was necessary to make microseismic measurements while the mineral under investigation was subjected to the pressure and temperature (P,T) environment corresponding to those at depth. A system has been developed capable of making *in situ* acoustic emission (AE) measurements on samples under P,T conditions representative of the upper mantle and transition zone. Experiments were performed in a 3000-ton multi-anvil press using an 18/11 octahedral cell with 6 piezoelectric transducers mounted on the rear side of the anvils. AE signals were collected at a sampling rate of 40 MHz using a triggered system and a data buffer for capturing full waveforms of AE events. The use of multiple transducers distributed in a microseismic array allowed for events to be located within the sample through manual or automatic arrival time picking and least squares inversion techniques. Uncertainty in location estimates was ~1mm. The multi-anvil apparatus constitutes an inherently noisy environment both acoustically and electrically, therefore methods of noise reduction were developed. This technique has been used to measure acoustic signals generated from the fracturing of quartz beads during high pressure deformation and to investigate the possibility that the phase transformation from olivine to spinel, known to occur in subduction zones, is associated with deep-focus earthquakes (300 – 690 km depth). The analog material fayalite (Fe_2SiO_4) was examined. Information about its synthesis and sintering is discussed. Results of AE experiments on samples under high pressure (P = 4-9 GPa) and high temperature (T = 773-1273 K) conditions in the spinel stability field, while experiencing deviatoric stress, showed acoustic events that locate within the sample in multiple experiments defined by the P,T envelope P = 3.8 – 8.4 GPa and T = 650 – 950 K. This is the first time an

olivine→spinel structured transition in a silicate mineral has demonstrated macroscopic faulting and associated microstructures, as well acoustic activity, under conditions that would normally promote plastic deformation. The system was also used to detect liquid↔solid phase transformations in Hg by measuring the abrupt change in sound velocity due to the intrinsic change in velocity between phases, and a change in delay between the triggering of an amplitude threshold and the arrival of the waveform.

Keywords: Deep-focus earthquakes, olivine→spinel transition, Fe_2SiO_4, acoustic emission, high pressure, high temperature, multi-anvil apparatus, transformational faulting, brittle/ductile transition, subduction

Acknowledgements

I would sincerely like to thank my supervisor Dr. Richard A. Secco for the opportunity he gave me to pursue my academic interest, and the advice, insight and constructive feedback he provided me with during my PhD. I would also like to thank him for recommending me for the instructor positions I was offered. In addition, there are several others that have assisted me throughout my doctorate for whom I owe a debt of gratitude. A special thanks goes to Wenjun Yong for all the help he gave me running experiments and fielding my many questions. I would like to thank Dr. Tony Withers and Sean Funk for synthesizing fayalite powder on my behalf so I could use it in my experiments. I am indebted to Jon Jacobs for his guidance and technical support, as well as Dr. Kristy Tiampo for her insights regarding inversion. Thank you to my advisory committee members Prof. Sean Shieh and Prof. Lauren Briens for all their advice and suggestions. I would also like to thank my co–students Innocent Ezenwa, Marie Burford, Soushyant Kiarasi, Reynold Sukara, Joshua Littleton and Ryan Sawyer for useful interactions. Finally, I would like to acknowledge the funding institutions that made my research possible. This work was supported by grants to R.A. Secco from the Canadian Foundation for Innovation (CFI), National Science and Engineering Research Council's (NSERC) Discovery Program and, Research and Technology Initiative, as well as Western University's Academic Development Fund. I also acknowledge my NSERC Post graduate scholarship (PGS) and Ontario Graduate Scholarship (OGS).

Table of Contents

List of Tables

List of Figures

List of Appendices

Chapter 1: Introduction

1.1 Earthquakes and seismology

Earthquakes are natural phenomena that occur when large volumes of the solid earth suddenly and catastrophically shift position causing rapid energy release. The amount of energy released during this process can be gigantic, equivalent to trillions of kilograms of dynamite. Some of the energy released is radiated out from the source in the form of low frequency acoustic, or seismic, waves that travel great distances within the earth at speeds of several kilometers per second. When these waves reach the surface they can cause the ground to violently shake resulting in enormous destruction of property and loss of life. Due to their disastrous effect on human populations, the study of earthquakes and the seismic waves they emit, have been investigated for hundreds of years by recording the earth shaking that occurs at the surface using seismometers. Because of the destructive power of these waves at the surface, they have attracted the interest of geophysicists, those involved in mineral petroleum exploration, engineers, architects and even politicians. Seismic stations have been installed worldwide to monitor ground motions, which are systematically recorded and analyzed by seismologists providing tremendous insight into the theory of plate tectonics as well as the interior structure of the Earth. Seismologists have also come up with a comprehensive theory of where and how often earthquakes occur, and the mechanism that causes brittle failure within the crust. Nevertheless, in spite of the extensive knowledge established regarding earthquakes, there is still a class of earthquakes that remains enigmatic to seismologists and geophysicists. These are the earthquakes that are not located within the crust but occur hundreds of kilometers below the surface within subducted lithosphere. These are the category of events known as “deep” earthquakes and the

mechanism responsible for them remains a mystery despite everything we have learned about their shallow counterparts.

1.2 The mystery of deep earthquakes

The first definitive evidence demonstrating that earthquakes could occur hundreds of kilometers below the surface came with the publication of a seminal paper in 1928 by the Japanese seismologist Kiyoo Wadati (Wadati, 1928) who showed some Japanese earthquakes were taking place at locations as deep as 300 km below the earth's surface. The following year Wadati (1929) went on to show that locations of deep earthquakes were not limited to a narrow range but occurred at all depths to at least as low as 500 km. This was immediately recognized as problematic for rock physicists since experiments on the fracturing process had shown that at low pressures, low temperatures and high strain rates rocks fracture, while at high pressures, high temperatures and low strain rates rocks become ductile and experience creep. Near the surface earthquakes occur due to brittle failure of rocks in response to shear stress, or frictional sliding on existing faults when shear stress overcomes the force of friction. However, in addition to shear stress, fracturing also depends on the confining pressure (or hydrostatic stress, σ_h) since fracturing requires microscopic cracks to form, grow and link up to generate a network of cracks large enough to manifest macroscopic fractures. Since confining pressure works to force crack closure, larger amounts of shear stress are required to overcome it as expressed approximately by the Coulomb criterion:

$$\tau_{fracture} = \tau_0 + \mu_{fracture}\sigma_h \qquad (1.1)$$

where $\tau_{fracture}$ is the shear stress required for fracture, τ_0 is a material dependent minimum value of shear stress required to initiate fracture under ambient conditions and $\mu_{fracture}$ is a

constant that, like τ_0, depends on the material. The shear stress required to overcome friction is typically lower than that required for fracture but it also depends on the confining pressure in a similar way since the force required to overcome frictional forces will increase with increasing confining pressures and equivalently, depth as described approximately by Byerlee's law:

$$\tau_{friction} = \tau_F + \mu_{friction}\sigma_h \qquad (1.2)$$

where all terms are defined as in (1.1) but with frictional sliding replacing fracture as the failure mechanism. τ_F and $\mu_{friction}$ again depend on the material. Figure 1 shows the results from laboratory experiments on the stress difference required to initiate fracture versus confining pressure.

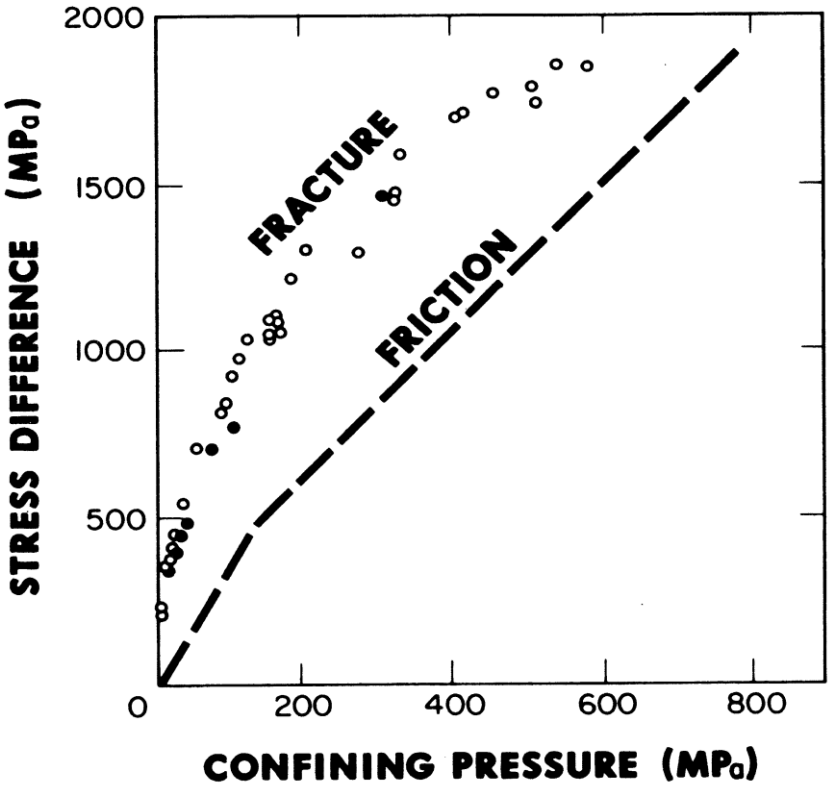

Fig 1.1: Experimental determination of shear stress versus confining pressure for solid samples of Westerly granite (open and closed circles). The dashed line is a summary of the experimental results for frictionally sliding on a plane. Although the relationship between shear stress and confining pressure is more complicated than the process described by equations (1.1) and (1.2), the amount of shear stress required for brittle failure to occur through fracture or frictional sliding increases sharply with confining pressure. Figure reproduced from Scholz, 2002.

The key feature to notice is that while eqns. (1.1) and (1.2) are somewhat simplistic approximations describing rock failure, it is clear that rock strength increases steeply with confining pressure. For high confining pressures, particularly when considerable surface area is in contact, the shear stress required to overcome friction approaches that required to initiate fracture. In addition to fracturing and frictionally sliding, under certain conditions shear stress may also cause rocks to deform plastically and undergo ductile flow as described by,

$$\tau_{ductile} = A\dot{\varepsilon}^{\left(\frac{1}{3}\right)}e^{\left(\frac{Q}{3RT}\right)} \qquad (1.3)$$

where A is a constant, $\dot{\varepsilon}$ is the strain rate, Q is the activation energy of ductile flow, R is the universal gas constant and T is the temperature. Ductile flow occurs as a result of the propagation of microscopic dislocations and disruptions of the crystal lattice. Because atoms vibrate more vigorously at higher temperatures, dislocations are also able to propagate more freely promoting ductile flow. The effect of increasing temperature causes the shear stress required to instigate flow to drastically decrease. While the descriptions of brittle failure and ductile flow depicted here are dramatically oversimplified, essentially flow becomes the dominant mechanism of failure when dislocations can propagate as easily as or easier than cracks. This is achieved under conditions of high confining pressure and high temperature. As depth increases in the Earth, pressure increases which inhibits brittle fracture and frictional sliding, and temperature also increases which promotes ductile flow. The combination of both these factors results in a certain depth where rocks become too strong to rupture and too weak to resist flow. This is known as the brittle-ductile transition. For this reason rocks are not expected to fracture below approximately 40-70 km as shown in Figure 1.2.

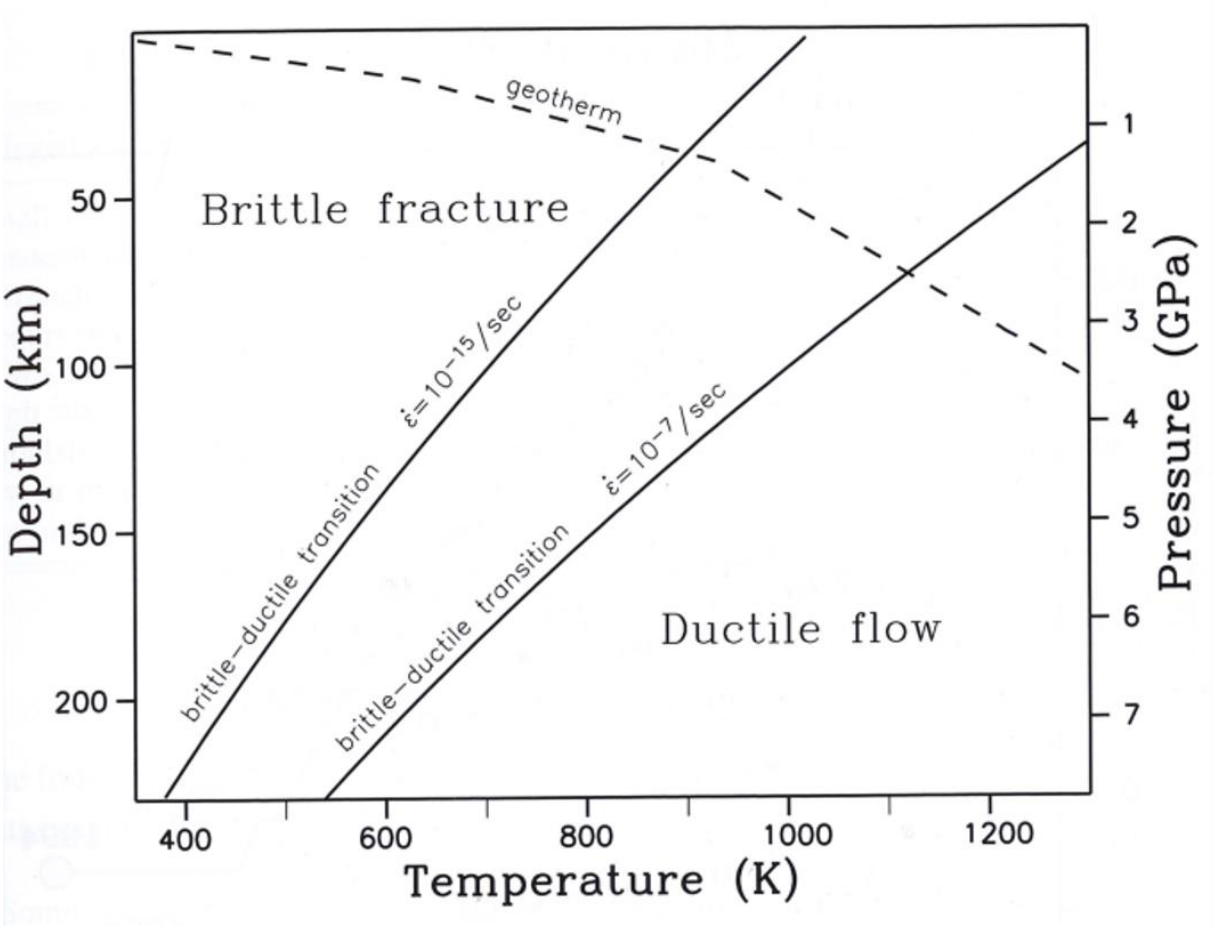

Figure 1.2: The approximate relationship between pressure, temperature and strain rate, and the corresponding depth at which the brittle-ductile transition occurs. Reproduced from Frolich (2006). The brittle-ductile transition curves are based on equations originating in Houseman and England (1986) and the geotherm is from Stacey (1992).

Nevertheless, observations have shown that even large earthquakes can occur at depths up to nearly 690 km (Rees and Okal, 1987; Stark and Frohlich, 1985), the largest of which occurred in 2013 below the sea of Okhotsk with a moment magnitude (M_w) of 8.3 and a depth of 607 km (Ye, 2013), surpassing the M_w = 8.3 earthquake of 1994 which occurred 637 km below Bolivia (Anderson et al., 1995). In fact, according to several earthquake catalogs, approximately one quarter of all earthquakes with M_w greater than 5 occur below 60 km and 5-10% of these occur below 300 km (see Table 1).

Catalog	Number; years	Shallow $h < 60\,km$	Deep $h > 60\,km$	Deep-focus $h > 300\,km$
Harvard; $M_W \geq 8.0$	13; 1977–2004	0.77	0.23	0.08
Abe; $m_B \geq 8.0$	13; 1897–1976	0.77	0.23	–
Harvard; $M_W \geq 7.0$	376; 1977–2004	0.73	0.27	0.09
Abe; $m_B \geq 7.0$	1110; 1897–1976	0.62	0.38	0.07
Harvard; $M_W \geq 5.6$	9403; 1977–2004	0.76	0.24	0.07
ISC; $m_b \geq 5.3$	18840; 1964–2000	0.70	0.30	0.05

Table 1.1: Percentage of deep earthquakes from multiple earthquake catalogs. Reproduced from Frohlich, 2006.

Figure 1.3 shows the number of global earthquakes annually versus depth.

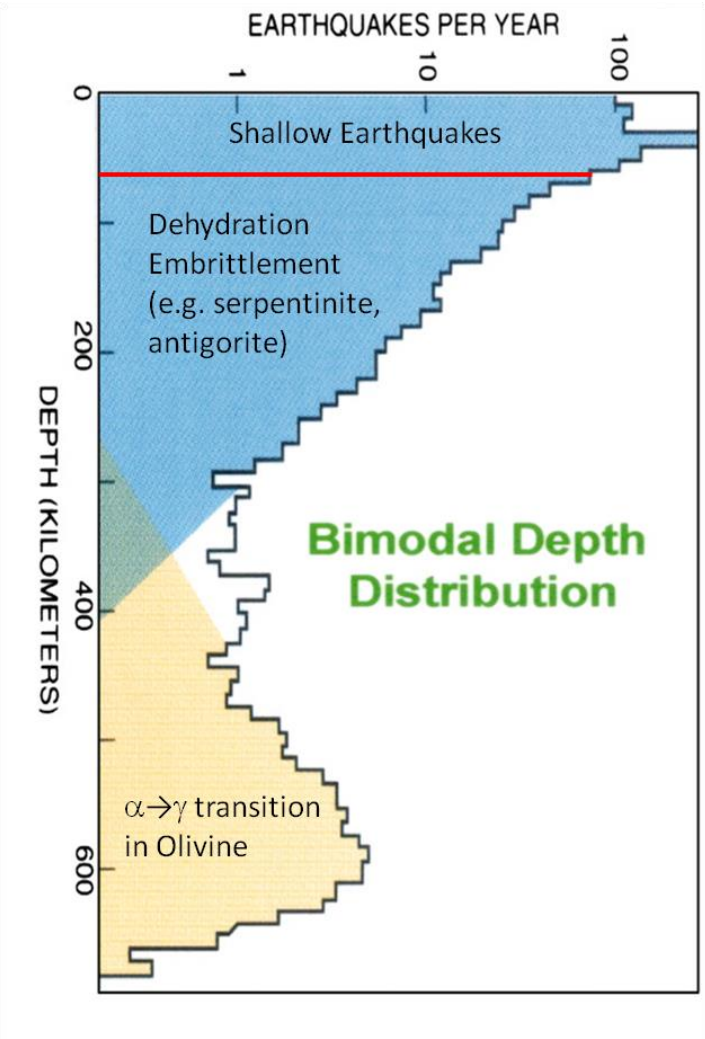

Figure 1.3: A histogram showing the bimodal distribution of the annual number of earthquakes as a function of depth. Above the red line earthquakes are considered shallow. The blue region, below the red line is thought to be a associated with dehydration embrittlement. In the cream coloured region, the mechanism responsible is thought to be associated with olivine transformation. Figure modified from Green, 1994.

This semi-log histogram indicates that about three quarters of all earthquakes are shallow (within 60 km of the surface) with a maximum near ~30 km, the most likely focal depth for shallow earthquakes to occur. The number then decreases approximately exponentially by a factor of 120 times less earthquakes per 100 km until a depth of about 300 km where it begins to increase to a local maximum around 600 km then abruptly decreases to zero at just above 690 km. Due to the bimodal distribution with depth it is speculated that the process responsible for deep seismicity may be different at different depths (Green and Houston, 1995). This led to the conclusion that a mechanism other than brittle failure must be responsible for deep seismicity. One such suggestion is that solid-solid phase transitions and dehydration reactions that occur at the elevated pressures and temperatures of the upper mantle may be responsible. In 1945, using H_2O as an analogue to silicates, Bridgman hypothesized that solid-solid phase transitions in earth materials may be responsible for deep earthquakes (Bridgman 1945). However, he also recognized that not all subduction transitions would be likely candidates and emphasized the fact that, for solid-solid phase transitions to be a viable mechanism for generating deep earthquakes, two criteria would need to be met. Firstly, the transformation must run rapidly to avoid dissipation of shear stress over time. Therefore, he speculated that any possible candidate must persist in the low pressure phase well into the stability field of the high pressure phase (i.e. remain metastable). This results when there is a lack of energy to activate the transformation to the lowest possible energy state. Secondly, for the reaction to continue it would need to be exothermic so that the heat released upon transformation could be used to promote further transformation of neighboring material and create a runaway scenario.

To distinguish between the two categories of deep earthquakes, the population between 60 km – 350 km depth is often referred to as intermediate-focus earthquakes (IFEQs) in contrast

to the population that occurs between 350 km – 690 km deep which are referred to as deep-focus earthquakes (DFEQs). To avoid confusion this nomenclature will be used here throughout the text. It should be noted that while Figure 1.3, accurately describes the global distribution of earthquakes with depth and displays such features as the bimodal distribution and the exponential fall off with depth, many of these features do not hold for individual subduction zones (Frohlich, 2006).

1.3 Intermediate-focus seismicity and dehydration of subducted lithosphere

At mid ocean ridges, ascending mantle convection cells experience a rapid decrease in pressure relative to the decrease in temperature which causes material to cross the solidus/liquidous causing mantle rock to melt and erupt at the bottom of the ocean. The interaction of molten lava with cold water induces prompt quenching of the lava forming solid rock. During this process water gets incorporated into the crystalline structure of hydrous phases such as serpentinite minerals near the surface of the newly formed oceanic crust and these hydrous mineral phases remain stable within the lithosphere for tens to over one hundred of million years as the plate slowly moves away from the ridge and approaches subduction. In addition, pelagic sediments accumulate on the ocean floor and lithify to form a layer of hydrous sedimentary mudstone containing both pore and chemically bound water. Together these rock layers form a hydrous layer several kilometers thick. Finally, there is increasing speculation that significant amounts of water can be incorporated into the lithospheric mantle. It is not entirely clear how surface fluids can bypass sediments and the crust to hydrate mantle peridotite, but the best suggestion is that when the plate is forced to bend between the outer rise and the trench axis,

normal faults occur that create pathways tens of kilometers deep for fluids to enter (Rupke et al., 2004; Kerrick, 2002; Peacock, 2001). Significant evidence that this is the case comes from high resolution, seismic reflection profiles which show images of normal faults that slice through the crust to more than 15 km deep into the lithospheric mantle (Ranero et al., 2003). The presence of water greatly increases the pore pressure of rocks, P_p, lowering the hydrostatic stress in Eqns 1.1 and 1.2 to an effective stress of $(\sigma_h - P_p)$. During subduction, the pressure and temperature conditions are eventually met which cause dehydration of hydrous phases to occur. This rapid reduction in effective stress, caused by the increase in pore pressure created by the presence of water, is thought to be strong enough to allow cracks to remain open and allow brittle fracture to occur. This process is known as dehydration embrittlement and is believed to be responsible for IFEQs (60-300 km depth), (e.g. Raleigh and Patterson, 1965; Meade and Jeanloz, 1991). This term also refers to the case when cracks are not filled with actual fluids, but fine grain solid byproducts of the dehydration process that are too weak to support shear stress. However, by approximately 300 - 400 km below the surface, the subducted material is thought to be nearly completely dehydrated (Green, 2010) and if there is any water that persists it remains locked in the crystalline structure of stable phases as dense hydrous magnesium silicates (DHMS) which can remain stable in the upper mantle in subducted slabs (Ohtani et al., 2001; Ohtani, 2005). As a consequence, the mechanism responsible for earthquakes occurring at greater depths is likely to be distinctly different.

1.4 Deep-focus seismicity and phase transitions in olivine

At both 410 km and 660 km depth there are globally observed discontinuities in seismic velocity. This region of Earth bounded by these two discontinuities is known as the mantle transition zone named after the phase changes that the mineral olivine, with approximate composition $(Mg_{0.9}Fe_{0.1})_2SiO_4$, undergoes at these depths. At 410 km depth, olivine (α-phase) transforms to wadsleyite (β-phase) with modified spinel structure followed by ringwoodite (γ-phase) which has spinel structure at 520 km depth (Ringwood and Major, 1966). At 660 km depth, ringwoodite decomposes into perovskite $(Mg,Fe)SiO_3$ plus ferropericlase (Mg,Fe)O defining the upper boundary of the lower mantle (Sakai et al., 2009).

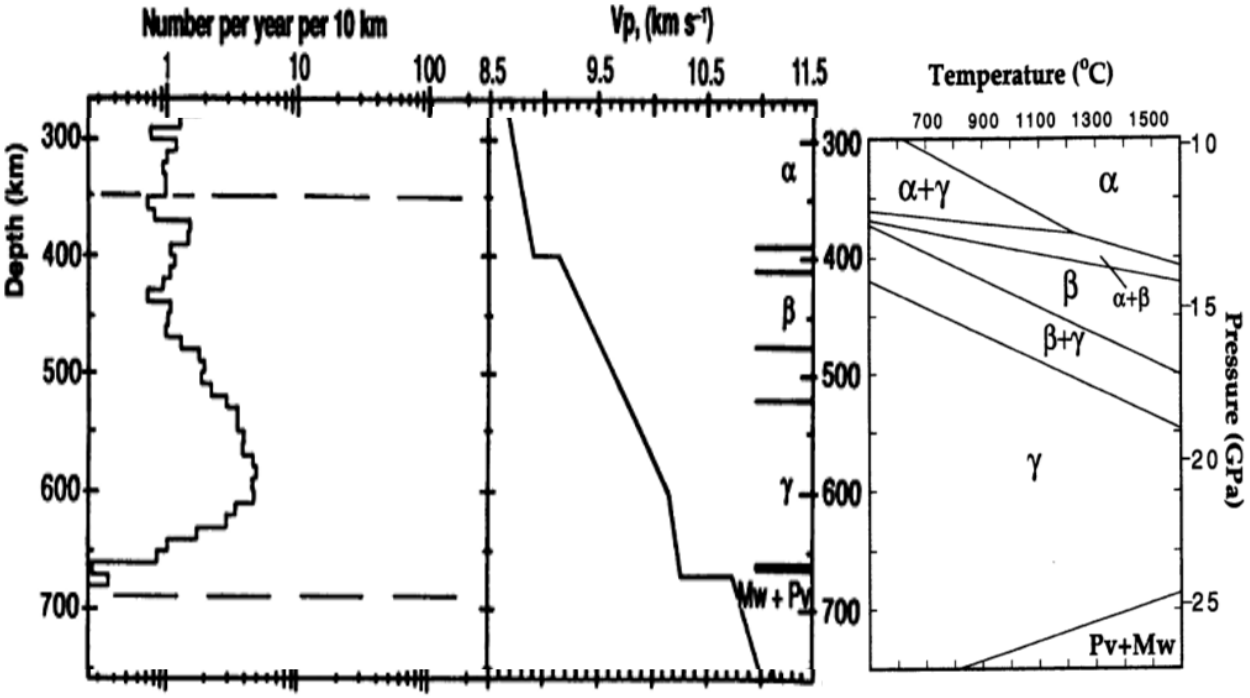

Figure 1.4: Comparison of the number of earthquakes (left), the p-wave velocity of the upper mantle (middle), and the phase diagram for $(Mg_{0.9},Fe_{0.1})_2SiO_4$ (right). In the pressure/temperature stability fields containing two phases the ratio Mg/(Mg+Fe) is of the coexisting phases are different. The depths at which the number of earthquakes begins to increase, closely coincides with velocity discontinuities occur within the mantle and the pressure/temperature transformation boundaries of $(Mg_{0.9},Fe_{0.1})_2SiO_4$. Figures of the number of earthquakes vs. depth and velocity vs. depth modified from Kirby et al, 1991. The olivine phase diagram reproduced from Kirby et al., 1996.

Because the depth of this transition closely resembles the local maximum in the distribution of earthquakes, it is widely speculated that the transition is in some way responsible for the presence of deep-focus seismicity (Green and Houston, 1995). However, unlike the velocity discontinuities that define the transition zone, which are witnessed globally, deep earthquakes, with very few (if any) exceptions, are restricted to subduction zones. After oceanic lithosphere is formed at mid ocean ridges, heat is removed through the surface by conduction causing the lithosphere to gradually cool and thicken over time. Figure 1.5 shows the age of oceanic lithosphere plotted vs. thickness compared to geotherms derived from a half space cooling model.

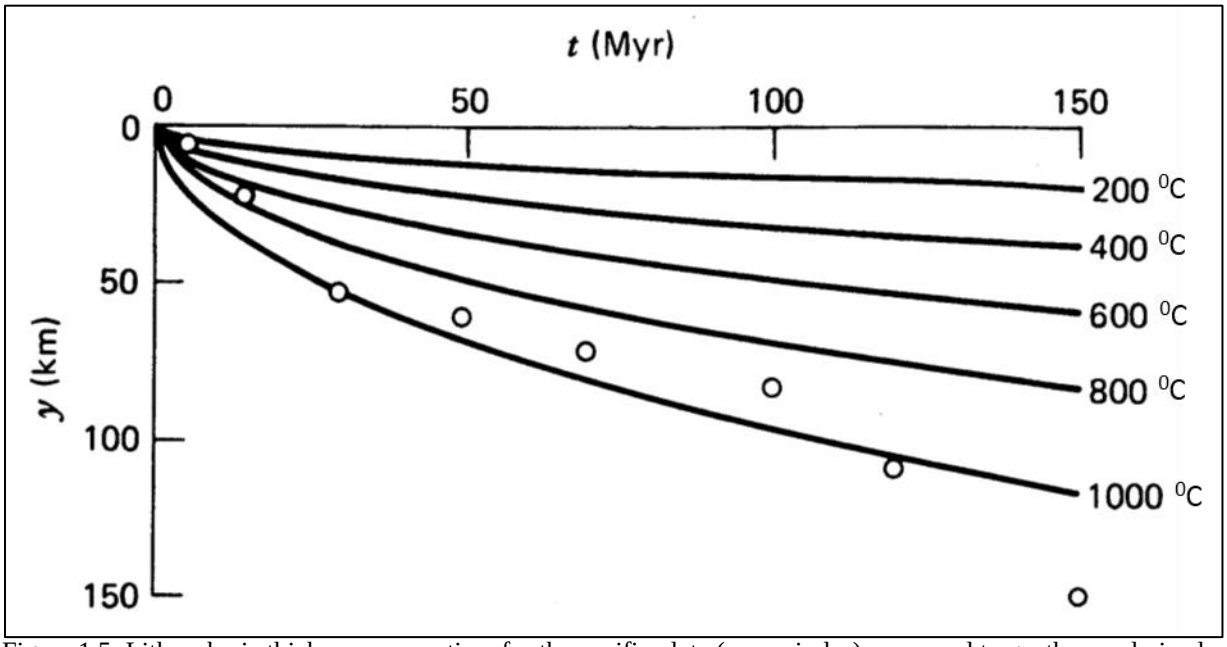

Figure 1.5: Lithospheric thickness versus time for the pacific plate (open circles) compared to geotherms derived from a half space cooling model (in ^{0}C). As the lithosphere moves away from the ridge, it cools due to heat loss through its surface and becomes thicker. Figure reproduced from Turcotte, 2002.

This demonstrates that the age of oceanic lithosphere, which is based on its distance from the spreading center and its tectonic velocity, is a direct proxy for its temperature at the time of subduction. The duration of time between formation and subduction of oceanic lithosphere is typically many tens to over one hundred million years allowing for substantial cooling to take

place, on the order of several hundred degrees Kelvin. This is significant given that rock is a very poor conductor of heat. During subduction, as the cold lithosphere descends into the mantle, it becomes progressively pressurized and slowly heated as a result of the diffusion of heat from the surrounding mantle. As a consequence, certain crystalline mineral phases that are stable near the surface undergo phase transitions and dehydration reactions as the pressure and temperature conditions of high pressure phases are met. However, many low pressure phases persist metastably well into the pressure field of the high pressure phase because the low pressure state requires activation energy, usually in the form of heat, to initiate the transformation. Several factors affect the thermal characteristics of the slab including heat generated by friction at the boundary between the upper surface of the slab, as well as latent heat released or absorbed from phase transitions, however the primary control on heat entering the slab is conduction from the surrounding mantle (Kirby et al., 1991). However, because rock is such a poor conductor of heat most upper mantle rocks, under upper mantle pressures and temperatures, have thermal diffusivities on the order of $\sim 5 - 7 \times 10^{-7}\ \frac{m^2}{s}$ (Gibert et al., 2003). The time required for the temperature of the surrounding mantle to equilibrate with the center of the slab is given by the thermal diffusion time expressed as

$$t = \frac{\left(L/2\right)^2}{K}$$

where L is the slab thickness and K is the thermal diffusivity. Assuming a slab thickness of 100 km and a thermal diffusivity coefficient of $6 \times 10^{-7}\ \frac{m^2}{s}$, the thermal diffusion time is ~65 Myr. Compare that to the ~20 Myr required for a slab with a 45^0 dip angle, moving with a speed of $5\ cm/yr$, to descend to the bottom of the transition zone. In other words, the interior of a

subducting slab will remain substantially colder than the surrounding mantle for more than 50 Myr after subduction, far longer than the time required to reach the bottom of the transition zone. Figure 1.6 shows a cross section of the thermal structure of a relatively rapidly descending subduction zone.

a)

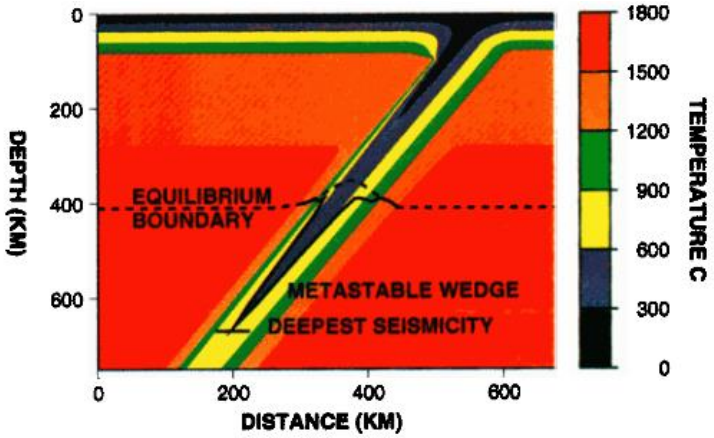

b)

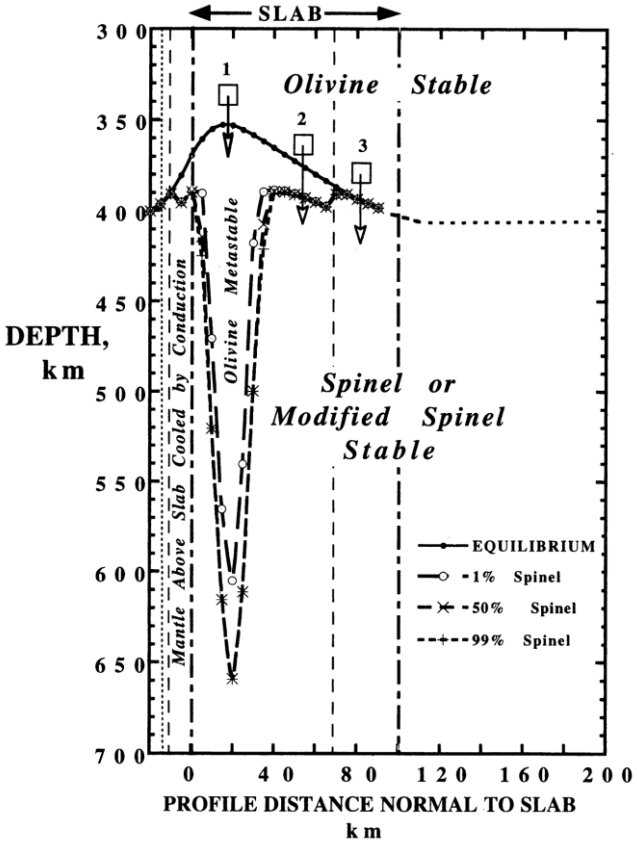

Figure 1.6: a) The cross section of a subduction zone showing the temperature profile of a rapidly subducting and relatively cool slab compared to the surrounding mantle. Because the interior of the slab is cooler than its surroundings olivine does not readily transform to its higher pressure polymorphs. The metastable olivine wedge is outlined in black. Note that it penetrates below the equilibrium phase boundary for the olivine → wadsleyite transition. b) A detailed mineralogical model for the Tonga slab. Region 1 represents a volume of peridotite containing olivine that survives metastabally beyond the olivine-spinel phase. Region 2 slightly bypasses the equilibrium boundary and reacts by a nucleation-controlled growth of the high pressure phase. Region 3, composed of warm slab material, converts olivine to spinel at a rate equivalent to the slab's descent rate. Both figures reproduced from Kirby et al, 1996.

Note that the interior is typically several hundred degrees less than the surrounding mantle and can differ by as much as 1000 K. This intra-slab thermal structure is determined by abnormally high seismic velocities, suggesting colder temperatures in the slab interior (Wittlinger et al, 2004; Van der Voo et al., 1999; Spakman et al., 1988). The low temperatures lead to a metastable volume of olivine in the interior of the slab that has not received enough heat to overcome the activation energy required to transform to its high pressure polymorphs (Kirby et al., 2010; Liu, 1983). The region shown in Figure 1.6 bounded by the black 600 °C geotherm delineates what is referred to as an olivine wedge.

1.5 Spatial clustering of deep earthquakes

Deep earthquakes occur with exceedingly few (if any) exceptions within subduction zones. Therefore, the mechanism responsible for deep earthquakes is inherently linked to the process of subduction. However, the spatial pattern of deep earthquakes varies widely with geographic region. Figure 1.7 is a cartoon showing the typical distribution of the locations of earthquakes within the subducting slab in cross section.

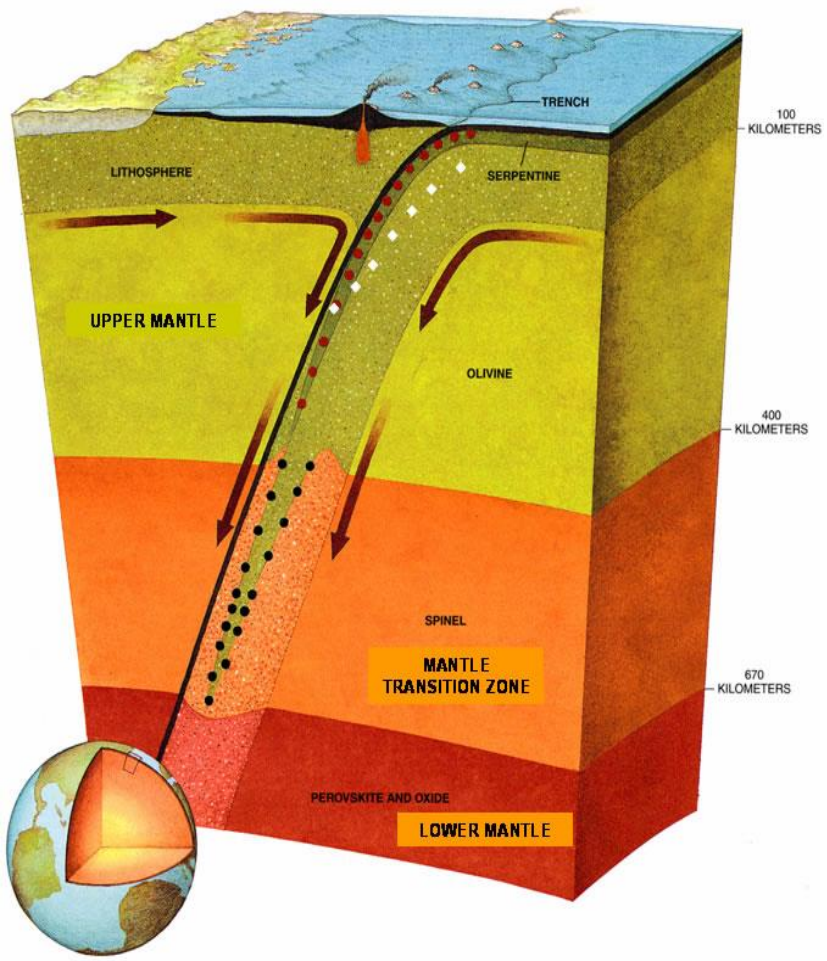

Figure 1.7: Cartoon depicting the cross section of a subduction zone showing the location of intermediate focus (red dots) and deep focus earthquakes (black dots) and the presence of a double seismic zone (white dots). The intermediate focus and deep focus earthquakes define a plane near the surface of the slab and perpendicular to the plane of subduction known as the Wadati-Benioff zone. The double seismic zone is a planar zone of earthquakes parallel to the Wadati-Benioff zone but separated from it by tens of kilometers. Figure reproduced from Green, 2005.

Above 300 km depth, earthquake hypocenters cluster within an inclined plane defining the upper ~10-15 km of the slab known as a Wadati-Benioff zone. The location of these earthquakes lends credibility to the hypothesis that dehydration embrittlement is responsible for intermediate focus seismicity since hydration takes place near the upper surface of the slab. Occasionally, some subduction zones will also display double seismic zones (Hacker et al., 2003). This is a zone of hypocenter clusters that begin at ~60 km depth and runs in a plane parallel to the Wadati-Benioff zone but it separated by ~20 km within the slab. The most likely explanation for this set of

earthquakes is dehydration embrittlement of saturated material, however it is unclear how water could penetrate so deep into the lithosphere. As mentioned in 1.3, one possible explanation is that water infiltrates faults generated by outer rise earthquakes allowing water to hydrate material up to 60 km below the surface (Rupke et al., 2004; Ranero et al., 2003; Kerrick, 2002; Peacock, 2001). Below ~300 km, earthquake hypocenters appear to cluster in a plane normal to the dip axis of the slab, but occur nearer the slab interior along the outer edge of the olivine wedge. However, Figure 1.7 is a simplification corresponding to global trends. For any particular subduction zone, the situation may be very different. Figure 1.8 shows the distribution of hypocenters for the Tonga and South America subduction zones. Both regions clearly display a well-defined Wadati-Benioff zone, however their specific features are quite distinct.

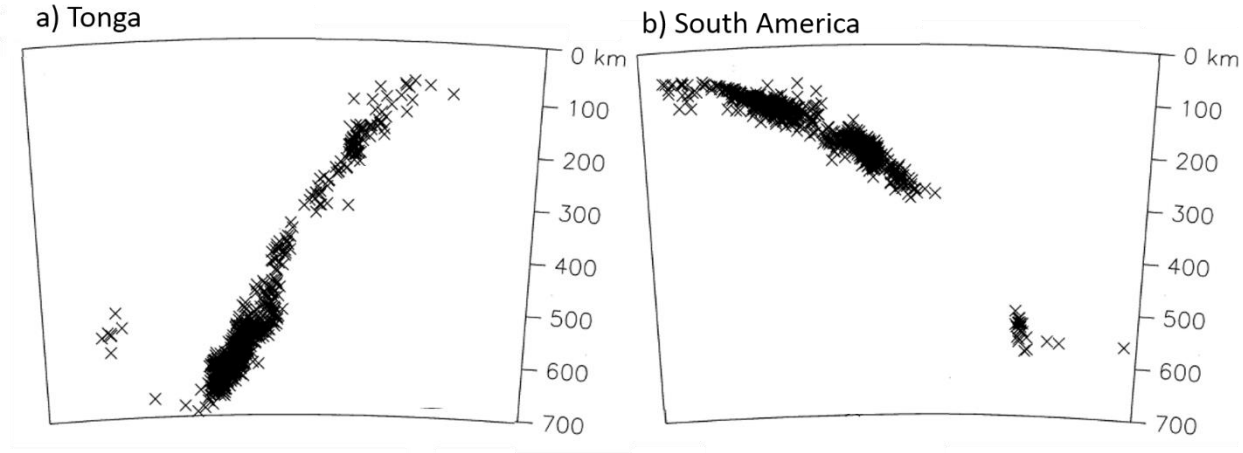

Figure 1.8: The locations of earthquakes in the a) Tonga and b) South American subduction zones. The vertical axis represents depth. In both cases the Wadati-Benioff zone is clearly defined, although the distribution of earthquake locations is quite different for each region. In Tonga seismic activity is dominated by deep earthquakes, whereas South America is dominated by intermediate seismicity and contains a large gap between 300-500 km where no earthquakes occur. In Tonga the gap is small and represents more of a thinning out. Both regions include deep "rouge" events that are not confined to the Wadati-Benioff zone. Figure reproduced from Frohlich, 2006.

1.6 Seismic radiation patterns of deep earthquakes

Very soon after deep earthquakes were confirmed it was recognized that they were mechanically different and scientists were quick to speculate that phase changes were responsible for their existence. Initially, the hypothesis went as follows: Several phase transitions occur during subduction, all of which experience negative volume change with transformation to the high pressure phase. It was speculated that when pressurized rock below the surface underwent a phase transition a void would be created in the vicinity of transformation owing to the decrease in volume of the high pressure phase. The burden of pressure at depth would cause the surrounding rock to respond by immediately imploding. The result is that an earthquake accompanies the sudden collapse as rock fills the void. The simplicity of this explanation is appealing however it suffers from a contradiction with observations of the seismic radiation patterns tied to deep earthquakes. A purely implosive source generates an initial contraction of the rock volume reacting seismically to the stress release of the collapse thus emitting p-waves radially from the source but does not generate s-waves. Consequently, the initial impulse of the signal on seismograms should display negative first motions for every seismometer in the entire array. However, despite numerous investigations carried out to detect implosive components (Gutenberg and Richter, 1937; Okal and Geller, 1979; Kawakatsu 1991, Kawakatsu 1996; Hara, 1996), the seismograms of deep earthquakes do not display any statistically significant implosive component of first motion. In fact, the radiation patterns corresponding to deep earthquakes represent nearly pure double-couple focal mechanisms. This is the radiation pattern caused by slip on a fault, the same focal mechanism responsible for shallow earthquakes. This is a curious fact since the mechanism responsible for deep earthquakes cannot be brittle failure (section 1.2), but whatever it is, it has to trigger slip on a fault, not a simple implosion. This means the

mechanism responsible, if it is related to phase transitions, must be connected to the process in a complex way as yet undetermined. Another curious fact is that deep earthquake seismograms rarely exhibit aftershocks, a trademark of every large shallow earthquake ever recorded (Frohlich, 2006). This observation is consistent with the phase transition hypothesis since after the transformation to the high pressure phase occurs, the mechanism is exhausted and cannot generate aftershocks.

1.7 The objective of this study

The controversy over what causes deep earthquakes has been ongoing for nearly 90 years and yet remains unsolved. What is clear is that deep earthquakes are fairly ubiquitous (~25% of all earthquakes), can be as large in magnitude as shallow earthquakes, occur at all depths between 60 – 690 km, exhibit double-couple focal mechanisms, and rarely, but occasionally, exhibit aftershocks. Based on their bimodal frequency with depth (Fig. 1.3), it is likely that the mechanism responsible for IFEQs and DFEQs are different; namely IFEQs are caused by dehydration embrittlement and DFEQs are related to the phase transitions in olivine. However, a major limitation of this hypothesis is that it suffers from a lack of persuasive experimental evidence to support it.

The goal of my thesis is to perform high pressure/ high temperature experiments on fayalite (Fe_2SiO_4), the iron end member of olivine, in order to test the hypothesis of whether or not the olivine-spinel transformation can be responsible for deep seismicity. In order to do this, a system for accurate detection of events inside a pressure cell needed to be developed. The following chapters will give a detailed outline of the current state of knowledge of experimental

tests of the mechanism of deep earthquakes at high pressure and temperature in the laboratory. They also include sections that outline the specifics of the experimental setup developed and used in experiments, how it locates events. Finally, experiments will be discussed including information on the experimental conditions at which they were run as well as the detailed discussions of the results and their geophysical interpretation.

1.8 References

Anderson, J.G., Savage, M., Quass, R., 1995. 'Strong' ground motions in North America from the Bolivia earthquake of June 9, 1994 (M_w = 8.3), *Geophys. Res. Lett.*, **22**, 2293-2296.

Bridgman, P.W., 1945. Polymorphic phase transitions and geological phenomena, *Am. J. Sci.* **243A**, 90.

Frohlich, C., 2006. *Deep Earthquakes*, Cambridge Univ. Press. Cambridge, England.

Gibert, B., Seipold, U., Tommasi, A., Mainprice, D., 2003. Thermal diffusivity of upper mantle rocks: Influence of temperature, pressure, and deformation fabric, *J. Geophys. Res.*, **108**, 1-15.

Green, H.W., 2010. Seismic evidence of negligible water carried below 400 - km depth in subducting lithosphere, *Nature*, **467**, 828-831.

Green, H.W., 2005. New light on deep earthquakes, *Scientific American*, 97-105.

Green, H.W. and Houston, H., 1995. The mechanics of deep earthquakes, *Annu. Rev. Earth Planet. Sci.* **23**, 169-213.

Green, H.W., 1994. Solving the paradox of deep earthquakes, *Scientific American*, 64-71.

Gutenburg, B., Richter, C.F., 1937. Materials for the study of deep-focus earthquakes (second paper), *Bull. Seismol. Soc. Amer.*, **27**, 157-183.

Liu, L., 1983. Phase transitions, earthquakes and the descending lithosphere, *Phys. Earth Planet. Int.*, **32**, 226-240.

Hacker, B.R., Peacock, S.M., Abers, G.A., Holloway, S.D., 2003. Subduction factory – 2: Are intermediate depth earthquakes in subducting slabs linked to metamorphic dehydration reactions?, *J. Geophys. Res.*, **108**, 2030.

Hara, T., 1996. Determination of the isotropic component of deep focus earthquakes by inversion of normal mode data, *Geophys. J. Int.*, **127**, 515-528.

Houseman, G. and England, P., 1986. A dynamical model of lithospheric extension and sedimentary basin formation, *J. Geophys. Res.*, **91**, 719-729.

Kawakatsu, H., 1996. Observability of the isotropic component of a moment tensor, *Geophys. J. Int.*, **126**, 525-544.

Kawakatsu, H., 1991. Insignificant isotropic component in the moment tensor of deep earthquakes, *Nature*, **351**, 50-53.

Kerrick, D., 2002. Serpentine seduction, *Science*, **298**, 1344-1345.

Kirby, S.H., Stein, E.A., Okal, E.A., Rubie, D.C., 1996. Metastable mantle phase transformations and deep earthquakes in subducting oceanic lithosphere, *Rev. Geophys.*, **34**, 261-306.

Kirby, S.H, Durham, W.B., Stern, L.A., 1991. Mantle phase changes and deep earth faulting in subducted lithosphere, *Science*, **252**, 216-225.

Liu, L., 1983. Phase transitions, earthquakes and the descending lithosphere, *Phys. Earth Planet. Int.*, **32**, 226-240.

Meade, C. and Jeanloz, R., 1991. Deep-focus earthquakes and recycling of water into the Earth's mantle, *Science*, **252**, 68-72.

Okal, E.A. and Geller, R., J., 1979. On the observability of isotropic seismic sources: the July 31, 1970 Columbian earthquake, *Phys. Earth Planet. Int.*, **18**, 176-196.

Ohtani, E., 2005. Water in the mantle, *Elements*, **1**, 25-30.

Ohtani, E., Toma, M., Litasov, K., Kubo, T., Suzuki, A., 2001. *Phys. Earth Plan. Int.*, **124**, 105-117.

Peacock, S.M., 2001. Are the lower planes of double seismic zones caused by serpentine dehydration in subducting oceanic mantle? *Geology*, **29**, 299-302.

Raleigh, C.B. and Patterson, M.S., 1965. Experimental deformation of serpentinite and its tectonic implications, *JGR*, **70**, 3965-3985.

Rees, B.A. and Okal, E.A., 1987. The depth of the deepest historical earthquakes, *Pure Appl. Geophys.*, **125**, 699-715.

Ranero, C.R., Phipps Morgan, J., McIntosh, K.D., Reichert, C., 2003. Bending, faulting and mantle serpentinization at the Middle America trench, *Nature*, **425**, 367-373.

Ringwood, A.E. and Major, A., 1966. Synthesis of Mg_2SiO_4-Fe_2SiO_4 spinel solid solutions, *Earth Plan. Sc. Lett.*, **1**, 241-245.

Rupke, L.H., Phipps Morgan, J., Hot, M., Connolly, J.A.D, 2004. Serpertine and the subduction zone water cycle, *Earth Plan. Sc. Lett.*, **223**, 17-34.

Sakai, T., Ohtani, E., Terasaki, H., Sawada, H., Kobayashi, Y., Miyahara, M., Nishijima, M., Hirao, N., Ohishi, Y. and Kikegawa, T., 2009. Fe-Mg partitioning between perovskite and ferropericalse in the lower mantle, *Am. Min.*, **94**, 7.

Scholz, C.H., 2002. *The Mechanics of Deep Earthquakes and Faulting*, (second edn.), Cambridge, U.K., Cambridge University Press, p.496.

Spakman, W., Wortal, M.J.R., Vaar, N.J., 1988. The Hellenic subduction zone: A tomographic image and its geodynamic implications, *Geophys. Res. Lett.*, **15**, 60-63.

Stacey, F.D., 1992. *Physics of the Earth,* (3rd edn), Brookfield Press, Brisbane Australia.

Stark, P.B. and Frohlich C., 1985. The depths of the deepest deep earthquakes, *J. Geophys. Res.*, **90**, 1859-1869.

Turcotte, D.L and Shubert, G., 2002. *Geodynamics*, (2nd edn), Cambridge Univ. Press, Cambridge, England.

Van der Voo, R, Spakman, W., Bijwaard, H., 1999. Tethyan subducted slabs under India, *Earth Plan. Sci. Lett.,* **171**, 7-20.

Wadati, K., 1928. Shallow and deep earthquakes, *Geophys. Mag.,* **1**, 161-202.

Wadati, K., 1929. Shallow and deep earthquakes (2nd paper), *Geophys. Mag.*, **2**, 1-36.

Wittlinger, G., Vergne, J., Tapponnier, Farra, V., Poupinet, G., Jiang, M., Su, H., Herquel, G., Paul, A., 2004. Teleseismic imaging of subducting lithosphere and Moho offsets beneath western Tibet., *Earth Plan. Sci. Lett.,* **221**, 117-130.

Ye, L., Lay, T., Kanamori, H., Koper, K., Energy Release of the 2013 Mw 8.3 Sea of Okhotsk Earthquake and Deep Slab Stress Heterogeneity, *Science*, **341**, 1380.

Chapter 2: Literature Review

As discussed in Chapter 1, the mechanism responsible for deep earthquakes cannot be the same as that responsible for shallow earthquakes. This is because at mantle pressure and temperature rocks are too strong for brittle failure to occur, but too weak to resist ductile flow. They also cannot be due to implosions accompanying solid-solid phase transitions. Such a mechanism would exhibit implosive first motions on seismograms which have not been found. A proposed mechanism responsible for deep-focus earthquakes (DFEQs), known as transformational faulting, speculates that phase transformations that occur in mantle minerals during subduction result in earthquakes. In particular, $(Mg_{0.9}Fe_{0.1})_2SiO_4$ is thought to be responsible for DFEQs due to its abundance and the coincident increase in seismicity with the depth of its known transitions to its high pressure polymorphs. To test this hypothesis a study was carried out using the iron end member of the $(Mg_{0.9}Fe_{0.1})_2SiO_4$ system, Fe_2SiO_4. This chapter discusses the pertinent information regarding the olivine→spinel transition, experimental evidence of high pressure, high temperature (HPHT) faulting, and the microseismic study of mechanical instability under HPHT conditions.

2.1 The mechanism and kinetics of the olivine→spinel transition in analogue materials

As a result of its relevance in the upper mantle and subduction processes, phase transformations in the $(Mg_{0.9}Fe_{0.1})_2SiO_4$ system and several structural analogues have been extensively studied experimentally. The olivine→spinel transition in Fe_2SiO_4 has been investigated in several studies to determine the phase diagram. This has been performed *via*

irreversible quench methods (e.g. Akimoto et al., 1965) and more recently by way of direct observation using *in situ* X-ray diffraction (XRD) techniques (Yagi et al., 1987; Ono et al., 2013). Figure 2.1 shows the phase boundaries derived from these experiments.

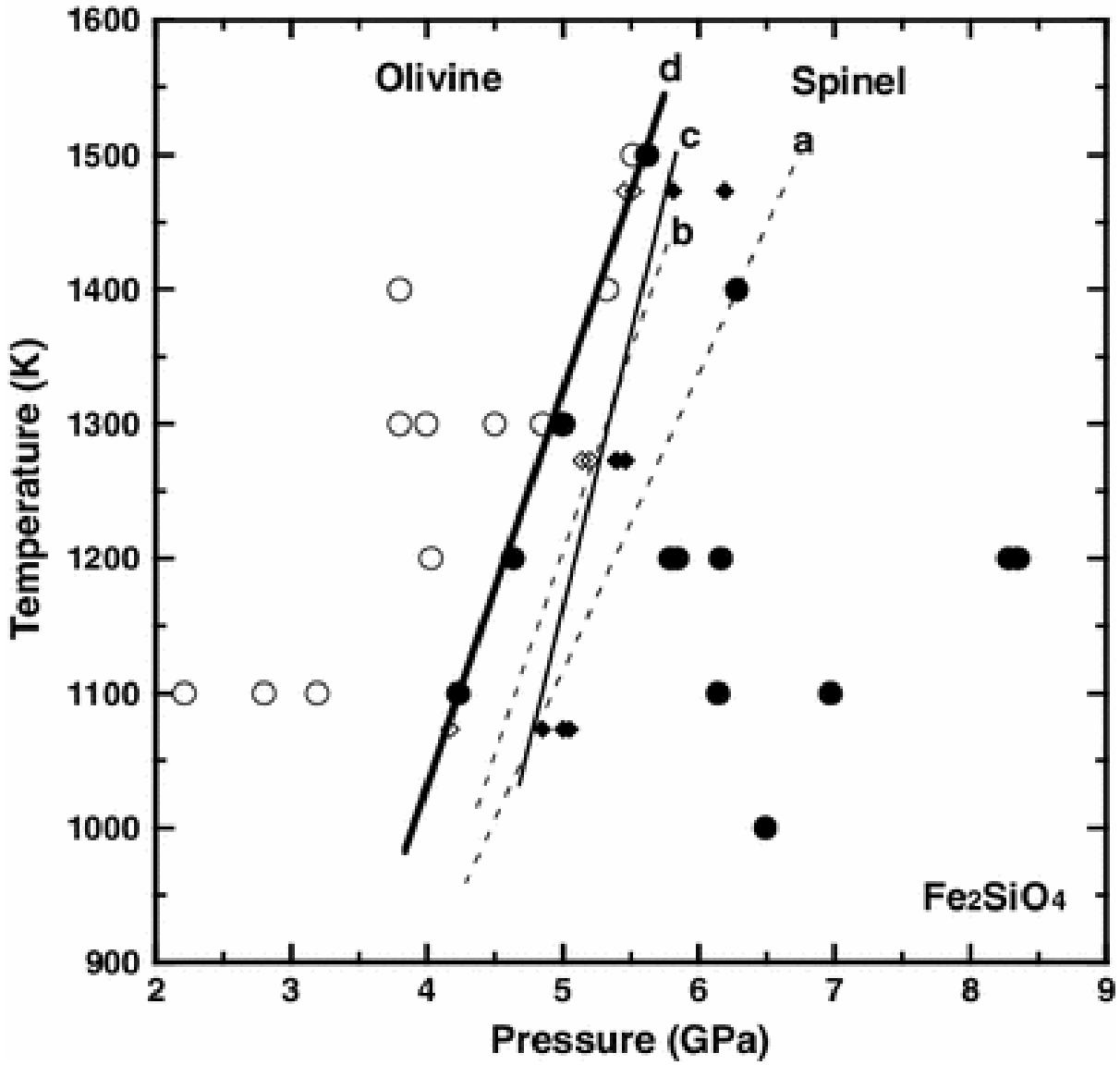

Figure 2.1: Experimental results and phase boundaries for Fe_2SiO_4 based on multiple studies. The dotted lines, **a** and **b**, are from Akimoto et al. (1965 and 1967, respectively) using a quenching method. The open and closed diamonds represent fayalite and ahrensite (spinel structure), respectively, using *in situ* X-ray diffraction technique (Yagi et al. 1987) calibrated using the equation of state of NaCl (Dorogokupets and Dewaele, 2007). The diamonds substantiate line **c**. The open and closed circles represent fayalite and ahrensite using *in situ* X-ray diffraction techniques from Ono et al. (2013) using the same EOS and determine the line **d**. Figure reproduced from Ono et al. (2013).

The phase boundary derived from Ono et al. (2013) will be used for the rest of this manuscript and is described by Equation 2.1:

$$P = 0.5 + 0.0034T \qquad (2.1)$$

where P is in GPa and T is in K. However, the P,T position of the olivine/spinel phase boundary does not provide a complete picture of the transformation since the transformation to the high pressure phase is kinetically controlled and requires activation energy to initiate. Furthermore, there are at least two mechanisms that the transformation can operate. Under (quasi)hydrostatic conditions fayalite and its structural analogues have been shown to transform to their high pressure polymorph(s) *via* diffusion controlled incoherent nucleation and growth on grain boundaries and triple grain junctions (Brearley et al., 1992; Yagi et al. 1987; Remsberg et al, 1988; Burnley and Green, 1989). In this mechanism, because grain boundaries act as nucleation sites for the transformation to initiate, grain size has a considerable effect on the transformation rate. In general, higher temperatures also increase rate. In addition, Yagi et al. (1987) and Inoue (1975) found that the transition to the high pressure phase occurred at pressures ~20% higher if the high pressure stability field was entered through isothermal compression as opposed to isobaric heating. The degree of metastability also has a significant effect on the reaction rate which increases the further away the reaction takes place from the phase boundary. The second mechanism which has been shown to operate in the olivine/spinel transformation is that of a pseudo-martensitic transformation. Martensitic transformations are diffusionless which allows the new phase to propagate with a velocity on the same order as the speed of sound in the material. The transformation is accomplished by shearing discrete volumes of material and leads to a definite orientation between the parent and daughter phases. In the case of Fe_2SiO_4 and other structural analogues the $\alpha \rightarrow \gamma$ transformation is not truly martensitic since it occurs through a

diffusionless oxygen sublattice transition coupled with short range diffusional cation reordering (Poirier, 1981). Deforming Mg_2GeO_4 olivine in a Griggs apparatus in the spinel stability field Burnley and Green (1989), showed that under high levels of non-hydrostatic stress (>2 GPa) a pseudo-martensitic mechanism dominated. In particular, nucleation of the spinel phase occured by a coherent, shear-induced, intracrystaline mechanism in contrast to the incoherent nucleation and growth mechanism favoured under more quasi-static conditions. The morphology of the reaction products is that of thin parallel lamellae which can develop through intracrystalline nucleation. Figure 2.2 shows an example of some spinel lamellae nucleated in Mg_2GeO_4 (Burnley, 2005).

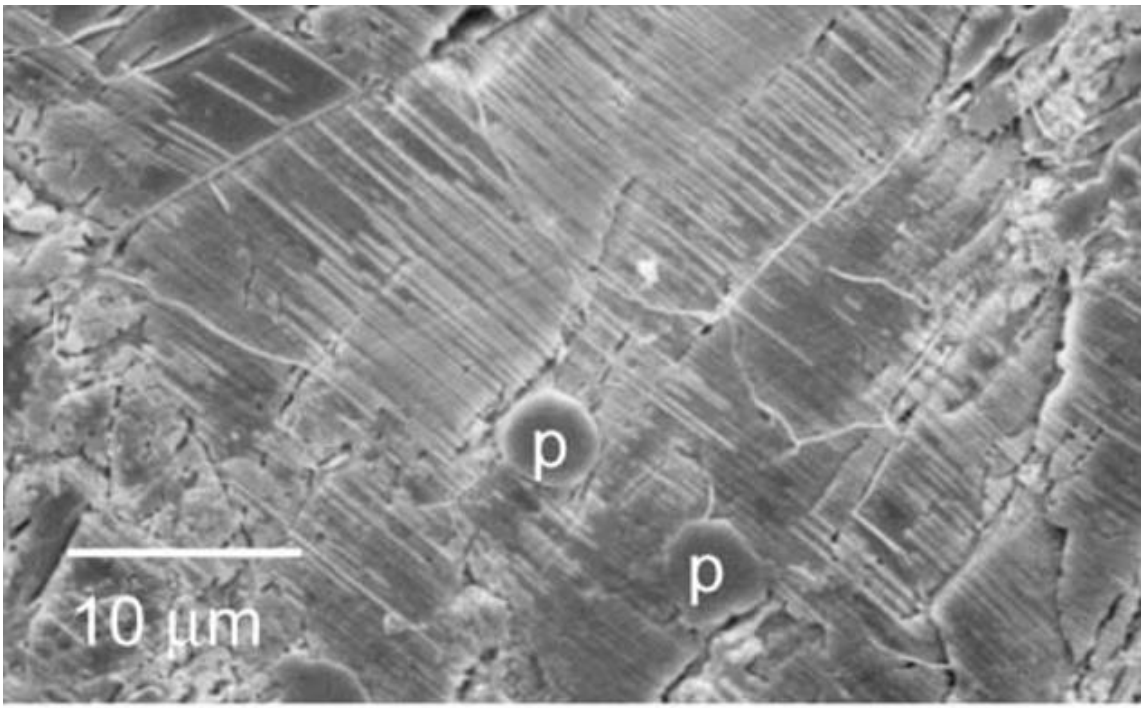

Figure 2.2: Two grains that contain a high density of lamellae. The boundary between the two grains runs from the center of the left side of the image to the top right hand corner. Lamellae in this sample are longer than in experiments that were conducted at lower temperatures. p represents Ge pyroxene. Figure reproduced from Burnley (2005).

The most significant factors that promote the coherent pseudo-martensitic transformation mechanism over the incoherent grain boundary nucleation mechanism is: 1) the level of

hydrostatic stress 2) the metastable overstep in pressure. Both effects tend to promote the growth of intracrystalline martensitic lamellae but their length tends to be affected by temperature where higher temperatures will extended their length. Using *in situ* time resolved synchrotron XRD Chen et al. (2001) were able to follow the structure refinements during the pseudo-martensitic $\alpha \rightarrow \gamma$ phase transition in Fe_2SiO_4. In particular, they were able to observe directly the delay in cation reordering relative to anions during transformation under non-hydrostatic conditions. Figure 2.3 shows the site occupancy as a function of temperature, which in their experiments is a proxy for time since they maintained a heating rate of 0.03 K/s. They were able to initiate the transformation at as low as 638 K at 6.9 GPa.

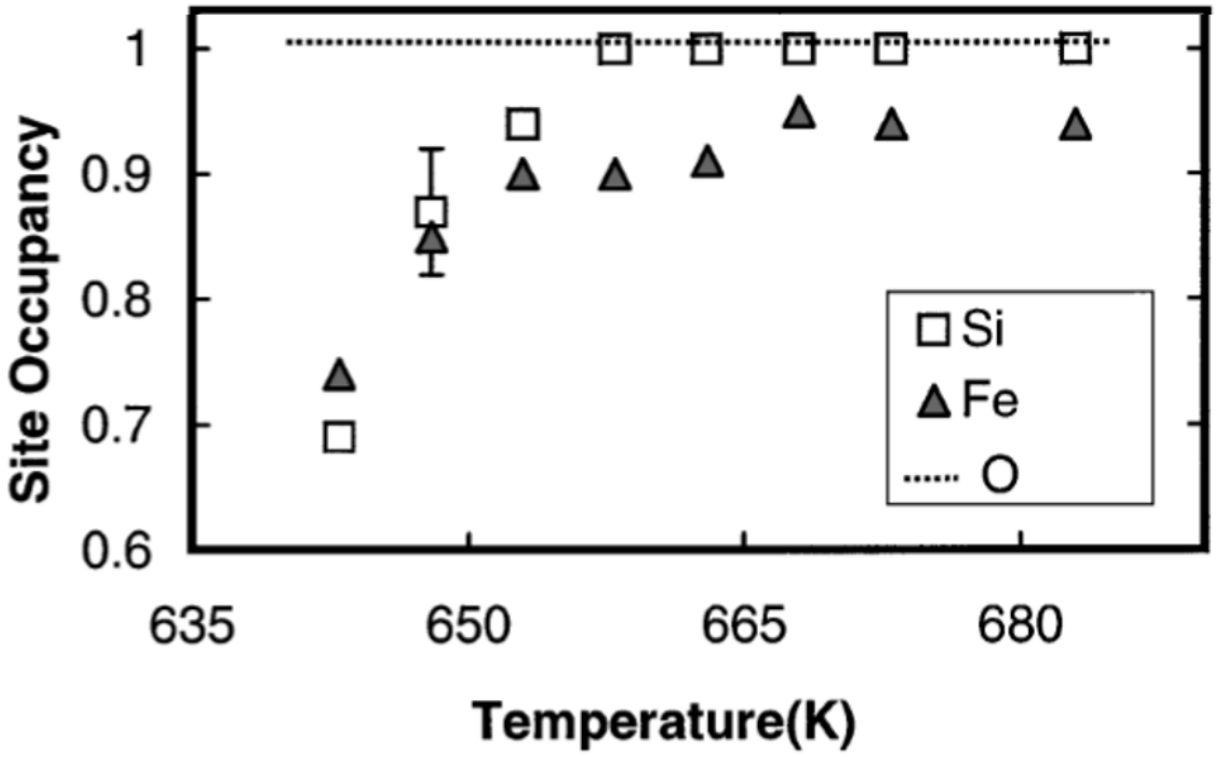

Figure 2.3: Site occupancies for Si, Fe and O during the olivine-spinel transition in Fe_2SiO_4. In this case temperature increases with time at a rate of 0.03 K/s. Note that the O occupancy is immediate and the Si and Fe cations follow. Figure reproduced from Chen et al., 2001.

In subsequent experiments, the same authors also found that Fe_2SiO_4 could initiate the transformation from $\alpha \rightarrow \gamma$ under static conditions at temperatures as low as 723 K at 5.7 GPa (Raterron et al, 2002). Stress was still a requirement for the pseudo-martensitic transformation to occur, however they inferred the stress localization related to the negative volume change of the transformation drove the pseudo-martensitic transformation mechanism. Both mechanisms are not mutually exclusive.

2.2 Transformational Faulting at High Pressure

2.2.1 High pressure faulting in ice and tremolite

More than 40 years after Bridgman's publication speculating that highly metastable, exothermic phase transitions may result in faulting under non-hydrostatic conditions (Bridgman, 1945), it was shown to exist in deformation experiments that studied the relationship between faulting and phase transitions by investigating the ice $I_h \rightarrow$ ice II and tremolite $\rightarrow$ diopside + talc transformations under metastable conditions (Kirby, 1987). He found, as is usual for brittle failure, rock strength increased steeply with confining pressure until a certain point where the shear stress required for fracture became independent of confining pressure and in some cases even decreased. The pressure where this occurred was strongly temperature dependent. Figure 2.4 shows the relationship between faulting and confining pressure for the ice $I_h \rightarrow$ ice II transition.

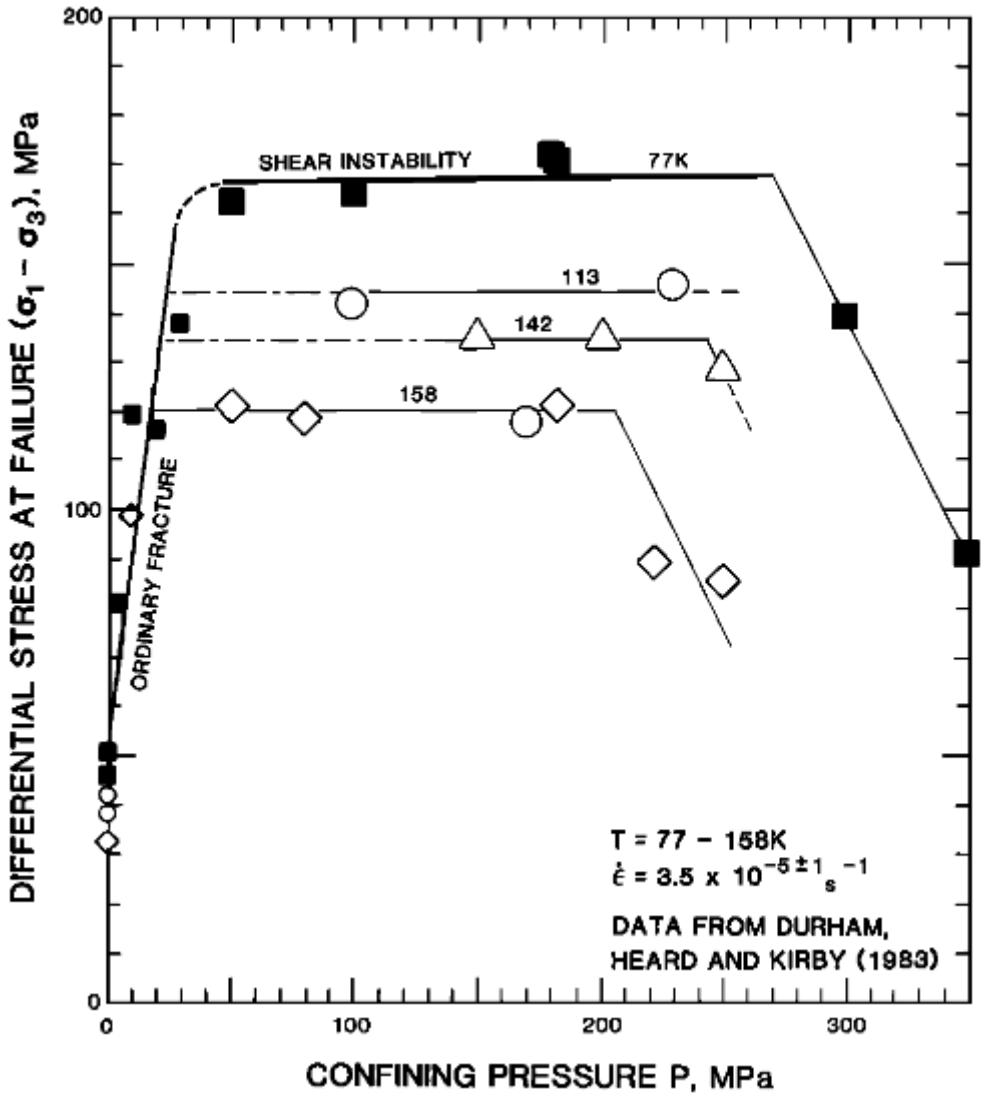

Figure 2.4: The effect of confining pressure on the shear stress required for failure in Ice for a range of temperatures. Note that at low confining pressures the shear strength required for failure increased but above a temperature dependent threshold the shear strength required for failure plateaus and even begins to decrease at high pressure. Figure reproduced from Kibry, (1987) based on data from Durham et al., (1983) and unpublished data from the same authors.

In addition to showing that faulting was not inhibited by confining pressure, it only occurred when the mean stress on the sample ($\sigma_m = (\sigma_1 + \sigma_2 + \sigma_3)/3$) was in the stability field of Ice II.

Figure 2.5 shows the mean stress and temperature conditions for failure compared to the phase diagram for ice.

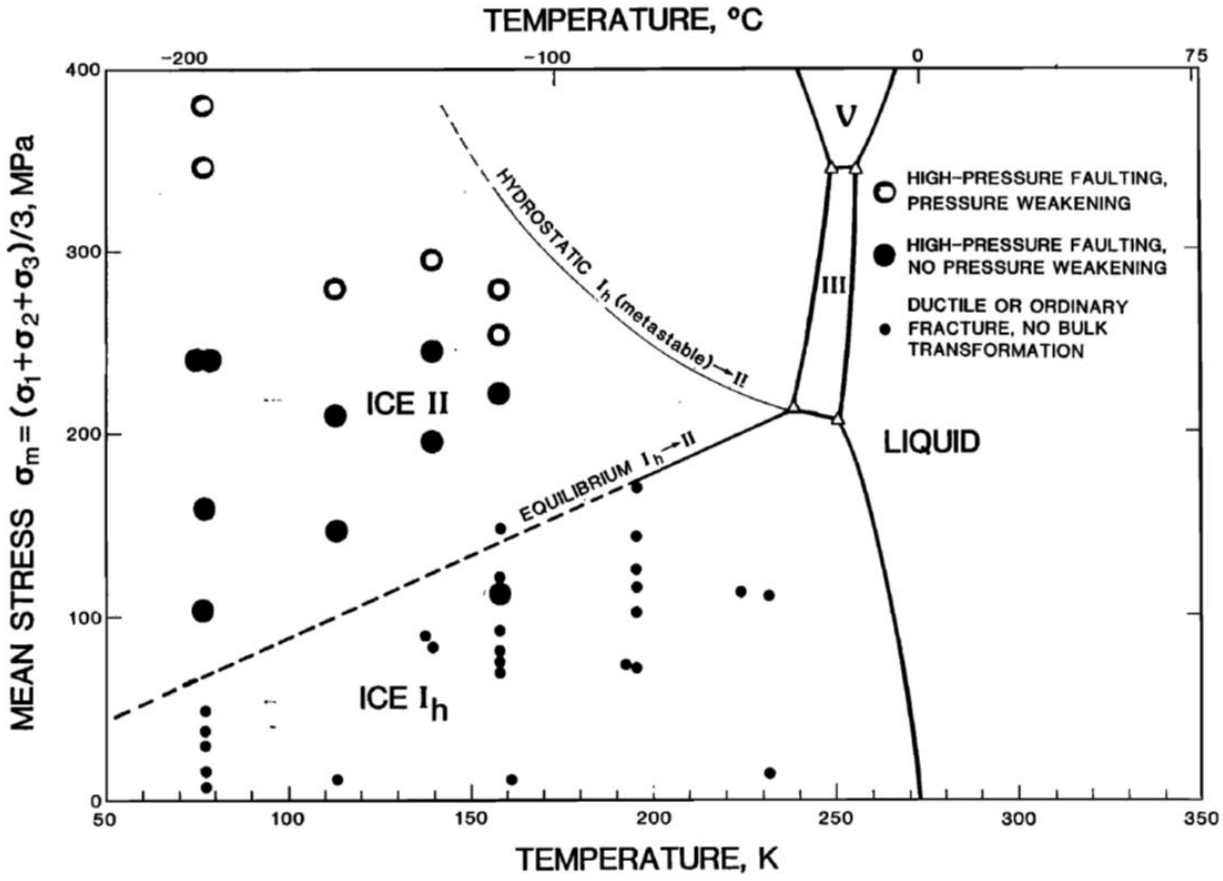

Figure 2.5: The mean-stress versus temperature conditions for triaxial tests on ice I_h. Based on data from Durham et al., (1983) and unpublished data from the same authors. Large open circles represent samples that experienced high-pressure faulting and pressure weakening, large solid circles represent high pressure faulting with no pressure weakening, and small solid circles represent ductile or ordinary fracture with no bulk transformation. Reproduced from Kirby, (1987).

Note that with only one exception, faulting only occurs in the ice II stability field. However, experiments performed at 195 K resulted in bulk transformation to ice II and did not experience faulting. They are not shown in Figure 2.5. Based on these results Kirby (1987) concluded that a necessary condition for a high pressure instability is that the σ_m vs. T conditions must be in the stability of ice II and bulk transformation to ice II does not occur. This hypothesis states that

transformation is localized in the shear zone and causes the instability, a theory previously articulated by Durham et al, 1983; Kirby et al., 1985 and Kirby, 1985.

Similar experiments were performed on polycrystalline tremolite (Kirby, 1987) under a constant strain of ~10^{-5} s^{-1}, at temperatures between 250 – 900 ^{0}C, and confining pressures of 0.1 – 1.8 GPa. At high pressure tremolite transforms to diopside + talc. As in the case of ice, high pressure faulting only occured when σ_m vs. T was in the high pressure stability field. Also consistent with the experiments in ice, faulted samples did not display bulk transformation, but instead occurred as fine grain material within the fault zone. Figure 2.6 shows the physical conditions of the experiments in relation to the phase diagram for tremolite.

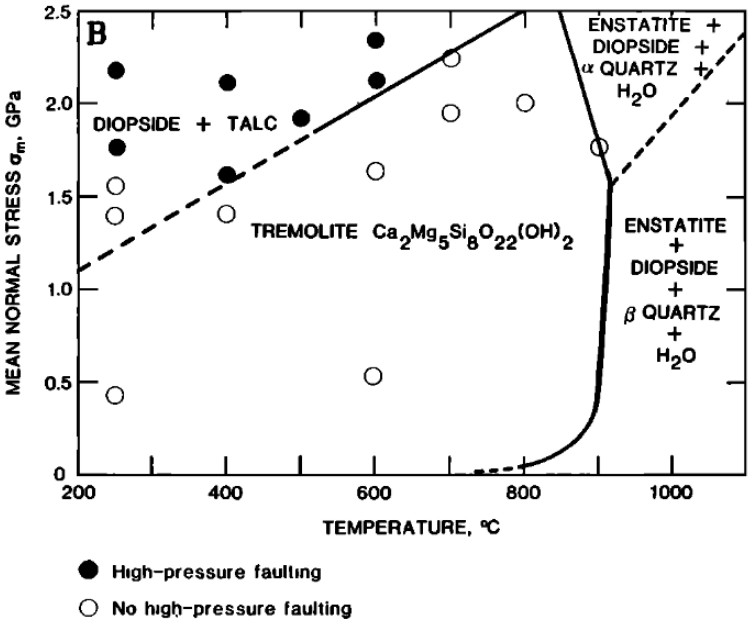

Figure 2.6: Physical conditions of the experiments on tremolite in relation to the phase diagram for tremolite. Closed circles represent samples that experienced high pressure faulting while open circles did not. Note that every sample that experienced faulting lies within the diopside + talc stability field. Figure reproduced from Kirby, 1987.

Kirby, (1987) was the first to display a new type of faulting that did not depend on confining pressure, but required partial transformation of the faulted material to a high pressure phase. This was the first experimental verification of a mechanism that could lead to faulting beyond the brittle-ductile transition and could operate at upper mantle pressure (σ_m > 2 GPa). However, the minerals that exhibited this type of faulting, ice and tremolite, do not exist in the mantle at the depths where DFEQs occur (300-690 km).

2.2.2 Transformational Faulting associated with the olivine→spinel transition

While Kirby et al., 1983 and Kirby et al., 1987 showed that transformational faulting could occur in some materials they had not shown its presence in materials characteristic of those found several hundred kilometers below the Earth's surface in subduction zones. The most likely candidate mineral for DFEQs is olivine, a mineral shown to transform to high pressure polymorphs at depth in the upper mantle (Ringwood, 1975) and expected to exist in a metastable state during subduction (Rubie and Ross, 1994). At ambient conditions olivine, which is magnesium orthosilicate with some of the magnesium replaced by ferrous iron, is a hexagonal lattice of oxygen atoms in which the silicon and metals occupy cavities. Under pressure, the lattice is compressed and the cavities diminish until they are too small to hold the silicon atoms and the mineral transforms to a higher density polymorph. Replacing the Si atoms with a larger atom with a similar configuration of valence electrons, such as Ge, is analogous to physically compressing the olivine lattice. Therefore, germanate olivine (Mg_2GeO_4) is identical in structure and chemistry to forsterite (Mg_2SiO_4), olivine's magnesium end member, with the exception that Si is replaced by Ge. Like forsterite it also undergoes a transformation analogous to that of

olivine → spinel, but occurs at lower pressure since the lattice cavities cannot accommodate the larger Ge atoms. In other words, the chemical pressure provided by the larger Ge atom requires less physical pressure to effect the transformation. This simplifies experiments designed to investigate phenomena associated with the olivine → spinel transition by reducing the pressure required to trigger the transformation in the laboratory, and therefore the sample size and complexity of experiments. For this reason, Ge-olivine is often used as a substitute for natural olivine with the assumption that it behaves analogously. In the presence of shear stress, Mg_2GeO_4 exhibited catastrophic faulting upon transformation from olivine → spinel under a narrow temperature range (Green and Burnley, 1989b). The results of their experiments fall into three categories: 1) At low temperatures (< 1000 K) the specimens were strong and ductile. Samples experienced a small degree of pseudo-martinsitic, shear-induced nucleation of spinel but growth of the nuclei is kinetically inhibited to the point that faulting does not occur. 2) At high temperatures (> 1300 K), abundant nucleation occurs and rapid growth of spinel was observed, but the specimens remained weak and ductile and did not exhibit faulting. 3) It is only in the temperature interval 1000 K – 1300 K that faulting occured. However, this temperature range can be extended to higher temperatures by increasing the strain rate by an order of magnitude to 10^{-3} s^{-1}. Figure 2.7 shows the P/T conditions where faulting occurred for experiments with strain rates of 10^{-5} s^{-1} - 10^{-4} s^{-1}, which is several magnitues lower than strain rates in the mantle.

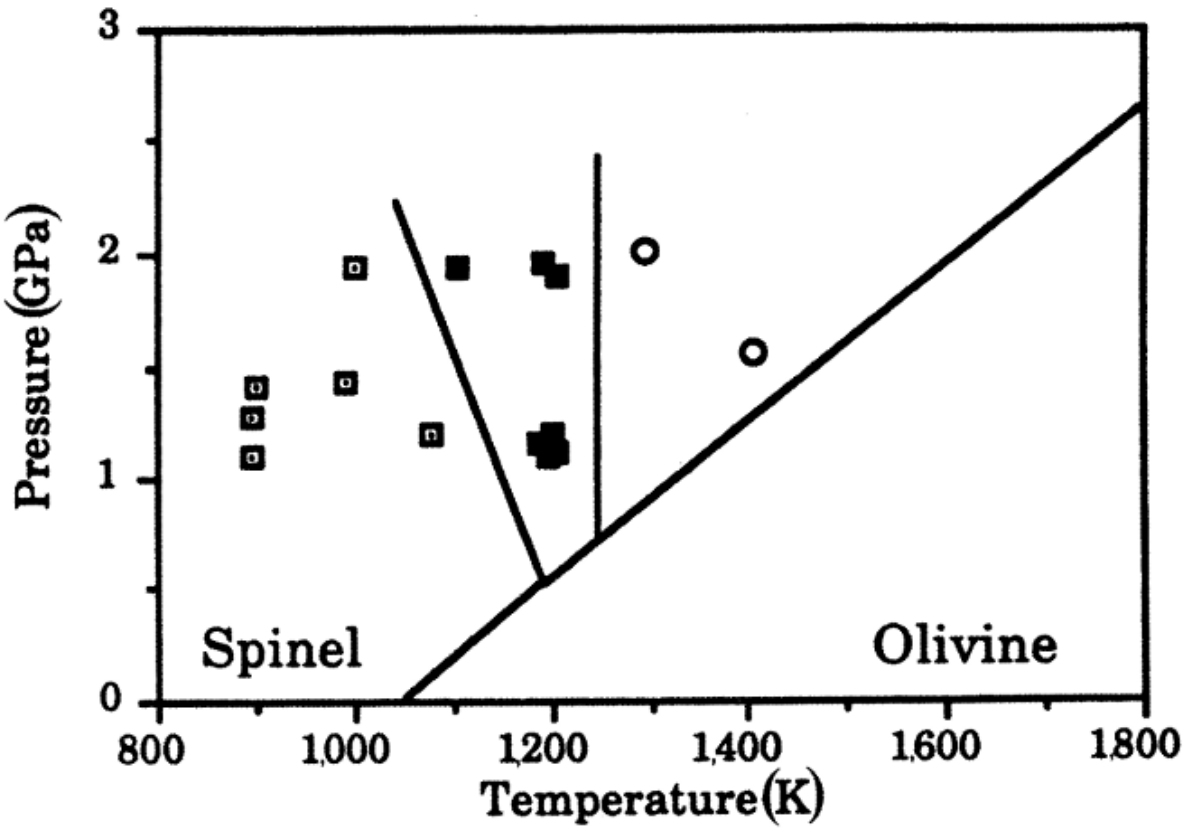

Figure 2.7: The P,T conditions of faulting upon transformation of metastable Mg_2GeO_4 olivine → spinel. Open squares represent specimens that were strong and ductile, open circles specimens that were weak and ductile, and closed squares represent specimens that failed. Figure reproduced from Burnley et al. (1991). Phase diagram from Ross and Navrotsky (1987).

Optical and electron microscopy of recovered specimens subjected to the P,T and strain rate conditions that led to faulting, show lenses of spinel with a strongly preferred orientation with respect to σ_1, the direction of maximum compressive stress, with most lenses perpendicular to σ_1. This comes in stark contrast to ordinary brittle failure where tensile cracks tend to preferentially orient parallel to the largest compressive stress. The spinel within the lenses is very fine-grained and sometimes developed in *en echelon* arrays. They referred to these structures as

"anticracks", a term developed to describe faulting in styolites (Fletcher and Pollard, 1981). Figure 2.8 shows an example of the anticracks that formed in a faulted sample of Mg_2GeO_4.

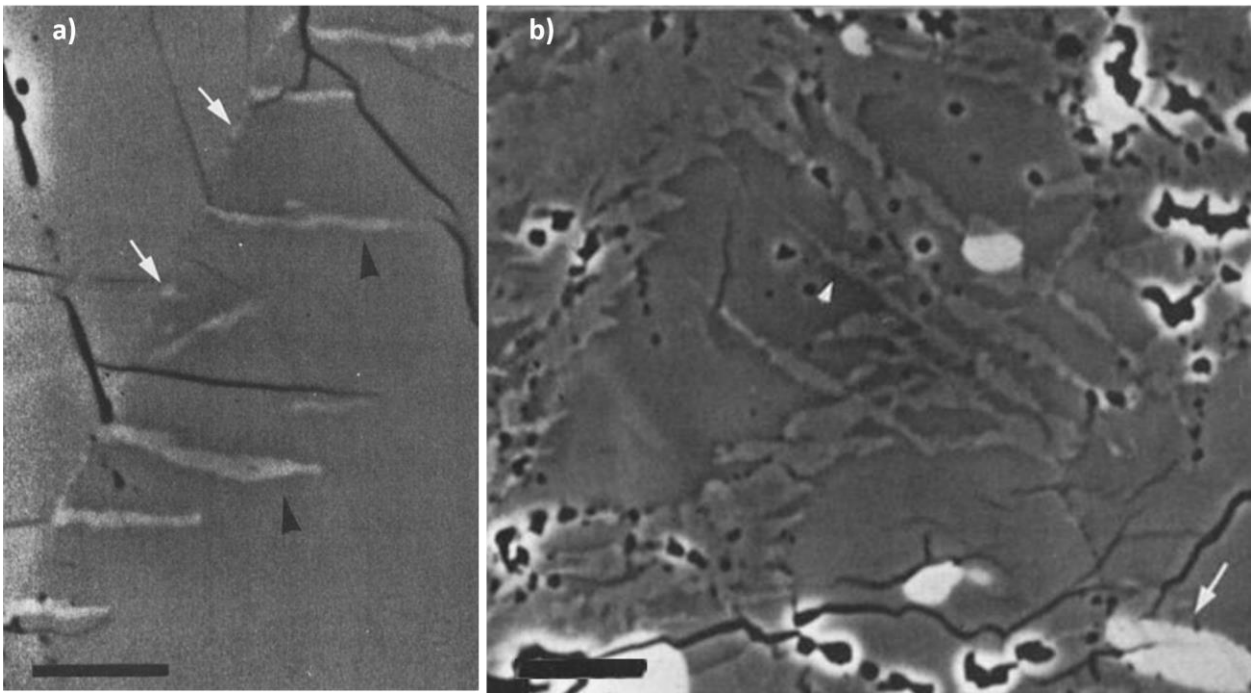

Figure 2.8: a) Anticrack lenses of spinel (black arrowheads) nucleated on a grain boundary between two olivine grains. Tiny spinel nuclei are also visible (white arrows). Scale bar 3 μm b) Image of the distribution of spinel lenses linking together in olivine. The lenses have nucleated on both grain and subgrain boundaries which are already decorated with tiny spinel nuclei (arrowhead). Spinel lenses have also nucleated on pyroxene inclusions (white arrow). Scale bar 10 μm. Figure modified from Burnley and Green (1991).

Anticracks are identical to tensional cracks (mode I Griffiths cracks) except the algebraic signs of the stresses and displacements are reversed. Figure 2.9 shows a comparison between the development of cracks and anticracks in faulted material.

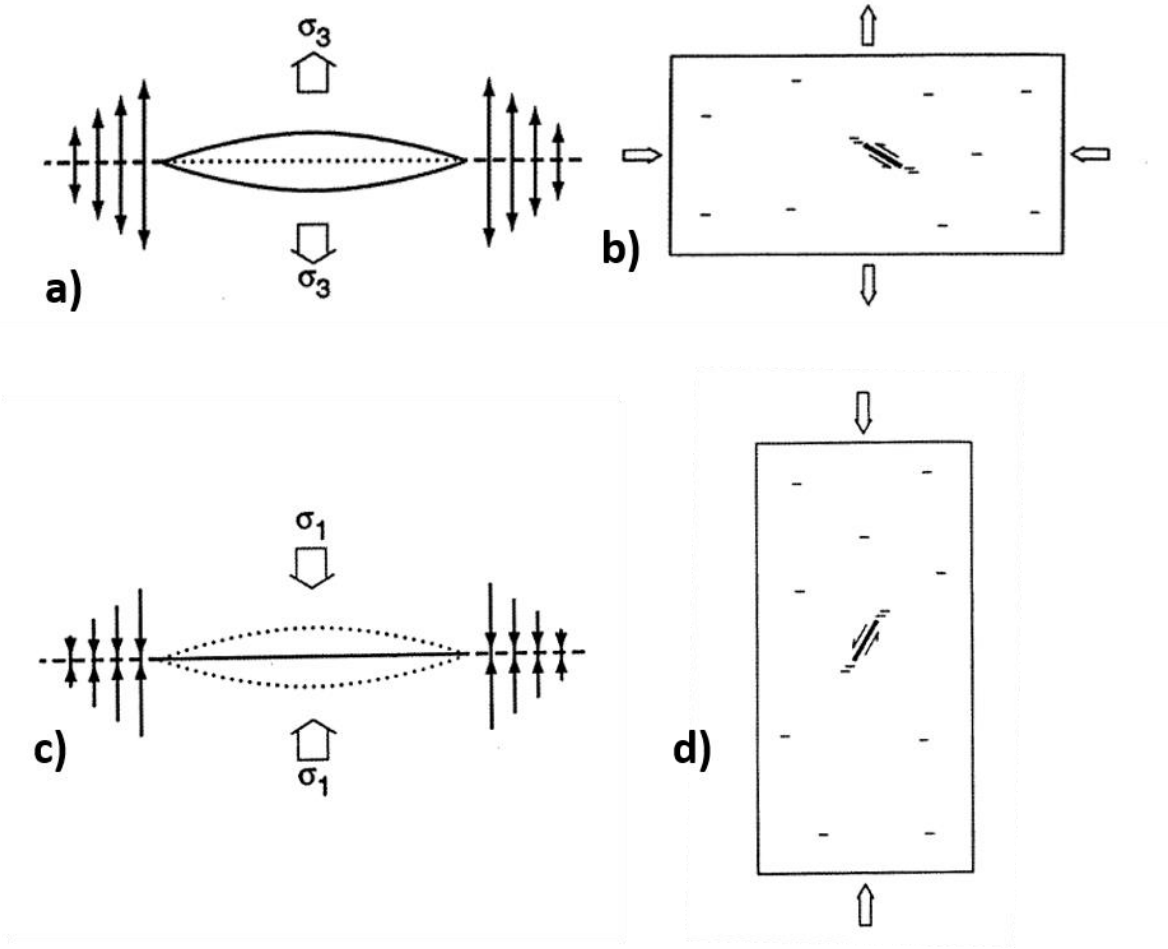

Figure 2.9: Comparison of mode I Griffiths cracks and anticracks. **a)** a remote tensile stress, σ_3, pulls open a small planar flaw (dotted line) yielding a lens shaped void with tensile stress concentration at its tips. Cracks are favoured when crack planes are oriented perpendicular to the smallest principal stress (σ_3). **b)** Brittle failure occurs when numerous cracks grow and link up with one another, allowing shear motion to occur along a macroscopic plane oriented at an oblique angle to the stress direction. c) A remote compressive stress, σ_1, initiates a volume reducing phase transition in a microscopic lenticular void (within dotted lines) which is filled with fine grained, low strength transformed material with the largest compressive stress concentration at its tips. Because the sign of the stress in **c)** is opposite to that of a), theory indicates that such cracks are favoured when crack planes are oriented perpendicular to the largest principal stress (σ_1). **d)** Failure occurs when numerous anticracks grow and link up with one another along shear motion to occur oblique to the principal stress direction but perpendicular to that **b)**. Figure modified from Green and Houston, 1995.

Consider a tensile stress that pulls open a small microcrack yielding a lens shaped void with tensile stress concentration at its tips. Such cracks are favoured when the smallest principal stress, σ_3, is perpendicular to the crack plane. Brittle failure occurs when microscopic cracks

grow and link up resulting in macroscopic shear motion oriented oblique to the stress direction. In contrast, anticracks occurs when fine-grained (< 1 μm) spinel forms in lens shaped regions whose plane is perpendicular to that of the largest compressive stress. Such fine-grained material operates similar to fluid-filled Griffith cracks. They lower the effective stress of the crack, but are unable to support shear stress. Their lens shaped geometry concentrates compressive stress at the tips of the lens promoting further anticrack growth. As a result of the exothermic nature of the olivine → spinel transition the heat released causes an increase in the local temperature encouraging the rate of formation. As in the case of mode I Griffiths cracks, they eventually link up and form a macroscopic network of spinel filled anticracks that cannot support shear stress. This results in a macroscopic fault in a plane oblique to the largest principal stress but oriented normal to the fault plane that would occur in the case of brittle failure. Green and Burnley (1989b) showed that the anticrack mechanism could lead to faulting as a result of phase transformation in minerals structures known to occur in the mantle. However, despite the success of the anticrack faulting model based on their results studying Mg_2GeO_4, several important questions still remained. Namely, can faulting occur at very high pressure, such as that found in the mantle's transition zone where the deepest earthquakes occur, and is germanate olivine Mg_2GeO_4 a truly reliable analouge? In particular, Mg_2GeO_4 transforms directly from $\alpha \rightarrow \gamma$ phase whereas natural olivine, which is dominated by forsterite the Mg end member of olivine, transforms to an intermediate β phase between the α and γ phases creating a two-phase stability field with preferential partitioning of iron into the denser phases (Katsura and Ito, 1989; Akaogi et el., 1989). The following year, Green et al. (1990) performed experiments on natural olivine in a multianvil apparatus at pressures and temperatures reflective of the mantle's transition zone. They inserted Al_2O_3 pistons along one compressive axis to generate a large component of non-

hydrostatic stress while the sample was under load. Samples were pressurized from 9 – 15 GPa, at temperatures of 1550 – 1650 K, with strain rates of ~ 2 $x10^{-4}$ s^{-1}. They were able to show that the same mechanism operating in the Mg_2GeO_4 can also operate in natural silicate olivine $(Mg,Fe)_2SiO_4$ during the onset of the olivine → wadsleyite ($\alpha \rightarrow \beta$) transition. Figure 2.10 shows a recovered specimen that experienced a macroscopic fault traversing the entire sample and microstructures displaying anticrack wadsleyite lenses.

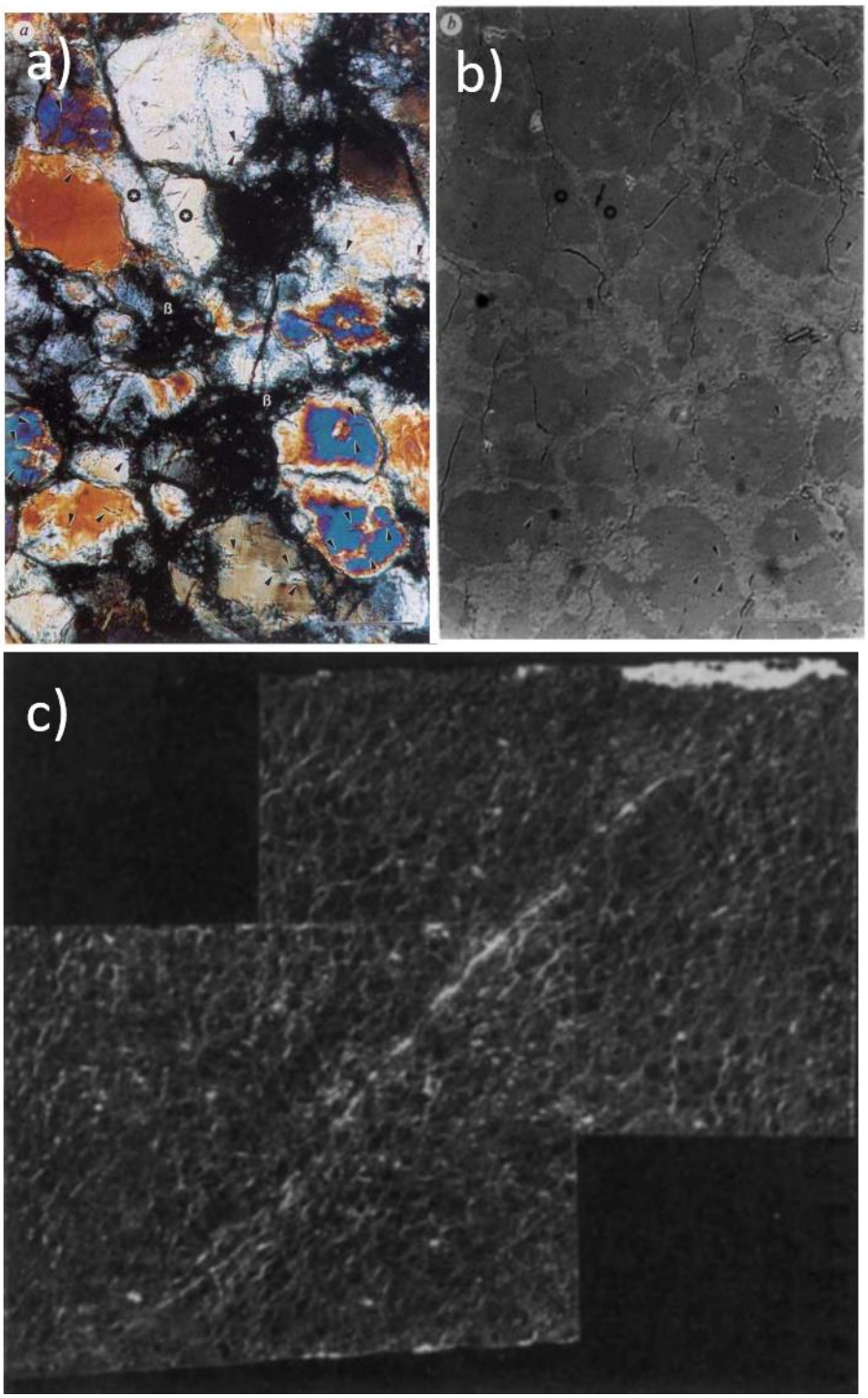

Figure 2.10: Anticrack associated faulting at very high pressure in natural olivine. a) Transmitted light image with crossed polarizers of the recovered specimen. Regions of transformation to the β-phase show low birefringence and are labelled β. The lenses have a strong preferred orientation in the E-W direction. The fault runs from the upper left to the lower right producing a right-lateral offset in an olivine crystal (stars). b) The same as that of a) in reflected light.The β-phase appears brighter than the olivine. It is distributed throughout the fault zone and on olivine grain and subgrain boundaries (arrowheads). The offset (arrow) in the olivine crystal (stars) is clearly visable as are the thin regions of β-phase along the fault. Scale bars 50 μm. c) Low magnification micrograph in obliquely incident light showing a fault that traversed the entire sample. Horizontal dimension in 3 mm. Images reproduced from Green et al., 1990.

The microstructures witnessed in this experiment are morphologically indistinguishable from those found in Mg_2GeO_4. They claim that the results of this experiment provide conclusive evidence that transformational faulting, resulting from the anticrack instability, was responsible for faulting that occurred at HPHT and not a result of brittle failure. They go on to assert that this provides strong support for the hypothesis that the anticrack mechanism is responsible for DFEQs.

In addition to the anticrack mechanism, a second class of microstructures which can lead to transformation-induced faulting was observed in magnesium germanate (Riggs and Green, 2005). They observed thin planar zones of spinel that form along crystallographic planes in deformed grains at temperatures cooler than those that allow significant development of anticracks. Figure 2.11 shows an example of this second class of structure that can lead to HPHT faulting.

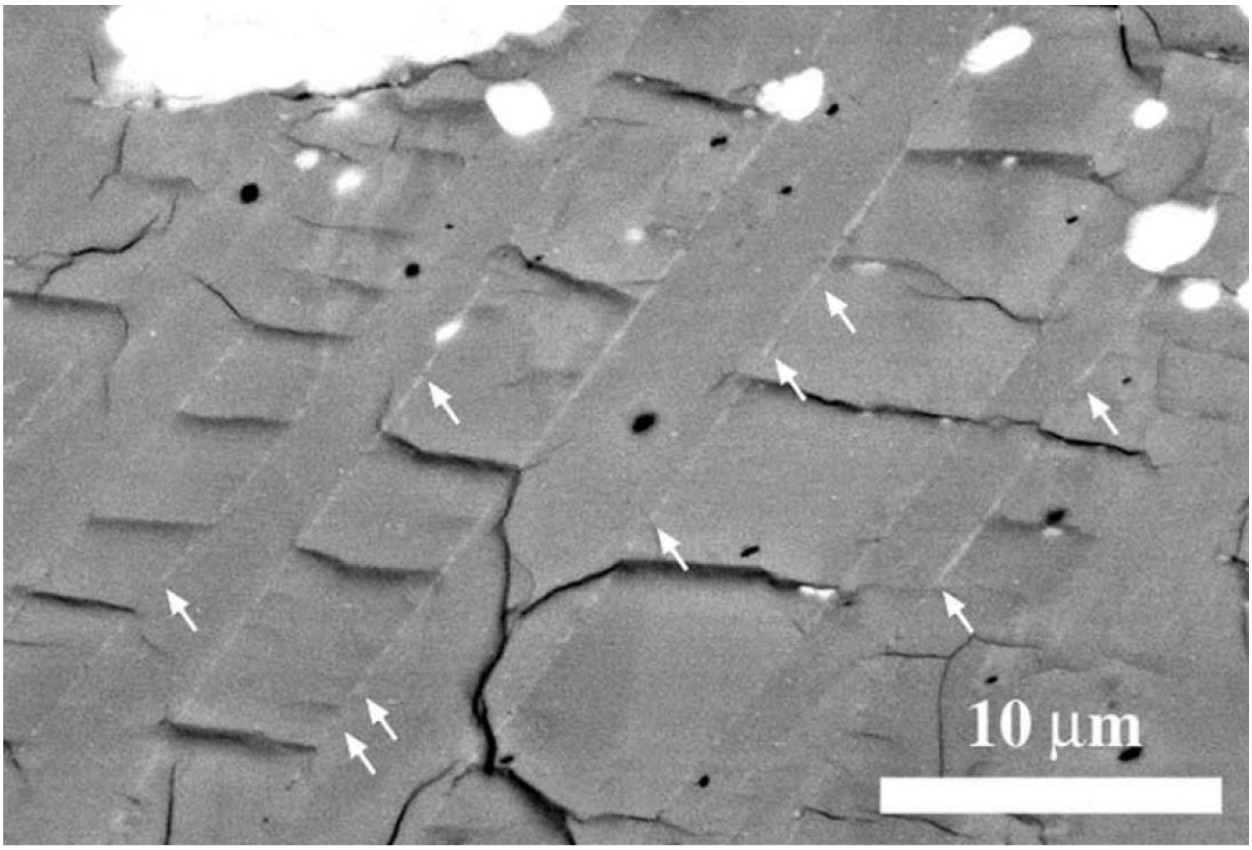

Figure 2.11: Image of planar transformation transformation structures developing along subgrain boundaries in Mg_2GeO_4 olivine. Arrows indicate discontinuous portions of the developing zones. The distribution of small unloading cracks between pairs of these zones was a typical signature of dislocation pileups produced in these experiments. Figure reproduced from Riggs and Green, 2005.

The development of these zones was shown to be rapid and only occurred after ~25% bulk strain. Increasing strain lead to progressive development of these zones, in turn leading to bulk shear failure once a continuous pathway of fine-grained spinel was formed that traversed the specimens.

2.3 Acoustic emission at high pressure and temperature

The results of Green and Burnley (1989b), Green et al. (1990), Burnley and Green (1991), Tingle et al. (1992) and Riggs and Green (2005) provided experimental justification for

the theory that solid-solid phase transitions of mantle minerals may be responsible for the existence of DFEQs. In addition they also presented a self-consistent theory analogous to brittle failure at low pressure and temperature. However, in addition to demonstrating that dynamic instabilities can occur at HPHT, confirmation that the instability is accompanied by elastic radiation is also required for any potential earthquake mechanism. The first experiment to measure AE at high pressure was that of Meade and Jeanloz (1989) who reported acoustic emissions associated with phase transformations in Si and Ge in the diamond anvil cell DAC at pressures as high as 70 GPa. They speculated that these emissions were produced by shear translations associated with displacive phase transformations. While neither Si nor Ge are relevant to a mantle composition, they did demonstrate that mechanical instabilities associated with phase transformation could produce acoustic signals. The same authors were also able to measure AEs generated by serpentine in the DAC at HPHT *via* two different mechanisms : 1) dehydration of serpentine at P,T conditions corresponding to 150 – 300 km depth and 2) amorphization of serpentine at conditions reflecting 500-650 km depth (Meade and Jeanloz, 1991). To test whether acoustic emissions accompanied faulting in Mg_2GeO_4 by the anticrack mechanism, Green et al. (1992) attached a pinducer (a springloaded piezoelectric transducer) to the base of the bottom anvil in their deformation Griggs apparatus to monitor acoustic activity throughout deformation. Experiments were performed on the type of Mg_2GeO_4 polycrystal used in previous high pressure faulting experiments and under similar experimental conditions (Green and Burnley, 1989b; Brunley et al., 1991). Two experiments were run that exhibited faulting in the recovered samples, with the faults running the entire length of each sample. Figure 2.12 shows the stress vs. strain curves compared to acoustic activity for both experiments.

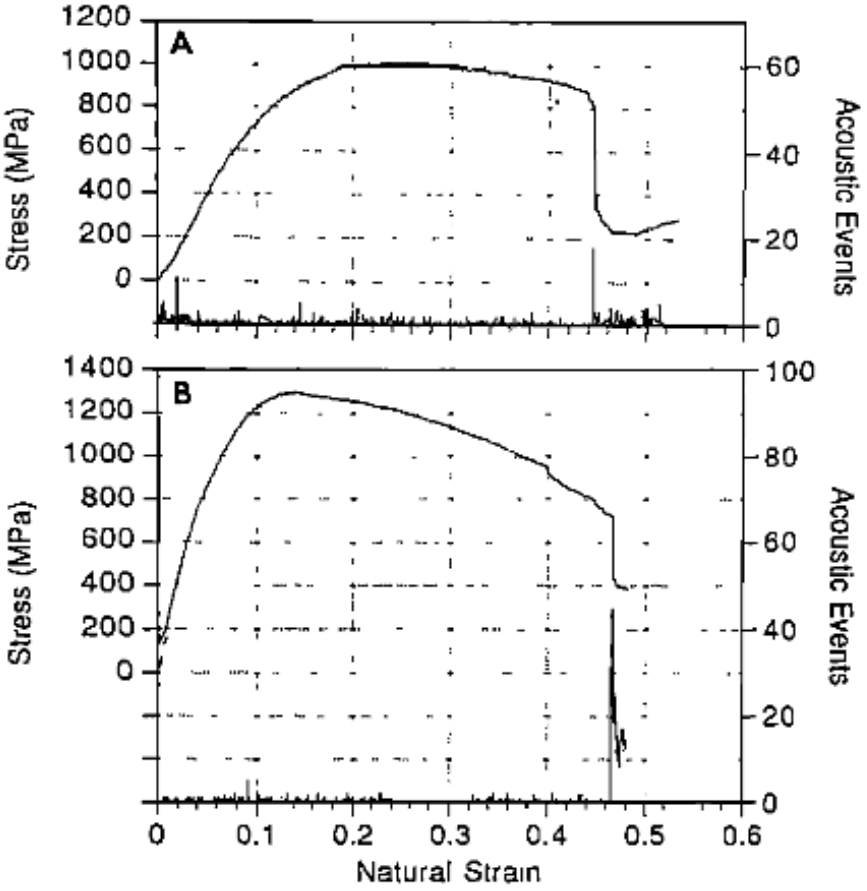

Figure 2.12: Stress-strain and acoustic emission plots two HPHT faulting experiments on Mg_2GeO_4. In both experiments, extensive plastic strain preceded failure and the stress began to fall before faulting was initiated. Acoustic emission was detected only during the abrupt stress drop accompanying faulting. Figure reproduced from Green et al., 1992.

Failure in the first sample occurred after 45% natural strain and differential stress of 800 MPa. The abrupt stress drop that occurred was accompanied by a burst of acoustic emissions. In the second experiment failure occurred at 700 MPa and 47% natural strain. Again, acoustic emissions accompanied the stress drop. Interestingly, neither experiment recorded any acoustic events associated with the generation of anticracks that precede faulting. The authors concluded that this may indicate that microanticracks form aseismically although any elastic energy they produce may have occurred outside the frequency range of their recording transducer, 2 KHz –

5MHz. This is an important result supporting the viability that the anticrack mechanism is responsible for DFEQs since it produces shear faulting, radiates elastic energy, functions at HPHT and occurs in mineral structures known to occur in the mantle at depths where DFEQs occur. In particular, further credibility is lent to their results since the anticrack mechanism was shown to behave in an identical manner at very high pressure (> 14 GPa) in natural olivine (Green et al., 1990). However, for more conclusive evidence that phase transitions are responsible for deep earthquakes experimental systems had to be developed that can operate at HPHT and perform more rigorous microseismic monitoring of the faulting process.

2.4 Microseismicity at high pressure and temperature

The first system developed with the potential of monitoring acoustic emission during deformation at very high pressure (> 20 GPa) and temperature (>2000 ^{0}C) using more than one acoustic sensor was Dobson et al., (2004) who incorporated acoustic capabilities into a multi-anvil apparatus. They achieved this by placing small piezoelectric transducers on the back truncations of two of the eight WC anvils that translate uniaxial compressive stress to an octahedral cell. Al_2O_3 pistons were placed into the octahedral cell in contact with the sample to act as waveguides that translate acoustic signals generated inside the sample and relay them to the piezoelectric transducers which convert mechanical energy (elastic waves) into an electrical signal. Figure 2.13 shows a schematic of their experimental setup.

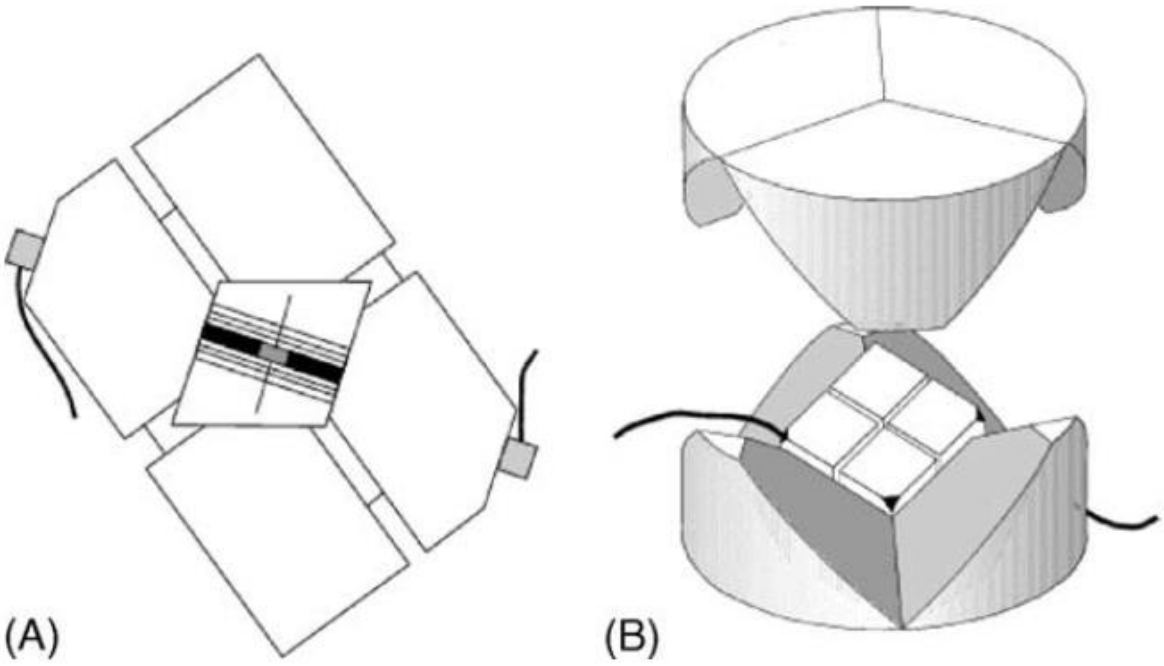

Figure 2.13: Schematic of the multi-anvil AE setup. (A) Cross-section of the octahedral cell and anvils. The transducers are mounted on the rear truncations of the anvils. The Al_2O_3 pistons that acoustically couple the sample to the anvils and provide an axis of deviatoric stress are shown in black. (B) The entire assembly placed between the first-stage wedges. Uniaxial compression of the wedges applies a load to the anvils which compress the sample. The transducers are placed in the gap between the wedges which approach one another under load but never touch. The cables exit through the gap. Figure reproduced from Dobson et al., 2004.

Because of its hardness, in addition to their functioning as waveguides, the Al_2O_3 pistons, inserted with their cylindrical axis parallel to the sample cylindrical axis, provide a direction of elevated stress along this direction (Karato and Rubie, 1997). This is an essential component of any experiment investigating deep earthquakes phenomena because multi-anvil apparatuses are typically designed to generate quasi-hydrostatic pressures, however deep earthquakes occur under non-hydrostatic conditions, therefore an axis of deviatoric stress must be generated. The amount of deviatoric stress generated depends upon the length and basal surface area of the Al_2O_3 pistons with longer pistons and small basal surface areas result in higher deviatoric stresses in the sample. Rapid sampling of acoustic data over the course of an experiment

generates extremely large amounts of data. In addition, compression of the octahedral cell and gasket formation during pressurization creates an inherently acoustically noisy environment in a multianvil apparatus, particularly at low pressures. To avoid being overwhelmed with massive amounts of insignificant data, the system sets an amplitude threshold that must be breached in order for the system to trigger an event. Using their system they were able to record AEs associated with antigorite dehydration at pressures up to 8 GPa (Dobson et al., 2002). To distinguish between events originating within the sample and those located outside it, they only considered events whose arrival times were within a Δt of 0.6 μs of one another which was the p-wave travel time through the sample. Figure 2.14 shows Δt vs. T for the experiment performed on antigorite at 4 GPa indicating the one-dimensional location of events along the assembly axis.

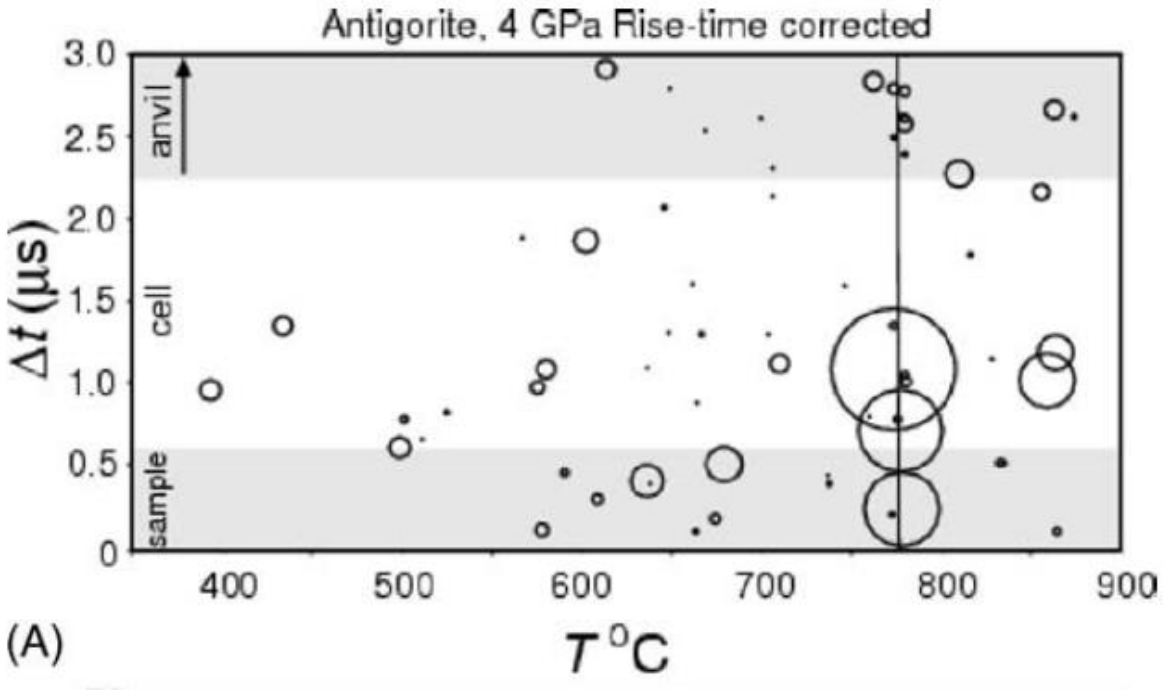

Figure 3.14: AE activity vs. temperature during antigorite dehydration. The size of each circle represents the energy of the event. Δt represents the difference in arrival time between transducers and is used as an indirect means of locating events within the pressure assembly. $\Delta t < 0.6$ μs are considered to have originated in the sample and is shown in grey along the bottom of the plot. Figure reproduced from Dobson et al. 2004.

They also carried out experiments to monitor AE during the olivine-wadsleyite transformation at 16 GPa. They observed faulting in the recovered sample and fine grained spinel was present in the fault zone, and they also recorded AE during heating between 1100 – 1200 ^{0}C however they suspect that faulting occurred at low pressure during cold compression and the AE was a result of readjustment of the cell associated with the negative volume change in the sample that accompanies transformation.

The next system of this kind was that of Jung et al. (2006). Their system is similar to that of Dobson et al. (2004) except they employ a total of four piezoelectric transducers instead of two which operate at a higher frequency range. The geometry of the sensors is that they are equidistant from the sample with three in the upper hemisphere, with respect to the sample, and one in the lower hemisphere. As a proof of concept they performed 6 experiments on WC samples with precut grooves located at either at the top, middle, or the bottom of the samples designed to act as predetermined sites for fracture upon pressurization. In each experiment, when fracturing of the WC samples occurred the authors reported hearing an audible sound accompanied by high energy AEs received in rapid succession at all four transducers. Figure 2.15 shows images of the fractured samples post recovery and the waveforms recorded by each transducer upon fracture.

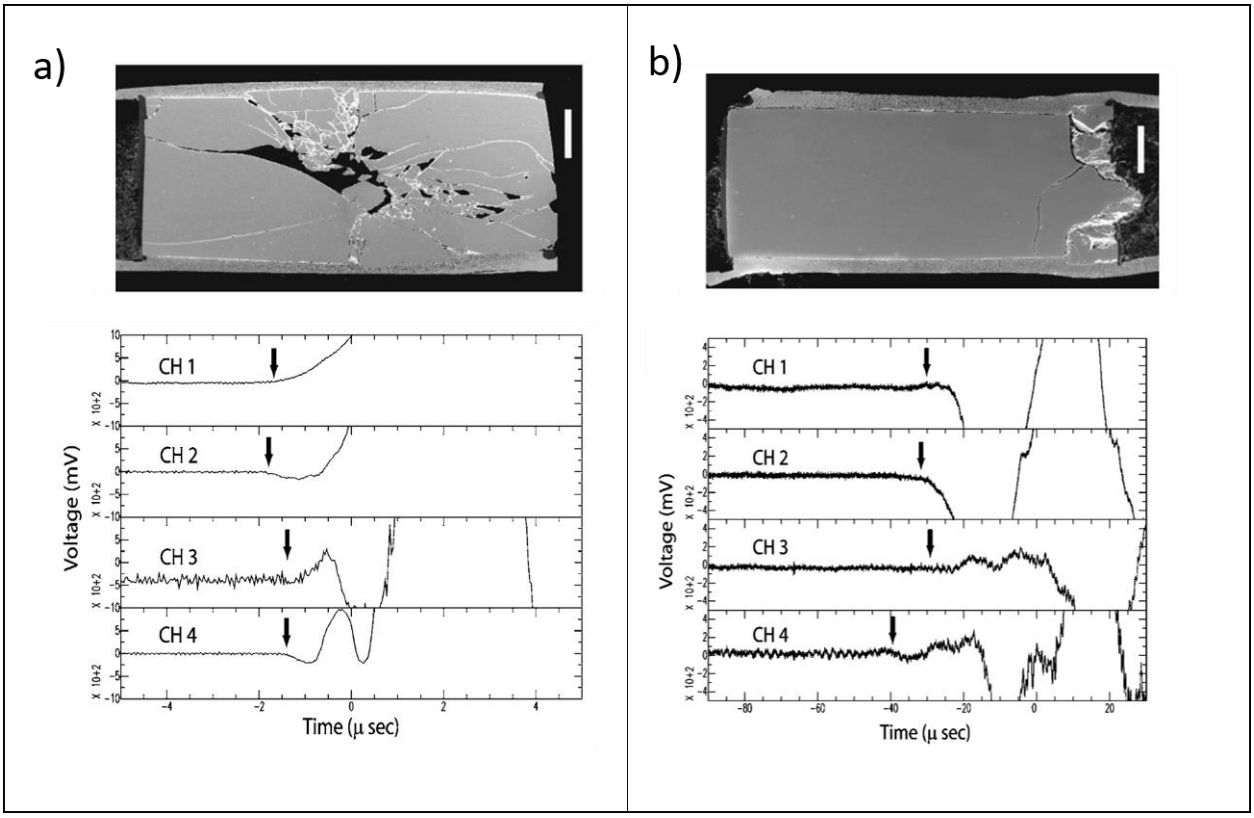

Figure 2.15: Images of the fractured WC samples and the waveforms generated during fracture. a) The fracturing of the WC occurred near the center of the sample. Note that the arrival times of the waveforms nearly coincide. b) Fracturing of the WC occurred near the bottom of the sample nearer to the transducer in the lower hemisphere. The wave arrived earlier on this transducer than the 3 stationed in the upper hemisphere, further away from the location of the fracture. Figure modified from Jung et al., 2006.

In the experiment where the WC sample fractured in the middle, the acoustic path length from the break point to the transducers was approximately equidistant, whereas in the experiment where the WC fractured near the bottom it occurred nearer to the single transducer in the lower hemisphere compared to the three transducers in the upper hemisphere. The authors claim they were able to determine the location of these acoustic events by measuring the delay in the arrival time of waves proceeding the transducer that received the initial impulse. The discrepancy in time between the first and last arrivals for the experiments that fractured at the middle and bottom of the sample are ~0.4 μs and ~10 μs respectively. However, the time required for an acoustic signal to travel the entire 7.5 mm length of the WC sample is ~0.5 μs for an acoustic

velocity of 6500 m/s for WC. Therefore, while it is possible the event they claim to have occurred near the center of the sample did originate within it, it probably occurred somewhere near the sample perimeter and the event they claim to have originated near the bottom of the sample likely occurred outside it. However, in principle, the system is capable of resolving the location of acoustic events within the sample in three-dimensions. Analysis of the polarity of the first motions of the waveforms could also be carried out to access information about the nature of faulting (i.e. implosion, explosion of shear). There is a mixture of polarities in the first motions for each event recorded which the authors claim indicates shear fracture took place in both experiments. This system was successfully used to record AEs associated with frictional sliding in serpentine at very high pressure (Jung et al., 2009).

The HPHT systems described above are both capable of monitoring AE under HPHT conditions in multi-anvil apparatuses. However, in both cases, to distinguish signals originating within the sample from those outside of it they rely on simply estimating the time required for an acoustic signal to traverse the sample and presume that if the earliest and latest signals of an acoustic event arrive in under this time they originated within the sample. While this is a reasonable assumption it does not uniquely determine that an event came within the sample since signals just outside the sample but very near the center of the pressure cell could arrive with a Δt below their requirement and masquerade as signals from the within sample. However, provided a system has 4 or more transducers it is possible to use arrival time data to invert for the location of an event. This was first achieved in the multi-anvil apparatus by de Ronde et al. (2007) who employed a total of 8 transducers, utilizing the rear truncations of every anvil. Using an automatic arrival time picking algorithm and a weighted least squares inversion algorithm they were able to locate events within the sample and pressure assembly to ~ 1mm accuracy.

Experiments on Al_2O_3 samples with pre-cut notches to initiate fracture were carried out to test their system and they found that more than 95% of AE events located within 2σ of the sample. Figure 2.16 shows a reflected light micrograph of the recovered sample and the locations of large events within the pressure assembly.

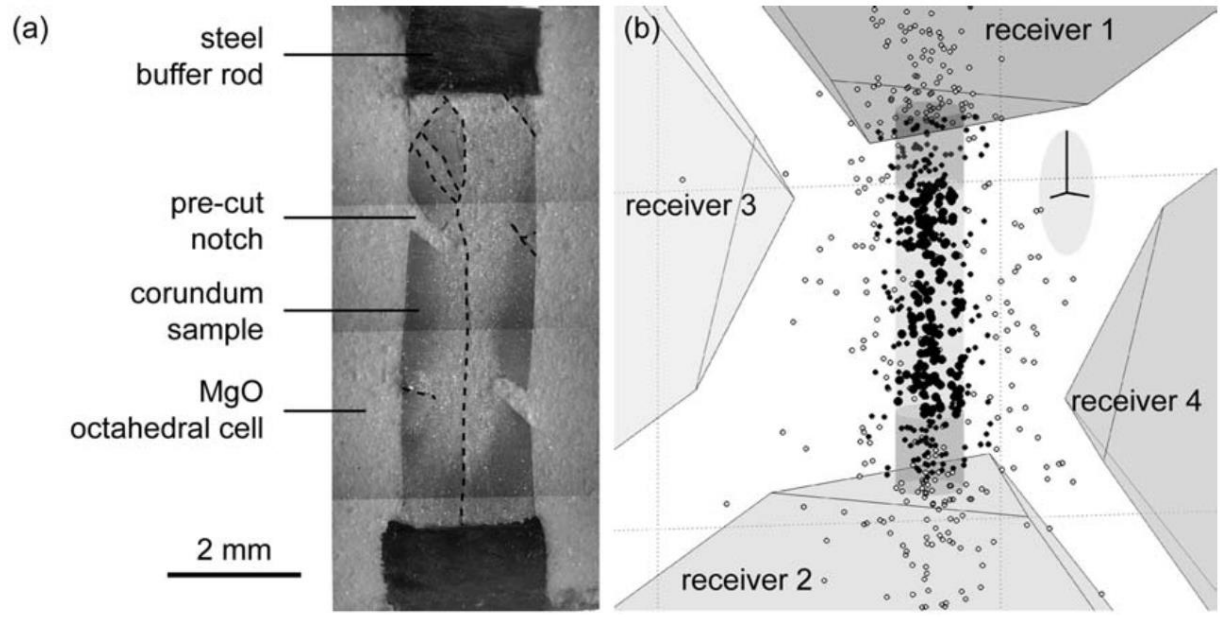

Figure 2.16: Deformation of Al_2O_3. (a) Reflected light micrograph of sample cross-section. The internal part of the sample is crushed, indicated by its light grey appearance. Brittle fractures (dashed lines) occur near the top of the sample and along its vertical axis. (b) 3D-view of the sample between four tungsten anvils, with hypocentres for events during axial compression to 4GPa. Hypocentre annotation: closed-large = inside the sample, closed-small = within 1σ from the sample, open-small = outside1σ from the sample. Figure modified from de Ronde et al., 2008.

Using the system just described, the same group was able to infer phase transitions *via* detecting an increase in acoustic activity associated with the readjustment of the pressure medium that accompanied the negative volume of the transition (Dobson et al, 2007; de Ronde and Dobson, 2008).

The most recent advancement in HPHT AE was developed by Gasc et al., (2011) who simultaneously collected high energy synchrotron radiation while recording acoustic activity during their experiments in a deformation DIA (D-DIA). The addition of synchrotron radiation

allows for the *in situ* collection of XRD and radiographic data which can be used to monitor the crystal structure and stress and strain state of the sample. Therefore any acoustic activity associated with dehydration or a phase transformation can be directly correlated. The D-DIA decouples stress and confining pressure which allows for far more control over deformation (Wang et al, 2003). Using this system, Schubnel et al. (2013) performed HPHT deformation experiments on Mg_2GeO_4 to test for transformational faulting. Figure 2.17 shows differential stress, strain and acoustic emission rate for an experiment where transformational faulting occurred.

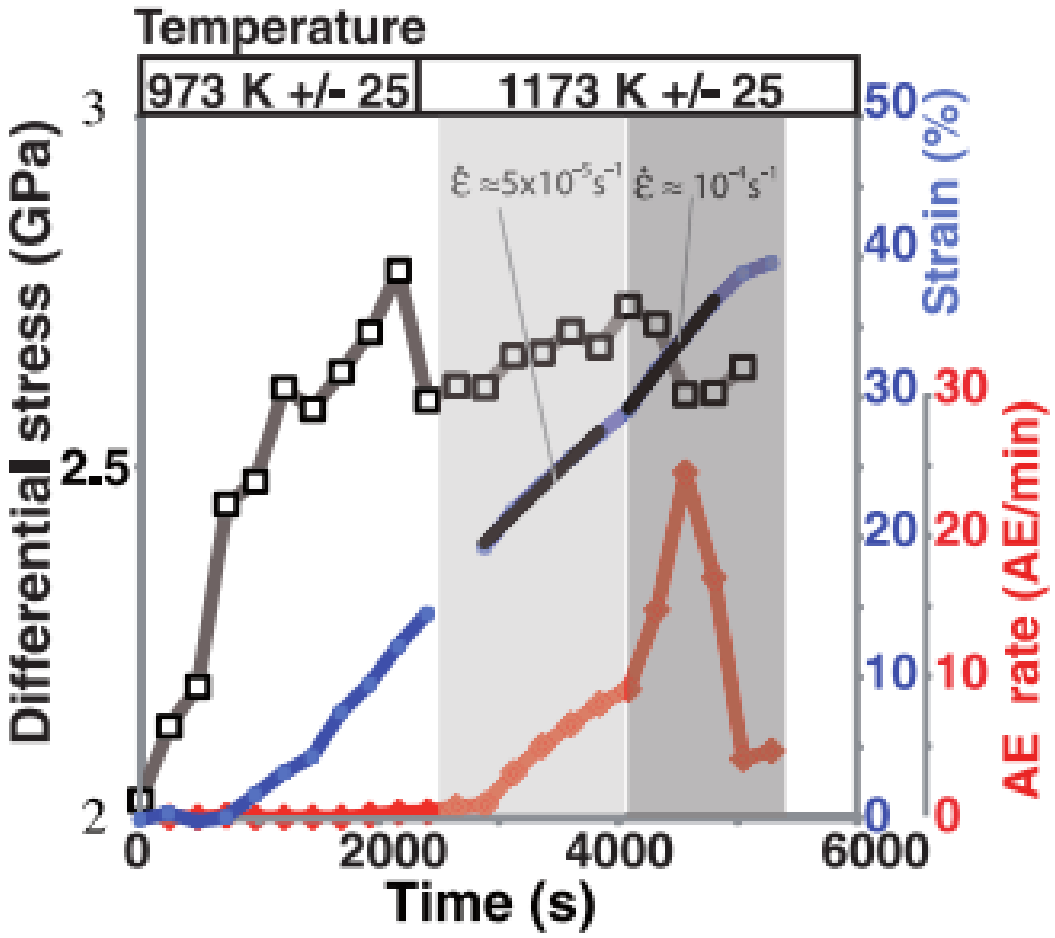

Figure 2.17: Evolution of temperature, differential stress, strain and AE during an experiment on metastable Mg_2GeO_4. Figure reproduced from Schubnel et al. (2013).

In this set of experiments they were able to directly link the onset of the phase transformation to a drop in stress accompanied by intense acoustic activity resulting from faulting under nominally ductile conditions. Similar to Green and Burnley (1989) and Burnley and Green (1991) they found that faulting only occurred in a narrow temperature window (1000 – 1250 K). Microstructural observations of the recovered samples displayed planar transformation features similar to Riggs and Green (2005) which they suspected caused dynamic weakening involving superplasticity of the nanocrystalline spinel reaction products. From this they inferred that the transformational faulting model and the shear instability model may not be mutually exclusive. Furthermore, moment tensor inversion of AE events displayed pure double-couple sources and the distribution of the number of events vs. magnitude obey the Gutenburg-Richter law which suggests the results they witnessed in their mm sized samples can be extrapolated to the tectonic processes responsible for DFEQ generation. Figure 2.18 shows T-K plot of the focal mechanisms for several events and the Gutenburg-Richter distribution for two experiments.

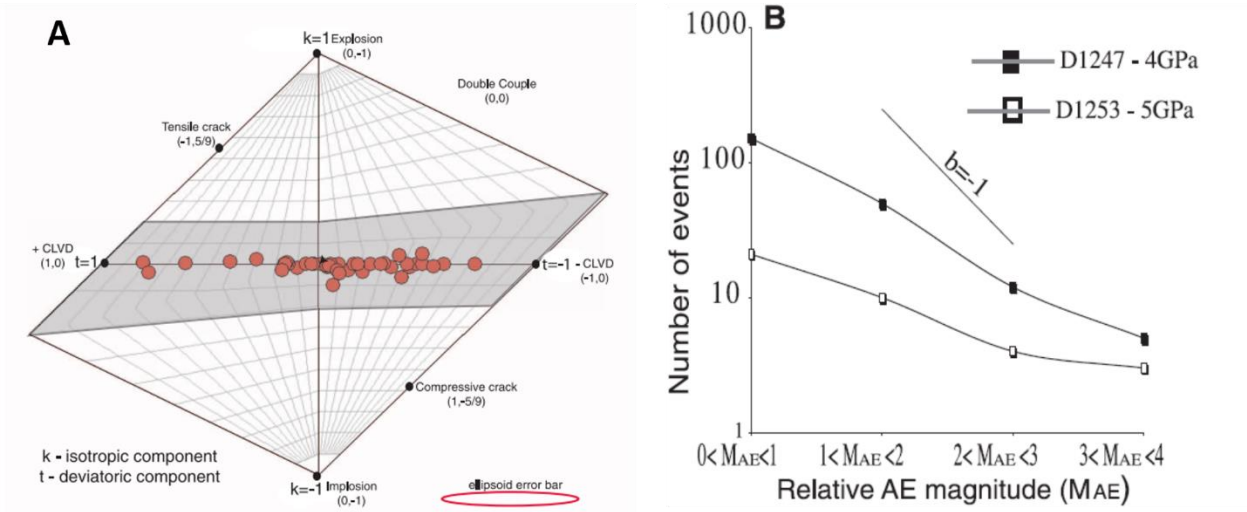

Figure 2.18: T-K and Gutenburg-Richter distribution for AE events collected during transformational faulting of Mg_2GeO_4. Figure modified from Schubnel et al. (2013).

More recently, the system just described was also used to measure AE associated with HPHT faulting during eclogitization of lawsonite-bearing blueschist (Incel et al., 2017) and dehydration of antigorite/olivine aggregates. Importantly, neither of these studies concluded that dehydration embrittlment was responsible for HPHT faulting, but instead attributed the mechanical instabilities witnessed to have resulted from different processes. In the case of Incel et al. (2017), they suggested that grain-size reduction during the transition from lawsonite-blueschist to lawsonite-eclogite was responsible for the weakening in a manner similar to transformational faulting. Ferrand et al. (2017) attributed faulting in their samples to a model that favours dehydration driven stress transfer as a process that can lead to dynamic weakening. While the interpretations of these studies are far from complete, there is intriguing evidence that the mechanism(s) operating in olivine structured minerals transforming to spinel may have direct relevance to IFEQs even though olivine does not transform to its high pressure polymorphs at these depths.

2.5 Conclusions

Transformational faulting has been shown to exist in a variety of materials under HPHT conditions where minerals are expected to behave in a nominally ductile manner. In particular, the analogue material Mg_2GeO_4 has repeatedly displayed HPHT faulting associated with the transformation from olivine→spinel. There are at least two mechanisms by which this can occur. One is the formation of spinel-filled anticracks in the olivine matrix once the phase transition has initiated. With time, more anticracks form and preexisting ones grow in directions perpendicular to the largest principal stress. Large stress concentrations develop around the tips of the anticracks,

and the growth of anticracks accelerates. Since the olivine → spinel transformation is exothermic, as the anticracks form and grow they release heat which promotes additional formation. Pre-existing micro-anticracks then link up until some critical anticrack density is reached at which point the bulk material loses its ability to support the applied stress and a macroscopic fault zone forms. This mechanism has also been shown to operate during the $\alpha \rightarrow \beta$ transformation in natural olivine at 9-14 GPa. The second mechanism, involves the presence of numerous thin planar transformation film like shear zones. Once local shear is initiated, the exothermic nature of the phase transition accelerates transition kinetics around the shear zone, which then propagates in a direction parallel to the initial shear displacement.

More recently, improvements in acoustic technology have allowed for the integration of AE systems with the multi-anvil apparatus which has been successful in measuring AE associated dehydration reactions under P,T conditions where IFEQs occur. Further development of these types of systems have led to accurate determinations of AE event location through the use of multiple transducers in microsseismic arrays. In particular, employing the use of such a system coupled with *in situ* synchrotron X-radiation has demonstrated that radiation of elastic strain energy accompanied mechanical instabilities in Mg_2GeO_4 which coincided with the presence of the $\alpha \rightarrow \gamma$ transition. Most convincingly, AE monitoring of the planar transformation mechanism revealed numerous events whose focal mechanisms indicated shear faulting similar to that observed for DFEQs. The same system has also shown that dehydration reactions can induce seismogenic HPHT faulting without undergoing dehydration embrittlement. These studies also reported b-values that match Gutenburg-Richter relationships observed for real earthquakes indicating that investigations on samples with volumes of a few mm can be scaled up to natural tectonic environments.

2.6 References

Akaogi, M., Ito, E. and Navrotsky, A., 1989. Olivine-modified spinel-spinel transitions in the system Mg_2SiO_4-Fe_2SiO_4: Calorimetric measurements, thermochemical calculation, and geophysical application. *J. Geophys. Res.*, **94**, 15671-15686.

Akimoto S, Fujisawa H, Katsura T, 1965. The olivine–spinel transition in Fe_2SiO_4 and Ni_2SiO_4. *J. Geophys. Res.*, **70**, 1969–1977.

Bridgman, P.W., 1945. Polymorphic phase transitions and geological phenomena, *Am. J. Sci.* **243A**, 90.

Brearley, A.J., Rubie, D.C. and Ito, E., 1992. Mechanisms of transformations between the α, β and γ polymorphs of Mg_2SiO_4 at 15 GPa, *Phys. Chem. Mineral*, **18**, 343-5-358.

Burnley, P.C. and Green, H.W., 1989. Stress dependence of the mechanism of the olivine-spinel transformation, *Nature*, **338**, 753-756.

Burnley, P.C. and Green, H.W., 1991. Faulting associated with the olivine to spinel transformation in Mg_2GeO_4 and its implications for deep-focus earthquakes, *J. Geophys. Res.*, **96**, 425-443.

Burnley P.C., 2005. Investigation of the martensitic-like transformation from Mg_2GeO_4 olivine to its spinel structure polymorph, *Am. Min.*, **90**, 1315-1324.

Chen, J., Weidner, D.J., Parsie, J.B., Vaughn, M.T. and Raterron, 2001. Observation of cation reordering during the olivine-spinel transition in fayalite by *in situ* synchrotron X-ray diffraction at high pressure and temperature, *Phys. Rev. Lett.*, **86**, 4072-4075.

Dobson, D.P., Meredith, P.G. and Boon, S.A., 2002. Simulation of subduction zone seismicity by dehydration of serpentine, *Science*, **298**, 1407-1410.

Dobson, D.P., Meredith, P.G. and Boon, S.A., 2004. Detection and analysis of microseismicity in multi anvil experiments. *Phys. Earth Planet In.*, **143-144**, 337-346.

Dobson, D.P., de Ronde, A.A., Welch, M.D. and Meredith, P.G., 2007. The acoustic emissions signature of a pressure-induced polytypic transformation in chlorite, *Am. Mineral*, **92**, 437-440.

Durham, W.B., Heard, H.C. and Kirby, S.H., 1983. Experimental deformation of polycrystalline ice: preliminary results, *J. Geophys. Res.*, **88**, B377-B392.

Ferrand, T.P., Hilairet, N., Incel, S., Deldicque, D., Labrousse, L., Gasc, J., Renner, J., Wang, Y., Green, H.W. and Schubnel, A., 2017. Dehydration-driven stress transfer triggers intermediate-depth earthquakes, *Nature*, **8**, 15247.

Gasc, J., Schubnel, A., Brunet, F., Guillon, S., Mueller, H.J. and Lathe, C., 2011. Simultaneous acoustic emissions monitoring and synchrotron X-ray diffraction at high pressure and temperature: Calibration and application to serpentinite dehydration, *Phys. Earth Planet In.*, **189**, 121-133.

Green, H.W. and Burnley, P.C., 1989. A new self-organizing mechanism for deep-focus earthquakes, *Nature*, **341**, 733-737.

Green, H.W., Young, T.E, Walker, D. and Scholz, C.H., 1990. Anticrack-associated faulting at very high pressure in natural olivine, *Nature*, **348**, 720-722.

Green H.W, Scholz, C.H., Tingle, T.N., Young, T.E. and Koczynski, T.A., 1992. Acoustic emissions produced by anticrack faulting during the olivine → spinel transition, *Geophys. Res. Lett.*, **8**, 789-792.

Green, H.W. and Houston, H., 1995. The mechanics of deep earthquakes, *Annu. Rev. Earth Planet. Sci.* **23**, 169-213.

Inoue, K., 1975. Development of high temperature and high pressure X-ray diffraction apparatus with energy dispersive technique and its geophysical applications, PhD. Thesis, Tokyo Univ., Tokyo.

Incel, S., Hilairet, N., Labrousse, L., John, T., Deldicque, D., Ferrand, T., Wang, Y., Renner, J., Morales, L. and Schubnel, A., 2017. Laboratory earthquakes triggered during eclogitization of lawsonite-bearing blueschist, *Earth Planet Sci. Lett.*, **459**, 320-331.

Jung, H., Fei, Y., Silver, P.G. and Green, H.W., 2006. System for detecting acoustic emissions in multianvil experiments: Application to deep seismicity in the Earth, *Rev. Sci. Instrum.*, **77**, 014501.

Jung, H., Fei, Y., Silver, P.G. and Green, H.W., 2009. Frictional sliding in serpentine at very high pressure, *Earth Planet Sci. Lett.*, **277**, 273-279.

Karato, S.-I. and Rubie, D.C., 1997. Toward an experimental study of deep mantle rheology: A new multianvil sample assembly for deformation studies under high pressures and temperatures, **102**, 20111-20122.

Kerschhofer, L., Dupas, C., Liu, M., Sharp, T.G., Durham, W.B. and Rubie, D.C., 1998. Polymorphic transformations between olivine, wadsleyite and ringwoodite: mechanisms of intracrystalline nucleation and the role of elastic strain, *Mineralogical Magazine*, **62**, 617-638.

Kirby, S.H., 1985. Localized polymorphic phase transformations as mechanisms for deep earthquakes, *Trans. Am. Geophys. Union*, **66**, 1086.

Kirby, S.H., Durham, W.B. and Heard, H.C., 1985. Rheologies of ices I_h, II and III at high pressures: a progress report in *Ices in the solar system*, J. Klinger et al., (eds.), D. Reidel Publishing Co., Dordrecht, Holland, p. 711-729.

Kirby, S.H., 1987. Localized polymorphic phase transformations in high-pressure faults and applications to the physical mechanism of deep earthquakes, *J. Geophys. Res.*, **92**, 13789-13800.

Katsura, T. and Ito E., 1989. *J. Geophys. Res.*, **94**, 15663-15670.

Meade, C. and Jeanloz, R., 1989. Acoustic emissions and shear instabilities during phase transformations in Si and Ge at ultrahigh pressures, *Nature*, **339**, 616-618.

Meade, C. and Jeanloz, R. 1991. Deep-focus earthquakes and recycling of water in the Earth's mantle, *Science*, **252**, 68-72.

Ono, S., Kikegawa, T. and Higo, Y., 2013. In situ observation of a phase transition in Fe_2SiO_4 at high pressure and high temperature, *Phys. Chem. Minerals*, **40**, 811-816.

Raterron, P., Chen, J. and Weidner, D.J., 2002. A process for low-temperature olivine-spinel transition under quasi-hydrostati stress, *Geophys. Res. Lett.*, **29**, 36-14.

Riggs, E.M. and Green, H.W., 2005. A new class of microstructures which lead to transformation-induced faulting in magnesium germanate, *J. Geophy. Res.*, **110**, B03202.

Ringwood, A.E., 1975. Composition and petrology of the earth's mantle. McGraw-Hill, New York.

de Ronde, A.A., Dobson, D.P., Meredith, P.G. and Boon, S.A., 2007. Three-dimensional location and waveform analysis of microseismicity in multi-anvil experiments, *Geophys. J. Int.*, **171**, 1282-1294.

de Ronde, A.A. and Dobson, D.P., 2008. Acoustic detetion of phase transitions at high pressure: Bismuth, chlorite and zinc sulphide, *High Pressure Res.*, **28**, 9-17.

Ross, N. and Navrotsky, A., 1987. The Mg_2GeO_4 olivine–spinel phase transformation. *Phys. Chem. Mineral.*, **14**, 473-481.

Rubie, D.C. and Ross, C.R., 1994. Kinetics of the olivine-spinel transformation in subducting lithosphere: experimental constraints and implications for deep slab processes, *Phys. Earth Planet Int.*, **86**, 223-241.

Schubnel, A., Brunet, B., Hilairet, N., Gasc, J., Wang, Y. and Green, H.W., 2013. Deep-focus earthquake analogs recorded at high pressure and temperature in the laboratory, **341**, 1377-1380.

Wang, Y.B., Durham, W.B., Getting, I.C. and Weidner, D.J., 2003. The deformation-DIA: a new apparatus for high temperature triaxial deformation to pressures up to 15 GPa, *Rev. Sci. Instrum.*, **74**, 3002-3011.

Yagi, T., Akaogi, M., Shimomura, S., Suzuki, T., Akimoto, S.-I., 1987. In situ observation of the olivine-spinel phase transformation in Fe_2SiO_4 using synchrotron radiation, *J. Geophys. Res.*, **92**, 6207-6213.

Chapter 3: High Pressure/High Temperature Acoustic Emission System Description and Operation

3.1 Introduction

A system has been developed at Western University capable of monitoring microseismicity under *in situ* conditions of HPHT in the laboratory. This was achieved by installing a microseismic array of ultrasonic transducers to a high pressure assembly that can be pressurized in the 3000 ton multi-anvil apparatus in the Experimental High Pressure/High Temperature Mineral Physics and Material Science Laborator y at Western University. Such a system is essential for studying the mechanism of deep earthquakes as it allows for the measurement of ultrasonic compressional waves emitted in association with mechanical instabilities that develop under HPHT conditions traditionally expected to resist rupture and faulting. The system described here allows for the rapid acquisition of high resolution ultrasonic acoustic waveforms which can be analysed for their relevance to faulting.

3.2 Experimental setup

The experimental assembly consists of an octahedral MgO pressure medium with 18 mm edge lengths surrounded by pyrophyllite gaskets. A cylindrical hole is drilled through the centroid of one of the octahedron's triangular faces and traverses the entire centroidal axis exiting the opposing face. This creates a cylindrical void within the octahedron. At the center of this void the sample is placed. The remaining space is typically occupied by cylindrical plugs on either side of the sample, a thermocouple to measure the temperature inside the cell, and a

furnace that surrounds the experimental configuration. Running a current through the furnace resistively heats the sample. The materials used and the dimensions of these components vary depending on the specifics of individual experiments. For precise details regarding different experimental cell designs see sections 4.2.1 and 6.5. The octahedron is enclosed within 8 tungsten carbide (WC) anvils, cubic in geometry, with 32 mm edge lengths. One corner of each anvil is truncated to create an equilateral triangle with 11 mm sides which applies force to one triangular face of the octahedron during pressurization. The opposite corner of each anvil, along a cube body diagonal, was also ground to create an equilateral triangle with 15 mm sides which was polished using 1 μm diamond paste to create a mirror finish. Figure 3.1 shows displays the mirror finish on the 15 mm anvil truncations.

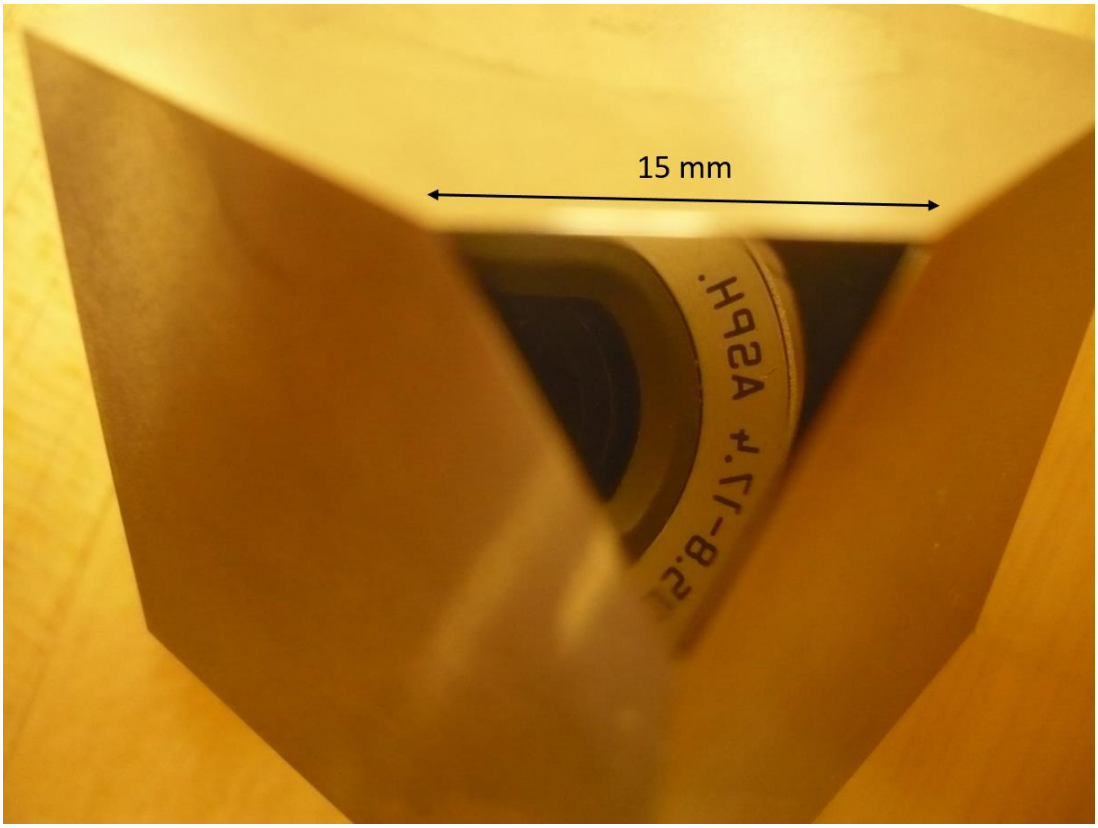

Figure 3.1: The mirror finish on the 15 mm WC anvil truncations. The focused image of the camera lens is due to the reflection of the image of the camera in the anvil truncation.

The absence of surficial asperities aids in acoustically coupling sonic waves travelling across the boundary of contacting resonant materials. Fastened to this surface are piezoelectric transducers, 5 mm in diameter and 3 mm in height, affixed using a thin layer of cyanoacrylate adhesive. This provides acoustic coupling with the anvils by permeating any irregularities on either components surface. A total of six transducers can be accommodated in the high pressure assembly to create the microseismic array shown in Figure 3.2. The remaining two anvils do not have the capacity to accommodate transducers since two truncations, which are in contact with the wedges of the pressure module do not have space for the transducers or a path for their wires to exit the pressure module.

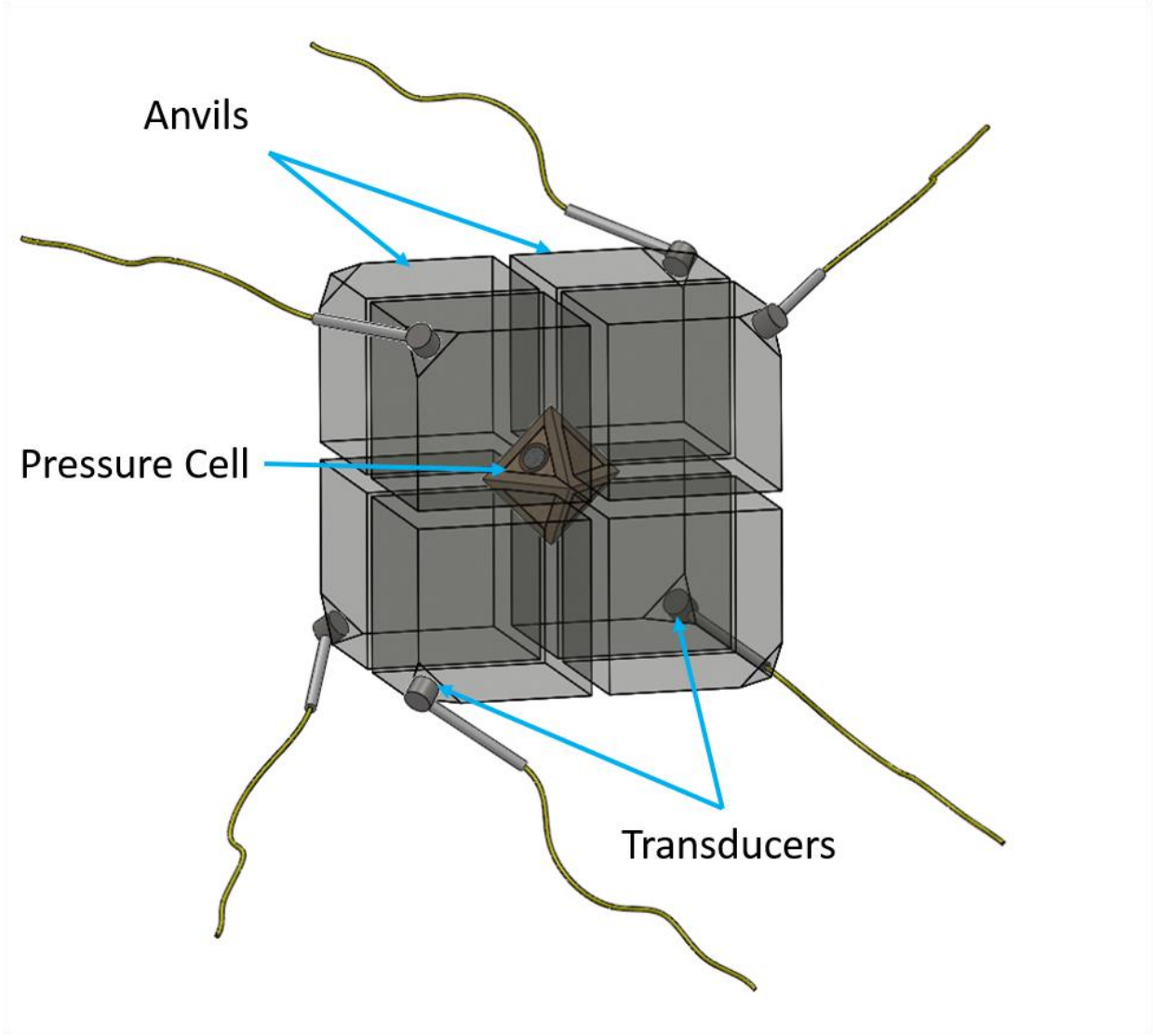

Figure 3.2: High pressure assembly showing the octahedron in the center surrounded by WC anvils with transducers attached to the rear truncated faces of six anvils.

Six phenolic plates 0.16 mm thick are glued to each side of the cubic pressure assembly of 8 WC anvils which act to hold it together and provide electrical isolation from the wedges of the press. The high pressure assembly is placed into the high pressure module and seated on the lower three wedges as shown in Figure 3.3.

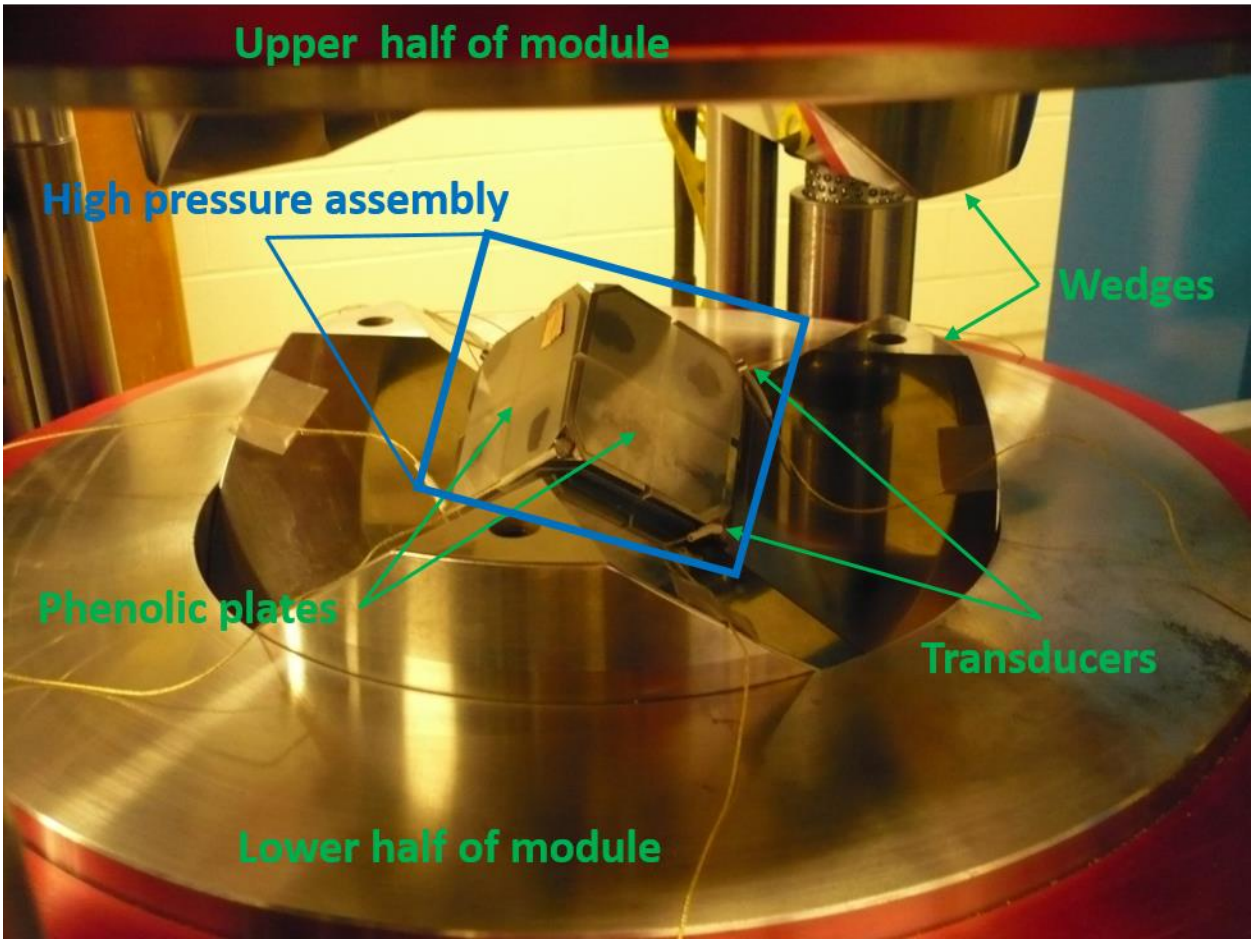

Figure 3.3: The high pressure assembly between the upper and lower wedges of the pressure module.

The pressure module is placed in the press and sits atop a hydraulic ram. The ram vertically compresses the module to load the anvils which translates force through the octahedron to generate quasi-hydrostatic pressure within the sample. The space between the upper and lower sections of the module allows for the transducer wires to exit the module and connect to pre-amplifiers, which are in turn connected to electronic acoustic processors connected to a computer. Figure 3.4 shows the entire microseismic system in operation under load.

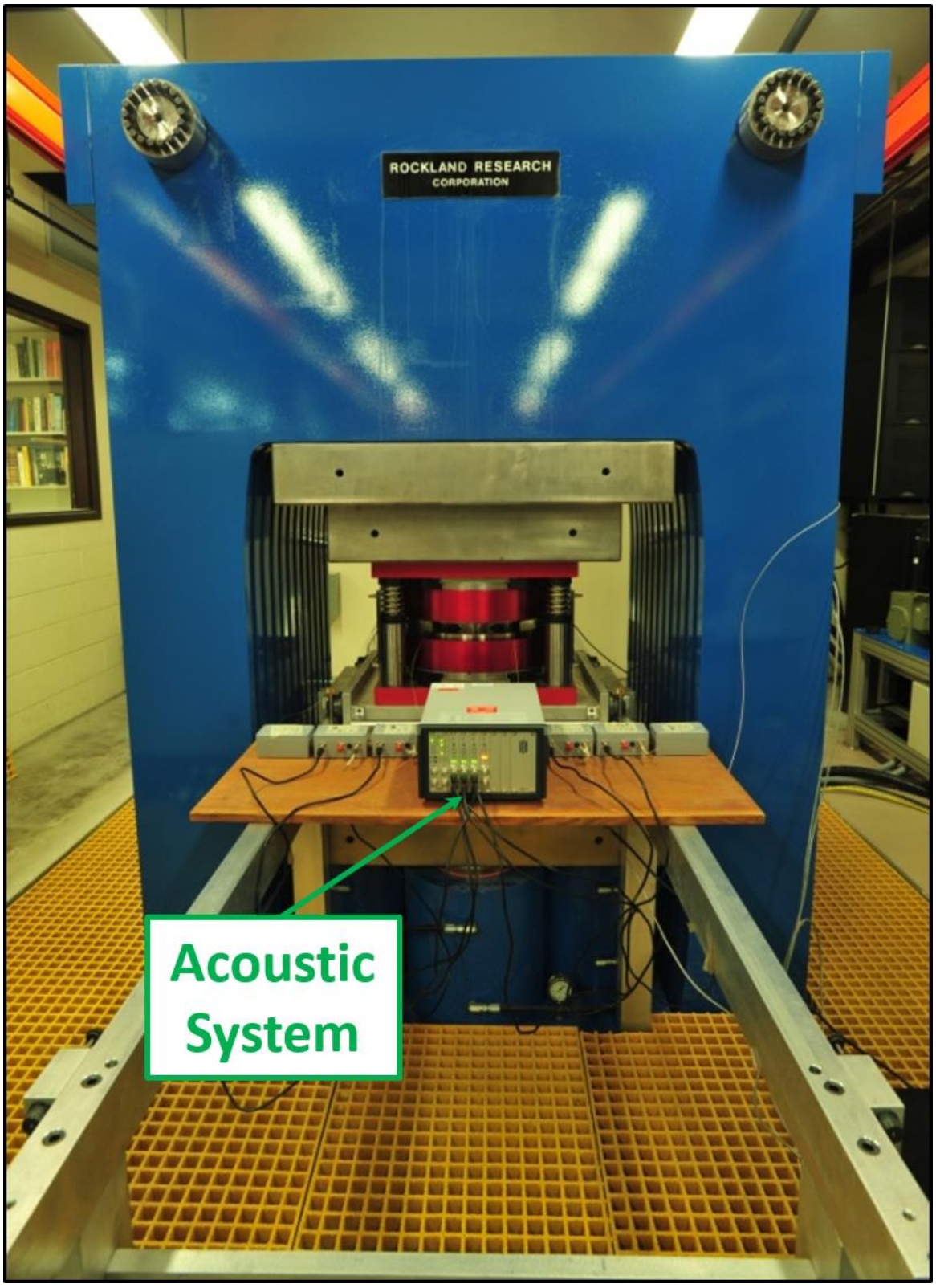

Figure 3.4: The entire HPHT AE arrangement consisting of the 3000 ton press (in blue), the pressure module (in red) and the acoustic transmission/receiving system (labelled).

3.3 Acoustic characteristics of the system

3.3.1 Transducer science and selection

In the laboratory microseismicity can be detected in the form of acoustic emissions (AE) which are high frequency (100's of kHz – 10's of MHz) strain waves that propagate at speeds similar to seismic velocities (several km/s). They are typically generated by crack propagation, volumetric changes or any process associated with localized stress release provided the physical phenomena responsible for their creation is rapid enough that the energy released cannot be dissipated by a slower process. This ensures that a fraction of the total energy released will be partitioned into elastic waves with the remainder partitioning into fracture energy and thermal energy (Kanamori and Rivera, 2006; Grosse, 2008). These waves can be detected by piezoelectric materials which convert strain energy into an electric charge that precipitates a voltage difference across the material. By connecting a wire to opposing sides of the piezoelectric material this voltage can then be measured. Choice of transducer requires consideration of several factors, some of which necessitate compromises that tend to benefit one characteristic at the expense of another. One factor encountered in HPHT AE applications is the limited volume permitted in the high pressure apparatus. Because it is necessary that the transducers not be crushed during an experiment, they must be small enough in diameter that they fit in the space between the upper and lower wedges of the pressure module which approach to within 7.5 mm apart while under load. This creates an upper bound on transducer diameter. Transducer height is less critical since the space between the upper and lower wedges of the module extends backward for several centimetres. Another approach that was considered was to accommodate the transducers entirely within the truncated volume. This is the approach used by Dobson et al., (2002; 2004) and Jung et al., (2006). However, the disadvantage of this approach

is that removal of a large volume of material from the anvils compromises their overall strength and increases the possibility of cracking under load. While fracturing of the cubes is an accepted operating cost incurred in high pressure research it is best avoided since each cube costs ~$500 dollars and should therefore be minimized. For a cylindrical transducer 7.5 mm in diameter and 4 mm in height a truncation edge length of 27 mm is required which would remove more than half the volume of the cube. For this reason it was decided that transducers would be required to fit within the space separating the upper a lower halves of the module instituting a strict adherence to an upper bound of 7.5 mm in transducer diameter. The disadvantage of this approach is that it severely limited the selection of commercially available transducers.

Another important factor in the choice of transducer is its frequency response. This dictates how sensitive the transducer is to a given range of frequencies. The ideal transducer would have a flat response over a very wide range of frequencies, however this is not possible in practice. Normally most acoustic emissions radiate elastic energy between 1 kHz and 10 MHz, but can emit energy at higher or lower frequencies under certain circumstances depending on the crack length and propagation velocity (Grosse, 2008). Several factors influence the frequency response of a transducer. Typically, they are composed of three major components: the active piezoelectric element, a mechanical wear plate/matching layer, and backing/damping layer as shown in Figure 3.5.

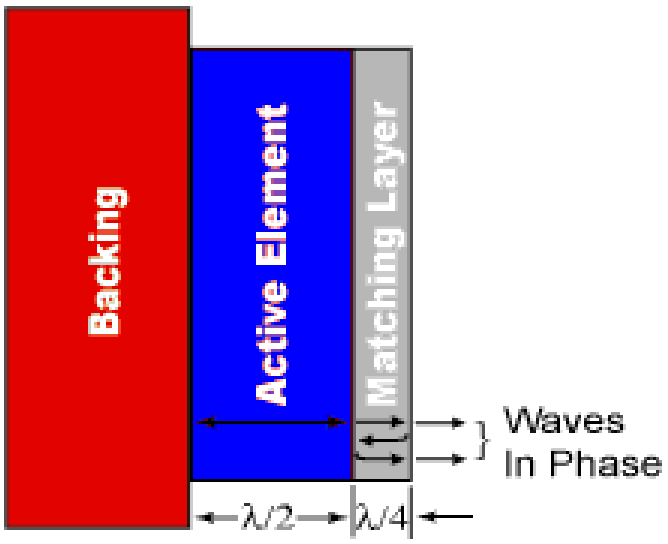

Figure 3.5: Schematic cross section of the typical structure of a transducer consisting of a ¼ wave matching layer/wear plate, the active element, and a backing/damping layer.

The most important factor that determines frequency response is the thickness of the piezoelectric element that converts mechanical energy to electric energy through the piezoelectric effect. For a piezoelectric crystal, the thickness of the crystal determines its resonant frequency where the resonant wavelength is twice that of the thickness of the active element. Therefore, thinner crystals exhibit better sensitivity at higher resonant frequencies, however decreasing the thickness of the crystal also results in an overall decrease in the integrated amount of energy converted from mechanical to electrical energy. Piezoelectric crystals with a free surface facing away from the anvil surface tend to have sharp mechanical resonances only ~100 – 200 kHz wide (Gautschi, 2002). The most common way to increase transducer bandwidth is through mechanical backing. The transducer crystal acts as a forced oscillator and placing a highly attenuating material on the free face of the active element acts to absorb acoustic energy. This provides mechanical damping and controls the oscillation of the crystal. In particular, damping broadens the response of the transducer on either side of the

resonant frequency and results in a much wider bandwidth for the transducer. The drawback is that a damped oscillator leads to a lower overall sensitivity (waves and oscillations). The ideal backing material should have high acoustic attenuation to promote a high level of damping and reduce ringing of the free surface. It should also match the acoustic impedance of the transducer crystal as closely as possible to maximize transmission into the attenuating unit and eliminate ringing in the active element (Gautschi, 2002). When these conditions are met, the result is a highly damped, broadband transducer with rapid rise and fall times (Ensminger, 1988). An important factor in the design of broadband transducers is the quality factor, *Q*, which can be defined in terms of the either the acoustic attenuation coefficient or the transducer frequency response:

$$Q = {\omega_{res}}/{\alpha} = {\omega_{res}}/{\Delta\omega_{fwhm}} \qquad (3.1)$$

where α is the attenuation coefficient, ω_{res} is the crystal resonant frequency and $\Delta\omega_{fwhm}$ is the full width at half maximum of the transducer resonance curve (Safari et al., 2008; King, 2009). Figure 3.6 shows theoretical response curves for several values of *Q*. Lower values of *Q* display much broader, flatter frequency responses but at the cost of a somewhat lower overall integrated power.

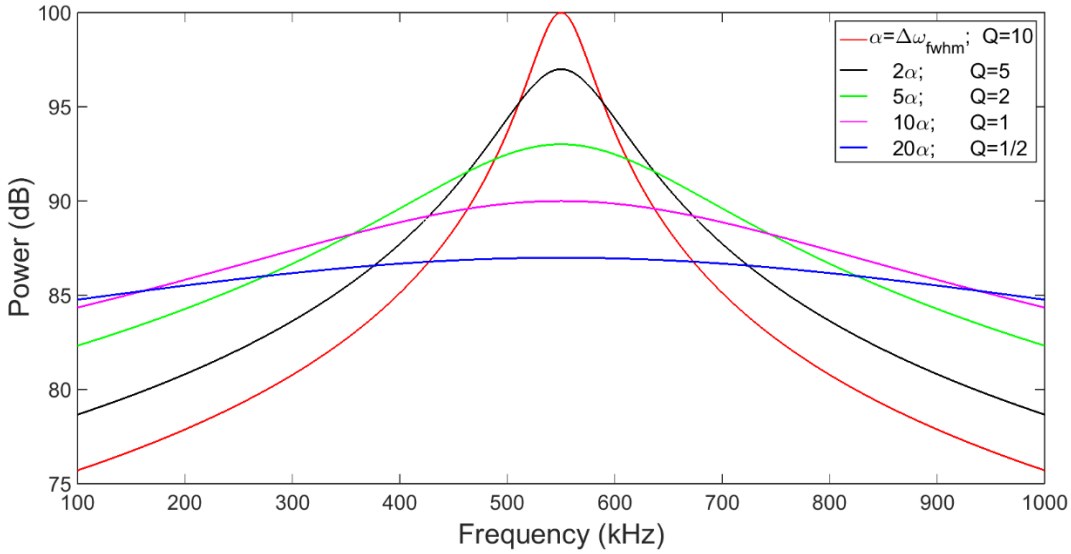

Figure 3.6: Frequency response curves for transducer crystals with a 550 kHz resonant frequency and different quantities of mechanical backing. Each curve represents a transducer with a different quality factor *Q*, with lower values of *Q* (which correspond to higher acoustic attenuation in the backing layer) producing broader frequency responses. The power is given in dB and normalized such that the highest power output (ω_{res} for *Q*=10) equals 100.

Backing materials are typically composed of a polymer matrix such as rubber or epoxy that incorporates a high density material such as tungsten in the form of dispersed flecks. The rubber or epoxy provides a high degree of acoustic attenuation while the metal fraction can be tailored to meet the requirements of acoustic impedance matching (Nguyen et al., 1996).

Finally, to transfer as much energy as possible from the material under test to the transducer and retain signal coherence, an impedance matching layer, or wear plate, is nestled between the active element and the material under test. Optimal impedance matching is achieved by sizing the matching layer so that its thickness is 1/4 of the desired wavelength (1/2 the thickness of the crystal). The use of a wear plate exactly half the thickness of the crystal maintains signal coherence since reverberations in the wear plate will remain in-phase when they enter the crystal. It also helps to reduce ringing in the crystal since a reflection in the crystal causing a rarefaction in the surface in the contact with the wear plate should, in theory, meet a compression in the wear plate in contact with the crystal acting to cancel out, or at least

minimize, crystal ringing. The material should also be hard to provide resistance to abrasion and have an acoustic impedance between that of the active element and the material under test or the transducer housing, whichever the wear plate is in contact with on the surface facing away from the crystal. It also helps to provide electrical isolation between the crystal and the anvils.

The sensors employed in our experiments are commercially available transducers manufactured by MISTRAS. They contain lead-zirconate-titanate (PZT) piezoelectric crystals fitted between Al_2O_3 wear plates and backing material containing a polymer impregnated with metal and have a relatively flat response to p-waves between 100 kHz and1 MHz with a resonant frequency of 550 kHz. This assembly is contained within a steel housing that acts to electrically shield the transducer and provide a degree of electrical isolation from the laboratory environment. The transducers are cylindrically shaped with a diameter of 5 mm and a height of 4 mm. Figure 3.7 shows a photo of the transducer and its frequency response as measured by the manufacturer, (http://www.mistrasgroup.com).

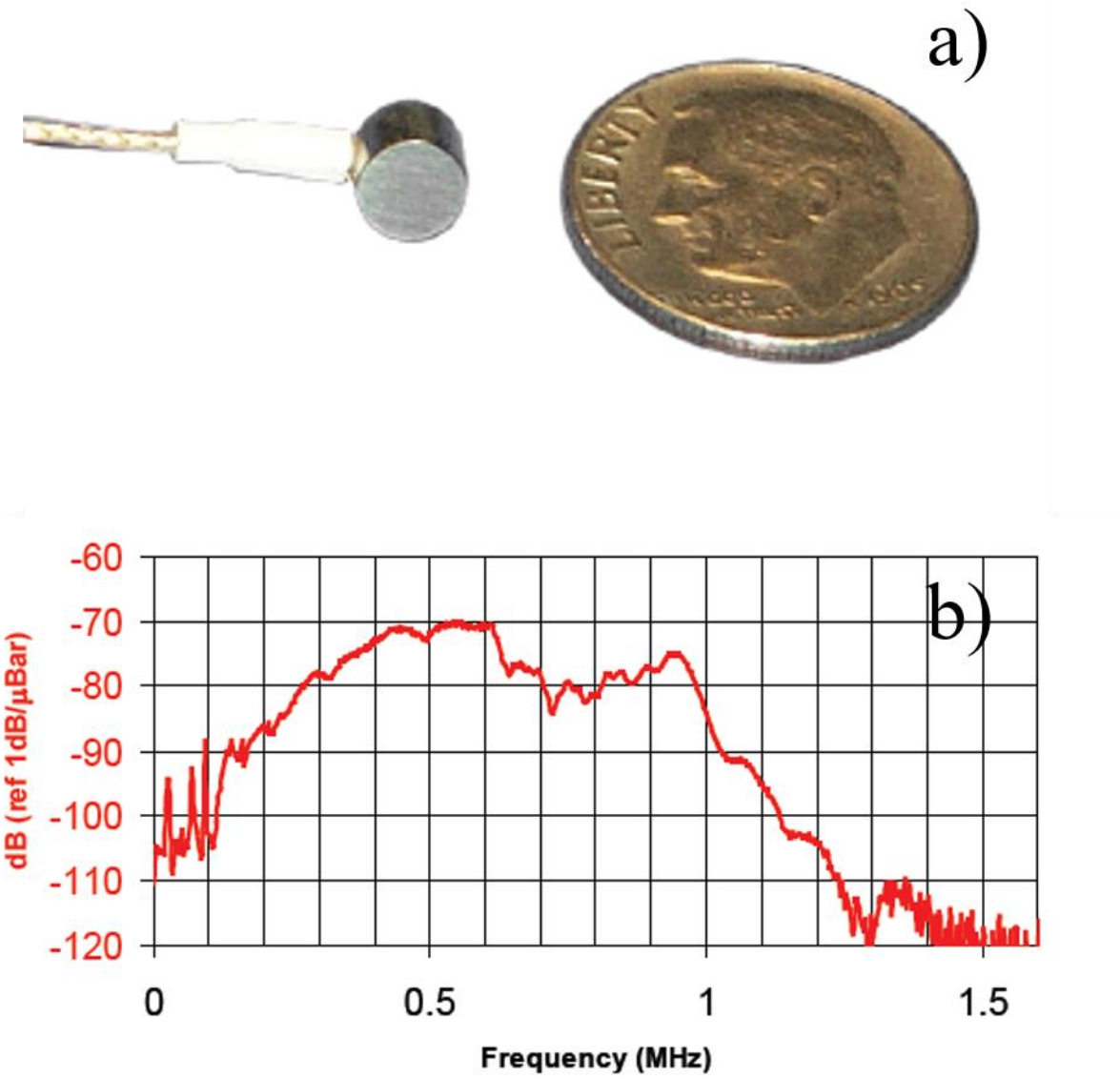

Figure 3.7: a) Photograph of transducer with an American penny for scale. b) Response function of transducer as measured by the manufacturer. Slight deviations from this response curve are exhibited for each transducer.

3.3.2 Electronic acoustic emission equipment

Acoustic emissions registered by the transducers are converted to an electrical signal that is sent along low impedance coaxial cables to pre-amplifiers. The pre-amplifiers employed in our experiments are the AEP3 model manufactured by Vallen Systemes. They feature adjustable

gain from 34 to 49 dB that can be controlled in real-time using Vallen's software. Amplified signals are sent *via* BNC cables to Vallen Systeme's AMSY-6 acoustic emission system housing four ASIP-2 signal processors consisting of two channels apiece for a possible total of eight channels. Each channel combines an analog processing unit and an analog-to-digital (A2D) board which digitizes the signal as well as providing various types of user controlled signal conditioning features. The maximum achievable sampling rate of the ASIP-2 A2D boards is 40 MHz which corresponds to a duration of 25 ns between samples. The resolution of the boards is 18 bits which for a peak amplitude of 100 V corresponds to a resolution of:

$$^{100\ V}/_{2^{18}} = 3.81\ \times 10^{-4} V\ per\ division. \qquad (3.2)$$

Because of the high sampling rate it is impractical to continuously measure data which, for a 10 hour experiment would lead to

$$\left(^{36000\ s}/_{25 \times 10^{-9}\ s}\right) \times 6\ channels = 8.64 \times 10^{12}\ data\ points, \qquad (3.3)$$

or several terra-bytes of accumulated data. To avoid this, the system operates on a triggered basis such that waveforms must possess a sufficient amplitude (i.e. exceed a user-defined threshold voltage) to be considered relevant enough to record. If the threshold is crossed on a given channel, the system registers a "hit" and records several features associated with it such as arrival time, peak amplitude, rise-time, duration, counts, integrated energy (between the first and last threshold crossing), and background noise (immediately before the hit). This information is transferred from the ASIP-2 processors to the computer for storage. A typical threshold value is 40 dB (using 40 dB pre-amplification) which is ~ 5-10 dB above the background level when the cell is not being pressurized, and culminates in ~ 1-2 hit(s)/minute over all channels under experimental conditions that include pressurization and heating. However, because the threshold

crossing must always follow the initial impulse of sonic energy, the system invokes a transient recording module, the TR-2 by Vallens Systemes, which continually records up to 2 GB of data per channel in a data buffer, but removes it if a hit is not triggered. However, since data are continuously recorded on each channel, if a hit is recorded, a user defined number of points prior to the threshold crossing are also recorded and can be stored to memory. Such a unit is crucial since it drastically reduces the amount of memory required for an experiment. This is accomplished by constantly assessing incoming data and so that only the most important information is recorded, while ensuring the capture of entire waveforms whose onset takes place prior to threshold crossing. Therefore, valuable information associated with the precise onset of the signal can be used for location analysis and event characterization. Figure 3.8 shows an example of a typical hit.

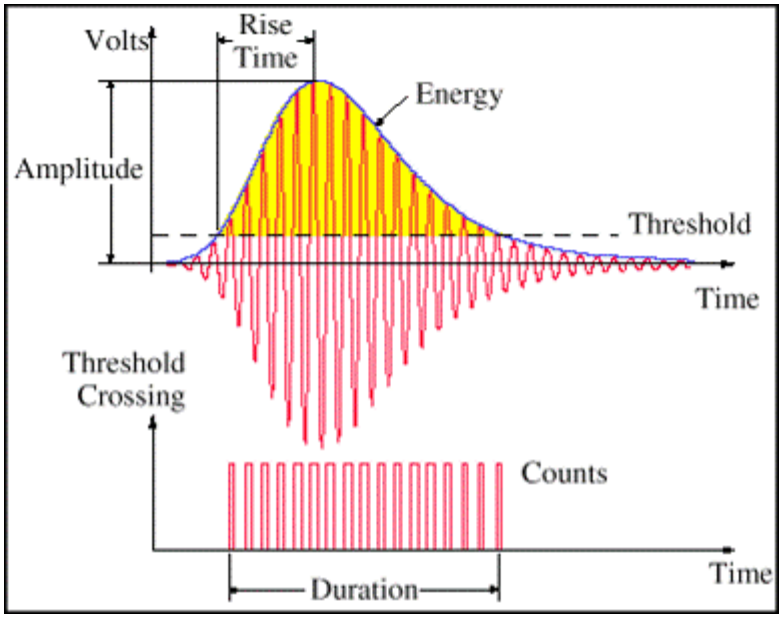

Figure 3.8: A schematic of a typical hit showing amplitude, risetime, energy and counts. All hit parameters are in reference to the user defined threshold value for the Vallen software.

Note that the arrival of the waveforms occurs prior to the threshold crossing. One of the limitations of the Vallen system is that it records the arrival time of the waveform and all other signal information as the time of threshold crossing causing erroneous arrival times. This problem will be discussed in more detail in chapter 4 with regards to event location analysis.

3.4 Acoustic Experiments

3.4.1 Measuring sample pressure in the multi-anvil apparatus

Determination of the internal pressure of the sample in the multi-anvil apparatus cannot be measured directly since it is not possible to directly access the sample while under load. Instead, the internal pressure of the sample is deduced by directly measuring the oil pressure in the press pumping system using a pressure transducer and relating this value to internal sample pressure through prior calibration. This was accomplished by carrying out experiments to infer the presence of phase transitions that occur at well-known pressures and temperatures and using these as calibration points in the relationship between the oil pressure and the sample pressure. In order to achieve this, two distinct methods were used. The first, which was used to calibrate the press at ambient temperature, measured the discontinuities in the resistivity of metals as a function of pressure which indicates the presence of a phase transition. The second technique, which was used to calibrate the press at 1200 ^{0}C, involved carrying out several experiments on materials that undergo phase transitions at HPHT. The HPHT phases remain metastable at ambient conditions in the recovered samples and could therefore be analyzed *via* XRD to ascertain the ratio of the high to low pressure phases. In this way, it was possible to bracket the phase boundary by running multiple experiments at similar HPHT conditions that resulted in

distinct phases or identified the presence of mixed phases. Figure 3.9 shows the calibration curves for sample pressure as a function of the oil pressure/force that were fit to the points acquired from each transition. The equation for each curve are as follows:

$$P_{sample,\,25^0C} = 0.00844(P_{oil}) - 5.29765 \times 10^{-7}(P_{oil})^2 \qquad (3.2)$$

at ambient conditions, and

$$P_{sample,\,1200^0C} = 19.3849 + \frac{(0.00348 - 19.3849)}{\left[1+\left({}^{P_{oil}}/_{1277.421}\right)\right]^{1.42298}} \qquad (3.3)$$

at 1200 ^{0}C, where P_{sample} is the sample pressure (in GPa) and P_{oil} is the oil pressure (in psi). Using these equations it is possible to estimate the sample pressure for any given oil pressure. Below about 1200 psi, both curves are similar to one another, but tend to deviate at higher pressures due to softening of the pressure cell as result of high temperature which lowers the efficiency of pressure transfer through the apparatus.

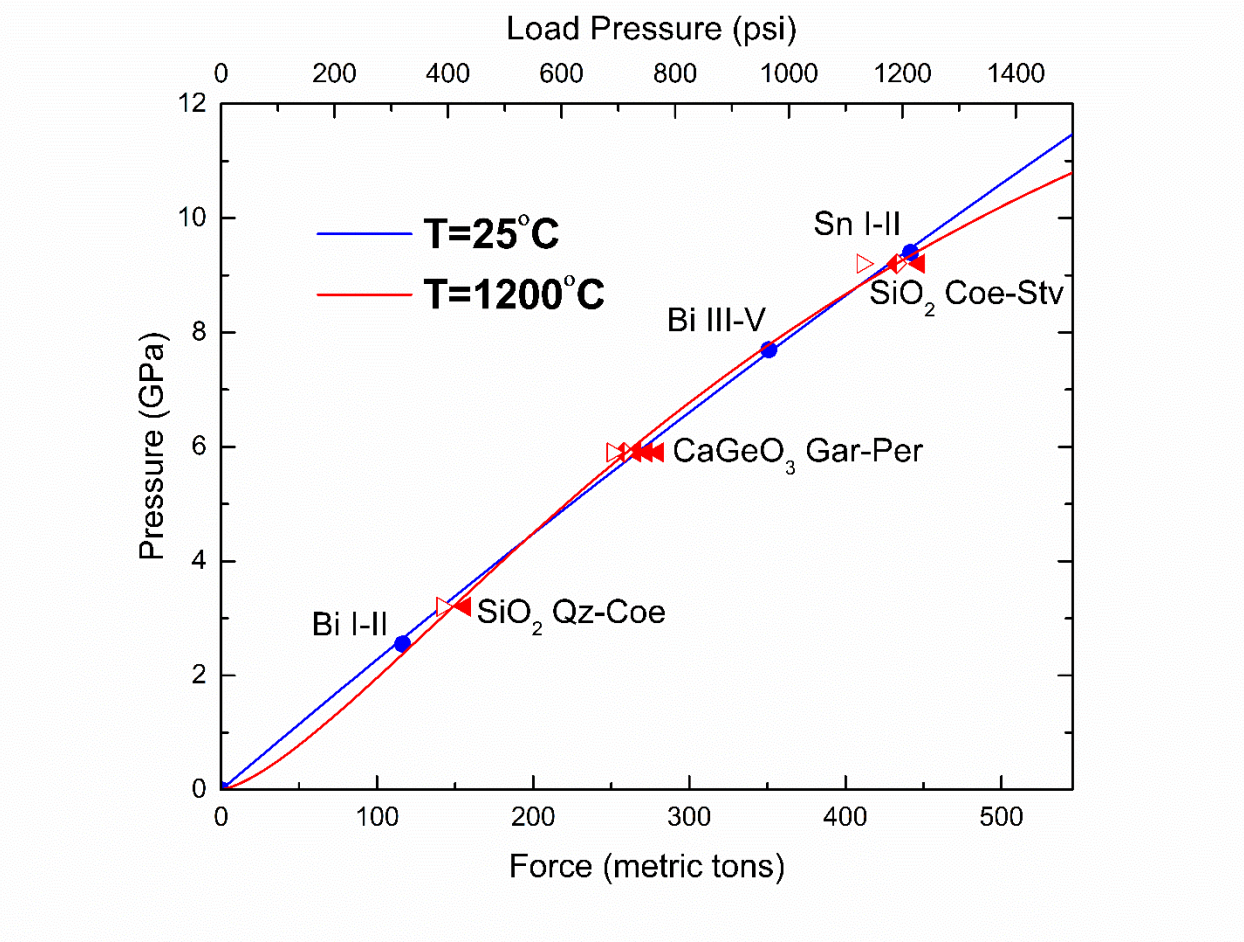

Figure 3.9: Cell pressure versus load curves for the 18/11 cell assembly up to 550 tons (pressure calibration experiments were carried out by Dr. Wenjun Yong).

3.4.2 Characterizing background noise as a function of pressure and temperature

In order to characterize the background noise associated with a typical experiment, several experiments were run using "dry" cells (cells without any sample or other components), Al_2O_3 samples with precut notches to initiate fracturing, and one cell with a AgCl sample. Figure 3.10 shows a cross section of the cell design for this experiment.

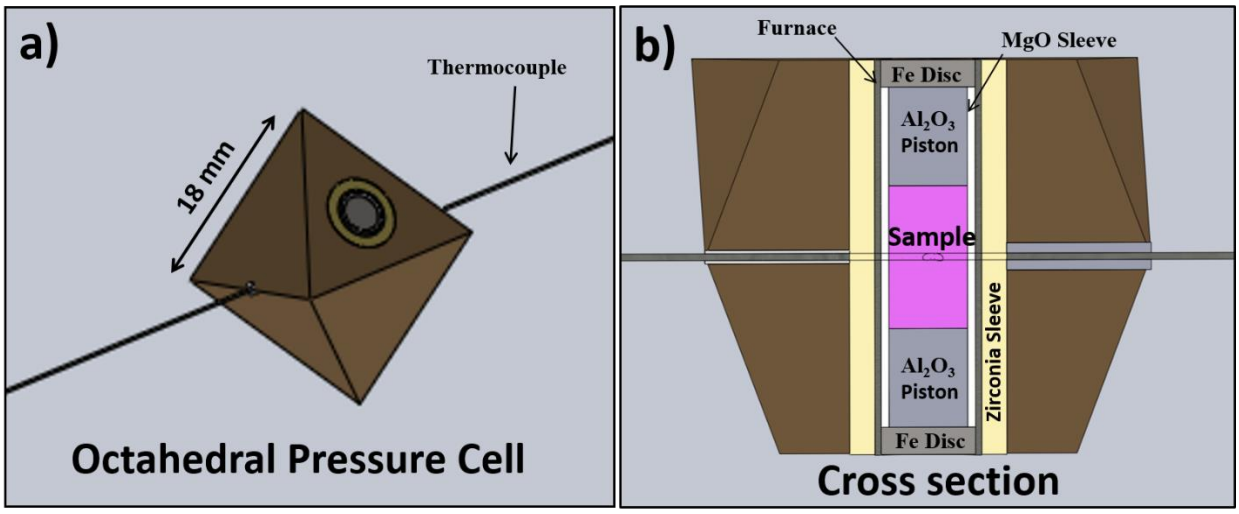

Figure 3.10: a) The 18/11 octahedral pressure cell for an experiment containing an AgCl sample. The thermocouple entered through the edge of one side and exited the opposite side. Its junction was located at the center of the octahedron. b) Cross section of cell shown in a) displaying all of the experimental components.

AgCl is a soft material that behaves aseismically under load and did not undergo any phase transitions at the P, T conditions achieved in the experiment. Therefore, all the acoustic activity recorded was acoustic noise generated by the other cell components during the pressurization process and electrically induced noise from the press pump and surroundings. Below are results for the experiment using the AgCl sample. At relatively low pressures (<140 psi or ~2 GPa), compaction of the cell and gasket formation generated high levels of acoustic noise that overshadowed any signals related to the sample. Figure 3.11 shows acoustic activity, measured in hit rate, as a function of time for a pressurization experiment using a AgCl sample. These spurious signals even persisted after pressurization stopped at 750psi (~6 GPa) due to adjustment of the pressure medium, but they eventually decayed to zero.

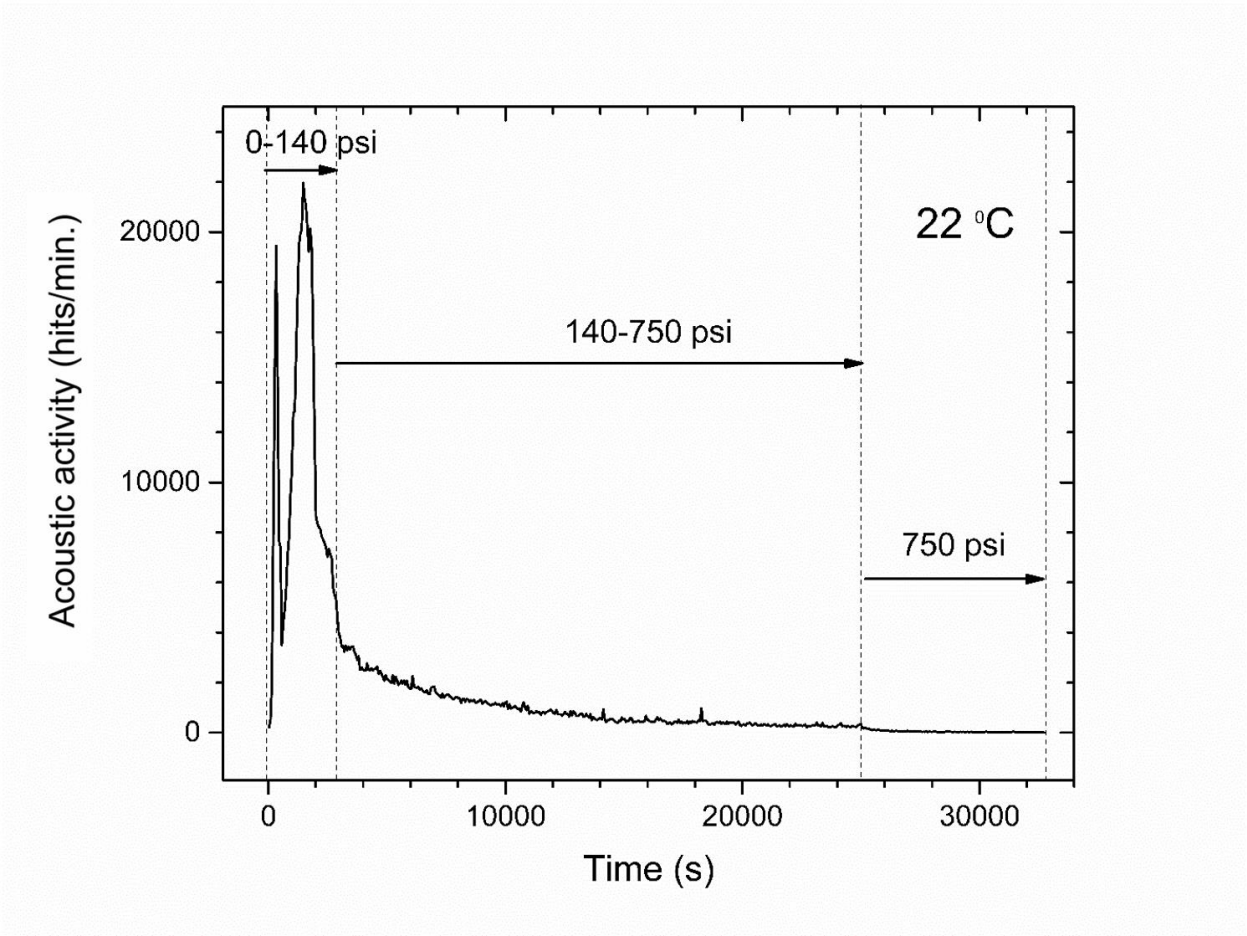

Figure 3.11: Acoustic activity (hits/minute) vs. experimental runtime for different pressurization regimes for an experiment on AgCl at ambient temperature. This can be considered the background acoustic rate for a sample that behaves aseismically and does not undergo any phase transitions.

The initial spike, arising within the first 100 s of the experiment is due to the fracturing of the phenolic plates that hold the anvils together. The second peak, occurring approximately 200 s later is due to compaction of the pressure cell and formation of the gaskets. Above ~140 psi, the gaskets are fully formed and the system starts to become far more acoustically quiet, however some of the remaining signals are due to electric noise induced by the press which is electrically controlled by a hydraulic pump. While the cell design, sample and the pressurization rate will affect the hit rate during an experiment, a pattern similar to that of Figure 3.11 is characteristic of every experiment. In subsequent experiments, attempts were made to minimize the three major

factors that generate noise during experiments: fracturing of the phenolic plates, compaction of the cell, and electrically induced noise from the press pump.

3.5 Reducing acoustic noise

3.5.1 Phenolic plates versus Teflon sheets

In an attempt to reduce the acoustic noise generated by the fracturing of the phenolic plates, the phenolic was replaced by 0.2 mm Teflon^{TM} sheets which were adhered to the anvils using cyanoacrylic adhesive. The purpose of the phenolic plates is to hold the anvils together before insertion into the pressure module and to electrically insulate the anvils from the press. Upon compression, as the anvils move closer together the phenolic plates are fractured, generating acoustic signals large enough to be audible in the laboratory. In addition, along the fracture surface asperities have the potential of scraping together and releasing frictional elastic energy during pressurization at higher loads creating further acoustic noise. Conversely, Teflon^{TM} is a ductile plastic and will bend under stress producing no acoustic emissions. Another important attribute of Teflon^{TM} is its melting temperature of 327 ^{0}C which is high enough to eliminate the possibility of melting at high temperature. Results are shown in Figure 3.12 comparing an experiments that Teflon^{TM} sheets and phenolic plastic carried out using the same pre-amplification (35 dB), threshold value (40 dB), and pressurization rate as that of the AgCl experiment. Notably absent from the experiment using Teflon^{TM} plates is the initial peak in hits caused by the fracturing of the phenolic plates. This indicates the Teflon^{TM} was soft and ductile enough to prevent the production of acoustic noise at this stage of pressurization. We also see that further pressurization was generally quieter with the Teflon^{TM} sheets at high pressure by

~400 hits per minute. This phenomenon even persisted at pressures above 4 GPa when the gaskets were fully formed and compaction of the cell was complete. Figure 3.13 shows that the energy associated with hits in the experiment using Teflon™ sheets was all but absent during gasket formation with an overall reduction at all pressures.

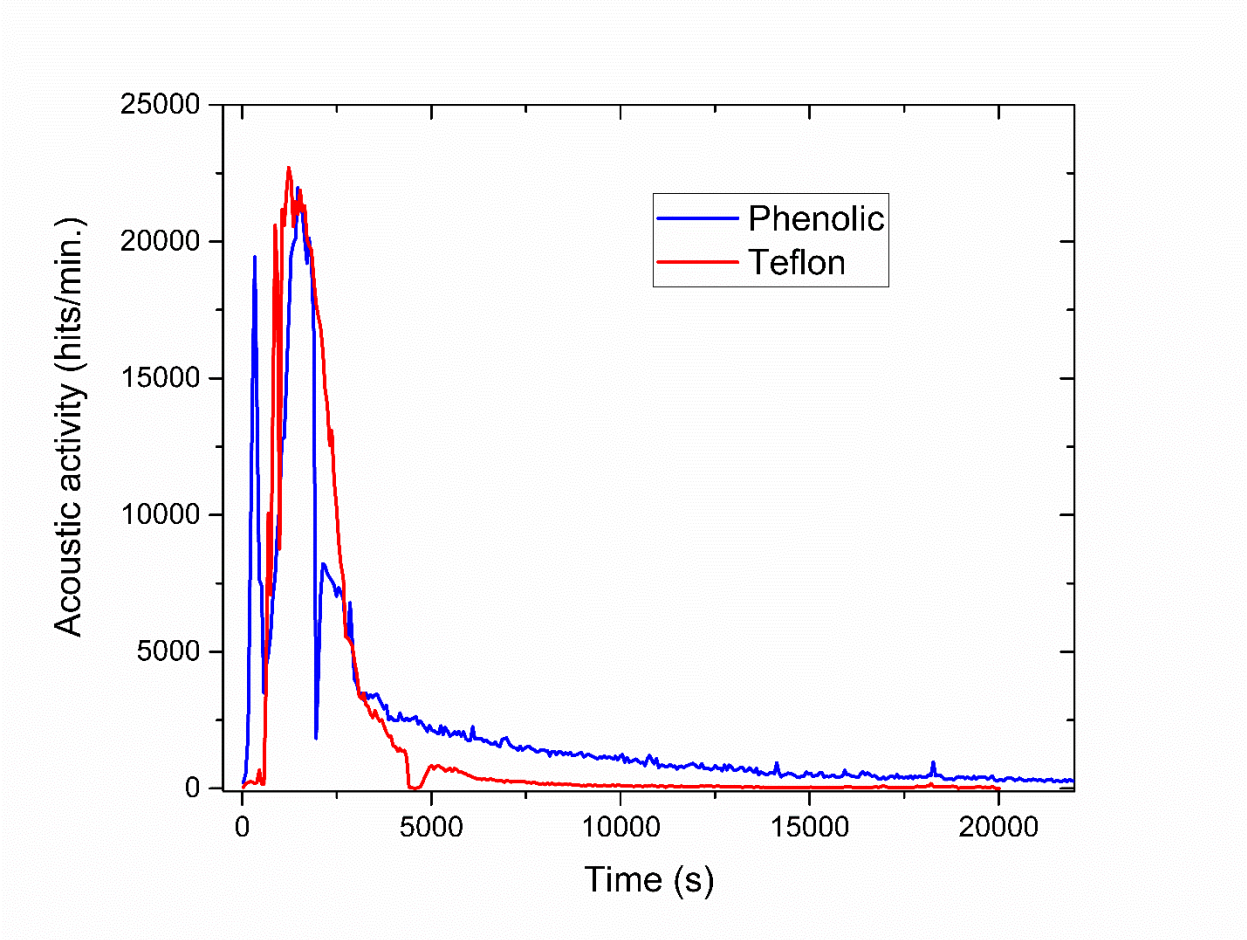

Figure 3.12: Comparison of background acoustic activity (hit rate/min.) vs. experimental run time for experiments employing phenolic plates in contrast to those with Teflon™ sheets.

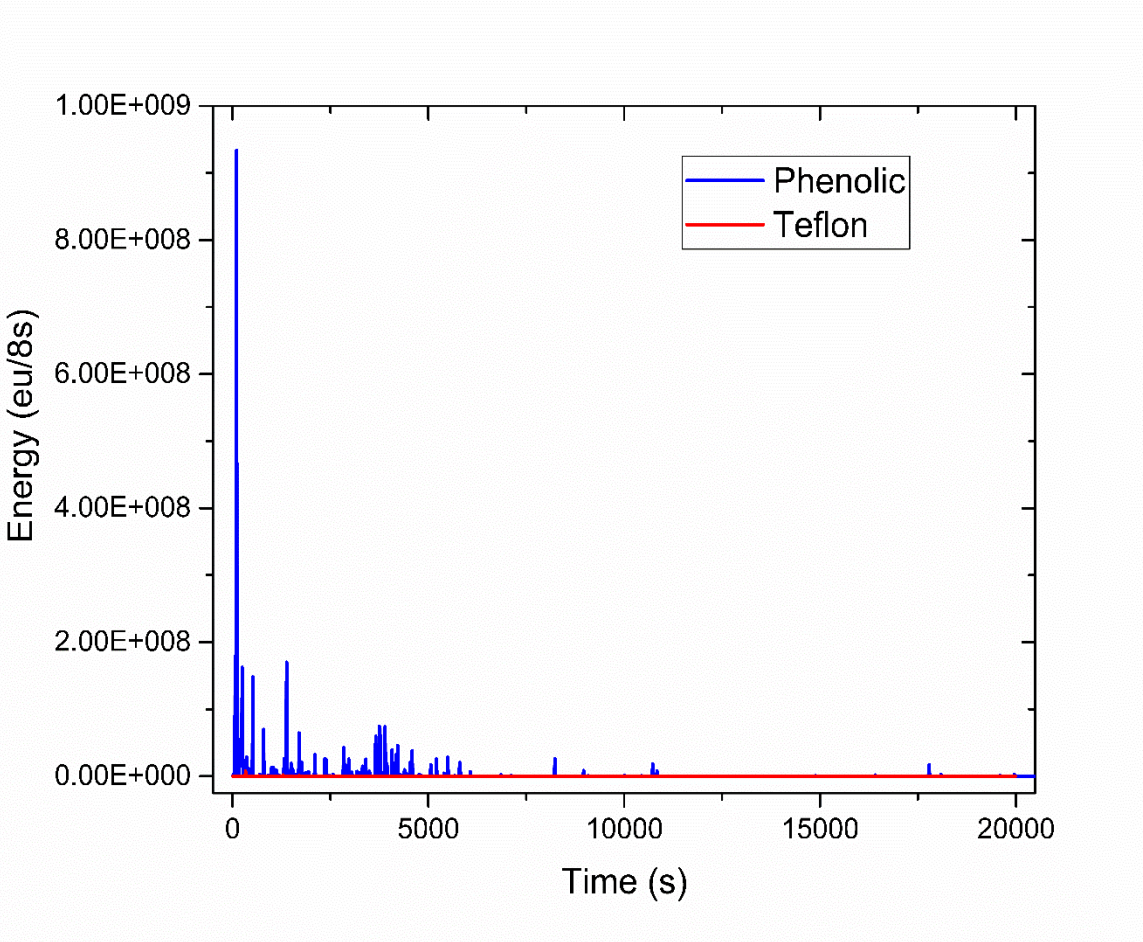

Figure 3.13: Comparison of background acoustic energy production for experiments employing phenolic plates in contrast to Teflon™ sheets.

However, while this experiment was a success in terms of reducing acoustic noise at all pressures, when the pressure module was opened to remove the anvils and the octahedron from the press a considerable problem was encountered. As a result of the ductility of Teflon™, it was lodged into the spaces between the wedges in the pressure module (see Figure 3.14**)**.

a) 

b) 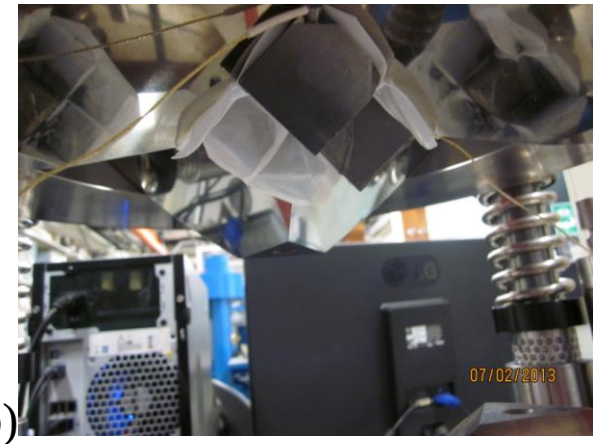

Figure 3.14: Lower (a) and upper (b) views of the module after the experiment using Teflon™ sheets. All six Teflon™ sheets became lodged between the sub-mm gap between the wedges making extraction and removal of the Teflon™ both cumbersome and time consuming as well as being potentially detrimental to the function of the press.

Removing the Teflon™ sheets from the press module required several hours of painstaking cutting, pulling and twisting to finally extract them. Therefore, because of the labourious work required to remove the sheets and the possibility of damage to the press module, which has the potential to affect the press calibration curve, unfortunately the use of Teflon™ had to be abandoned. Instead, the six phenolic plates used to hold the cubes together were cut into four sections each (24 total) and glued separately to each anvil face in contact with the module then placed in the press individually. This worked to remove the acoustic activity generated by the fracturing of the phenolic plates while still maintaining electrical isolation from the press. Figure 3.15 shows the anvils in the pressure module with the individual phenolic sections glued separately.

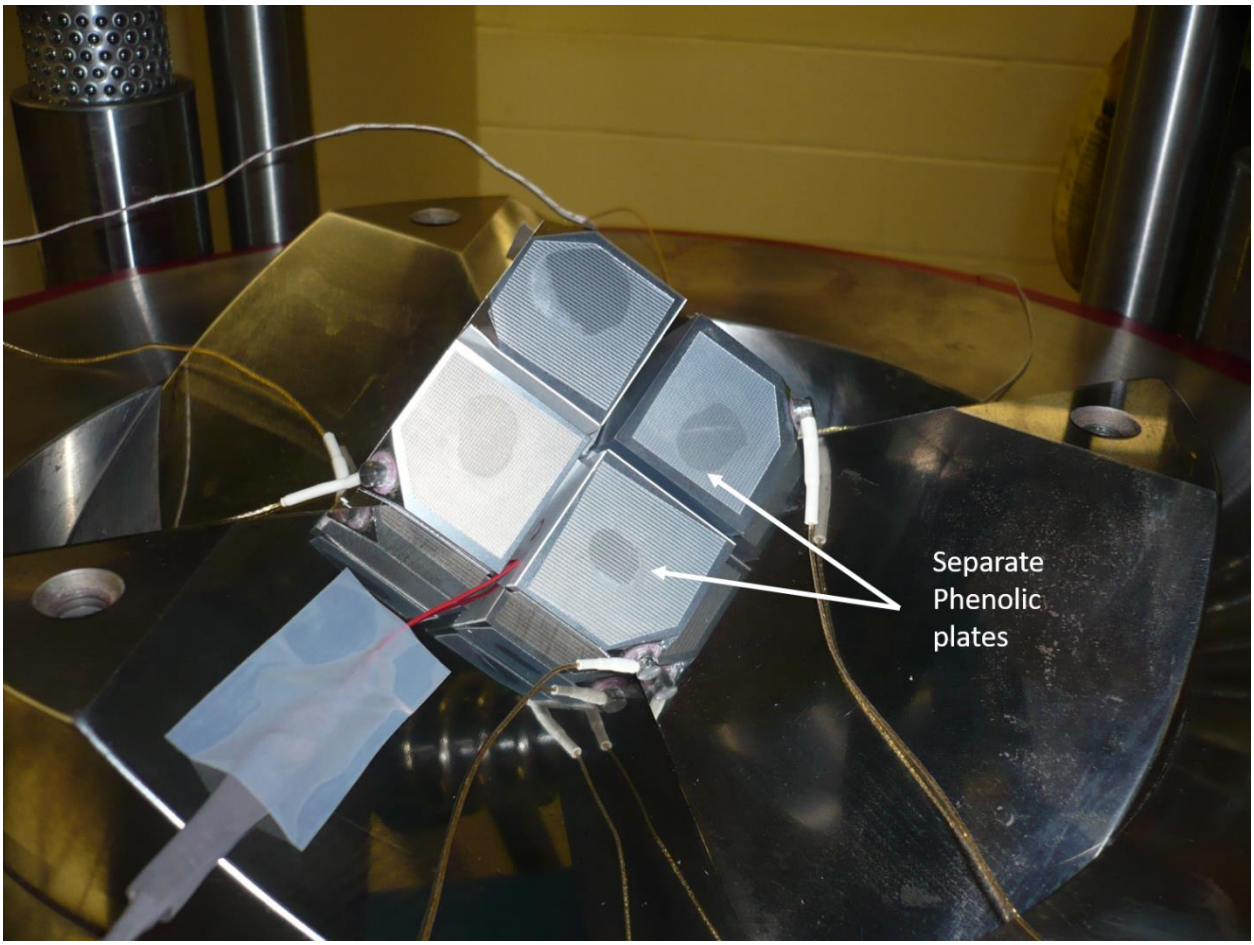

Figure 3.15: Image of the pressure assembly in the module. Note that the phenolic plates are glued to each individual anvil face in contact with the pressure module.

3.5.2 MgO versus a pyrophyllite pressure medium

Another strategy implemented to eliminate some of the background acoustic noise was to try and reduce the sonic energy associated with the compaction of the pressure medium. This was done by replacing the MgO octahedron with a pyrophyllite octahedron with the same dimensions. In order to achieve this, the octahedron needed to be manufactured in house. This was accomplished by drawing a three-dimensional model in the CAD program SolidWorks^{TM}, converting this geometric information into a *.stl* file and having the part automatically fabricated to a very high degree of precision on our 4-axis CNC Roland mill in the Earth Sciences Machine

Shop. Figure 3.16 shows the CAD design for a batch of two cells to be machined at once in the Roland Mill shown in Figure 3.17. Figure 3.18 shows the output from the mill after fabrication.

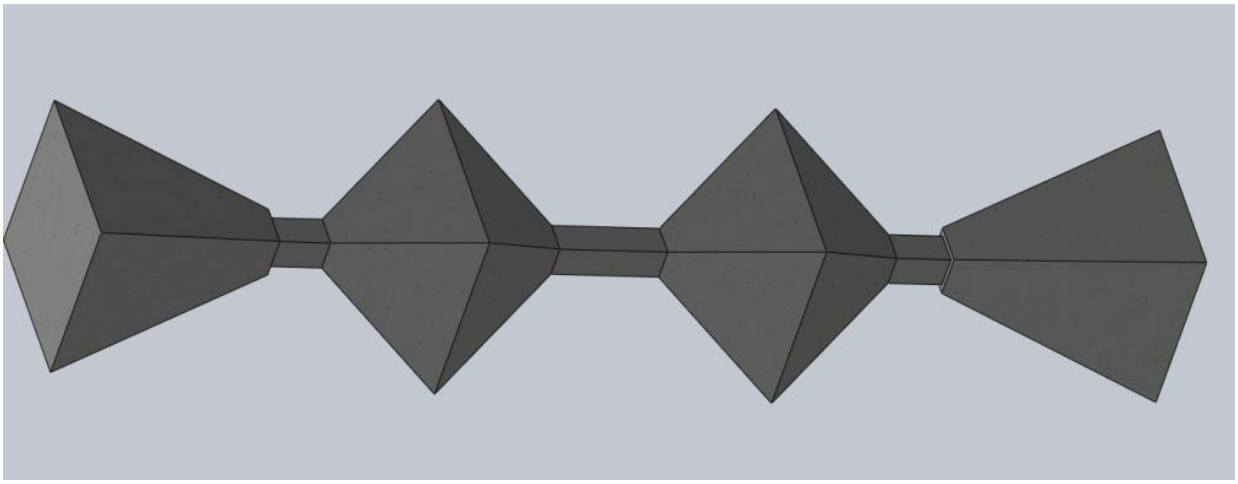

Figure 3.16: 3D CAD representation of the part containing two 18/11 octahedral cells to be manufactured on our 4-axis CNC mill. Roland mill in the Earth Sciences Machine Shop.

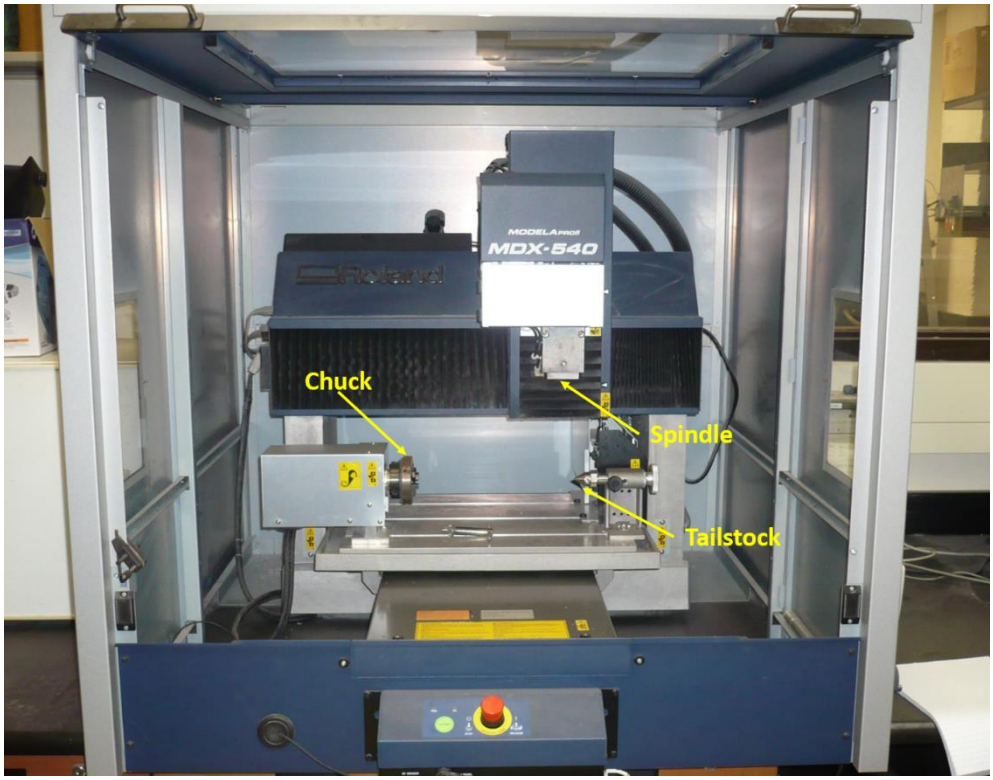

Figure 3.17: Our four-axis CNC Mill in the Earth Sciences Machine Shop. It is the MODALApro MDX-540 manufactured by Roland.

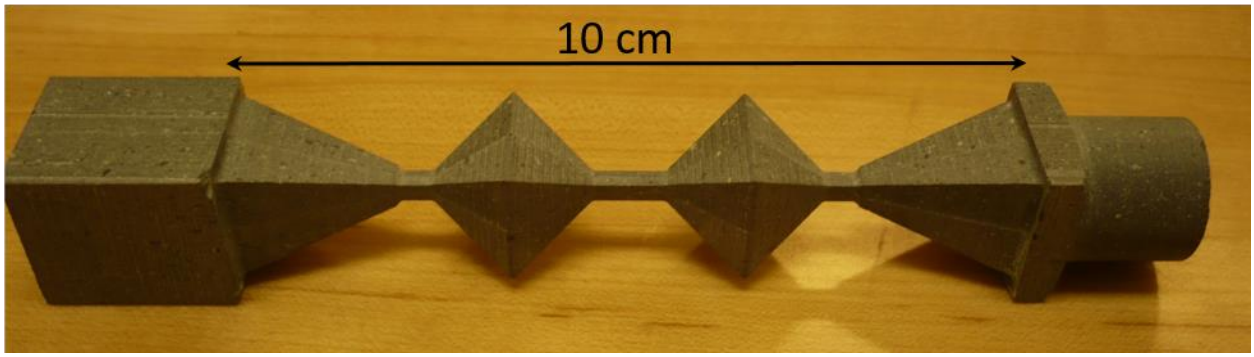

Figure 3.18: Part consisting of two 18/11 octahedra machined to high accuracy from a billet of pyrophyllite based on the coordinates exported from the CAD design of Figure 3.15.

An individual octahedron could then be broken from the part and filed to the desired shape.

Figure 3.19 shows a pyrophyllite octahedron ready for use in an experiment.

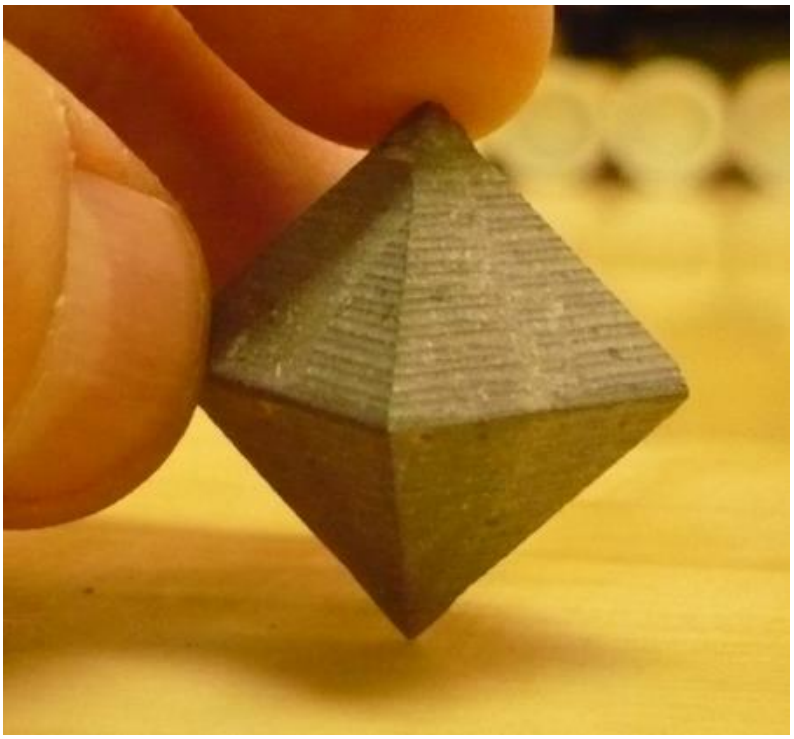

Figure 3.19: Individual pyrophyllite octahedron with the same dimensions of the 18/11 MgO octahedra used in HPHT AE experiments. The textured finish on each octahedron face are relic terraces from the step-machining process.

Measurements of the axial dimension of each direction of the octahedron showed that they were in agreement with the MgO octahedra to within ± 0.05 mm which is in accordance with the accuracy of the MgO octahedra manufactured by the Consortium for Materials Properties Research in Earth Sciences (COMPRES). Results for this experiment, as compared to that of the experiment with the AgCl sample, are shown in terms of hit rate (Figure 3.20) and energy (Figure 3.21). Again the pre-amplication, threshold value, and pressurization rate were identical in each experiment.

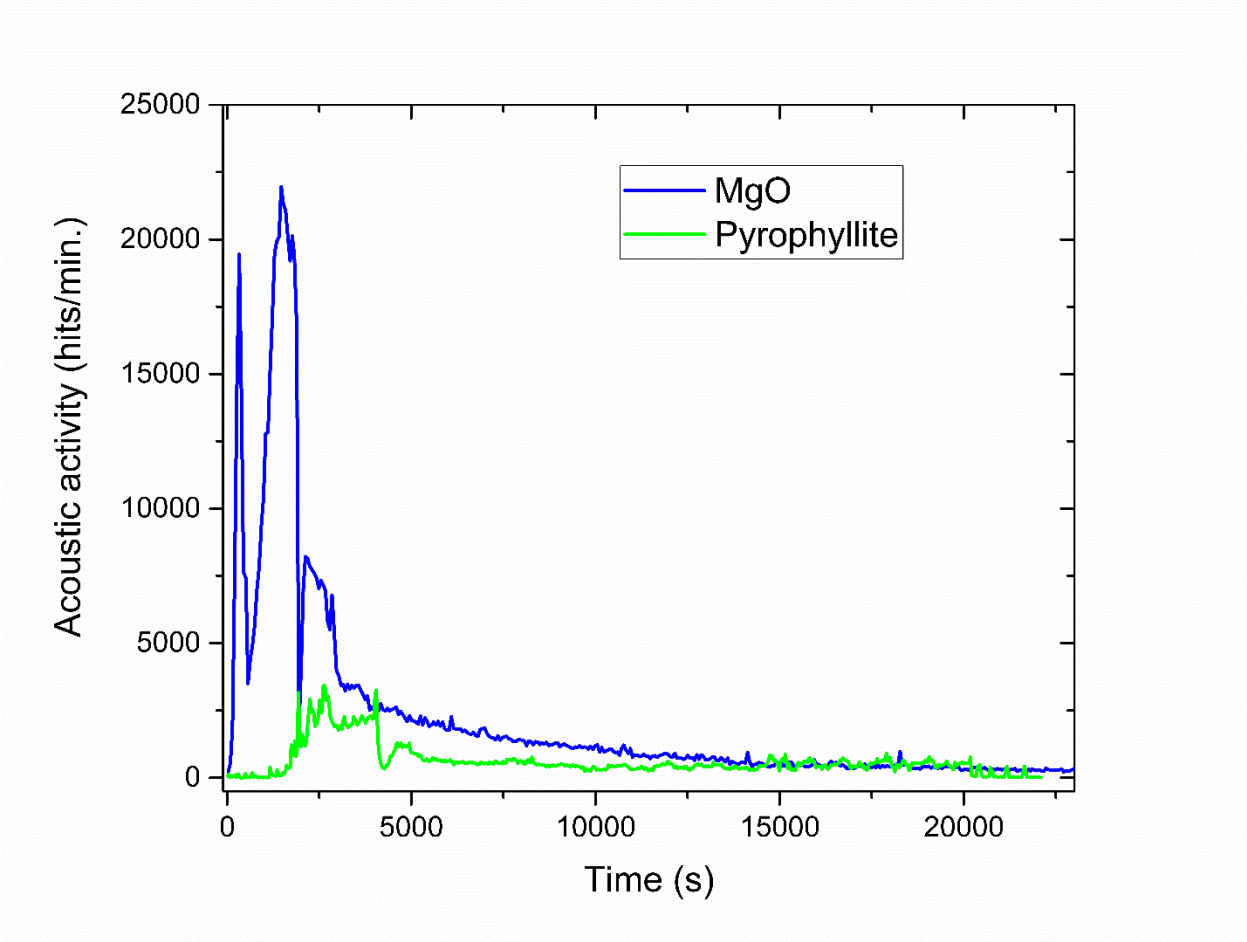

Figure 3.20: Comparison of background acoustic activity (hit/min.) vs. experimental runtime for experiments employing a pyrophyllite octahedron in contrast to that of MgO.

At low pressure we see that the overall hit rate is significantly reduced with the use of the pyrophyllite pressure medium. In particular, the acoustic noise associated with the flow of the much softer pyrophyllite cell is substantially reduced compared to ~30% compaction of MgO. Strangely, the phenolic plates appear not to have generated large numbers of hits for the pyrophyllite octoahedron as was the case for MgO. However, evidence of the fracturing of the phenolic plates at low pressure can be witnessed in the energy vs. time plot shown in Figure 3.21.

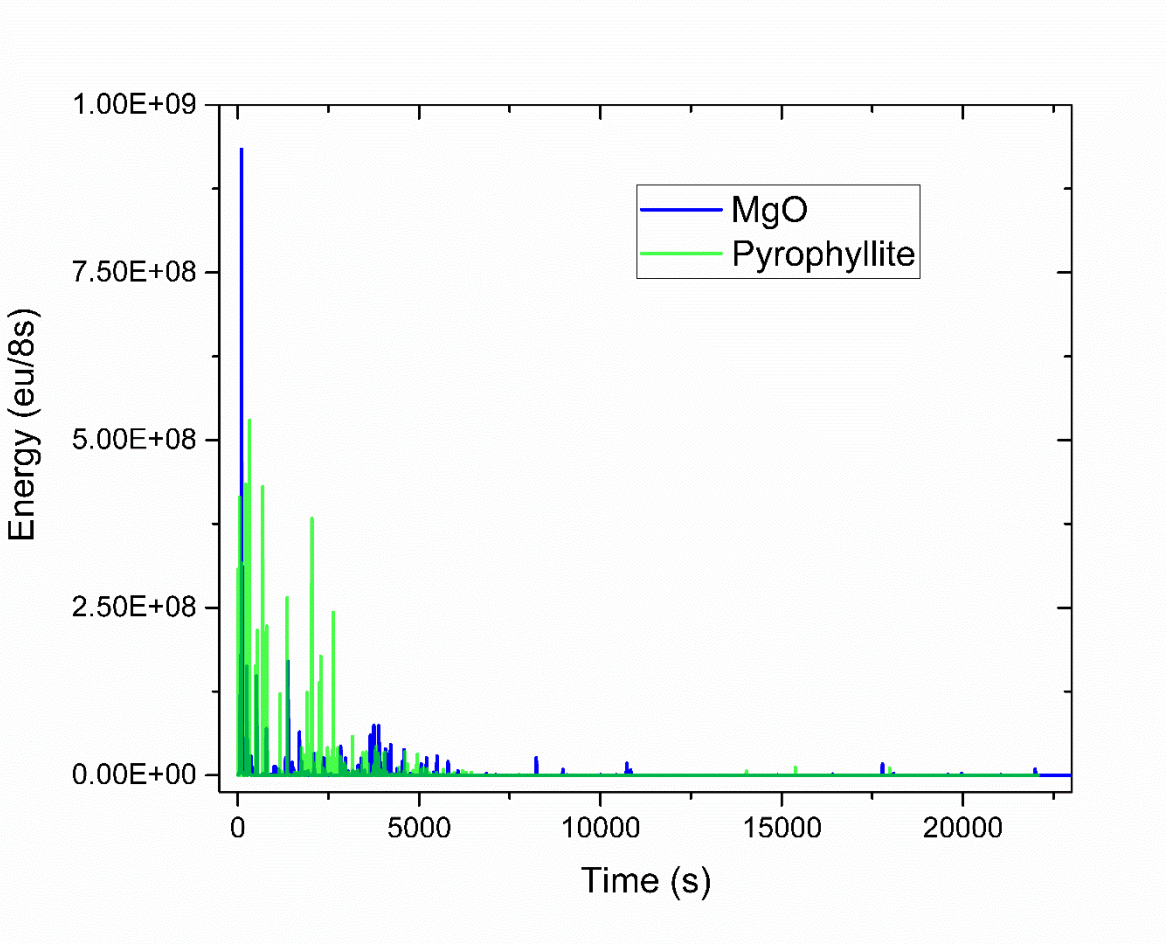

Figure 3.21: Comparison of background acoustic energy production for experiments employing MgO and pyrpohyllite cells.

In fact, the amount of overall energy released during compression of the pyrophyllite cell appears to be more than the MgO cell indicating that the pyrophyllite generates a fewer number of high energy hits during the compaction/flow and gasket formation stage of pressurization. This may be a result of poor acoustic transfer through the pyrophyllite, perhaps as a result of higher attenuation and a larger number of grain boundaries in this material that scatter acoustic waves. If this is indeed the case, it would prove problematic for use in HPHT AE experiments since it would be less effective in transferring acoustic energy from the sample to the transducers. More importantly, while the relatively low hit rate could be interpreted as an improvement in the acoustic noise generated, at least in terms of its overall activity, at higher pressures where experiments on silicate minerals are to be carried out there appears to be little, if any, benefit. A switch from MgO to pyrohyllite octohedra would have also required recalibration of the oil pressure to cell pressure curve already established for 18/11 octahedra (See Figure 3.9). For these reasons it was deemed both impractical and unnecessary to switch to a pyrophyllite pressure medium, however it does demonstrate that the choice of pressure medium can have a large impact on the level of acoustic activity. Indeed, boron epoxy cells have been shown to generate very low amounts of AE during compaction (Gasc et al., 2011), but proved difficult to fabricate into octahedra.

3.6 Reducing electrical noise

Another significant source of spurious signals is electrical noise produced by the press pump. Whenever the press pumping system is running there is a certain amount of electrical background noise which is always present. In the previous experiments described, most of the

spurious hits triggered from electrically induced noise were eliminated by using a relatively low pre-amplification (32 dB) and frontend filtering. Since these signals tend to have short bursts of energy interspersed by periods of relative quiet it is possible to drastically lower the number of overall hits recorded by imposing a frontend filter that requires at least 5 counts to trigger a hit. Using a relatively low pre-amplification lowers the overall amplitude of the signal so that with a threshold value of 40 dB the threshold is seldom crossed by signals that originate purely through electric induction. However, the drawback to this approach is that low pre-amplification may overlook acoustic signals of potential value. Also, acoustic signals large enough to be recorded will contain electrically induced noise superimposed on top of them. For these reasons it was imperative to devise a solution that would electrically isolate the transducers from the cubes. Signals of electronic origin are easily distinguished by analyzing the waveforms they produce. Figure 3.22 compares a typical waveform created by an acoustic hit to that of a signal generated by electrically induced noise. Electrically induced signals tend to be characterized by their distinctive time series. One possible means of removing this signal would be to utilize a bandpass filter, however the frequency spectrum of the electrical noise indicates that it is composed of a wide band which overlaps with those of acoustic hits (see Figure 3.23).

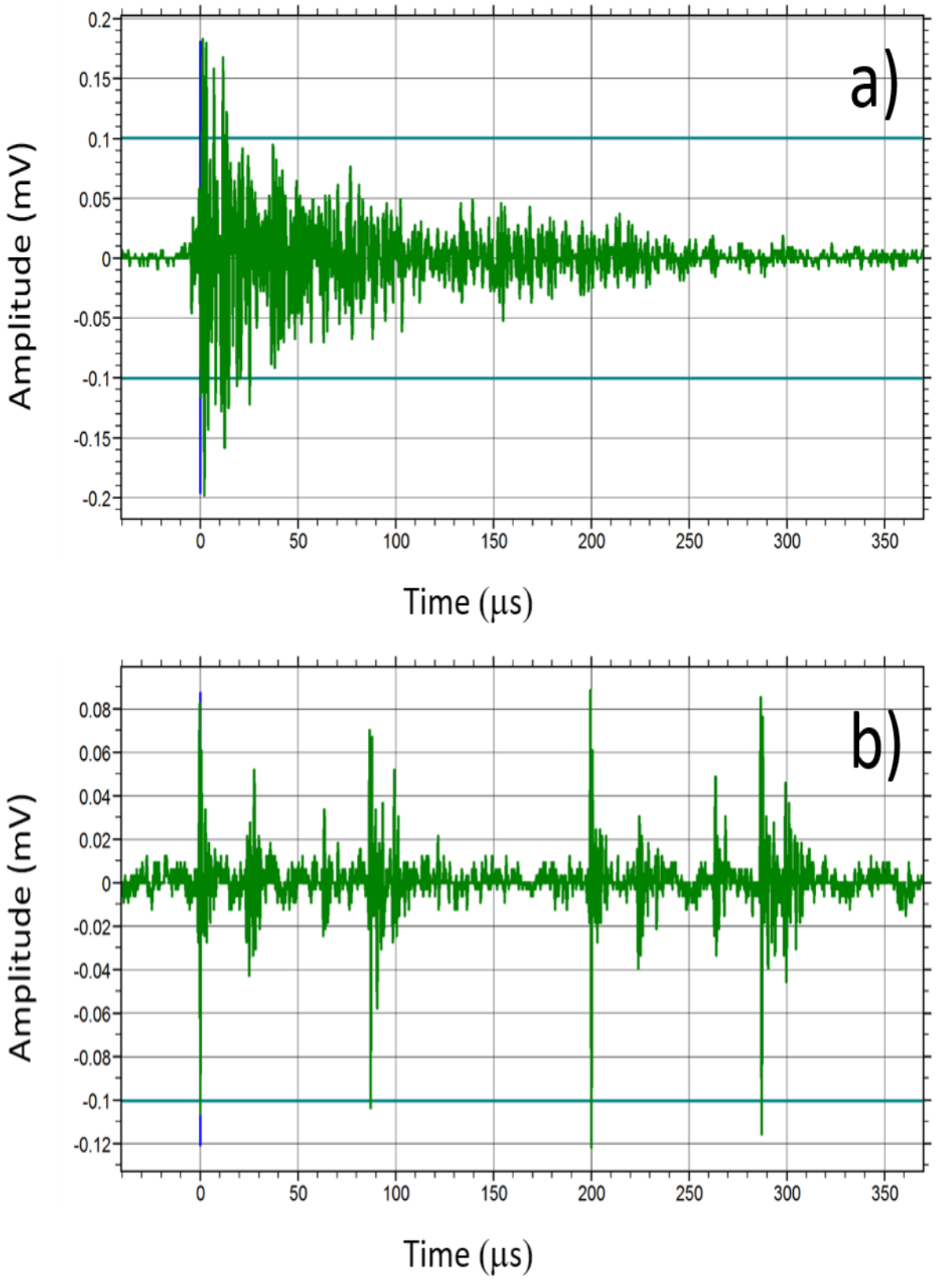

Figure 3.22: a) Typical time series for an acoustic waveform. b) Typical time series for a waveform generated by electrical noise due to the press pump.

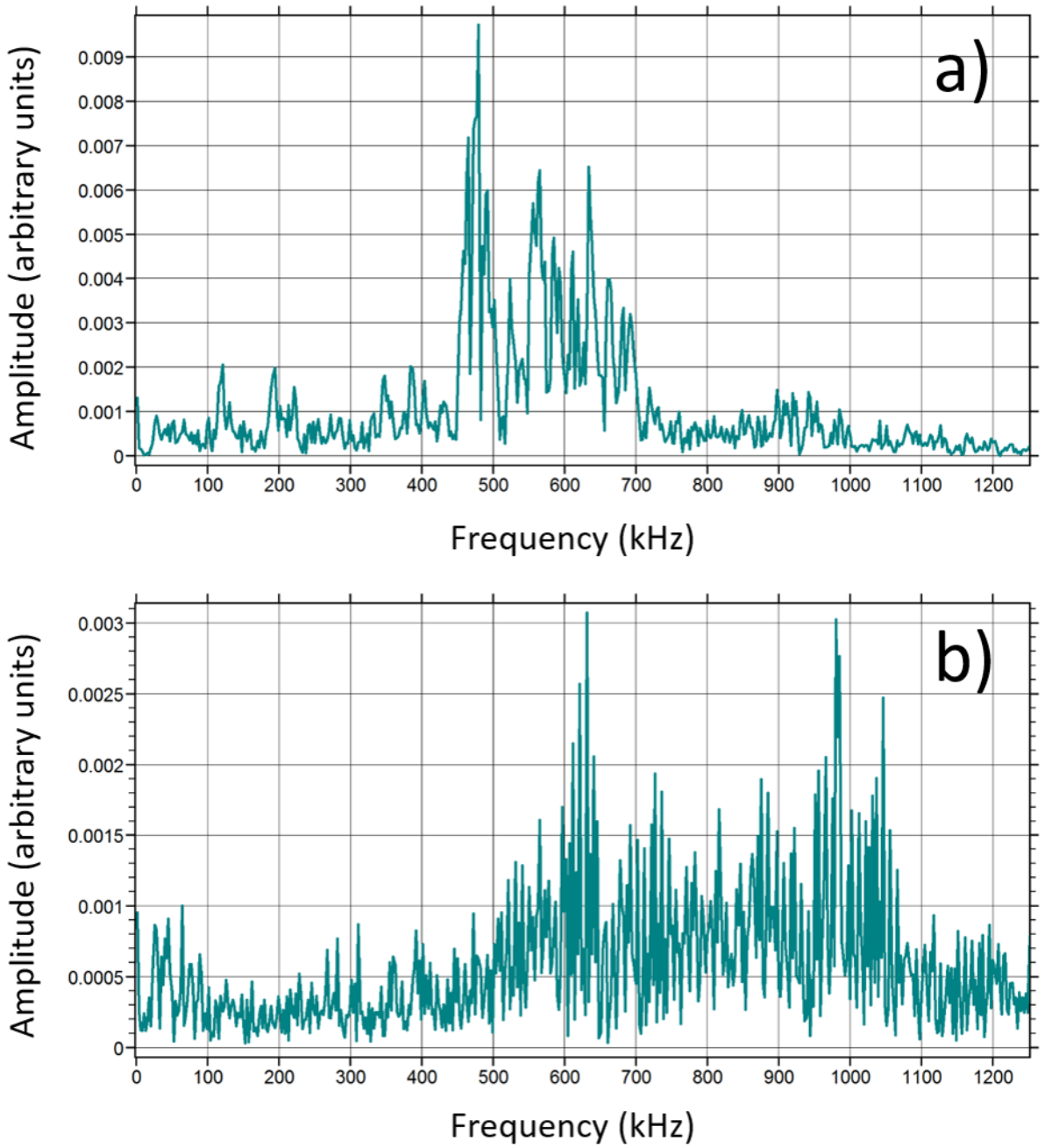

Figure 3.23: a) Frequency spectrum for a typical acoustic hit. b) Frequency spectrum for a hit generated by electrical noise from the press' pump.

Therefore, in order to maintain the integrity of acoustic signals received but eliminate the electrical noise, 0.1 mm thick Diamonite^{TM} discs were glued to the anvil truncations between the

anvils and the transducers as shown in Figure 3.25. The extremely high resistivity of the Diamonite™ electrically insulates the transducers from the anvils to the transducers as shown in Figure 3.24.

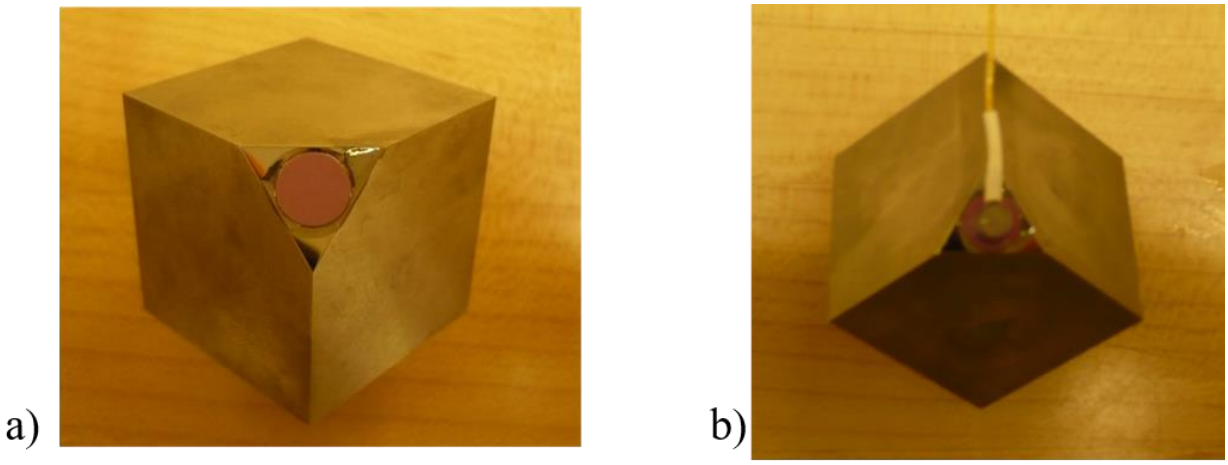

Figure 3.24: a) Diamonite™ disc adhered to the anvil's rear truncation. b) Transducer fastened to the Diamonite™ disc which is sandwiched between the transducer and the anvil providing electrical insulation.

Diamonite™ is a diamond analogue material made from 94% finely powdered pink sapphire (Al_2O_3) and a binder molded under high pressure and sintered at high temperature. It is as hard as WC (9+ on Moh's scale) and is resistant to acids, alkalis and most other corrosive materials. In particular, it has a very high electrical resistivity of 1×10^8 Ωcm and electrically insulates the anvils from the transducers. To test the efficacy of the Diamonite™ discs three of the six anvils with transducers were equipped with the Diamonite™ discs (channels 3, 4 and 5), while two were adhered directly to the anvils with cyanoacrylic glue (channels 1 and 2). On the remaining anvil, the transducer was adhered with a high viscosity version of cyanoacrylic glue to test if the glue provided enough insulation to combat the electric noise to a degree that the Diamonite™ was unnecessary, thus eliminating the need for another potentially reflective boundary. Figure 3.25 shows the number of hits received during pressurization to 140 psi using 40 dB pre-amplification and a 40 dB threshold. During this stage of pressurization, acoustic energy is far

larger than that of electrically induced signals and therefore exclusively dominates hit generation. Therefore, during this phase of pressurization the acoustic performance of channels with and without the Diamonite™ discs can be directly compared since the influence of electrically induced noise is effectively removed.

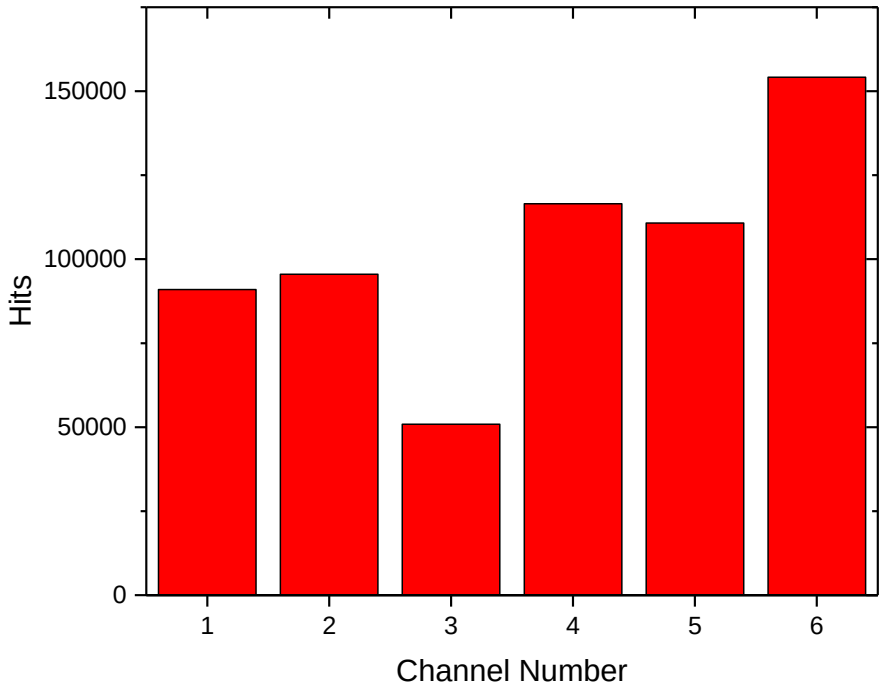

Figure 3.25: Number of hits for each channel from 0 – 140 psi; channels 1 and 2 do not employ Diamonite™ discs; channels 3, 4 and 5 employ Diamonite™ discs; channel 6 uses a high viscosity cyanoacrylic glue.

We see that each channel registered a similar amount of overall acoustic activity and channels 4 and 5, which utilize the Diamonite™ discs actually collected more hits than channels 1 and 2 without the Diamonite™. Above 140 psi the system is far quieter acoustically since the gaskets are mostly formed and the cell is nearly fully compacted. Therefore, electrically generated signals dominate the overall activity of the transducers. Figure 3.26 shows the number of hits accumulated on each channel during pressurization from 140 psi – 570 psi.

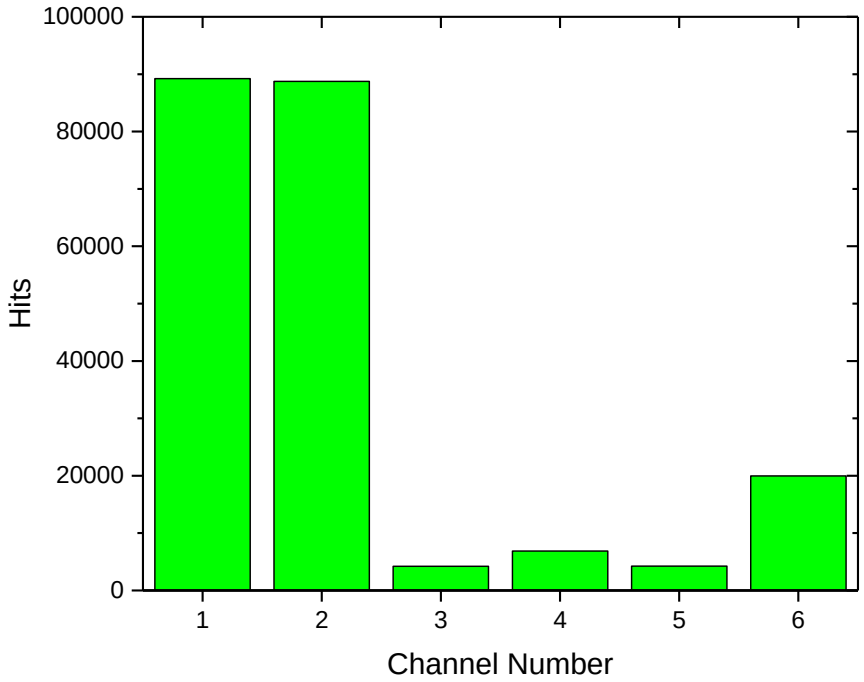

Figure 3.26: Number of hits for each channel from 140 – 570 psi; channels 1 and 2 do not employ Diamonite™ discs; channels 3, 4 and 5 employ Diamonite™ discs; channel 6 uses a high viscosity cyanoacrylic glue. The high ratio of hits accumulated by channels 1 and 2 compared to the others is due to spurious signals generated by electrically induced hits caused by the press pump.

Compared to the transducers without the Diamonite™ discs (channels 1 and 2), those employing Diamonite™ (channels 3, 4, and 5) register far less hits. Channel 6, which used the high viscosity glue, saw some improvement over that of no insulation but was still susceptible to a degree of electrically generated hits. Further proof that electrical noise was responsible for the hits recorded by the channels without electrical insulation can be witnessed in the level of root-mean-square (RMS) noise in each channel which is a measure of the RMS variation in signal the moment before the threshold is crossed. Figure 3.27 shows the value of the RMS noise as a function of pressure from 140 psi – 570 psi.

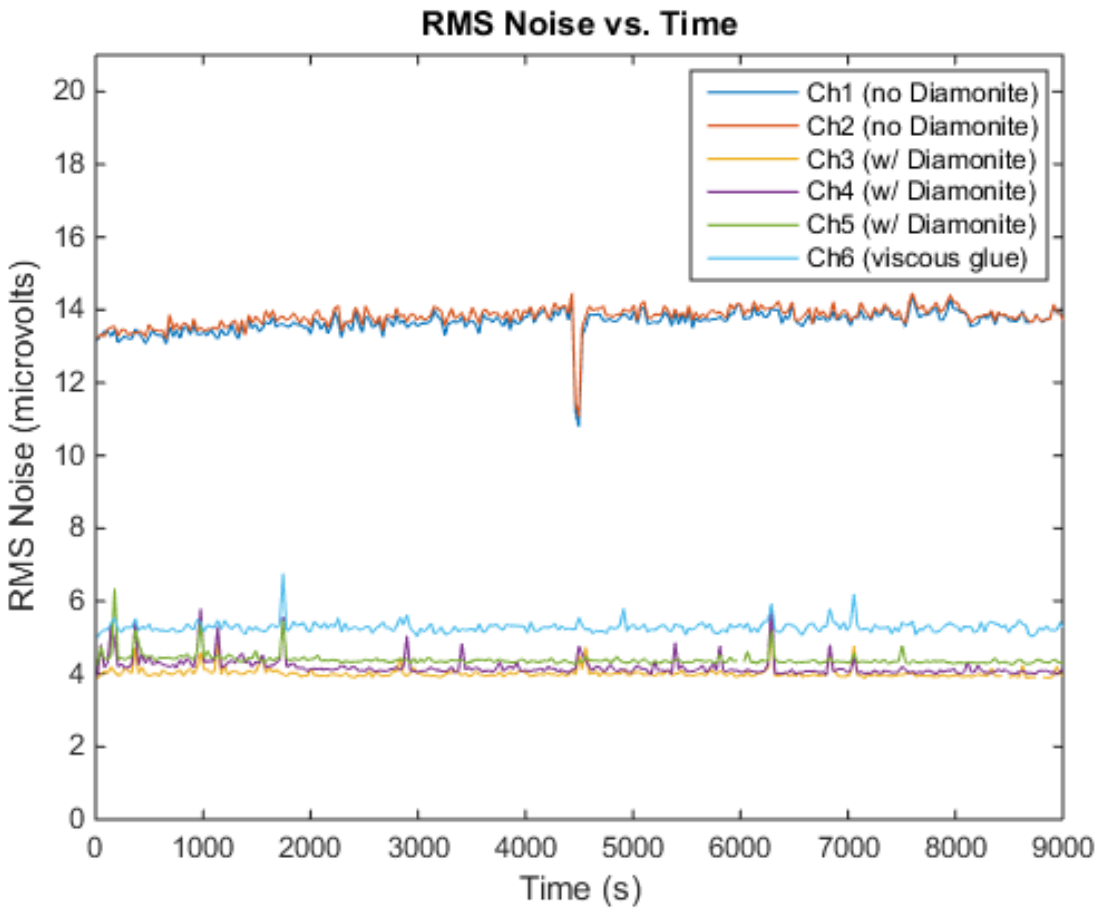

Figure 3.27: RMS noise for each channel from 140 - 570 psi. Note that channels 1 and 2, which do not employ the use of the Diamonite™ discs, are ~ three times higher than channel 3, 4 and 5 which employ Diamonite™ discs. Channel 6, which was adhered to the transducer with viscous cyanoacrylic glue is also higher that of channel 3 -5.

Note that the RMS noise is more than three times higher than that of each channel containing the Diamonite™. Channel 6, with the high viscosity glue, is higher as well.

3.7 Measuring pressure with the Vallen system

Another development made to the system was to enable pressure to be directly measured by the Vallen A2D boards and plotted along with other acoustic information in the Vallen software. The Vallen ASMY-6 is equipped with four parametric input channels that are capable

of measuring voltage from a separate input other than a piezoelectric transducer. This allows for the input of a pressure transducer, shown in Figure 3.28, which is installed along the oil line of the press. It converts the pump oil pressure to a voltage which can then be digitized and recorded on the computer hard drive as a function of any other acoustic parameter.

Figure 3.28: Photograph of the pressure transducer connected to the pressure line of the press pump.

The pressure transducer voltage is linearly related to units of oil pressure whose calibration curve can be entered into the Vallen software to convert mV to psi. This allows the oil pressure to be measured *in situ* and graphically observed in real time during an experiment permitting quick access to pressure and the pressurization rate in psi/s by measuring the slope of the oil pressure versus time curve. Figure 3.29 shows a plot generated and exported from the Vallen software which was created in real-time during an experiment.

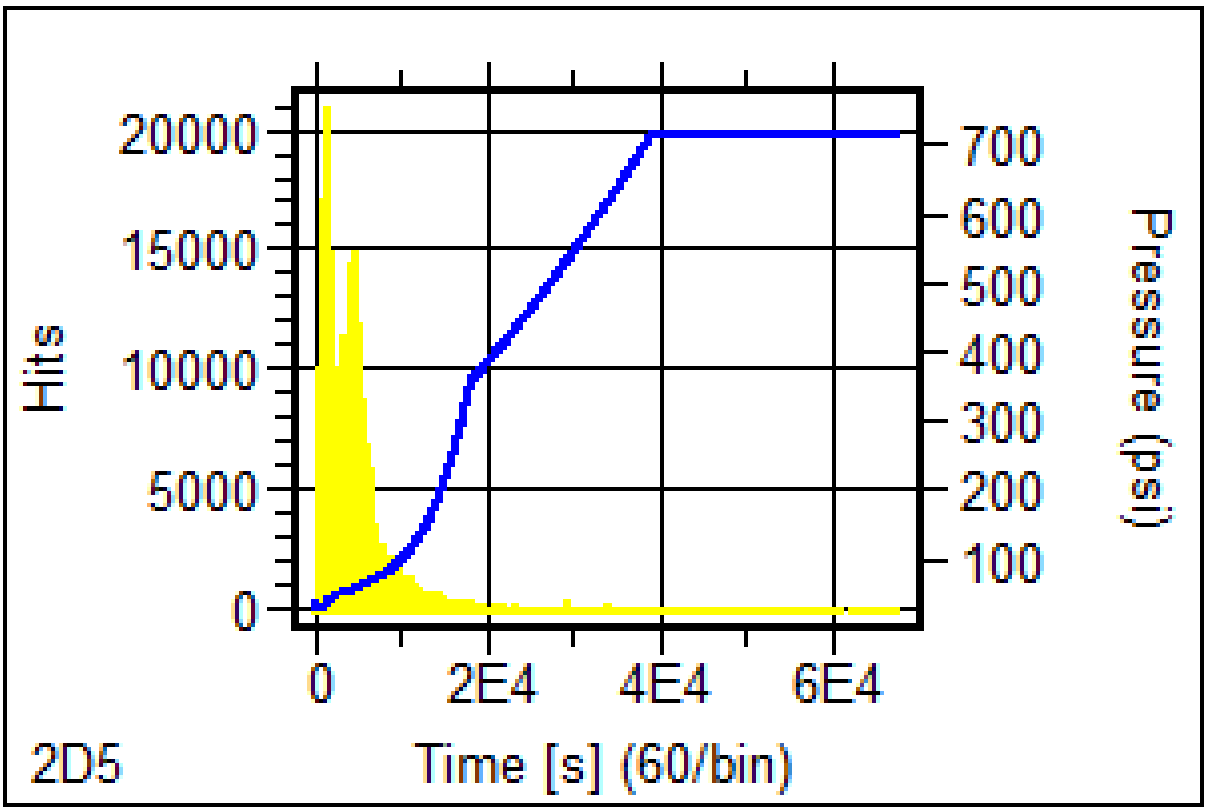

Figure 3.29: Pressure versus time (blue) and hits versus time (yellow) plotted on the same graph. The pressure was measured at 10 Hz using one of the parametric inputs. This graph was exported directly from the Vallen software.

Due to the non-linearity of the oil pressure versus sample pressure curve (see Figure 3.9) the sample pressure must be extracted using the calibration curves of equations 3.2 or 3.3. This is achieved during experiments by consulting the oil pressure versus calibration pressure curve directly, but can be plotted against any experimental parameter post-experiment by extracting the

oil pressure measurements (in psi) from the Vallen software and converting them to units of GPa. The sampling rate of the parametric inputs is far lower than that of the piezoelectric transducers, however it is adjustable to up to 10 samples/s which resolves the pressure to better than 0.1 psi per datum when the syringe pump motor is working at 100 percent. This is far superior to the accuracy of manually copying pressure measurements from the press control panel whose resolution is 1 psi.

3.8 Conclusions

A system has been developed in the Experimental High Pressure/High Temperature Mineral Physics and Material Science Laboratory at Western University that is capable of measuring ultrasonic acoustic emissions under *in situ* conditions of HPHT in a multi-anvil apparatus. It utilizes a microseismic array of a six piezoelectric transducers, adhered to the rear truncations of tungsten carbide anvils which convert mechanical vibrations, in the form of ultrasonic waves, to electrical impulses. The signal voltages are pre-amplified and fed into the AMSY-6 acoustic emission system manufactured by Vallen Systemes which utilizes their ASIP-2 processing boards to digitize and collect data with a sampling rate of up to 40 Hz. Due to the vast amount of data recorded during a typical experiment, the system works on a triggered basis that only collects data considered valuable based on a user defined voltage threshold. Since triggering of a hit takes place after the onset of the waveform the system makes use of transient recorders on each channel which continuously record and remove data unless the threshold is crossed. This ensures that data prior to triggering is recorded and the entire waveform is captured, digitized and stored. Steps were taken to reduce both acoustic and electrically generated noise making the

system enhancing the ability to discriminate between signals generated in the sample compared to other spurious sources. In particular, the HPHT AE system discussed in this chapter is capable of generating and detecting acoustic signatures associated with microscopic faults in silicate minerals and can therefore be applied to the experimental study of DFEQ triggering mechanisms.

3.9 References

Dobson, D.P., Meredith, P.G. and Boon, S.A., 2002. Simulation of subduction zone seismicity by dehydration of serpentine, *Science*, **298**, 1407-1410.

Dobson, D.P., Meredith, P.G. and Boon, S.A., 2004. Detection and analysis of microseismicity in multi anvil experiments. *Phys. Earth Planet In.*, **143-144**, 337-346.

Gasc, J., Schubnel, A., Brunet, F., Guillon, S., Mueller, H.J. and Lathe, C., 2011. Simultaneous acoustic emissions monitoring and synchrotron X-ray diffraction at high pressure and temperature: Calibration and application to serpentinite dehydration, *Phys. Earth Planet In.*, **189**, 121-133.

Gautschi, G., 2002. *Piezoelectric Sensorics: Force, Strain, Pressure, Acceleration, and Acoustic Emission Sensors, Materials and Amplifiers*, Springer-Verlag Berlin Heidelberg.

Grosse,C.U., 2008. *Acoustic Emission Testing*, 2008. Springer-Verlag Berlin Heidelberg.

Jung, H., Fei, Y., Silver, P.G. and Green, H.W., 2006. System for detecting acoustic emissions in multianvil experiments: Application to deep seismicity in the Earth, *Rev. Sci. Instrum.*, **77**, 014501.

Kanamori, H. and Rivera, L., 2006), Energy Partitioning During an Earthquake, in *Earthquakes: Radiated Energy and the Physics of Faulting* (eds R. Abercrombie, A. McGarr, G. Di Toro and H. Kanamori), American Geophysical Union, Washington, D. C..

King, G.C., 2009. *Vibrations and Waves*, John Wiley & Sons, UK

Ensminger, D. *Ultrasonics, Second Edition*, Marcel Dekker Inc., New York, New York, 1988, pp. 154-155.

Nguyen, N.T., Lethiecq, M., Karlsson, B. and Patat, F., Highly attenuative rubber modified epoxy for ultrasonic transducer backing applications, *Ultrasonics*, **34**, 669-675 (1996).

Safari, A. and Akdogan, E.K., 2008. *Piezoelectric and Acoustic Materials for Transducer Applications*, Springer-Vergland US.

Chapter 4: Detection of a pressure-induced liquid ⇌ solid phase transformation by measuring sound velocity in a multi-anvil apparatus

A technique for detecting phase transitions in the multi-anvil apparatus was developed that measures the change in longitudinal sound velocity as a function of pressure. In particular, the system measures the time for pulsed ultrasonic signals to travel through a high pressure assembly along three acoustic paths simultaneously with a sample in the center. Upon phase change from liquid to solid, the sound velocity shows an abrupt increase due to the intrinsic increase of velocity in the sample and a reduced delay between the triggering of an amplitude threshold and the arrival of the waveform. As a proof of concept, results are shown for elemental Hg as it undergoes pressure-induced liquid ⇌ solid transitions at room temperature. The technique discussed in this chapter was published in *High Pressure Research*, (Officer and Secco, 2015), and can be viewed online at: **http://dx.doi.org/10.1080/08957959.2015.1035715**.

4.1 Introduction

Measuring the precise pressure at which phase transformations occur in multi-anvil apparatuses is an ongoing challenge in high pressure science due to the incapability of directly accessing the sample under high pressure conditions. Therefore, indirect methods of investigation must be invoked to measure physical properties that infer the occurrence of phase transformations. Such information is critical in determining the high pressure behavior of materials. In particular, determining the precise HPHT point of transition, based on known phase

transformations, is essential in calibrating confining pressure within the high pressure apparatus as a function of the oil pressure in the pistons. Typically, HPHT phase boundaries are determined by bracketing the boundary between the phases of recovered samples. However, this technique requires that the high pressure polymorphs do not revert to their low pressure structure upon removal of pressure and requires many experiments at varying P, T conditions to achieve accurate results. *In situ* determination of material phase boundaries has been carried out for a long time by witnessing discontinuities in resistivity of transforming phases for example (e.g. Bridgman, 1938; Block, 1978; Balog and Secco, 1999), and more recently by detecting acoustic emission associated with the rapid collapse and reconfiguration of the sample and pressure assembly during structural transformations with associated volume changes (de Ronde et al., 2008), or by performing X-ray diffraction using synchrotron radiation to observe directly the change in the atomic structure of the sample (e.g. Zhang et al., 1996; Yagi et al., 1987; Suzuki et al., 2000). Another possibility for in situ determination of a phase transformation is by examining the contrast in sound velocity between two distinct phases. Acoustic activity has been observed in multi-anvil apparatuses using interferometric techniques to measure the travel time of an acoustic pulse and its echo across a sample (Li et al., 1996a and 1996b). While this technique is highly accurate in its determination of sound velocity at elevated pressures and temperatures, particularly when it is accompanied by synchrotron radiation for *in situ* sample length determination as a function of pressure (Darling et al., 2004; Li et al., 2004; Mueller, 2013), it has rarely been used to detect *in situ* velocity in a phase transforming sample (Kung et al., 2004). Measurements of the sound velocity of liquid samples have been made in large volume presses (Song et al., 2011; Jing et al., 2014), but so far this approach has only recently been employed to distinguish between liquid/solid phases and to monitor the transition using a

pulse echo (i.e. single transducer) configuration (Xu t al., 2014). Since the longitudinal sound velocity depends only on the bulk modulus, density and the shear modulus, which is zero in a liquid but non-zero in a solid, liquid ⇌ solid phase transformations will typically exhibit the largest velocity contrast between phases. One such element that is liquid at ambient conditions but solidifies at elevated pressure is mercury (Hg), which transforms from a liquid to a solid at ~1.2 GPa and ambient temperature (Bridgman, 1911; Schulte and Holzapfel, 1993; Secco and Schloessin, 1986; Molinor et al., 1980; Klement et al., 1963). By measuring the travel time of an ultrasonic wave that travels through a pressure cell containing a Hg sample as a function of pressure, it is possible to detect the pressure of the liquid ⇌ solid phase transformation by measuring the discontinuity in travel time during the transition.

4.2 Methods

4.2.1 Experimental setup and the acoustic system

High pressure experiments were performed in the 3000 ton multi-anvil press at Western University. Calibration of the sample pressure vs. load is reported elsewhere in the previous chapter. The experimental setup consisted of an octahedral MgO pressure medium with 18 mm edge lengths surrounded by pyrophyllite gaskets. A hole was drilled through the center of the octahedron to accommodate the Hg sample which was encased in a Teflon™ or BN sample container. The sample was cylindrical in geometry with a length of 5.1 mm and a diameter of 2.5 mm. To minimize leakage of the liquid Hg sample into the surrounding pressure medium, so-called “double capsule” sample containers were constructed (see Figure 4.1).

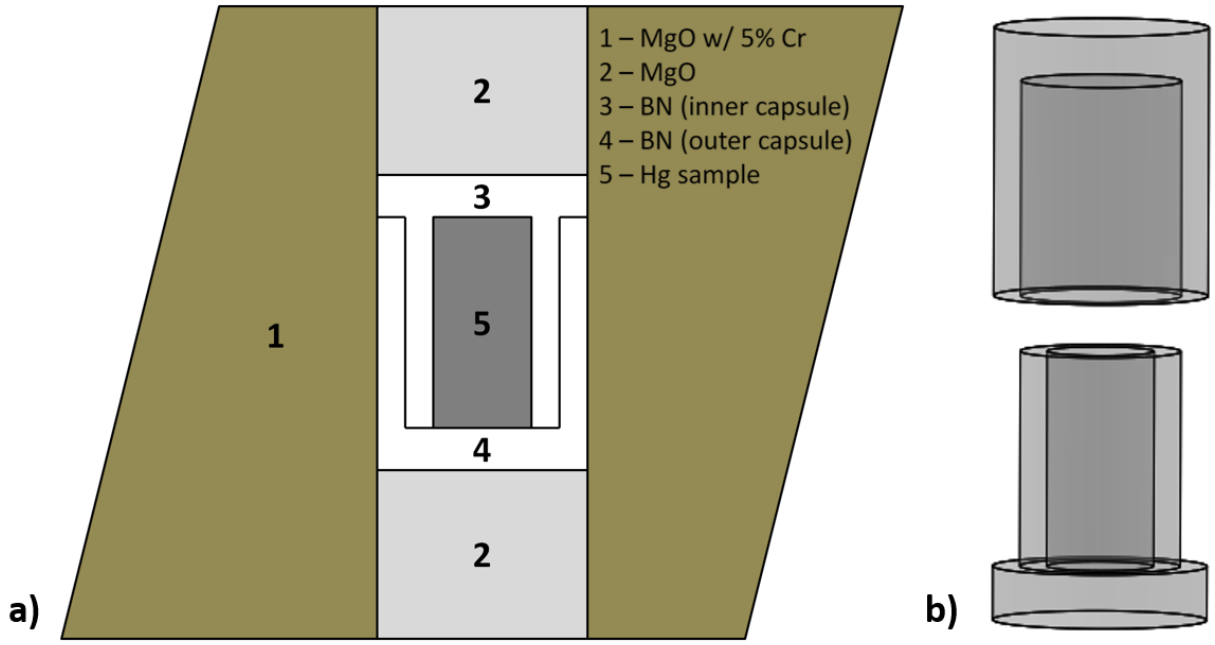

Figure 4.1: a) Cross section of the cell assembly used for high pressure Hg phase transition experiments. b) Image of the "double capsule" sample container used to minimize leakage of liquid Hg during the experiment.

The 18/11 octahedron was enclosed within the high pressure assembly described in chapter 3. The Vallen AE system is capable of generating acoustic pulses which propagate outward from the pulsing transducers where they are registered and recorded by the surrounding transducer array. By recording the time of a pulse sent from one transducer and the arrival time of that signal recorded by the transducer geometrically opposite in the transducer array, it was possible to estimate the travel time of the acoustic signal through the high pressure assembly. By performing travel time measurements as a function of pressure, it was possible to deduce the pressure at which the phase change occurs by witnessing the abrupt change in travel time that accompanies the change from liquid to solid Hg and *vice versa*.

4.2.2 Measuring Travel Time

During an experiment, the distances between transducers in the pressure assembly are reduced as the gaskets are formed and the ~30% initial porosity in the octahedron is diminished

as a result of compaction. In order to estimate the coordinates of the transducers in three-dimensional space as a function of pressure, the path length between opposing faces of recovered octahedra was measured for several experiments that attained a wide variation in maximum pressures as shown in Figure 4.2. Since little elastic rebound of the octahedron occurs after the load is removed, and the shape of the anvils remains essentially independent of pressure, the x, y, z positions of the transducers can be calculated as a function of pressure by fitting a curve that best fits the changes in octahedral axial length. Also shown in Figure 4.2 is the travel time vs. pressure for an octahedron containing no sample or any other assembly components. Cell compaction results in both densification and a decrease in the distance between transducers. Both of these effects act to decrease the travel time as a function of pressure as shown in Figure 4.2. The blue curve shows travel time as a function of pressure as measured by the system. The red curve, which displays shorter travel times, was generated by correcting for the effect of diminishing path lengths with pressure based on the axial length change with pressure (shown in green). As pressure increases and compaction of the pressure medium approaches completion, the travel time and corrected travel time approach one another.

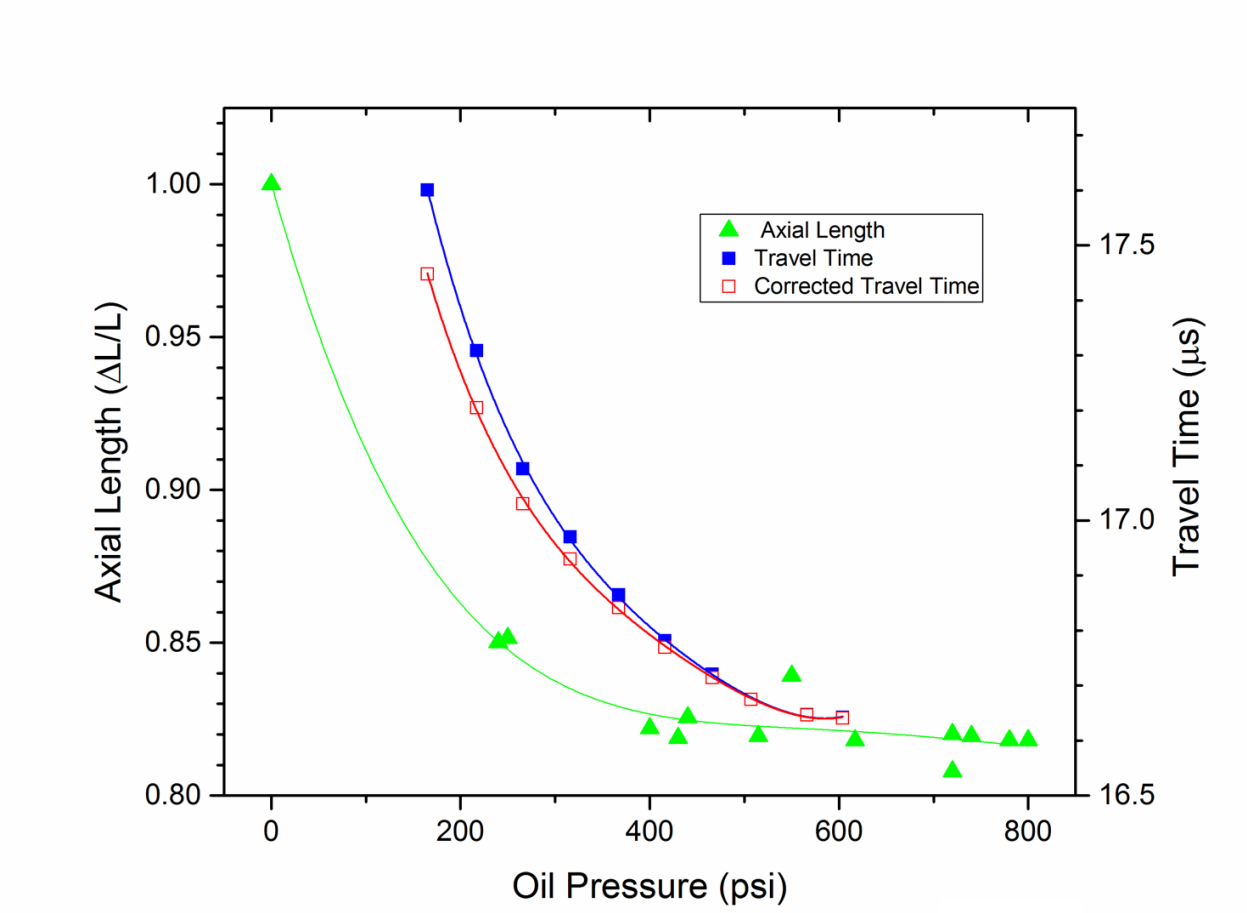

Figure 4.2: The axial length of the octahedron as a function of pressure normalized to the axial length of the octahedron at ambient pressure is shown (upward facing triangles). Measurements are based on the axial lengths of octahedra recovered from several experiments and are plotted against the highest pressure achieved in those experiments. A fourth-order polynomial is fit to the data. Travel time as a function of pressure is plotted for a dummy octahedron containing no sample (solid squares). Travel time for rays traveling equivalent path lengths vs. pressure (open squares) are based on corrections made using the axial length measurements shown here. They account for the decrease in the length the pulsed signal travels during compression. Both travel time curves were fit using second-order polynomials.

In order to accurately detect travel time discrepancies upon pressurization, such as caused by a phase transforming sample, the effect of decreasing length would need to be taken into account. However, this effect need only be taken into account below ~500 psi during initial pressurization at which point compaction of the pressure medium is essentially complete. Further pressurization or subsequent depressurization/re-pressurization does not affect the path length since the cell experiences little to no elastic rebound. To measure the travel time required for a signal to travel

along a straight line path between opposing transducers, the Vallen software allows for user-controlled, time-coordinated pulsing which records the moment a signal is sent from the pulsing transducer and the arrival time at the remaining transducers in the array. However, one of the limitations of the Vallen system is that it records the arrival time of the signal at the moment of threshold crossing instead of the initial impulse of wave energy. To get the true arrival time, other techniques must be employed such as manual picking or a picking algorithm. Nevertheless, an upper bound on the travel time may be estimated by simply assuming that the time of threshold crossing and the true arrival time are concurrent. This is a reasonable assumption provided the arriving signals are sufficiently impulsive, as is the case for the travel time curve shown in Figure 4.2, however as the signal is attenuated during transmission through the assembly, particularly along the cylindrical axis of the sample, the difference between true arrival time and threshold crossing becomes more pronounced as shown in Figure 4.3.

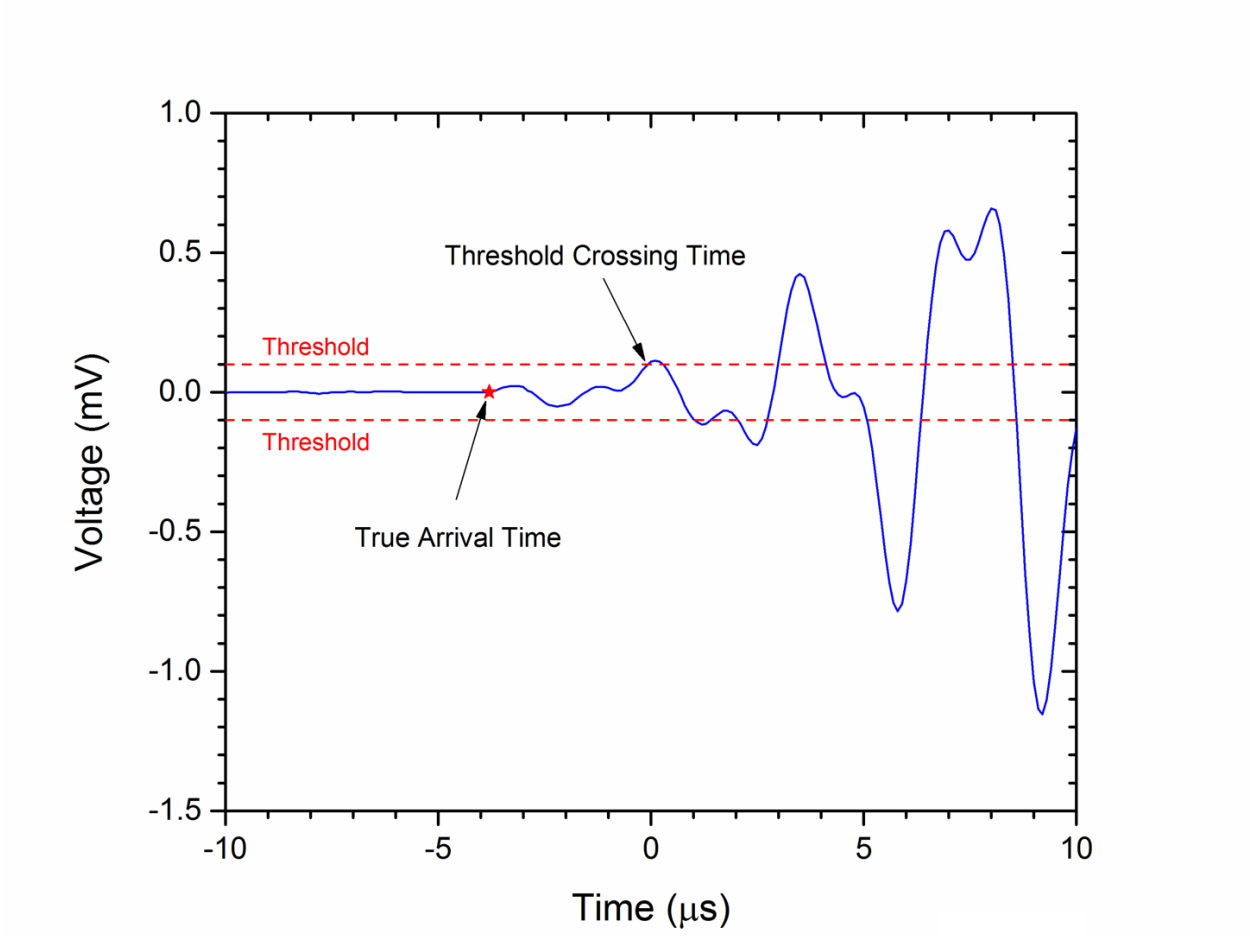

Figure 4.3: The discrepancy between the true arrival time and the time of threshold crossing for a typical signal. For the experiments referred to here, the discrepancy was generally between 3–4 μs.

Therefore, the value of the user-selected threshold is crucial in the system's estimation of travel time. The lower the threshold, the closer it is to approximating the true arrival time, whereas higher thresholds act to increase the travel time estimation. The result is that signal attenuation and sound velocity estimation of the assembly are inherently linked in a non-linear fashion. During a liquid to solid phase transition, the attenuation will decrease since acoustic energy transfer is more efficient in the solid state than the liquid state and also generally leads to better acoustic coupling of pressure cell components. When all of the sample, or a significant portion of it, has solidified this leads to the manifestation of earlier threshold crossings which correspond to

earlier arrival times and therefore shorter travel times. In addition, the velocity through the solid phase is higher than the liquid phase, due to elevated contributions from the bulk and shear moduli, further lowering the travel time estimation. Both these effects will contribute to a marked decrease in travel time across the phase boundary for a liquid to solid phase transition. The reverse scenario is true for the transition from a solid to a liquid. By optimizing the relationship between the threshold value and the sound velocity, it is possible to maximize the travel time difference across the phase boundary and elucidate the phase change. Typically, this is achieved with threshold crossings that occur within <0.5 μs after the onset of the waveform.

4.3 Experiments

At relatively low pressures (<2 GPa), compaction of the cell and gasket formation generate high levels of acoustic noise overshadowing any signals related to the sample as discussed in Chapter 3. Under these conditions, large uncertainties arise in velocity estimates as the system often confuses specious signals with the arrival of pulsed signals. This problem is further exacerbated by the high uncertainties in precise transducer position that are prominent at low pressure. Because Hg solidifies at ~1.2 GPa at ambient temperature, acquiring high-quality travel time data during the first pressurization run was impractical for this particular transition. However, once the pressure assembly reached a given load and was held there for the time required for a steady state to occur, depressurization and re-pressurization cycles did not generate acoustic noise provided pressure was not increased beyond the highest value achieved in earlier cycle(s). Above ~2 GPa, the level of noise was significantly reduced and continued to exponentially decrease upon further pressure increase. Therefore, pressure was increased to a

maximum of 3.5–4 GPa before measurements were taken. Data collection commenced on the first depressurization cycle and continued through re-pressurization and the second depressurization cycle. Pulsing runs were carried out at ~20 psi intervals – equivalent to ~0.2 GPa - far away from the transition pressure, but were performed more rapidly (~5–7 psi or ~0.05–0.07 GPa) near the transition boundary. The Vallen system was set to send a 100 V peak-to-peak (Vpp) pulse with a pulse width of 5.2 μs in the frequency range 90–210 kHz (−12 dB points). Since the low end of the operating frequency (i.e. receiving mode) of the transducers overlaps at the high end of the pulse frequency (transmitting mode), a large pulse signal voltage, such as 100 Vpp, creates a voltage of only ~1.5 mV in the transducer receiving the pulse after 40 dB pre-amplification. Pulsing runs consisted of sending five successive pulses from a single transducer separated by 500 ms each. The system then began pulsing from the next consecutive transducer in the array in an iterative fashion that repeatedly cycled through all six transducers until the pulsing run was manually stopped. Pulsing runs were operated for ~5 min at every given pressure resulting in ~100 pulses per transducer allowing for statistically relevant averaging of 100 travel time measurements. At a given pressure, for each set of opposing transducers, measurements were carried out with one transducer functioning as a pulse generator while the opposite transducer received pulses, then their roles were reversed and the pulsing transducer became the receiver of the pulses from the opposite transducer. Therefore, for each set of opposing transducers, two estimates of travel time along the same ray path but in opposite directions were obtained from ~100 velocity measurements each, at every pressure. Since pulsed signals are assumed to travel along straight ray paths that minimize the distance between the pulsing and receiving transducers, we expect pulsed signals traversing equivalent paths to produce equivalent results leading to an opportunity for further averaging. If there is a large

discrepancy between travel time measurements along the same path, but in opposite directions using different transducers as pulse sources, it is likely an indication of angled interface boundaries that produce direction-dependent scattering which is asymmetric in opposite directions. In most cases this effect is small and an average of the velocity estimation for opposite directions was made. The geometry of the assembly is such that one set of transducers passed signals through the sample along the sample axis while the two other sets of transducers sent signals that passed through obliquely at an angle of 70.5°. Figure 4.4 shows the acoustic paths between the three sets of opposing transducers with respect to the sample and octahedron.

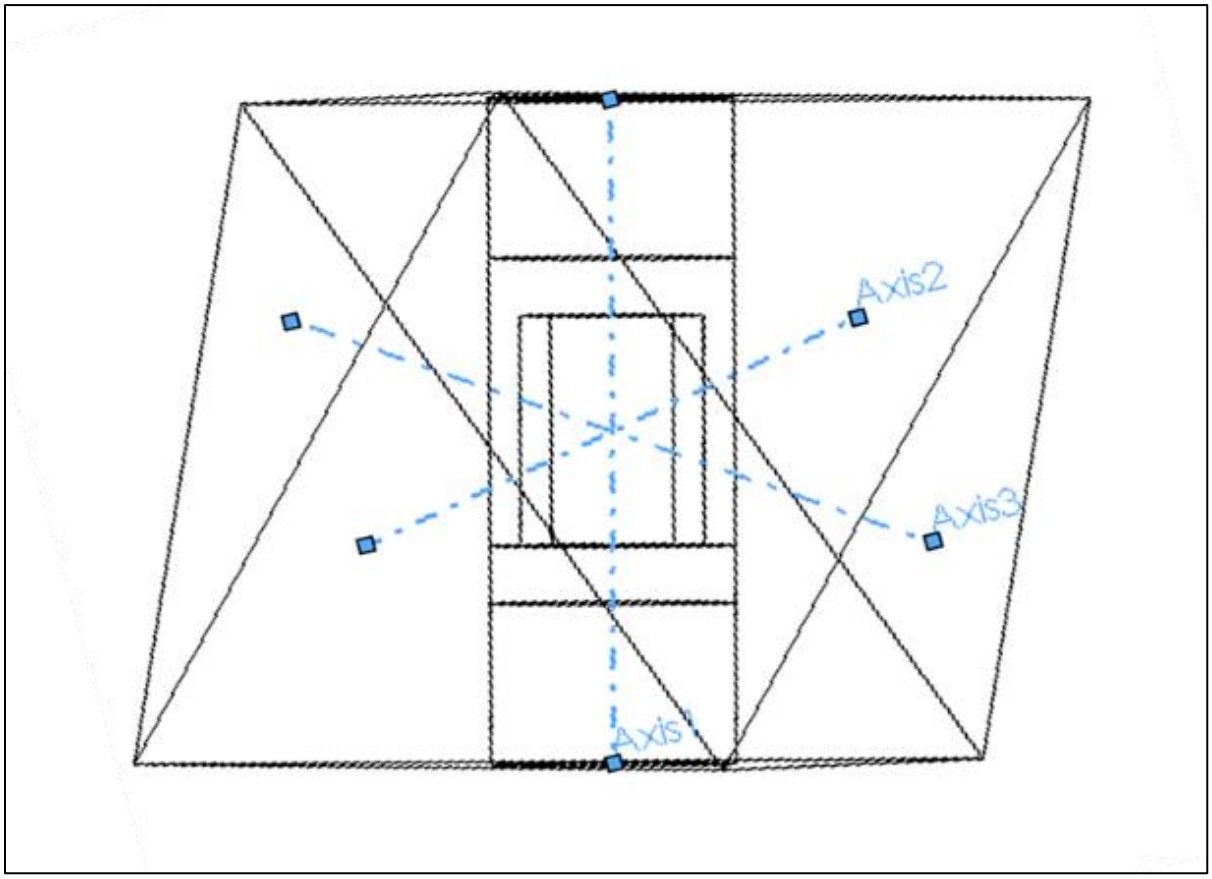

Figure 4.4: Image of the acoustic paths between opposing transducers with respect to the sample and octahedron. A total of six transducers provides the three sets of acoustic paths that travel through the sample. One path is parallel to the sample axis and the other two intersect the sample obliquely at an angle of 70.5 ^{0}.

4.4 Results and discussion

Figure 4.5 shows a comparison of travel times for the first depressurization cycle of an experiment using a Teflon™ sample container. Each travel time vs. pressure curve indicates an independent ray path showing the transformation in Hg from solid to liquid. The travel time for rays traveling parallel to the sample axis is longer due to the relatively large amount of comparatively slow, highly attenuating Hg in their path. The ray paths that contact the sample obliquely are similar due to similar ray paths, however they are not identical. This is a result of slight differences in material dimensions, attenuation, and interface angles on each ray path.

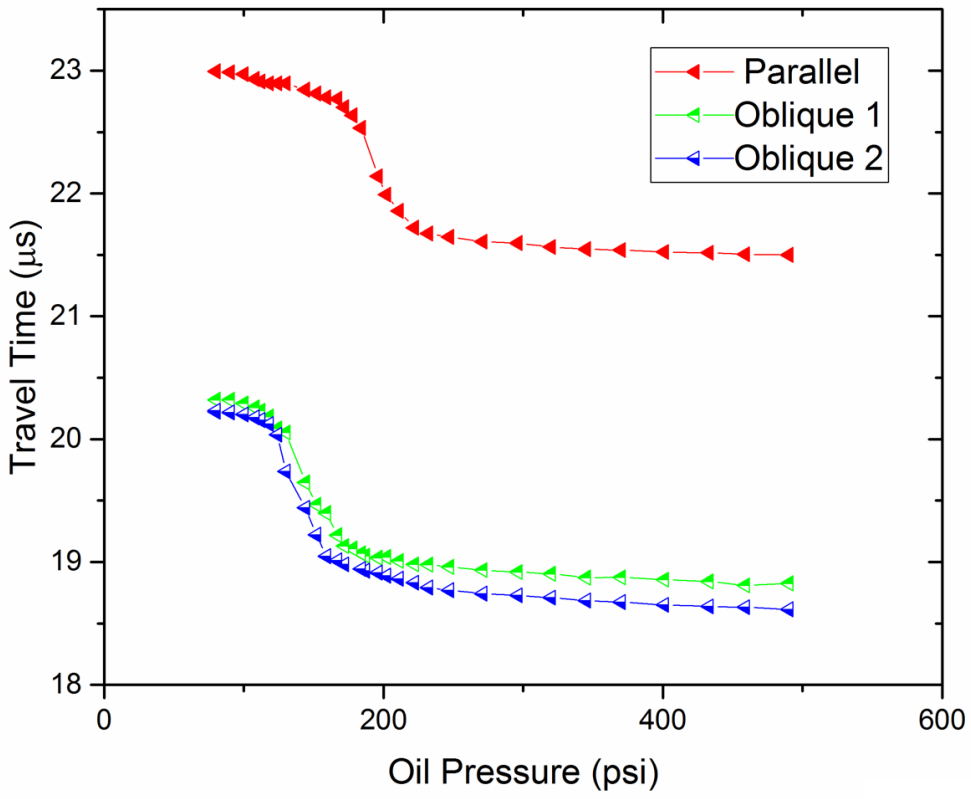

Figure 4.5. Comparison of travel time vs. pressure during the first depressurization cycle for each independent ray path. The travel times for rays traveling parallel to the sample axis are longer since this path passes through the largest amount of Hg, the slowest component in the assembly. The travel times for the paths that contact the sample obliquely are similar but not identical.

The advantage of using three independent ray paths is that it allows the user to evaluate the similarity of results from independent paths and choose the path that best displays the transition. In addition, it also provides redundancy for potential transducer failure during an experiment. Results are presented in Figure 4.6 for two experiments: one using a BN sample container, and the other using a Teflon™ sample container. In both experiments, samples were subjected to two pressurization/depressurization cycles, however data taken during the first pressurization cycle are not reported since the signal is inaccurate below 2 GPa due to background acoustic activity and poor estimation of path length as discussed earlier.

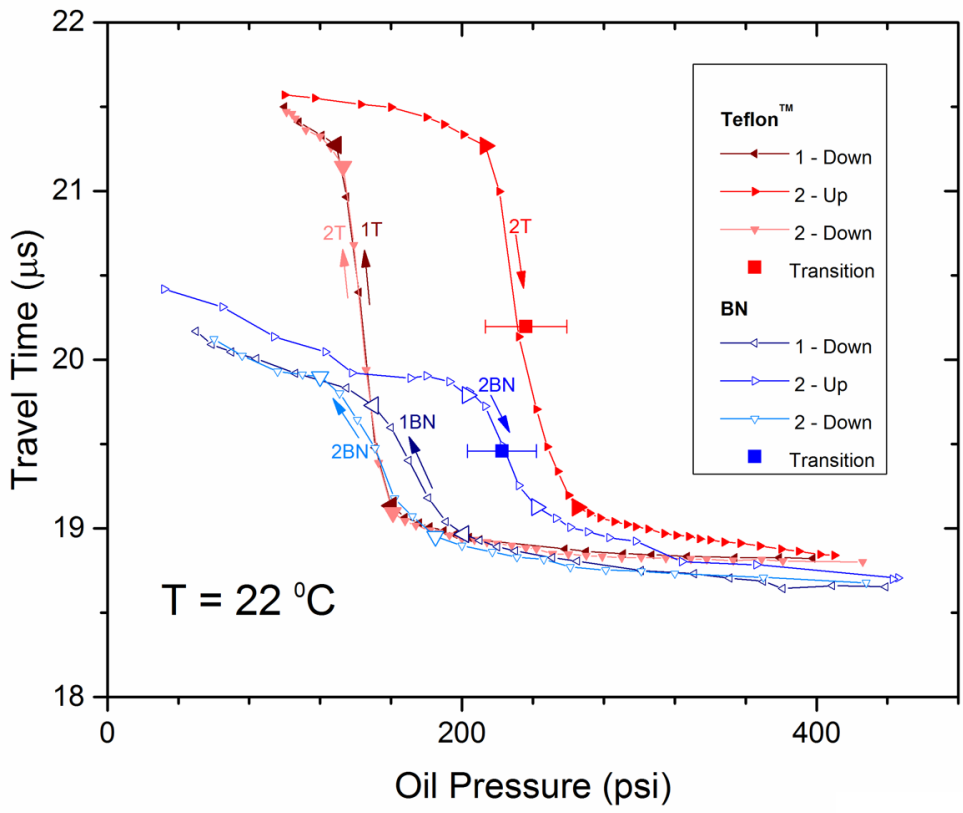

Figure 4.6: Travel time vs. pressure for pressurization (up) and depressurization (down) cycles for two experiments using Teflon™ (red) and BN (blue) sample containers. Large triangles represent the onset and conclusion of the phase change for each pressurization/depressurization cycle.

Figure 4.6 clearly shows the presence of the pressure-induced liquid ⇌ solid-phase transition in Hg indicated by the abrupt discontinuities in the travel time vs. pressure curves. What makes the transition so obvious are the combined effects of the sharp contrast between the sound velocity of liquid and solid Hg and the delay between the true arrival time and the threshold crossing time as shown in Figure 4.3. The Hg Lα phase transition occurred at 236 ± 23 psi and 223 ± 19 psi for the Teflon^{TM} and BN experiments respectively. According to the calibration of sample pressure as a function of hydraulic load for this press, based on the Bi I-II, Bi III-V and Sn I-II ambient temperature phase transformations as calibrants (see Figure 3.9), the accepted value of the Hg L-α transition pressure at ambient temperature, which occurs at ~1.2 GPa (Bridgman, 1911; Schulte and Holzapfel, 1993; Secco and Schloessin, 1986; Molinor et al., 1980; Klement et al., 1963), corresponds to an oil pressure of 142 psi. The fact that the pressure values of solidification are higher in these experiments than what is predicted from our original calibration is possibly due to the fact that data were collected during the second pressurization and first and second depressurization cycles. Our press is calibrated on the first pressurization cycle and any further pressurization cycles could display hysteresis which affects the sample pressure vs. oil pressure calibration in the pressure cell. In this case, it is feasible that the transfer of stress from the loading components of the press to the sample was less efficient than the first run making it appear that the transition occurred at elevated pressure. Thus, the slightly higher values of pressure at the Hg L-α solidification transition may be artifacts of pressure cycling. This is further complicated by the fact that Hg itself has been shown to exhibit hysteresis in sound velocity after repeated cycles of temperature induced freezing and melting (Borisov et al., 1998). Alternatively, since we are measuring the oil pressure where we detect the phase change we can use these values to define data points on a calibration curve that uses Hg L-α, Bi I-II, Bi III-V

and Sn I-II as calibrants. Figure 4.7 compares the calibration curves of oil pressure vs. sample pressure calculated with and without the Hg transition data.

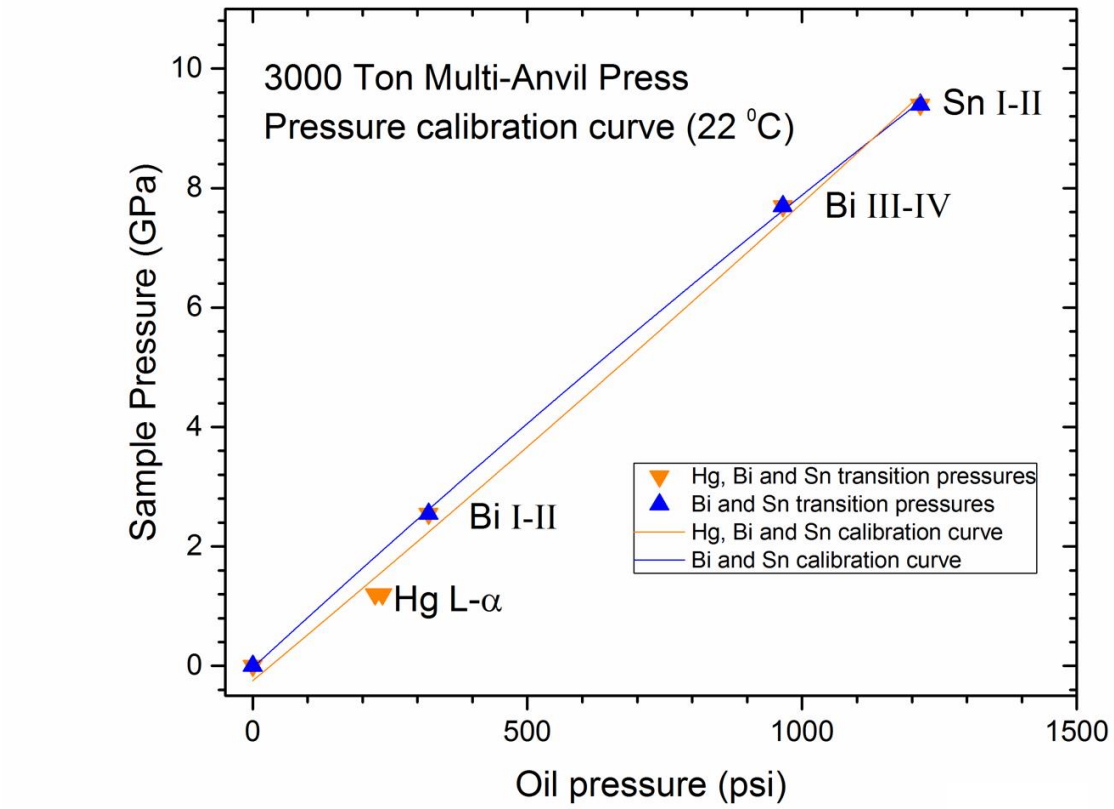

Figure 4.7: Sample pressure as a function of oil pressure for the 3000 ton multi-anvil press at ambient temperature. The blue calibration curve is based on the known transition pressures for Bi I-II, Bi III-V and Sn I-II (upward facing triangles).[23] The orange calibration curve includes the two Hg L-α transition pressures measured in this study (downward facing circles). Error bars are within the symbol size. Both sets of data were fit with second-order polynomials.

Incorporating the Hg L-α data results in a more linear calibration relation and lowers the overall efficiency of pressure generation in the sample at low loads but increases the efficiency at high loads.

4.5 Conclusions

Measuring travel time as a function of pressure was effective in displaying pressure-induced liquid ⇌ solid phase transitions in a multi-anvil apparatus. As a proof of concept, the liquid ⇌ solid phase transitions in Hg were used, but this method could be extended to other materials that undergo liquid ⇌ solid transformations. It may also prove useful in determining amounts of partial melt in an experiment as well as transition kinetics if the travel time is monitored with time. One advantage of this non-destructive technique is that the measurement system is emplaced fully outside the pressure assembly and few if any modifications are required to the experimental assembly for the technique to be employed, unlike traditional velocity measurements that require specific cell designs. Therefore, it can easily be added to experiments to provide additional information or utilized in situations when other methods used to determine phase transitions cannot be used. This method also has the potential to be used to measure the sound velocity of samples under HPHT conditions if the following requirements can be met. Firstly, it requires the precise value of the velocity and lengths of all components as a function of pressure. Secondly, corrections would need to be made to distinguish the time of threshold crossing and the true arrival time making this method, as described here, ill-suited for this purpose. However, as we have shown, changes in the relative travel time of ultrasonic signals traveling through a high pressure assembly can be exploited to detect pressure-induced liquid ⇌ solid phase changes for three independent ray paths simultaneously.

4.6 References

Balog P, Secco RA., 1999. High pressure and temperature behaviour of electrical resistivity of hcp metals Ti, Zr and Gd. *J. Phys.: Condens. Matter* 11,1273-1287.

Block S. 1978. Round-robin study of the high-pressure phase-transition in ZnS. *Acta Cryst. Suppl.* **A34**, S316.

Borisov BF, Charnaya EV, Plotnikov PG, Hoffman WD, Michel D, Kumzerov YA, Tien C, Wur CS., 1998. Solidification and melting of mercury in a porous glass as studied by NMR and acoustic techniques. *Phys. Rev. B.*, **58**, 5329-5335.

Bridgman PW., 1911. Mercury, liquid and solid under pressure. *Proc. Am. Acad. Arts Sci.*, **47**, 347-438.

Bridgman PW., 1938. The resistance of nineteen metals to 30,000 kg/cm^3, *Proc. Am. Acad. Arts Sci.*, **72**, 157-205.

Darling KL, Gwanmesia GD, Kung J, Li B, Liebermann RC, 2004. Ultrasonic measurements of the sound velocities in polycrystalline San Carlos olivine in multi-anvil, high-pressure apparatus. *Phys. Earth Planet Inter.*, **143-144**, 19-31.

Jing Z, Wang Y, Kono Y, Yu T, Sakamaki T, Park C, Rivers ML, Sutton SR, Shen G., 2014. Sound velocity of Fe-S liquids at high pressure: Implications for the Moon's molten outer core. *Earth Plan. Sci. Lett.*, **396,** 78-87.

Klement Jr. W, Jayaraman A, Kennedy GC., 1963. Transformations in mercury at high pressures. *Phys. Rev.*, **131**, 1-6.

Kung J, Li B, Uchida T, Wang Y, Neuville D. Liebermann RC., 2004. *In situ* measurements of sound velocities and densities across the orthopyroxene → high-pressure clinopyroxene transition in $MgSiO_3$ at high pressure. *Phys. Earth Planet Inter.*, **147**, 27-44.

Li B, Jackson I, Gasparik T, Liebermann RC., 1996a Elastic wave velocity measurement in multi-anvil apparatus to 10 GPa using ultrasonic interferometry, *Phys. Earth Planet Inter.*, **98**, 79-91.

Li B, Gwanmesia GD, Liebermann RC., 1996b. Sound velocities of olivine and beta polymorphs of Mg_2SiO_4 at Earth's transition zone pressures. *Geophys. Res. Lett.*, **23**, 2259-2262.

Li B, Kung J, Liebermann RC., 2004. Modern techniques in measuring elasticity of Earth materials at high pressure and high temperature using ultrasonic interferometry in conjunction with synchrotron X-radiation in multi-anvil apparatus. *Phys. Earth Planet Inter.*, **143-144**, 559-574.

Molinor GF, Bean V, Houck BJ, Welch B., 1980. The mercury melting line up to 1200 MPa. *Metrologia.*, **16**, 21-29.

Mueller HJ., 2013. Measuring the elastic properties of natural rocks and mineral assemblages under Earth's deep crustal and mantle conditions, *Geodyn.*, **71**, 25-42.

Officer, T. and Secco, R.A., 2015. Detection of a P-induced liquid ⇌ solid phase transformation using multiple acoustic transducers in a multi-anvil apparatus, *High Pres. Res.*, **35**, 289-299.

de Ronde AA, Dobson DP, 2008. Acoustic detection of phase transitions at high pressure: Bismuth, chlorite and zinc sulphide, *High Pressure Res.* **28**, 9-17.

Schulte O, Holzapfel WB., 1993. Phase diagram for mercury up to 67 GPa and 500 K. *Phys. Rev. B.*, **48,** 14009-14012.

Secco RA, Schloessin HH., 1986. On-line p,T calibration based on well known phase transitions. *J. Appl. Phys.*, **60**, 1625-1633.

Song W, Liu Y, Wang Z, Gong C, Guo J, Wenge Z, Xie H., 2011. Measurement method for sound velocity of melts in large volume press and its application to liquid sodium up to 2.0 GPa, *Rev. Sci. Instrum.*, **82**, 086108.

Suzuki A, Ohtani E, Morishima H, Kubo T, Kanbe Y, Kondo T, Okada T, Terasaki H, Kato T, Kikegawa T., 2000. *In situ* determination of the phase boundary between wadsleyite and ringwoodite in Mg_2SiO_4. *Geophys. Res. Lett.*, **27**, 803-806.

Yagi T, Akaogi M, Shimomura O, Suzuki T, Akimoto S., 1987. *In situ* observation of the olivine-spinel phase transformation in Fe_2SiO_4 using synchrotron radiation, *J. Geophys. Res.*, **92**, 6207-6213.

Yang H. and Secco RA., 1999. Melting boundary of Fe-17%Si up to 5.5 GPa and the timing of core formation. *Geophys. Res. Lett.*, **26**, 263-266.

Zhang JZ, Li B, Utsumi W, Liebermann RC., 1996. *In situ* X-ray observations of the coesite-stishovite transition: reversed phase boundary and kinetics, *Phys. Chem. Miner.* **23**, 1-10.

Chapter 5: Hypocentral Location Analysis

5.1 Introduction

When a fracture or frictional sliding occurs within the high pressure assembly, acoustic energy is radiated outward from the source in the form of ultrasonic waves and, provided the energy involved in the process is sufficiently high, results in multiple transducers registering hits from the same source in rapid succession. Here we define such an incident as an acoustic "event". The use of six transducers in an array surrounding the sample provides suitable coverage to obtain the location of events by inverting arrival time data received at each transducer. The ability to locate the position of AE sources is essential in the experimental investigation of the mechanism of deep-focus earthquakes since it allows for the distinction of sources that originate within the sample from those that occur outside of it. The most significant factors needed to accurately resolve the spatial and temporal parameters of such an event are specified guidelines that associate and classify hit cascades on multiple transducers into distinct events, detailed estimates of the positions of each transducer in three dimensional space, a velocity model, and precise determination of the arrival times.

5.2 Defining Events using the Vallen Systemes Event Builder

In order to classify which hit cascades should be grouped together into an event originating from a common source, guidelines (or criteria) needed to be established. Events are determined based on timing criteria by grouping together hits that occur on multiple transducers in rapid succession. This is achieved by defining a time window such that if multiple transducers register hits within this timeframe they will be grouped together into an event and treated as

deriving from the same source. The time window that determines events is entered into the Event Builder settings of the Vallen software package which automatically classifies events based on these criteria. The event builder time criteria are the D1X-Max, the DTNX-Max and the First Hit Channel Discrimination Time (FHCDT). The most important is DT1X-Max which defines the time window of an event. If two or more transducers receive hits within this timeframe, they constitute and event and will be grouped as such. If at least four transducers register signals within this timeframe it is possible to calculate the spatial and temporal parameters of the event. The timer starts with the first hit of an event and once it expires the event is closed. In order to collect events that occur anywhere within the high pressure assembly they should remain open for at least the duration of the travel time required for an acoustic signal to traverse the longest straight line path in the setup. In this case, that is the travel time between any two diagonally opposed transducers, which is ~16-18 μs, depending on the pressure. A general rule of thumb in AE testing is to compile events within a time period spanning 1.5 times this value (Leaird, 1997). However, to ensure that events were not overlooked as a result of the delay between the true arrival of the signal and the threshold crossing, this timeframe was extended to 50 μs. This guarantees that any signals with arrival times within 25 μs of the first signal in the event will be recorded since 25 μs is the typical duration of data acquisition stored in the data buffer prior to the threshold crossing. The DTNX-Max defines a time window between two consecutive hits of an event and is reset with every hit. Once it expires the event is closed. Since the spatial configuration of the transducers is symmetric about the centroid of the sample there is no reason to close an event based on arrival time differences between any consecutively hit transducers. For this reason, DTNX-Max was set equal to DT1X-Max essentially deactivating it. The FHCDT defines the minimum time period after the last threshold crossing and first hit of a new event. In

other words, if the FHCDT expires the next threshold crossing defines a new event. FHCDT is reset every time a new hit is detected until it eventually expires. After expiration the Event Builder is armed again and ready to assemble a new event from subsequent hits. The FHCDT should be on the order of the lifetime of a burst from an AE source. This ensures that hits caused by reflections will not initiate an event. For example, consider an AE source originating in a gasket. It reaches the nearest transducer and starts a new event. When the first reflection arrives at the same sensor the preceding event may already be closed and a new event will be spuriously initiated, unless however, the FHCDT has not expired, in which case a new event will not be started. If the FHCDT is too short it is possible that events will be initiated by reflections within the assembly, however the danger of setting it too long is that two unrelated events occurring within this time window will not trigger separate events since the FHCDT is not closed. For convenience, the FHCDT was set equal to the DT1X-Max. By setting all three criteria to 50 μs ensures that any time 4 or more hits occur within this time window they will be logged as events and can be located. Figure 5.1 shows the settings for the Event Builder.

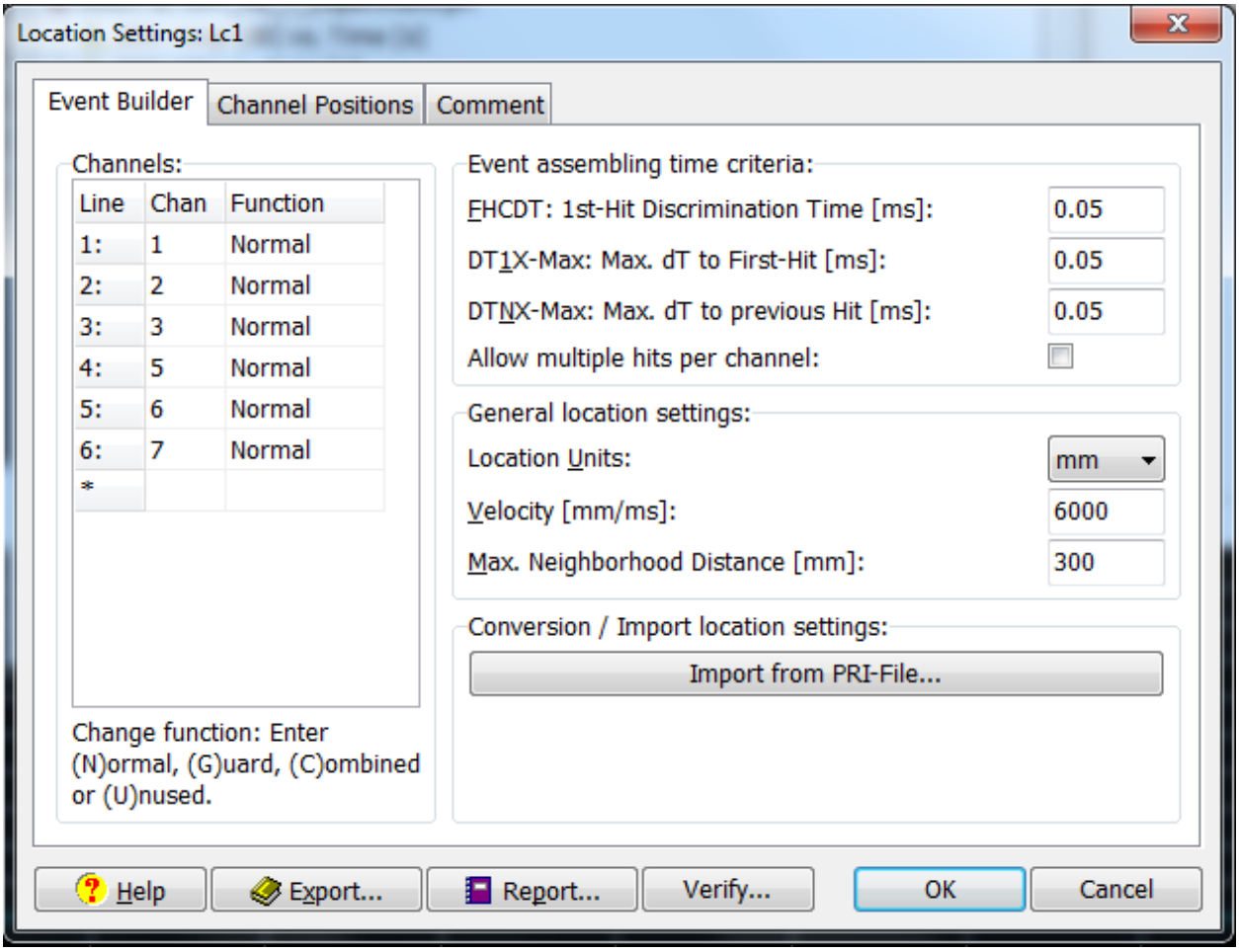

Figure 5.1: The Vallen Systemes Event Builder defines events based on user defined time criteria.

5.3 Determination of transducer position

The relative locations of the transducers as a function of pressure was obtained using the procedure discussed in section 4.2.2 of the previous chapter and is plotted in Figure 4.2. In the Cartesian coordinate system defined by the cube created when all the anvils are in contact with the octahedron, each transducer is located at (±29.7, ±29.7, ±29.7) mm, with respect to the centroid of the cube and sample at the origin, and the cylindrical sample tilted 18.2^0 in azimuth and inclination. These coordinates can then be entered in the Event Builder in the Vallen

software package. Figure 5.2 shows the Channel Positions screen in the Vallen Location Settings dialogue window.

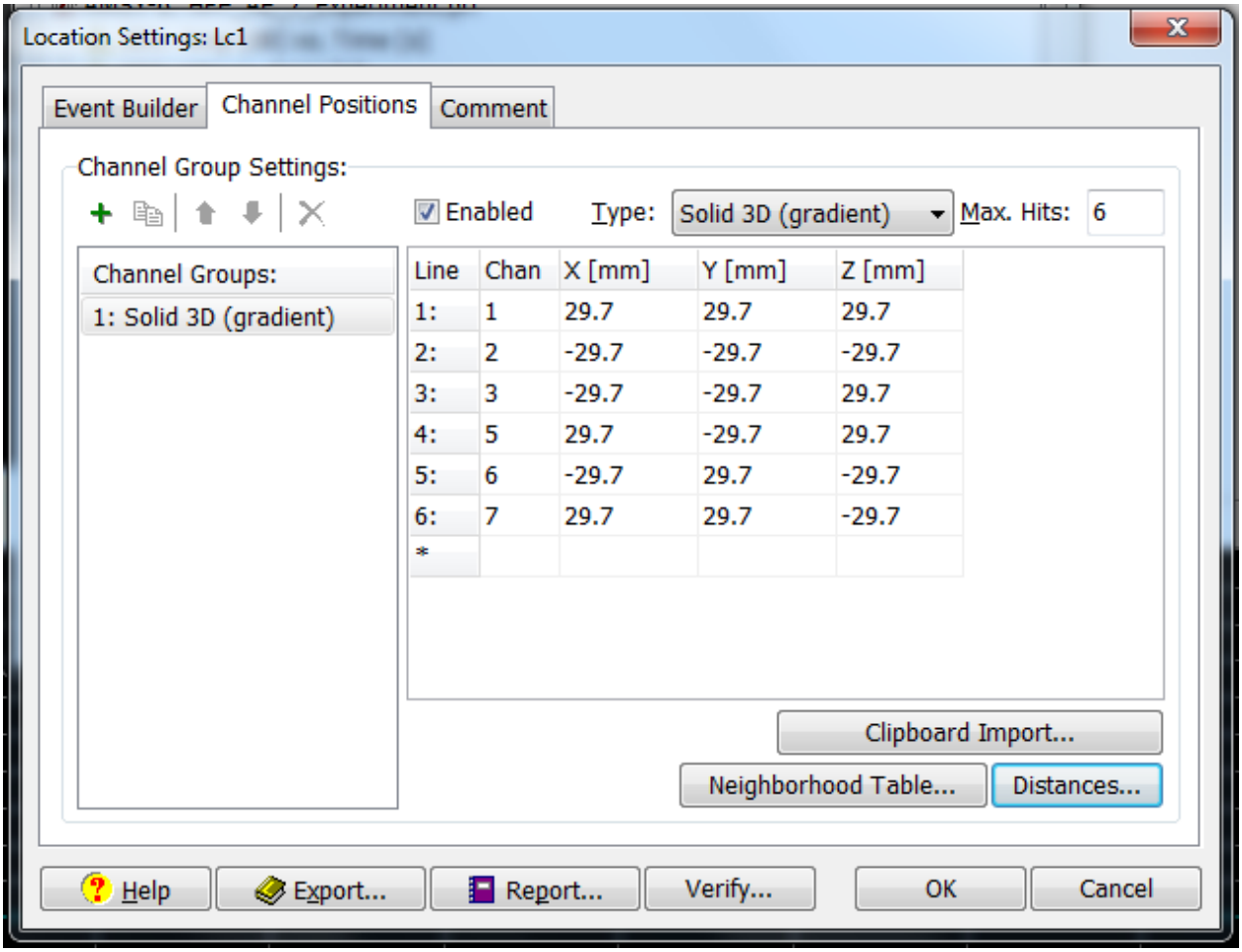

Figure 5.2: x,y,z positions of transducers inputted into the Vallen software.

Using the coordinate system described above where each transducer is located at (±29.7, ±29.7, ±29.7) mm is convenient for setting up the experiments, however a more natural system to use when relating located events to the sample is one in which the z-axis is along the cylindrical axis of the sample with the x- and y-axes located in a plane orthogonal to it. Figure 5.3 shows a

graphical representation of the relationship between the coordinate systems defined by the cube and the sample.

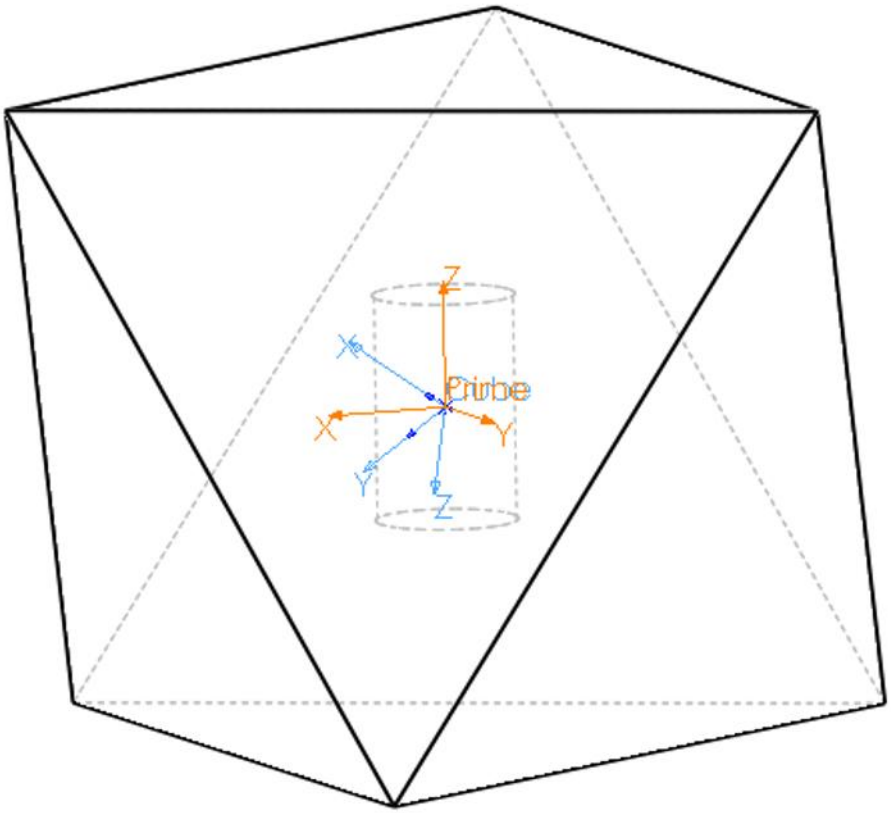

Figure 5.3: The two different coordinate systems used based on the cube created when all the anvils are in contact with the octahedron (blue/cube) compared to the coordinate system whose z-axis is defined by the sample cylindrical axis with the x- and y-axes are in a plane orthogonal to it (orange/prime).

Transforming from the cube defined coordinate system (x, y, z) to the sample defined coordinate system (x', y', z') can be achieved using the following transformation equation:

$$\begin{bmatrix} x' \\ y' \\ z' \end{bmatrix} = \begin{bmatrix} \cos(35.3°) & \cos(65.9°) & \cos(65.9°) \\ \cos(90.0°) & \cos(180° - 45.0°) & \cos(45.0°) \\ \cos(54.7°) & \cos(180° - 54.7°) & \cos(180° - 54.7°) \end{bmatrix} \begin{bmatrix} x \\ y \\ z \end{bmatrix} \quad (5.1)$$

This transforms the locations of the transducers to,

	x (mm)	y (mm)	z (mm)
Channel 1	48.2	0.0	-17.0
Channel 2	-48.2	0.0	17.0
Channel 3	-24.1	41.7	-17.0
Channel 4	24.1	-41.7	17.0
Channel 5	24.1	41.7	17.0
Channel 6	-24.1	-41.7	-17.0,

in the new coordinate system with the z-axis located along the sample cylindrical axis.

5.4 Determination of the velocity structure

Knowing the transducer positions and the travel time between opposing transducers allows for the calculation of the combined velocity of the high pressure assembly using the simple relationship,

$$v = \frac{\Delta d}{\Delta t} \quad (5.2)$$

where *v* is velocity, *d* is distance and *t* is the travel time. This is done automatically by the Vallen software by sending high energy pulses that travel through the high pressure assembly from each transducer to its geometrically opposite counterpart and recording the arrival time. Although the arrival time of the pulses are recorded as the time the impulse crosses the threshold, increasing the energy of the incoming pulse and lowering the threshold ensures that the waves are impulsive

enough that they intersect the threshold in < 100 ns of the arrival of the waveform. This results in an estimate of velocity that is slower than the actual p-wave velocity to less than 1% of its actual value, which is smaller than the uncertainty in travel time from pulse to pulse. For this reason, more than 100 pulses are performed per transducer to allow for statistical averaging. Figure 5.4 shows the combined velocity of the high pressure assembly as a function of pressure for several experiments performed using the cell assembly developed for experiments on sintered faylite samples.

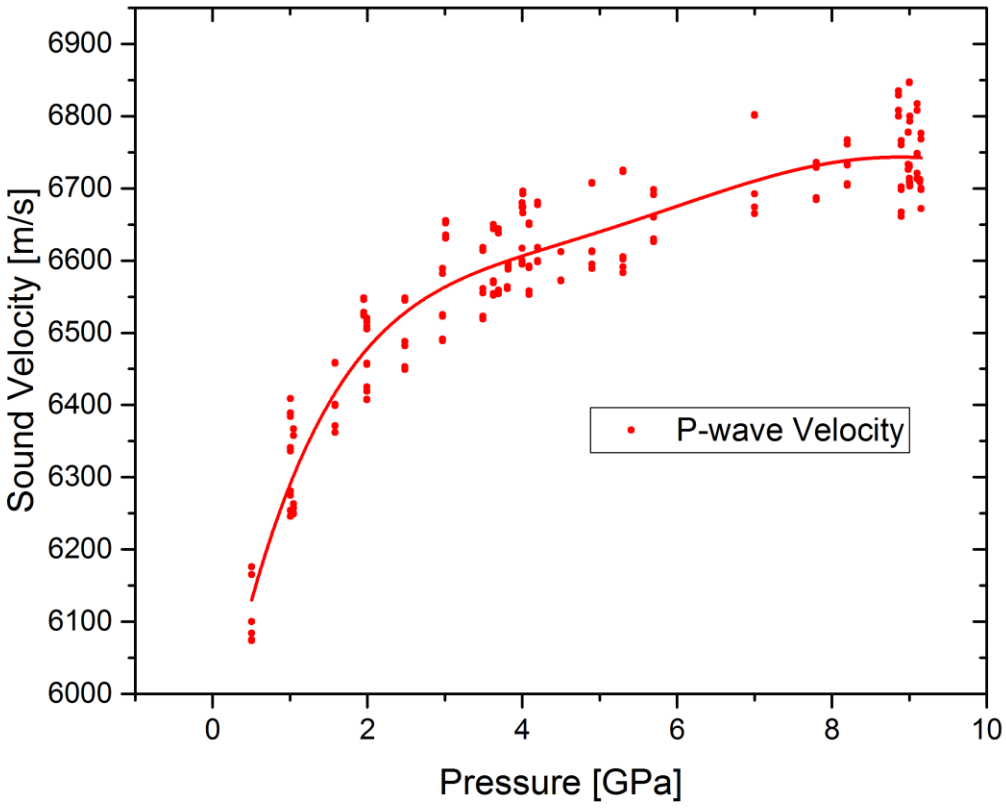

Figure 5.4: The combined velocity of all components in the high pressure assembly based on transducer positions and the travel time between pulsing transducers and those diagonally opposite from them.

Typical velocity measurements are approximately 6.2 – 6.7 mm/μs for fully solid media depending on the details of the octahedral assembly and the pressure reached. During experiments where a sample is strained under HPHT conditions, the velocity of the entire assembly is measured before and after deformation. The entire system is treated as a homogeneous velocity medium and reflects the composite velocity which is dominated by the WC anvils. The anvils comprise the bulk of the sample assembly and the velocity of WC changes little with temperature, which tends to decrease velocity, and pressure, which tends to increase velocity. This value is then entered into the Vallen Location Processor and used to calculate the location of events.

In addition to assuming a homogeneous velocity medium, the Vallen Location Processor also assumes straight line paths from the event to the transducers which is less accurate for signals originating outside the pressure cell. This is especially true for events originating in the gaskets and the phenolic plates since they must traverse a circuitous path involving reflections and refractions during their journey from the events source to the transducers. This effect degrades the overall accuracy of events that develop outside the octahedron and becomes worse as they approach the extremity of the high pressure assembly. However, this is not significant since events originating outside the sample are of little consequence. More importantly, acoustic rays arising from events that do occur within the sample will experience refractions at internal cell boundaries. To overcome this problem a more representative velocity model is required, but due to the symmetry of the high pressure assembly, signals from events that originating near the center of the high pressure assembly (i.e. within the sample) will travel similar ray paths and encounter material boundaries at relatively acute angles. For this reason the presence of refractions for signals coming from the sample are expected to be of minor significance.

5.3 Vallen Systemes Location Analysis

Based on time criteria, the Vallen software automatically classifies signals recorded in rapid succession on multiple transducers as events and calculates their hypocenters based on a velocity model (see section 5.2.3) for the high pressure assembly and the locations of the transducers in the microseismic array (see section 5.2.2). The event data, including location, channel number, time, amplitude, etc. are recorded in a list (see Table 5.1) and their positions are plotted in a 3-D diagram in relation to the positions of the transducers as shown in Figure 5.5.

Id	DSET	HHMMSS	MSEC	NSEC	CHAN	A	R	THR	E(TE)	PA0	TRAI	X	Y	Z	CNTS	SIGS
		[hhmmss]	[ms.µs]	[ms.µs]		[dB]	[µs]	[dB]	[eu]	[mV]		[mm]	[mm]	[mm]		
La Label 1: '13:04 Resume'																
DT Wednesday, January 13, 2016, Host Time: 1:04 PM																
LE	1174	00:07:34	139.0766	139.076550	6	63.3	9.6	40.0	209E01	366.563	125	-9.31	4.71	-12.25	116	5
Ht	1175	00:07:34	139.0783	139.078350	7	60.3	13.4	40.0	832E00	366.563	126				104	
Ht	1176	00:07:34	139.0797	139.079700	3	62.2	40.2	40.0	282E01	366.563	127				222	
Ht	1177	00:07:34	139.0809	139.080850	1	59.2	22.4	40.0	951E00	366.563	128				128	
Ht	1178	00:07:34	139.0821	139.082050	5	56.5	21.4	40.0	465E00	366.563	129				79	
LE	1180	00:07:34	149.9941	149.994150	6	58.8	18.4	40.0	602E00	366.563	130	-21.52	-1.71	-33.99	56	6
Ht	1181	00:07:34	149.9945	149.994450	2	66.0	14.4	40.0	205E01	366.563	131				75	
Ht	1182	00:07:34	149.9970	149.996975	7	56.2	12.2	40.0	249E00	366.563	132				44	
Ht	1183	00:07:34	149.9981	149.998100	3	53.9	21.2	40.0	404E00	366.563	133				53	
Ht	1184	00:07:34	150.0040	150.003975	5	47.5	17.0	40.0	640E-1	366.563	134				13	
Ht	1185	00:07:34	150.0051	150.005125	1	49.4	14.4	40.0	143E00	366.563	135				29	
LE	3473	00:11:58	900.9335	900.933550	6	57.3	13.2	40.0	244E00	353.438	426	-21.67	11.24	-22.76	37	4
Ht	3474	00:11:58	900.9371	900.937050	2	53.9	24.2	40.0	192E00	353.438	427				30	
Ht	3475	00:11:58	900.9392	900.939175	7	52.0	7.2	40.0	733E-1	353.438	428				17	
Ht	3476	00:11:58	900.9412	900.941175	3	48.3	31.8	40.0	848E-1	353.438	429				15	
LE	4065	00:13:44	5.2817	5.281750	6	64.1	16.6	40.0	130E01	354.688	492	-114.99	8.96	-52.35	55	6
Ht	4066	00:13:44	5.2823	5.282275	2	68.2	15.0	40.0	516E01	354.688	493				83	
Ht	4067	00:13:44	5.2874	5.287375	3	60.3	23.8	40.0	140E01	354.688	494				161	
Ht	4068	00:13:44	5.2908	5.290800	7	59.9	15.6	40.0	449E00	354.688	495				51	
Ht	4069	00:13:44	5.2934	5.293400	1	51.7	20.0	40.0	578E00	354.688	496				111	
Ht	4070	00:13:44	5.2964	5.296425	5	48.3	33.8	40.0	125E00	354.688	497				21	

Table 5.1: The Vallen software builds events and displays the hit data for individual events.

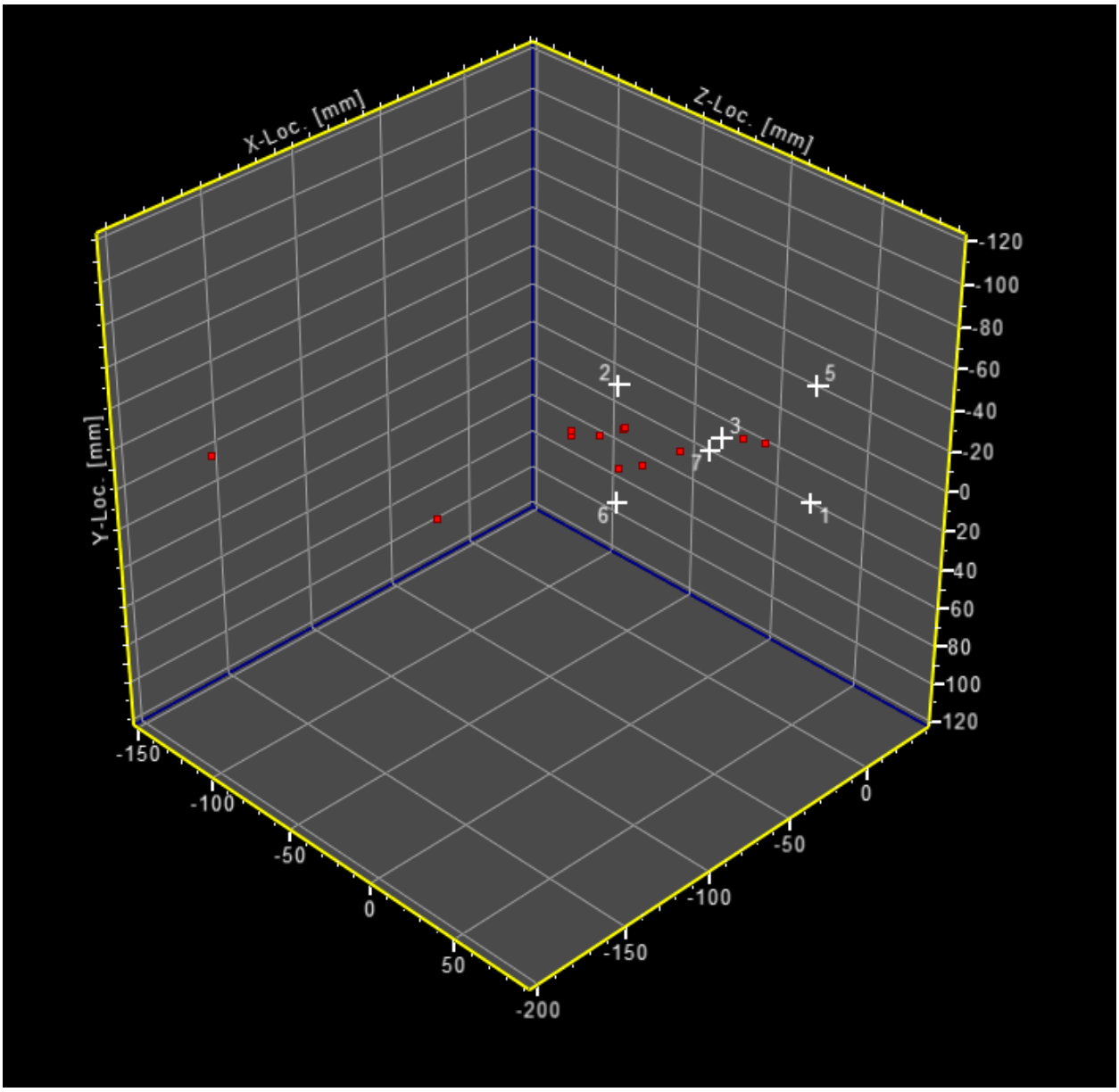

Figure 5.5: Three dimensional plot showing the locations of events (red dots) with respect to the transducer positions (shown as crosses and numbered based on channel number) as displayed by the Vallen system software. Channel 7 was used in place of channel 4 in this particular experiment.

However, a significant limitation of the Vallen software package is that it defines hit parameters in terms of the threshold crossing and not the initiation of acoustic energy. This is particularly significant when determining hypocentral location since a discrepancy of up to 10 μs can exist between the time of threshold crossing and the true arrival time. Such a discrepancy would place

the source of the event 65 mm further from the transducer than the actual location of the event for a velocity of 6500 m/s. This is clearly an unacceptable degree of accuracy since it is many times greater than the long axis of the cylindrical samples used in the experiments. Therefore, in order to improve estimates of event locations it is essential that the arrival times of signals are determined more precisely. Ideally, the arrival times should be determined to within 0.1 μs leading to submillimeter accuracy in event location. Therefore, in order to determine the locations of events it is necessary to re-pick the arrival times and use these newly chosen arrival times as inputs into a location algorithm instead of relying on the locations predicted by the Vallen software. The Vallen Event Builder is still used to classify signals into events with more than four transducers involved, but more precise arrival times are determined from the waveforms of the signals associated with those events created by the Event Builder using new software developed in this study.

5.5 Determining arrival times

The detection of microseismic signals is based on separating actual signals from ambient noise. Since microseismic signals and background noise usually differ in character and frequency content, it is often possible to distinguish them on a seismogram. In particular, seismic signals are generally characterized by impulsive onsets, high frequency, an exponential envelope, and decreasing signal frequency with time, while background signals are distinguished by their low amplitude and low-frequency signature (Lee and Stewart, 1981). As explained in the last section, the Vallen system records arrival times as the time of threshold crossing instead of the initiation of the waveform. The most reliable method of picking arrival times is generally considered to be

manual picking of the onset of the waveform based on visual inspection of the seismogram (Aki and Richards, 2002). For small numbers of events (<30) this technique is accurate and the total number of picks can be carried out in a reasonable amount of time since the total number of waveforms involved will be less than 200. To expedite this process a Matlab program was written that automatically plots each waveform, allowing the user to zoom into the region of interest and determine which point indicates the arrival of the waveform, and prompts the user to enter the number of the data point corresponding to the onset of the waveform (see Appendix 1). This will be a number between 1 and 2000, since the 2001st point in the time series corresponds to the point of threshold crossing, but is usually between 1800 and 2000. The program then calculates the new arrival time of the waveform based on the time of threshold crossing, the data point chosen, and the sample rate of the time series, and stores this information in memory.

5.4.1 Automatic picking of waveform arrival times based on the Akaike Information Criterion

As the number of events increases, it becomes increasing untenable to manually pick arrival times since the number of events can be in the hundreds of thousands, particularly during the initial pressurization stage when acoustic noise is high and events are created essentially continuously. Therefore a method of automatic picking was developed which can be applied to large data sets. It is based on the Akaike Information Criterion (AIC), which is a test of the relative quality of a statistical model for a given data set (Akaike, 1974). For a given data set *y* comprised of *n* samples, in this case the voltage vs. time data comprising a waveform, the AIC can be computed at the k^{th} point using the equation,

$$AIC(k) = k\ln\{var[y(1:k)]\}+(n-k-1)\ln\{var[y(k+1:n)]\}, \qquad (5.3)$$

where ln{ *var[]* } represents the natural logarithm of the variance of *y* from point *1* to point *k* (in the first term) and from *k+1* to *n* (in the second term). Eqn. (5.3) represents a simplified version of the generalized AR-AIC picker which neglects the order of the autoregressive (AR) process since it is much smaller than the number of samples (Maeda, 1985). By computing the AIC for several values of *k* before and after the onset of the p-wave, the breakpoint can be ascertained by finding which *k* corresponds to the minimum value of the AIC. Qualitatively this can be described as follows. The waveform can be separated into two distinct, locally stationary, time series modeled as an AR process (Sleeman and van Eck, 1999). The first time series is that of background noise with mean zero and variance zero, while the second time series is that of the wave itself which is defined by a high amplitude impulse and situated adjacent to the first time series. For low values of *k*, before the onset of the wave, the first term in Eqn. (5.2) will be a relatively small number since the variance will be near zero. The second term will also be relatively small since it contains a contribution of the first part of the time series which has a small variance. As *k* increases the AIC will decrease until the onset of the wave when the first term is composed entirely of background noise and the second term is composed entirely of the wave. After this point the AIC will increase rapidly with increasing *k*. The *k* where the AIC is minimized determines the optimal separation of the two stationary time series, and thus is interpreted as the phase (or wave) onset (Sleeman and van Eck, 1999). In other words, the AIC is minimized for the point *k* when the two time series are the most different from one another, namely at the beginning of the wave. Figure 5.6 shows an example of the AIC as a function of point number for an automatically chosen arrival time.

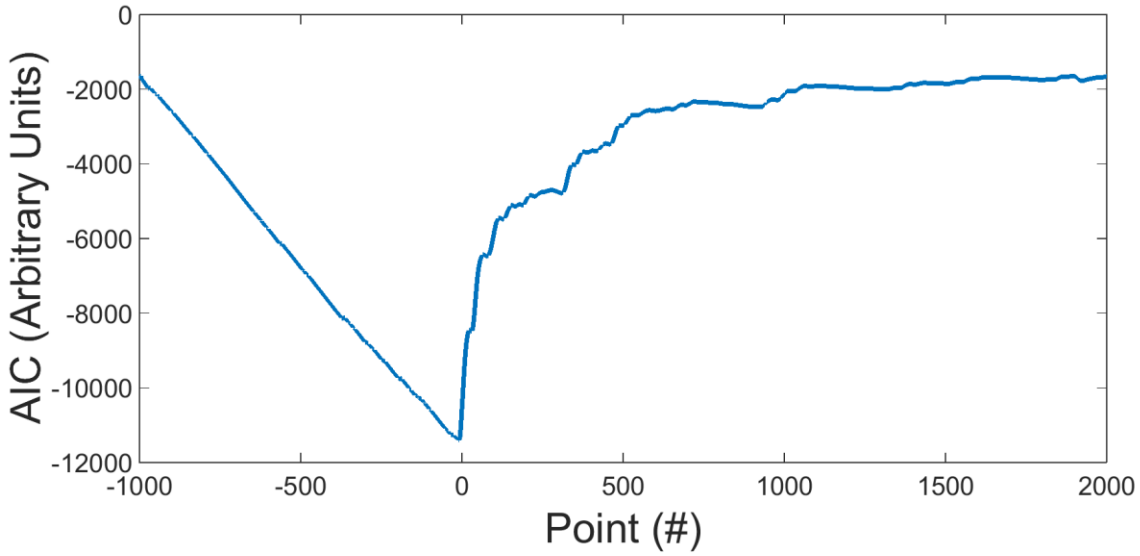

Figure 5.6: The AIC as a function of point number for an automatically chosen arrival time. Point number zero defines the point associated with crossing the threshold. The minimum of this function defines the arrival point of the waveform.

Since the AIC algorithm selects the arrival of the waveform as the global minimum of the AIC function it is important to ensure that the window selected on which the algorithm is performed contains the onset of the wave which requires *a priori* knowledge of its position in time. However, this is rarely a problem since the time of threshold crossing and the onset of the waveform occurs within 25 μs for every waveform. As a general rule it is suggested that the window contain an approximately 1:2 ratio of the number of points before and after the initial breakpoint of the wave (Zhang et al., 2003.). Since most waveforms exhibit breakpoints within 5 μs of the threshold crossing it is usually reasonable to utilize a window 3000 points in length that uses the threshold crossing point to define the 1:2 ratio. In doing so, variation in window selection delivers little improvement. This effect only becomes problematic for low amplitude signals that initiate long before (e.g. >10 μs) the threshold crossing. In this case it effectively amounts to poor window selection and can result in inaccurate breakpoint picks. Another factor

that can influence the accuracy of the AIC picking algorithm is the signal/noise (S/N) ratio of the waveform (Zhang et al., 2003). Waveforms with a low S/N ratio can exhibit multiple minima and may result in a global minimum that does not correspond to the arrival of the wave or may shift the global minimum a number of points away from the true arrival point. When compounded with the burden of poor window selection the results for AIC picks for low amplitude signals can be further compromised. For these reasons the AIC automatic picking algorithm is most effective for relatively large impulsive signals.

Now that the arrival times at each transducer for a given event can be accurately re-determined, it is possible to input these data into an inversion algorithm and estimate event location.

5.6 Event Location Inversion

5.6.1 Generalized non-linear least squares inversion

For each microseismic event that occurs at some position within the high pressure assembly that generates enough AE energy to be recorded on four or more transducers, it is possible to locate the hypocenter of the source. Consider n transducers, stationed at positions x_i, y_i, z_i, where $i = 1,2,3,4,5 \text{ or } 6$ corresponding to the i^{th} transducer in the array, and assume they detect an event with arrival times d_i^{at}. The arrival time at the i^{th} transducer depends on the origin time of the event, t, the three dimensional location, x, y, z of the event, and the velocity, v, with which the acoustic wave travels from the source to a given transducer. In general, v will be a

function of position, however for the homogeneous velocity structure assumed in our system the physical model that describes the system can be written using the equation,

$$d_i^{at} = \frac{1}{v}[(x - x_i)^2 + (y - y_i)^2 + (z - z_i)^2]^{1/2} + t, \qquad (5.4)$$

where *x, y, z* and *t* are the model parameters that determine a particular set of arrival times. In our application *v* is a known constant which is measured using the technique described in section 5.2. The d_i^{at} values are acquired through manual or automatic picking and x_i, y_i, z_i are determined through the processes described in section 5.1. The goal is to compute model parameters *m = [x,y,z,t]* (the event location and origin time) based on the data d_i^{at} (the newly chosen arrival times) for a given event such that,

$$d = A(m), \qquad (5.5)$$

where *A* is an operator which uses the elements of the model parameters *m* to produce the data *d*. In our application *A* is a [4,5 or 6]x4 matrix whose rows represent one of the six transducers in the array and the 4 columns represent each coordinate associated with the model parameters; 3 of which represent the three spatial coordinates of the transducers and the 4th is time. In index notation Eqn. (5.5) can be written as

$$d_i = A_{ij}(m_j) \qquad (5.6).$$

Eqns. (5.5) and (5.6) are examples of a forward modelling problem and requires knowledge of *m*, the time and location of the event, however, this is the unknown quantity we aim to estimate. Therefore, given d_i^{at}, the observed arrival times, we need to determine a model that best fits them which can be achieved using Geiger's method of earthquake location (Geiger, 1912; Stein

and Wysession, 2003; Shearer, 1999; Lay and Wallace, 1995). In order to do this we begin with a starting model m^0, which is an estimate of the origin time and location of the event based on *a priori* considerations. Preferably this should at least approximate the true position and origin time of the event, which for us can be considered to occur within the high pressure assembly. Using Eqn. (5.3), our initial model predicts an arrival time of

$$d_i^0 = A(m_j^0) \qquad (5.7)$$

for the i^{th} transducer. Since we know the arrival times, to test the validity of our guess we can compare the observed arrival times with those predicted by the initial guess using the equation

$$\Delta d_i^0 = d_i^{at} - d_i^0 \qquad (5.8)$$

However, since our initial estimate of the model is in general incorrect, we would expect $\Delta d_i \neq 0$. We therefore seek changes Δm_j to our model such that

$$m_j^1 = m_j^0 + \Delta m_j \qquad (5.9)$$

will bring the predicted data closer to the observed arrival times. Since the data in our application do not depend linearly on the model parameters we linearize the problem by expanding the data in a Taylor series keeping only the linear term,

$$d_i \cong d_i^0 + \sum_j \left.\frac{\partial d_i}{\partial m_j}\right|_{m^0} \Delta m_j. \qquad (5.10)$$

This equation can be written in terms of the difference between the observed data and those predicted,

$$\Delta d_i^0 \equiv d_i^{at} - d_i^0 \cong \sum_j \frac{\partial d_i}{\partial m_j}\Big|_{m^0} \Delta m_j^0. \qquad (5.11)$$

If we define a partial derivative matrix as

$$G_{ij} = \frac{\partial d_i}{\partial m_j}, \qquad (5.12)$$

then Eqn. (5.11) then becomes

$$\Delta d = G\Delta m, \qquad (5.13)$$

or in index notation

$$\Delta d_i = G_{ij}\Delta m_j, \qquad (5.14)$$

The matrix is formed by taking partial derivatives of the data vector of equation (5.2) with respect to each of the four model parameters such that,

$$G_{i1} = \frac{\partial d_i}{\partial m_{1=x}} = \frac{(x-x_i)}{v}[(x-x_i)^2 + (y-y_i)^2 + (z-z_i)^2]^{-1/2},$$

$$G_{i2} = \frac{\partial d_i}{\partial m_{2=y}} = \frac{(y-y_i)}{v}[(x-x_i)^2 + (y-y_i)^2 + (z-z_i)^2]^{-1/2}, \qquad (5.15)$$

$$G_{i3} = \frac{\partial d_i}{\partial m_{3=z}} = \frac{(z-z_i)}{v}[(x-x_i)^2 + (y-y_i)^2 + (z-z_i)^2]^{-1/2},$$

and

$$G_{i4} = \frac{\partial d_i}{\partial m_{4=t}} = 1. \qquad (5.16)$$

Since only the linear term in the Taylor series expansion was kept, Eqn. (5.13) is a vector-matrix equation representing a system of simultaneous linear equations that maps changes in model parameters onto improvements in the fit to the data. In theory, Δm could be solved by inverting *G* in Eqn. (5.13), however this is unlikely to work in practice since any errors in the data will lead to inconsistent equations, and therefore no solution. For example, there are potentially measurement errors in identifying the proper arrival time as well as systematic errors associated with a simplistic velocity model. In this realistic scenario no one model can estimate the true model exactly. Furthermore, in the case of events consisting of arrival times from all six transducers there are more individual measurements of data than model parameters. In other words, in Eqn (5.14) *i* ranges from 1 to 6 representing the arrival times at each of the six transducers and provides up to six equations (or rows in G_{ij}), while *j* ranges from 1 to 4 representing *x*,*y*,*z* and *t* providing 4 unknowns (or columns in G_{ij}). Since the number of equations is equal to the number of rows in G_{ij} and the number of unknowns is equal to the number of columns in G_{ij} the result is that G_{ij} is a 6x4 matrix and is not square and therefore, overdetermined. However, the more transducers that measure an event leads to generally more accurate location estimation (de Ronde et al., 2007). Therefore we seek a solution for *m*, that best fits the predicted data, d_i, to the observed data, d_i^{at}, based on minimizing the square of their misfit, or residuals, x^2, as described by their standard deviations, σ_i, of the observed data such that,

$$x^2 = \sum_{i=1}^{6} \frac{1}{\sigma_i^2} \left(\Delta d_i - \sum_{j=1}^{4} G_{ij} \Delta m_j \right)^2. \qquad (5.17)$$

In order to minimize the misfit it is necessary to take partial derivatives of Eqn (5.17) with respect to the model parameters Δm_k and set them to zero where *k* is a dummy index from 1 to 4 representing the model parameters *x,y,z* and *t* in the same way as *j* (i.e. x = *1*, *y = 2*, etc.). Since the models parameters are independent, the partial derivative of one with respect to another is zero unless the indicies are equal such that

$$\frac{\partial \Delta m_k}{\partial \Delta m_j} \delta_{jk}, \qquad (5.18)$$

where δ_{jk} is the Kronecker delta function and

$$\delta_{jk} \equiv \begin{matrix} 1 \; if \; j = k \\ 0 \; if \; j \neq k \end{matrix}\Big\}. \qquad (5.19)$$

Applying the aforementioned procedure to Eqn (5.17) and invoking Eqns. (5.18) and (5.19) yields

$$\frac{\partial x^2}{\partial \Delta m_k} = 0 = 2 \sum_{i=1}^{6} \frac{1}{\sigma_i^2} \left(\Delta d_i - \sum_{j=1}^{4} G_{ij} \Delta m_j \right) G_{ik} \qquad (5.20)$$

or

$$\sum_{i=1}^{6} \frac{1}{\sigma_i^2} \Delta d_i \, G_{ik} = \sum_{i=1}^{6} \frac{1}{\sigma_i^2} \left(\sum_{j=1}^{4} G_{ij} \Delta m_j \right) G_{ik}. \qquad (5.21)$$

Eqn. (5.21) can further be simplified by assuming that the variances are equal for each transducer ($\sigma_i^2 = \sigma^2$) and factoring it out yielding,

$$\sum_{i=1}^{6} \Delta d_i \, G_{ik} = \sum_{i=1}^{6} \left(\sum_{j=1}^{4} G_{ij} \Delta m_j \right) G_{ik}, \qquad (5.22)$$

which can be rewritten in matrix notation as

$$G^T \Delta d = G^T G \Delta m, \qquad (5.23)$$

where G^T is the transpose of G. Therefore, $G^T G$ in Eqn. (5.23) is a square matrix and therefore has an inverse which can be multiplied to Eqn. (5.23) on the left hand side to yield

$$\Delta m = (G^T G)^{-1} G^T \Delta d. \qquad (5.24)$$

The operator, $(G^T G)^{-1} G^T$, is known as the generalized inverse of *G* and operates on the data to calculate the "best" model based on the criteria that the square of the misfit is minimized.

5.6.2 Procedure for applying generalized non-linear least squares inversion to hypocentral location of AE events in the HPHT assembly

To invoke the method described in section 5.5.1, to hypocentral location in the HPHT assembly described in section 3.2 requires performing the following steps:

1. Begin by guessing a starting model m^0 (source location and origin time) that is preferably close to the actual hypocenter. In our case we generally start with the origin (center of the high pressure assembly) and time zero such that our model vector is $m^0 = [0, 0, 0, 0]$. By assuming that the event occurred at time "0" simply means that the solution will have a negative value for the time component in the final model indicating the event preceded its arrival at the transducers for a finite velocity model.
2. Use Eqn (5.4) to calculate d^0 predicted from m^0, a first estimate of the data based on our initial estimate of the model.
3. Evaluate the misfit to the data by calculating the residual vector

$$\Delta d^0 \equiv d^{at} - d^0 \qquad (5.25)$$

4. Evaluate the partial derivative matrix of Equation (5.9) about the starting model;

$$G_{ij} \left.\frac{\partial d_i}{\partial m_j}\right|_{m^0}.$$

5. Calculate the change in the starting model by finding $(G^T G)^{-1} G^T$ and substituting it, along with Δd^0, into Eqn (5.24) to obtain Δm^0. Δm^0 is the initial change in the starting model. This generates a new model,

$$m^1 = m^0 + \Delta m^0 \qquad (5.26),$$

which is an improvement on the initial guess.

6. The process can now be taken back to Step 1 and the new model, m^1, can used to find the new set of data, d^1, predicted by this model using Eqn (5.4). In this case the residuals $(\Delta d^1)^2 < (\Delta d^0)^2$ since m^1 is a better fit to the actual model than m^0.
7. Continue steps 1-6 in an iterative manner until $\sum_{i=1}^{6} (\Delta d_i^n)^2$ is appreciably small indicating the model changes little with each iteration. The tolerance placed on the $(\Delta d^n)^2$ is $\sum_{i=1}^{6} (\Delta d_i^n)^2 - \sum_{i=1}^{6} (\Delta d_i^{n-1})^2 < 0.001$ mm and usually requires only 3 to 6 iterations.

5.7 Event location results using the inversion algorithm based on accurately chosen arrival times

5.7.1 The path taken to estimate the position of an event based on linearizing about a starting model

The process of inverting for location of an event based on linearizing about a starting model can be schematically illustrated by showing how a new model is estimated after each successive iteration until a final estimation of the event location is obtained. Figure 5.7 shows a graphical representation of the path taken for the *x, y, z* and *t* components for a typical event relocated by inverting accurate arrival time data using the procedure just described. Each component initially starts at position zero (i.e. the origin) and moves linearly in increments toward the final estimate of the position by improving the misfit of the data after each iteration. Once it reaches the best estimate of the position of the event, in a least squares sense, subsequent iterations no longer change the location. The negative value for the time component indicates that the event occurred prior to the arrival of acoustic energy at the transducers. In this case the event was generated within a gasket and displayed a substantial difference between the event location calculated by the Vallen software compared to that of the inversion algorithm.

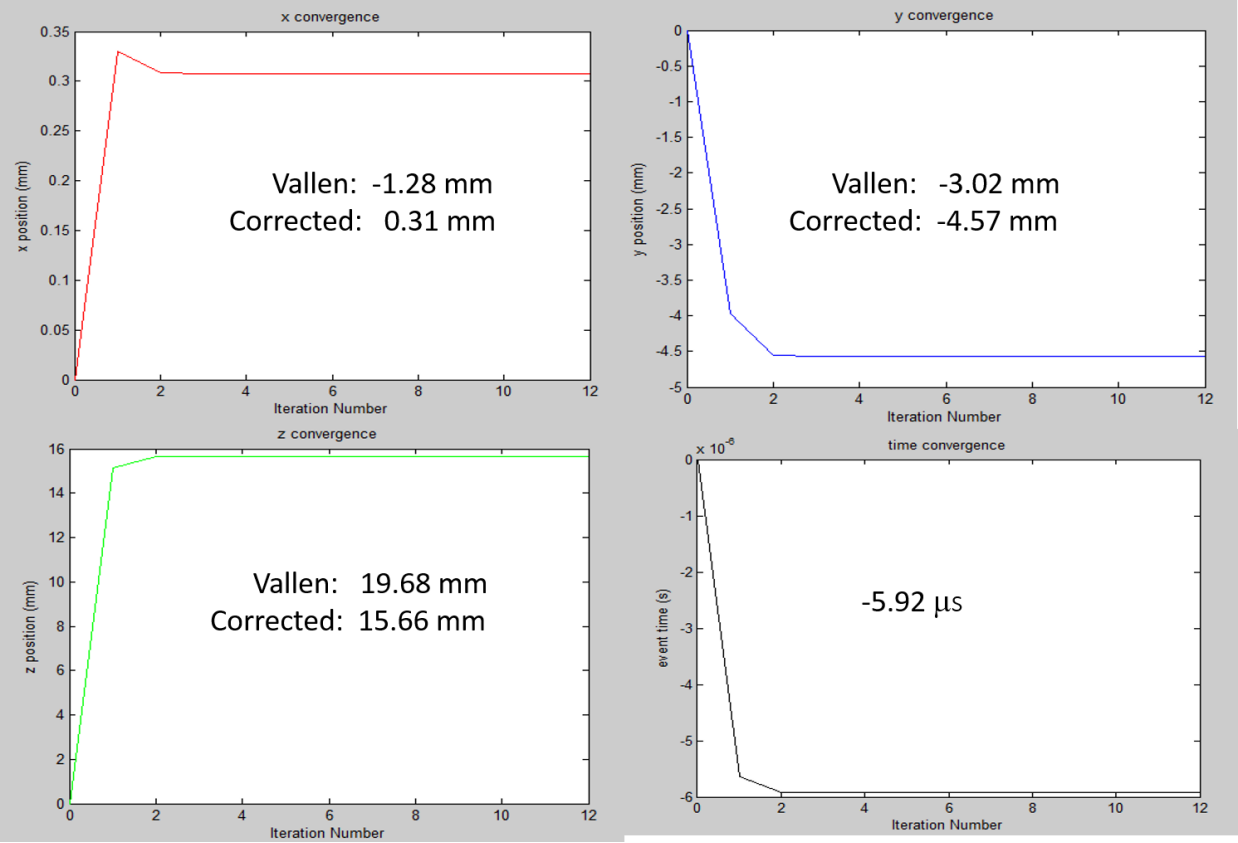

Figure 5.7: Schematic illustration of the approach of the x, y, z and t components of a located event. Each spatial component starts at the origin and time starts at an arbitrarily defined time zero. For each successive iteration, each component linearly approaches the final estimation of the event location by minimizing $\sum_{i=1}^{6}(\Delta d_i^n)^2$ in a least squares sense. Once the estimation of the event location reaches its final position it no longer varies with successive iterations more than a set tolerance of 0.001 mm. The calculation of a negative time value indicates that the event occurred -5.92 µs before the threshold crossing of the first registered transducer.

The algorithm, in addition to calculating the location of an event and writing it to a text file, also outputs the energy of the event averaged by the number of signals used to locate it, as well as the pressure at which the event occurred and the value of sound velocity inputted to invert for it. Table 2 shows the results of the first 10 events located in an experiment measuring the acoustic activity generated by the pressurization of quartz beads.

Event	Sigs	x	y	z	t	E	P	v
#	#	(mm)	(mm)	(mm)	(s)	(a.u.)	(GPa)	(m/s)
1	6	2.15	1.84	-1.25	385	246200	0.64	6179
2	6	2.45	0.79	-1.53	439	649667	0.66	6186
3	6	-2.08	1.27	-1.23	448	74717	0.66	6188
4	6	3.02	-0.11	-1.09	471	507667	0.67	6189
5	6	-0.81	-0.24	-1.39	473	1349833	0.67	6189
6	6	-1.87	0.66	-0.48	478	65300	0.67	6191
7	6	-0.36	1.56	-1.94	495	29033	0.67	6191
8	6	5.51	-1.52	-4.96	501	35250	0.67	6191
9	6	2.48	-0.82	-0.16	505	312667	0.68	6193
10	6	1.18	2.24	-0.69	509	1818667	0.68	6193

Table 5.2: The output for 10 events generated by the pressurization of quartz beads. The data calculated for each event is the event number, number of signals used in the iteration, the x,y and z position of the event, the time at which it occurred during the experiment, the event energy (E) averaged by the number of hits, the pressure at which it occurred, and the velocity used in the inversion algorithm.

5.8 Comparison of the acoustic location algorithm on quartz beads versus AgCl powder

In order to test the accuracy of the location algorithm, experiments were run comparing the acoustic activity of quartz beads and AgCl powder. These materials were selected for their contrasting mechanical behaviour. Quartz displays brittle behaviour and were expected to generate a large amount of acoustic activity during cold compression due to porosity loss and crushing and/or pulverization of the beads (Wong et al., 1997; Gasc et al., 2011). Conversely, AgCl which is a ductile material is expected to deform plastically and therefore aseismically. The starting material for the quartz experiment, shown in Figure 5.8, consisted of irregularly shaped quartz beads with an average thickness of approximately 200 - 400 μm.

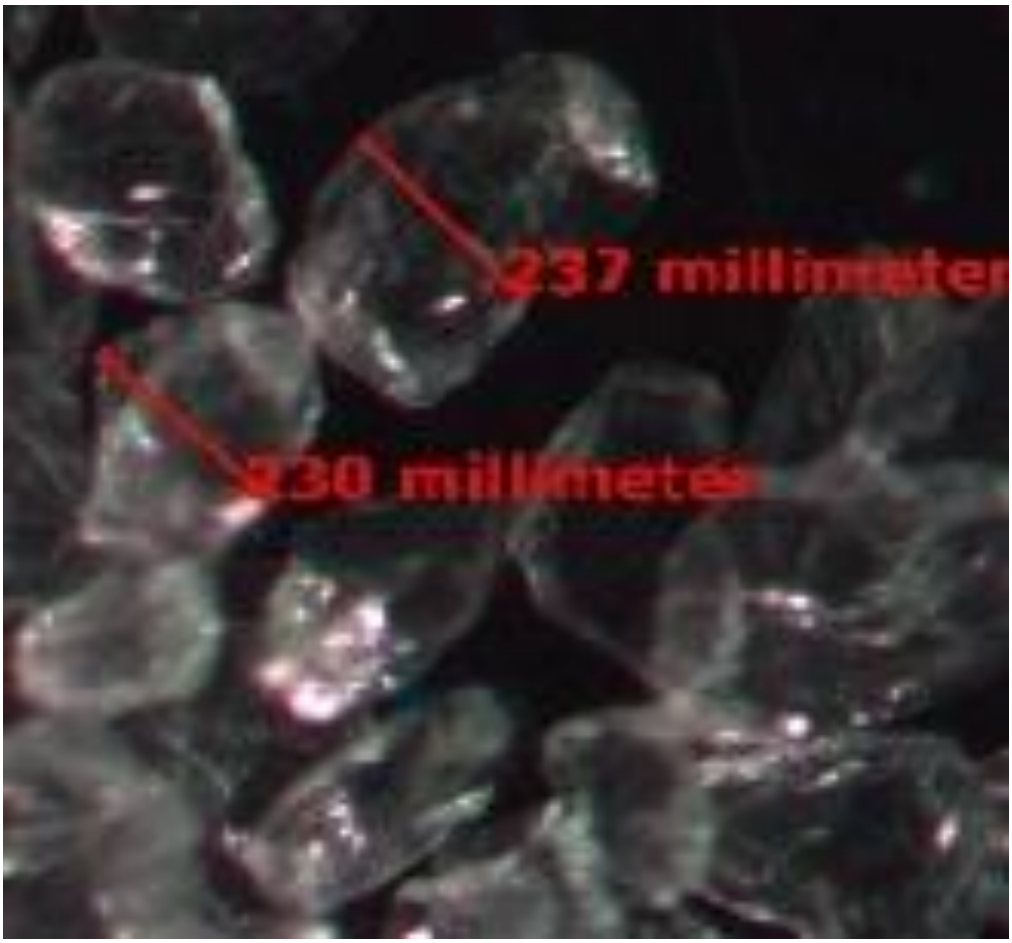

Figure 5.8: Starting material for the quartz bead experiment. Quartz beads consisted of irregular SiO_2 beads approximately 200 to 400 μm in diameter. Due to the angular nature of the starting material the sample volume contained a large amount of porosity.

The AgCl sample consisted of fined grained AgCl < 5 μm in diameter that due to its softness could be packed so that it contained virtually no porosity. Both experiments were carried out under identical conditions so their results could be compared directly. These included two stages. The first was cold compression to 4 GPa with a pressurization rate of 25 MPa/min., a pre-amplification of 35 dB and a threshold of 40 dB. The second stage consisted of pressurization from 4 to 8 GPa with a pressurization rate of 120 MPa/min., a temperature of 923 K, pre-amplification of 40 dB and a threshold of 40 dB, which mimics the conditions used during deformation experiments on sintered fayalite. The cell assembly in both experiments was

identical to that of experiments performed on sintered fayalite samples which contain Al_2O_3 pistons to generate non-hydrostatic stress, a cylindrical sample 3 mm in diameter and 5 mm in length, and a thermocouple exiting the octahedron through a face intersecting the sample cylindrical axis, so the results of these experiments could be compared directly to that of faulting experiments on fayalite. Therefore, results from these experiments could be used to test whether the system generates spurious acoustic activity under the operational conditions of transformational faulting experiments since neither the quartz nor AgCl samples were expected to produce acoustic signals under HPHT conditions.

One of the difficulties involved in testing the location procedure is that at relatively low pressure (< 2 GPa), the high pressure assembly is overwhelmed by 1000's of acoustic events generated from compaction of the MgO octahedron and gasket formation. In order to reduce the number of acoustic events to be relocated, only those which were registered by all six transducers and located by the Vallen software to within ± 5 mm about the origin in the x,y and z directions were relocated. As expected, during stage 1 of the experiment which involved cold compression to 4 GPa, the quartz beads were far more acoustically active generating a total of 448 events that met the aforementioned criteria compared to only 18 for that of AgCl. Of these 225 locate within the quartz sample and 4 locate within the AgCl sample based on arrival times picked by the AIC automatic picking algorithm. Figure 5.9 shows the results of the event locations with respect to the position of the sample. Events that locate within the sample are displayed in red and events that locate outside the sample are shown in blue. During stage 2 of the experiment, where acoustic data were collected from 4 to 8 GPa at 923 K with a pressurization rate similar to that of HPHT faulting experiments on fayalite, did not result in any

events that locate within the sample for either quartz or AgCl demonstrating that the system is acoustically quiet under these experimental conditions.

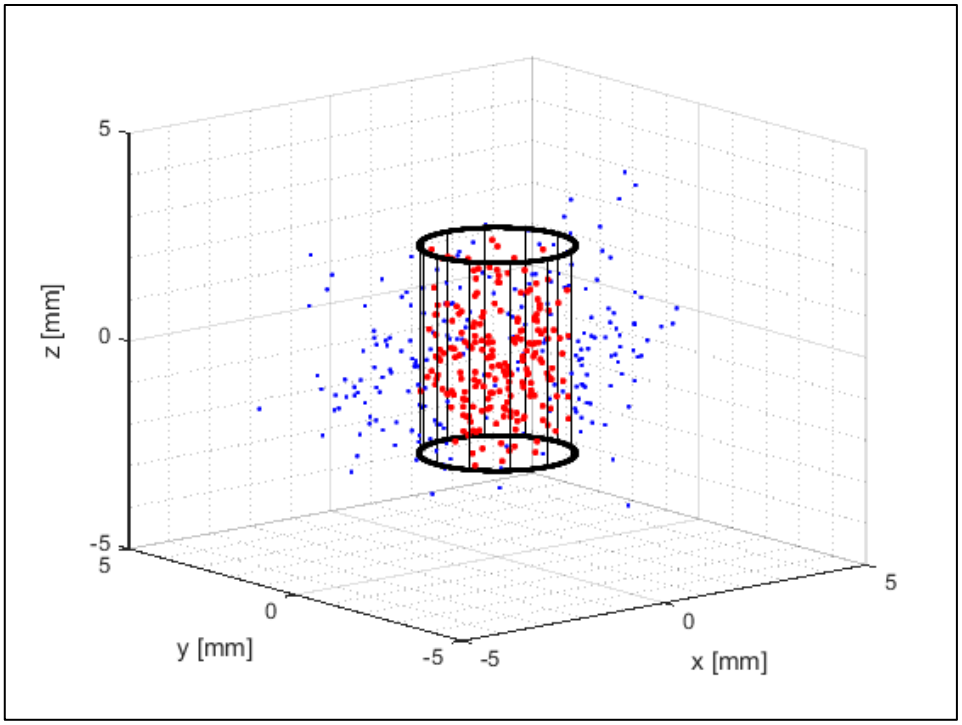

a)

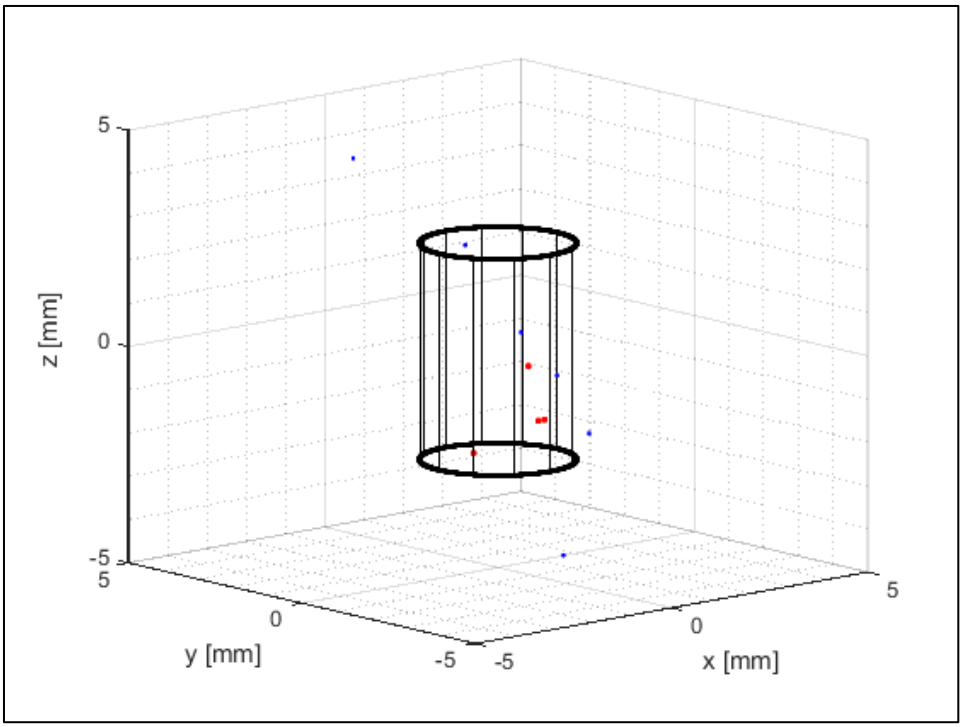

b)

Figure 5.9: **a)** Acoustic events associated with pressurization of quartz beads. Several hundred events were located during the first phase of the experiment, 228 of which locate within the sample. **b)** Acoustic activity associated with the pressurization of an AgCl sample. Far fewer events occurred in this sample compared to that of quartz beads. Neither experiment generated events within ± 5 mm about the origin in the x,y and z directions as calculated by the Vallen software during stage 2 of the experiment indicating that the system is acoustically quiet during the operational conditions of HPHT experiments on fayalite.

These results indicate that it is possible to detect and locate acoustic signals generated by a 3 mm diameter by 5 mm long cylindrical sample, implying that sonic energy due to faulting in fayalite can also be detected and linked to the sample. The large number of events that locate outside the sample in quartz is likely a combination of uncertainty (see section 5.8) as well as a significant number of events occurring as a result of compaction of the MgO pressure medium. The lack of a comparable number of events in the AgCl experiment where compaction also occurs is due to the large amount of porosity in the quartz sample leading to a far more uneven compaction rate inducing rapid strain release in the pressure medium compared to the smooth compaction rate experienced by the AgCl. This is supported by the fact that very few events were located above and below the sample within the Al_2O_3 pistons which would be expected since the uncertainty along the z-axis is larger than that of the x- and y-axes (see section 5.8). It should also be noted that 4 events were located within the AgCl sample near the periphery. These are likely a result of either compaction of the pressure medium or reverberations in the furnace that were imperfectly located.

5.9 Uncertainty in event location

Uncertainties associated with the velocity model as well as the picking of the true arrival times will be reflected in the determination of the event locations. While it is difficult to estimate the uncertainty associated with the velocity model and beyond the scope of this study, the uncertainty connected with the automatic picking algorithm can be estimated by comparing the discrepancy between manually and automatically picked arrival times. This was done for 998 arrival times that were chosen for acoustic hits recorded during the compression of quartz beads.

Figure 5.10 shows the difference in the number of samples between those manually and automatically picked hits where the difference in time between each sample is 0.025 μs.

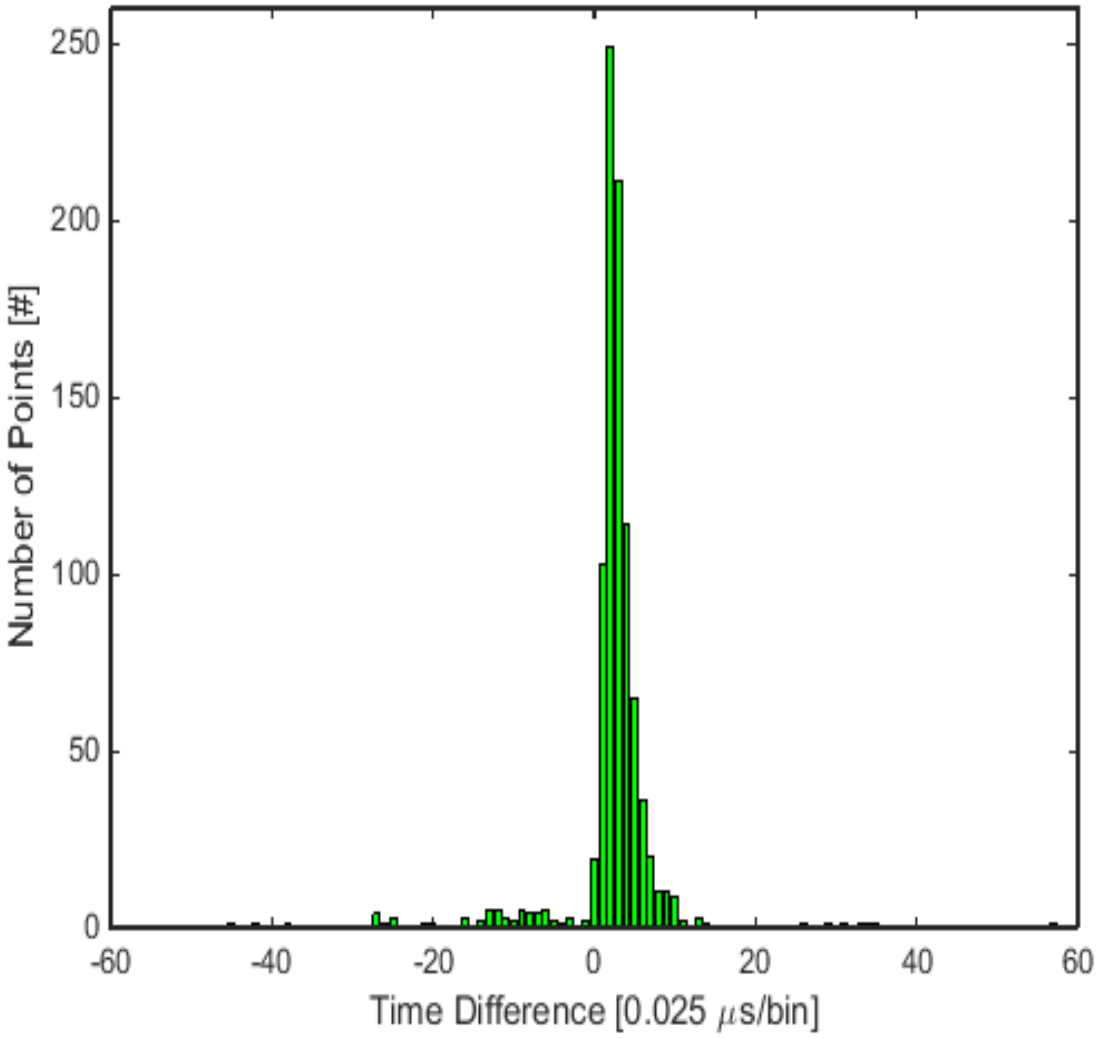

Figure 5.10: Histogram of the difference between manually picked arrival times and those picked using the AIC algorithm.

If we assume the manually picked arrival times to have infinite accuracy there is a consistent bias in the automatic picks that tends to pick the arrival time later than the manual picks leading to an average offset of 0.102 μs. This is in part related to the relative lengths, in number of samples, of the two windows used in the AIC picking algorithm (see section *5.4.1*). However, since the final

location calculated by the inversion algorithm is determined only by the relative difference in arrival times and we assume that all the transducers are equally biased, the effect on the determination of event location is removed and the offset can be effectively eliminated resulting in a mean of 0. Furthermore if we assume that the histogram in Figure 5.10 can be represented by a Gaussian function and that errors between transducers are uncorrelated and equal the uncertainty analysis becomes greatly simplified such that,

$$\sigma_d^2 = \sigma^2 \delta_{ij}, \qquad (5.27)$$

and the model variance-covariance matrix becomes,

$$\sigma_m^2 = \sigma^2 (G^T G)^{-1}. \qquad (5.28)$$

(Stein and Wysession, 2003). While strictly speaking, the arrival time errors are not exactly Gaussian, and slight differences in errors between transducers may arise as a result of differing frequency responses and/or inconsistent coupling, these assumptions are considered adequate to obtain a reasonable estimate of event location uncertainty. As with the location, the model variance-covariance matrix can be inverted for using the same matrix *G* in successive iterations and a value of σ_t = 0.148 μs derived from the Gaussian function. The results in the model variance covariance matrix,

$$\sigma_m^2 = \begin{bmatrix} \sigma_{xx}^2 & \sigma_{xy}^2 & \sigma_{xz}^2 & \sigma_{xt}^2 \\ \sigma_{yx}^2 & \sigma_{yy}^2 & \sigma_{yz}^2 & \sigma_{yt}^2 \\ \sigma_{zx}^2 & \sigma_{zy}^2 & \sigma_{zz}^2 & \sigma_{zt}^2 \\ \sigma_{tx}^2 & \sigma_{ty}^2 & \sigma_{yz}^2 & \sigma_{tt}^2 \end{bmatrix}, \qquad (5.29)$$

where the standard deviations of each parameter are given by the square roots of the diagonal elements. In general, the off-diagonal elements are non-zero and represent correlations between uncertainties in the model parameters. In addition, by extracting the submatrix,

$$\begin{bmatrix} \sigma_{xx}^2 & \sigma_{xy}^2 \\ \sigma_{yx}^2 & \sigma_{yy}^2 \end{bmatrix} \qquad (5.30)$$

and diagonalizing it to find the eigenvalues $\lambda^{(1)}$ and $\lambda^{(2)}$ and the associated eigenvectors $\begin{bmatrix} x_1^{(1)} \\ x_2^{(1)} \end{bmatrix}$ and $\begin{bmatrix} x_1^{(2)} \\ x_2^{(2)} \end{bmatrix}$ an error ellipse can be constructed with semi- major and semi-minor axes given by $\sqrt{\lambda^{(1)}}$ and $\sqrt{\lambda^{(2)}}$ respectively, oriented in a direction given by $\tan^{-1}\left(x_1^{(1)} \Big/ x_2^{(1)}\right)$. By performing the same procedure on the remaining submatrices $\begin{bmatrix} \sigma_{xx}^2 & \sigma_{xz}^2 \\ \sigma_{zx}^2 & \sigma_{zz}^2 \end{bmatrix}$ and $\begin{bmatrix} \sigma_{yy}^2 & \sigma_{yz}^2 \\ \sigma_{zy}^2 & \sigma_{zz}^2 \end{bmatrix}$ the entire 3-dimensional volume of uncertainty for a confidence level of 1σ can be obtained. Table 3 shows the uncertainty calculations for the events shown in Table 2 including the standard deviation in x,y and z positions, the standard deviation in t, as well as the dimensions and orientation of the error ellipses in the (x,y), (x,z) and (y,z) planes.

Event	σ_x	σ_y	σ_z	σ_t	ee_smin_xy	ee_smaj_xy	ee_xy_or	ee_smin_xz	ee_smaj_xz	ee_xz_or	ee_smin_yz	ee_smaj_yz	ee_yz_or
#	(mm)	(mm)	(mm)	(μs)	(mm)	(mm)	(degrees)	(mm)	(mm)	(degrees)	(mm)	(mm)	(degrees)
1	0.56	0.56	1.12	0.06	0.56	0.56	-45	0.56	1.12	-45	0.56	1.12	-45
2	0.56	0.56	1.12	0.06	0.56	0.56	-45	0.56	1.12	-45	0.56	1.12	-45
3	0.56	0.56	1.12	0.06	0.56	0.56	-45	0.56	1.12	-45	0.56	1.12	-45
4	0.56	0.56	1.12	0.06	0.56	0.56	-45	0.56	1.12	-45	0.56	1.12	-45
5	0.56	0.56	1.12	0.06	0.56	0.56	-45	0.56	1.12	-45	0.56	1.12	-45
6	0.56	0.56	1.12	0.06	0.56	0.56	-45	0.56	1.12	-45	0.56	1.12	-45
7	0.56	0.56	1.12	0.06	0.56	0.56	-45	0.56	1.12	-45	0.56	1.12	-45
8	0.56	0.57	1.13	0.06	0.56	0.57	-45	0.56	1.13	-45	0.57	1.13	-45
9	0.56	0.56	1.12	0.06	0.56	0.56	-45	0.56	1.12	-45	0.56	1.12	-45
10	0.56	0.56	1.12	0.06	0.56	0.56	-45	0.56	1.12	-45	0.56	1.12	-45

Table 5.3: Uncertainty associated with the first 10 events located for the quartz beads experiment. The algorithm calculates the standard deviations in x,y,z and t (σ_x , σ_y, σ_z, σ_t) as well as the error ellipses in the (x,y), (x,z) and (y,z) planes denoted by ee_smin[coordinates] and ee_smaj_[coordinates] where ee represents error ellipse, [coordinate] represents the particular coordinate pair of the ellipse, and smaj and smin represents the semi-major and semi-minor axis respectively. Their orientation is given by ee_[coordinates]_or which is always angled -45^0 to the positive abscissa axis resulting from the geometry of the transducers.

The average standard deviations in the model parameters for all 448 events are σ_x = 0.567 mm, σ_y = 0.566 mm, σ_z = 1.13mm and σ_t = 0.06 μs, and the average of the semi-major and semi-minor axes of the error ellipses are ee_smaj_xy = 0.566, ee_smin_xy = 0.567, ee_smaj_xz = 1.13, ee_smin_xy = 1.12, ee_smaj_yz = 1.13, and ee_smin_yz = 1.12. The size of the semi-major and semi-minor axes of the error ellipses is based directly on the size in the uncertainty in position. All of the error ellipses are oriented with their semi-major axis angled at -45^o to the positive abscissa axis for each coordinate pair and result solely from the geometry of the transducer positions. For each event the uncertainty in the location of the z-coordinate is larger than the x and y as a result of poorer coverage along the z-axis since no transducers are placed on the back truncations that intersect the z-axis.

The entire Matlab™ inversion program for event location and associated uncertainties, including step by step comments describing each line of code is given in Appendix 1.

5.10 Conclusions

By employing multiple transducers in a microseismic array a method has been devised that allows for the determination of the location of acoustic events that originate within the high pressure assembly. Such a procedure is critical since it can distinguish between acoustic emissions generated within the sample from those that develop in the surrounding pressure medium. Event location is achieved by inputting the arrival times of acoustic signals and inverting for the location based on an iterative process that linearizes the problem and minimizes the misfit in a least squares sense. Events are automatically classified based on time criteria that are inputted into the Vallen software package. However, because the Vallen software defines the arrival time of signals as the point at which the signal crosses a voltage threshold, and not the initiation of the wave, the true arrival time is estimated either by manual selection or automatically by finding the minimum value of the Akaike Information Criterion. These re-determined arrival times are then inputted into the inversion algorithm which uses the positions of the transducers and homogeneous velocity model to compute the locations of events. The sensitivity of the system has been tested using quartz beads and AgCl samples. Hundreds of AE's were collected during cold compression of quartz beads, 228 of which located within the sample. The large number of events that were located in the surrounding pressure medium during this experiment probably resulted partly from uncertainty in the location algorithm, but the majority were likely a result of the inhomogeneous compaction rate of the pressure medium resulting from a highly porous sample. Comparatively, only 18 events were recorded during cold compression during an experiment containing an AgCl sample with an indistinguishable cell design and identical experimental conditions. Of the 18 only 4 events were located within the sample near its periphery. Because the sample is soft, it is unlikely that they originated within it

and probably arose due to mechanical instabilities in the pressure medium or reverberations in the furnace. During rapid pressurization at 923 K neither experiment generated events within the sample or the pressure medium suggesting that the system is acoustically quiet under the HPHT conditions of deformation experiments carried out on sintered fayalite.

5.11 References

Akaike, H., Markovian representation of stochastic processes and its application to the analysis of autoregressive moving average process. *Ann. Inst. Stat. Math*., **26**,363-26,387, 1974

Aki, K. and Richards, P.G., 2002. *Quantitative Seismology: Second Edition*, University Science Books, Mill Valley, California, USA.

Gasc, J., Schubnel, A., Brunet, F., Guilln, S., Mueller, H.-J. and Lathe, C., 2011. Simultaneous acoustic emissions monitoring and synchrotron X-ray diffraction at high pressure and temperature: Calibration and application to serpentinite dehydration, *Phys Earth Planet Inter.*, **189**, 121-133.

Geiger, L., 1912. Probability method for the determination of earthquake epicenters from the arrival time only (translated from Geiger's 1910 German article), *Bull. St. Louis Univ.*, **8**(1), 56-71.

Lay, T. and Wallace, T.C., 1995. *Modern Global Seismology*. Academic Press, London, UK.

Lee, W.H.K. and Stewart, S.W., 1981, *Principles and Applications of Microearthquake Networks*. Academic Press, New York, NY, USA.

Leaird, J.D., 1997, *Acoustic Emission Training Guide – How to Ensure an Accurate and Valid Acoustic Emission Test*, Greensland Publishing Co., Church Hill, TN.

Maeda, N., 1985, A method for reading and checking phase time in auto-processing system of seismic wave data: Zisin, 38 (2), 365-379 (in Japanese with English abstract).

Officer, T. and Secco, R.A., 2015. Detection of a P-induced liquid ⇌ solid-phase transformation using multiple acoustic transducers in a multi-anvil apparatus, *High Pressure Research*, **35**, 289-299.

de Ronde, A.A., Dobson, D.P., Meredith, P.G. and Boon, S.A., 2007. Three-dimensional location and waveform analysis of microseismicity in multi-anvil experiments, *Geophys. J. Int.*, **171**, 1282-1294.

Shearer, P.M., 1999. *Introduction to Seismology*. Cambridge University Press, 40 West 20th Street, New York, NY, USA.

Sleeman R and van Eck, T. 1999. Robust automatic P-phase picking: An on-line implementation in the analysis of broad-band seismogram recording. *Phys Earth Planet Inter.*, **113**, 265-275.

Stein, S. and Wysession, M., 2003. *Introduction to Seismology, Earthquakes and Earth Structure*. Blackwell Publishing, 350 Main Street, Malden, MA, USA.

Wong, T.F., David, C. and Zhu, W., 1997. The transition from brittle faulting to cataclastic flow in porous sandstones: Mechanical deformation, *J. Geophys. Res.*, **102**, 3009-3025.

Zhang, H., Thurber, C. and Rowe, C., 2003. Automatic P-wave arrival detection and picking with multiscale wavelet analysis for single-component recordings, *Bulletin of the Seismological Society of America*, **93**, 1904–1912.

Chapter 6: Experimental Methods

6.1 Introduction

In order to generate a faulting instability in a rock, the rupture front must be able to traverse several grains in the mineral assemblage. For this to occur, the mineral assemblage must constitute a continuum in which grains are physically connected at their boundaries with little to no porosity (Aki and Richards, 1980). A monolithic sample with little porosity also transfers acoustic signals with much lower distortion and attenuation (Shearer, 1999). Because fayalite occurs only rarely in nature, and usually as only a small percentage of the mineral assemblage that make up rocks, it was necessary to synthesize experimental samples within the laboratory in order to produce a fayalite sample suitable for high pressure/high temperature (HPHT) faulting experiments. To achieve this required two separate procedures: synthesis of fayalite powder in a 1 atm gas mixing furnace using a stoichiometric combination of quartz (SiO_2) and hematite (Fe_2O_3) and hot pressing of the powder at HPHT to produce a monolithic sintered sample. A study was carried out in the 3000 ton multi-anvil apparatus at Western University on samples of sintered fayalite under metastable conditions in the ahrensite stability field. In addition to monitoring the pressure, temperature and pressurization rates throughout the experiments, piezoelectric sensors were employed in combination with an acoustic emission system, to monitor acoustic signals generated in the experimental environment whose purpose is to ascertain whether there is an acoustic signature that accompanies the transformation. Typical experiments included initiating the olivine → spinel phase transition in Fe_2SiO_4, under

metastable conditions, in the presence of non-hydrostatic stress, while the sample was being strained, and monitoring acoustic signals associated with it.

6.2 Synthesis of fayalite powder

The fayalite powder was synthesized by Dr. Tony Withers and Sean Funk in a gas mixing furnace at the University of Minnesota. The starting material for the fayalite powder was composed of a stoichiometric mixture of hematite (Fe_2O_3) and quartz (SiO_2) powders with a molar weight ratio of SiO_2:Fe_2O_3 = 0.2734. After mixing with an agate pestle and mortar to achieve a grain size of < 10 μm, the starting material was reacted at 1373 K for 24 h in a combination of CO–CO_2 gas, adjusted to buffer oxygen fugacity at a value of two log units below fayalite– hematite–quartz equilibrium. The starting material was then further ground and the process repeated to ensure that all the starting material reacted and achieved homogeneity. Figure 6.1 shows the X-ray diffraction (XRD) pattern of the reaction product which is dominated by fayalite.

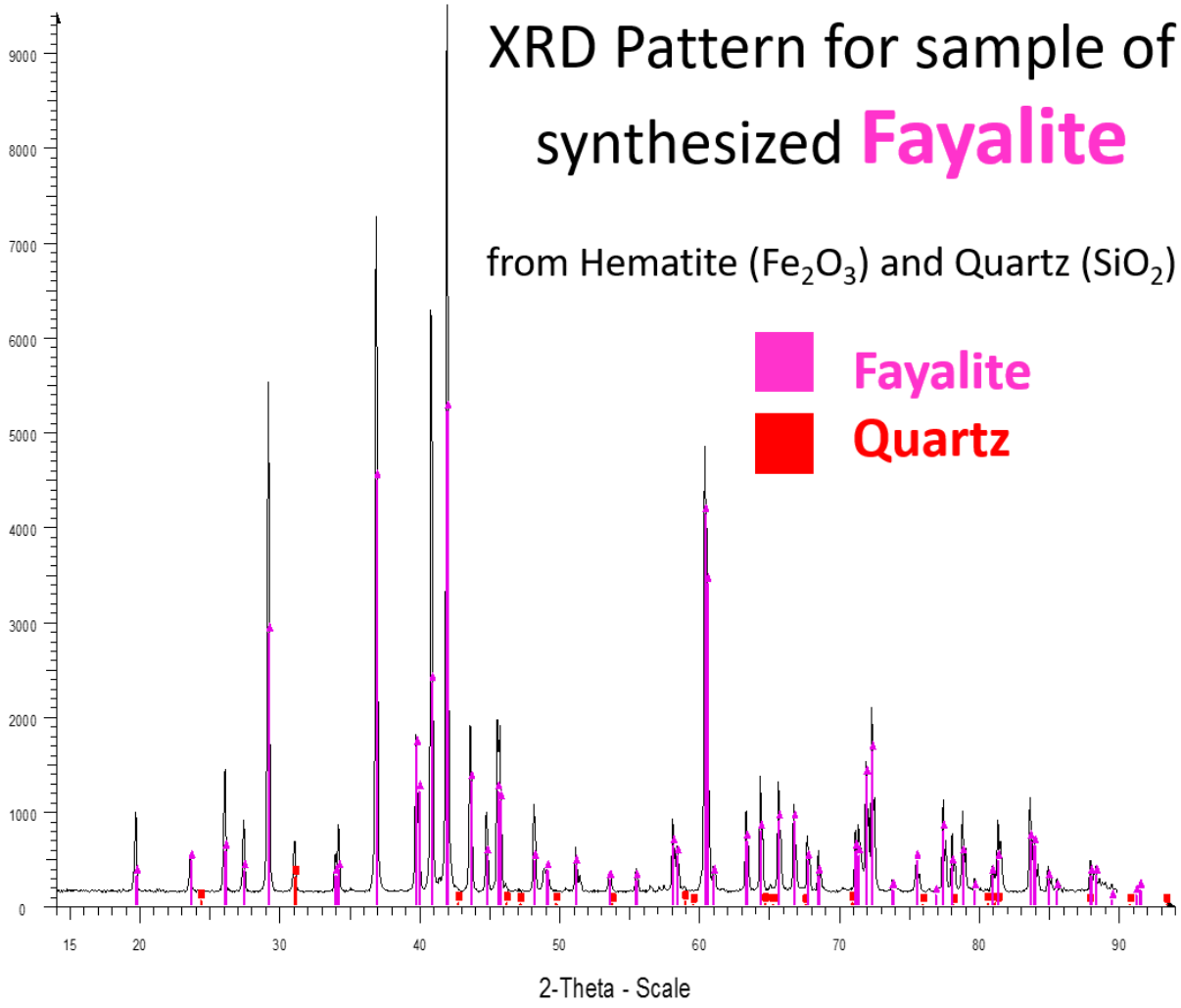

Figure 6.1: XRD pattern displaying the structural makeup of the synthesized powder. The pink peaks, which dominate the pattern, correspond to fayalite. The red peaks correspond to quartz.

Figure 6.2 shows the grain size of the synthesized powder. Grains typically ranged from 1 to 10 μm in size with a tendency toward smaller grain sizes.

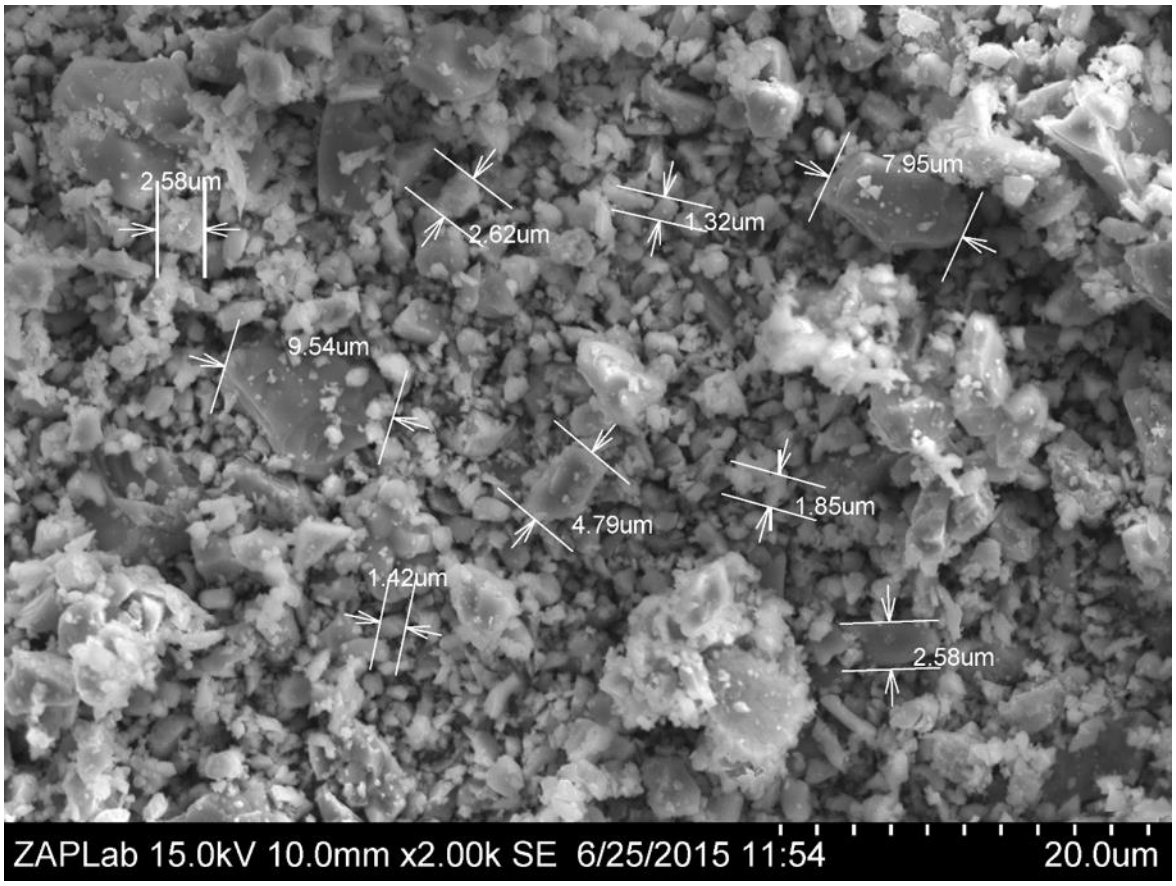

Figure 6.2: SEM image of the starting material used for sintering. Grains vary in size from 1 to 10 μm with a tendency towards smaller grain sizes. In some cases further grinding was carried out and reduced most of the largest grains to < 5 μm.

Prior to sintering, further grinding reduced the overall size of the largest grains to < 5 μm, but grains were rarely reduced to < 1 μm.

6.3 Sintering Experiments

6.3.1 Experimental cell design and the 1000 ton multi-anvil apparatus

To produce a sample that could support transformational faulting extending over multiple grains required sintering of the fayalite powder. This was achieved in the 1000 ton cubic anvil press at Western University, shown in Figure 6.3. The press is capable of reaching 5 GPa and 2500 ^{0}C using 1.00" (25.4 mm) truncations of the WC anvils.

Figure 6.3: The 1000 ton cubic anvil press at Western University.

6.3.2 Cubic Cell Design

The high pressure cell was cubic in geometry with 1.25” (31.75 mm) edges and composed of a pyrophyllite pressure medium. A cylindrical hole is drilled through the center of one of the cubic faces and traverses the entire cube with axial symmetry about the centroid creating a cylindrical hole where the experimental components are placed. This included the powder sample which is packed into an Ag sample container located at the center of the assembly. Ag was chosen for its chemical inertness with fayalite, a melting temperature which is above the sintering temperature, ease of machining, and relatively low cost. The Ag sample containers, including their lids, were fabricated from solid Ag rods using a lathe. The chamber of the sample container, after the lid is press fit into place, is 5.7 mm long and 3.2 mm in diameter. This results in samples that are 5.2 to 5.4 mm in length and 3.0 mm diameter. The length of the sample can be polished to a length of 5.0 mm for use in acoustic emission experiments. To ease removal of the sintered fayalite from the Ag container after the sintering experiment the wall thickness of the Ag is machined to < 0.25 mm. In order to fill the chamber with fayalite powder with a minimum of porosity, it was compacted using a combination of tapping it with a pin gauge and a hammer, and compacting it using a vice. To ensure that the sample container was not deformed during this process it was placed in a brass ring. Inside the high pressure cell, a BN sleeve and discs surrounded the sample container on all sides. Because of the softness of BN, it acted to minimize non-hydrostatic stress that can cause deformation of the cylindrical geometry of the sample. Heat was generated by passing a current through a cylindrical graphite sleeve that extended the entire length of the cube. A ZrO_2 sleeve and discs surrounded the BN parts to provide thermal insulation. This helped minimize the thermal gradient within the cell. The remaining space was filled with pyrophyllite sleeves and plugs. Once all the parts were contained

within the pressure cell a 1 mm hole, that penetrated the entire length of the cell, was drilled perpendicular to the sample axis with a 5.5 mm offset with respect to the center of one cubic face. This allowed for the insertion of a W-Re thermocouple that was used to monitor temperature throughout the duration of the sintering process. Figure 6.4 shows a cross section of the experimental pressure cell displaying all the components.

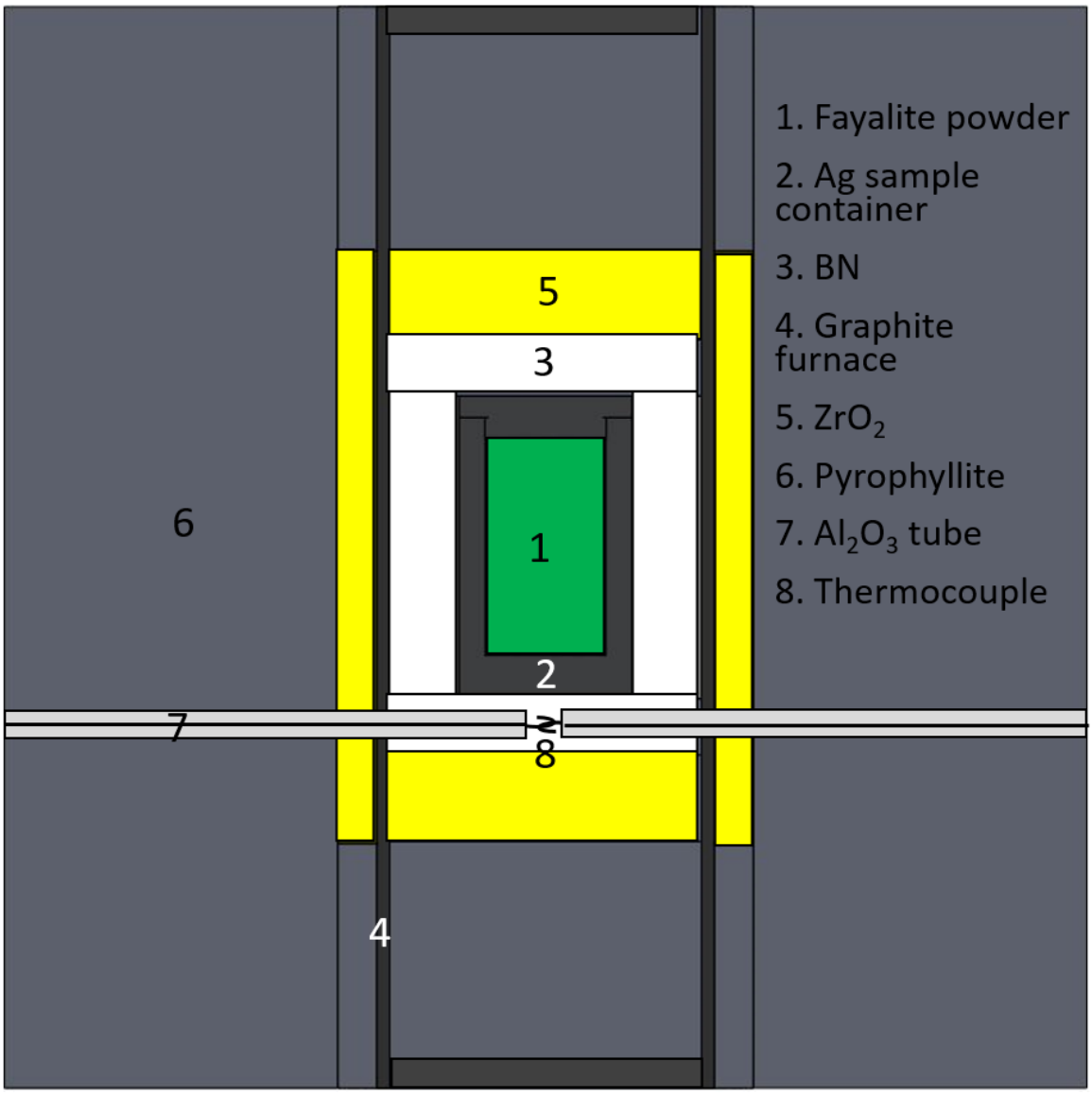

Figure 6.4: Cross sectional cell design for HPHT sintering experiments detailing all components.

6.3.3 Sintering Experiments: Experimental Procedure

The most important factors concerning sintering a sample were: ensuring the fayalite powder was well packed into the sample container, pressure, temperature, dwell time at elevated pressure and temperature, depressurization rate, and careful removal of the sintered sample from the sample container after the experiment. To a lesser extent the cooling rate was also a factor. To ensure well sintered samples, variations of the aforementioned factors were varied until suitable and repeatable results were successfully achieved.

It is important that the sample remained in the P,T stability field of fayalite. If ahrensite was created, then it would not be possible to test the transformational faulting hypothesis since ahrensite remains metastable at ambient conditions and therefore would not have the opportunity to undergo a phase transition during deformation experiments. Another constraint on the P,T conditions was they should not extend beyond the melting curve of the Ag sample container. In this case, the Ag could have migrated and led to mixing with the fayalite or to distortion of the sample geometry. Phase diagrams of Fe_2SiO_4 and Ag are given in Figures 6.5 and 6.6 respectively and were used to place constraints on the experimental P,T conditions of experiments.

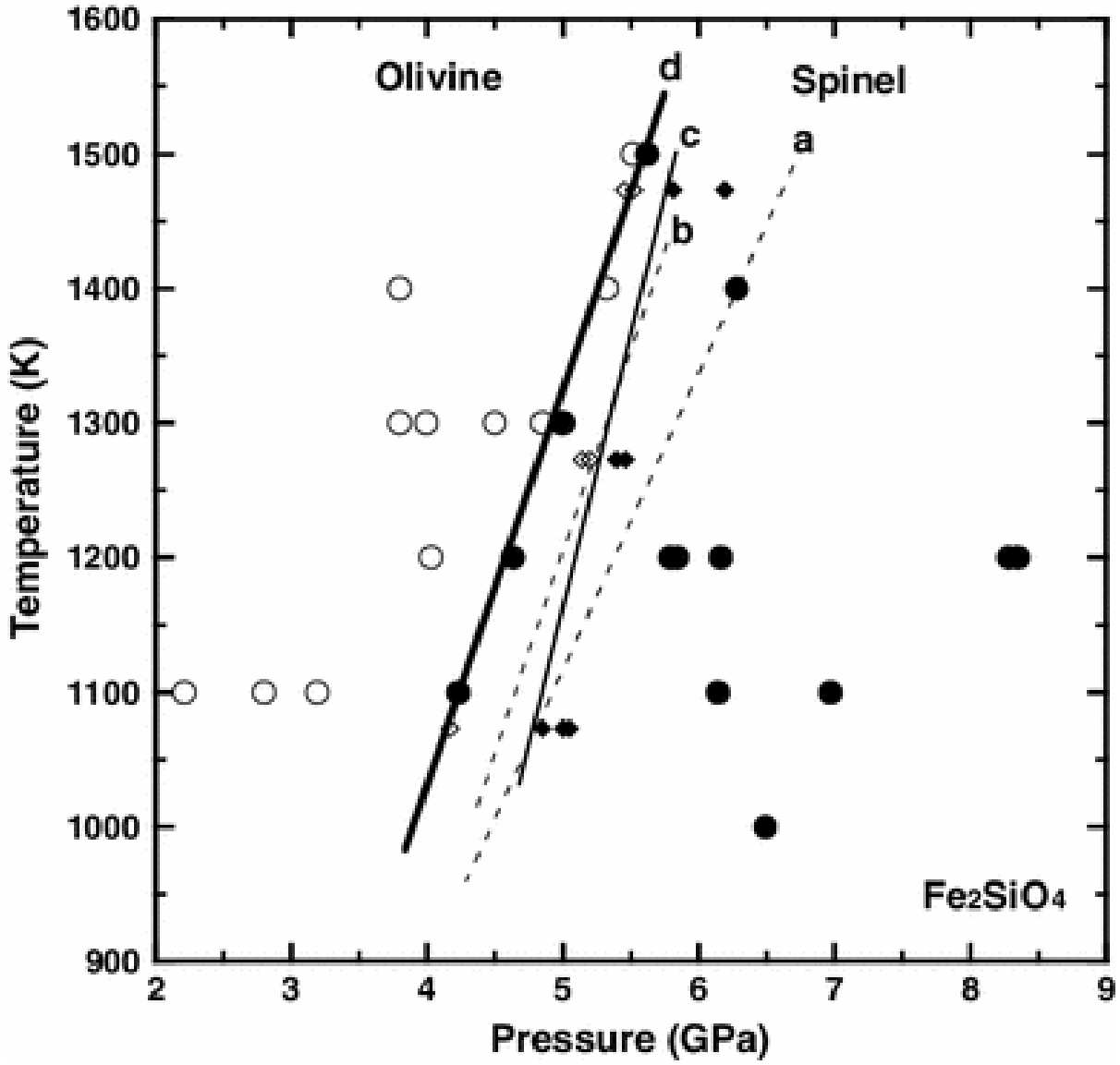

Figure 6.5: Experimental results and phase boundaries for Fe_2SiO_4 based on multiple studies. The dotted lines, **a** and **b**, are from Akimoto et al. (1965 and 1967, respectively) using a quenching method. The open and closed diamonds represent fayalite and ahrensite (spinel structure), respectively, using *in situ* X-ray diffraction technique (Yagi et al. 1987) calibrated using the equation of state of NaCl (Dorogokupets and Dewaele, 2007). The diamonds substantiate line **c**. The open and closed circles represent fayalite and ahrensite using *in situ* X-ray diffraction techniques from Ono et al. (2013) using the same EOS and determine the line **d**. Figure reproduced from Ono et al. (2013).

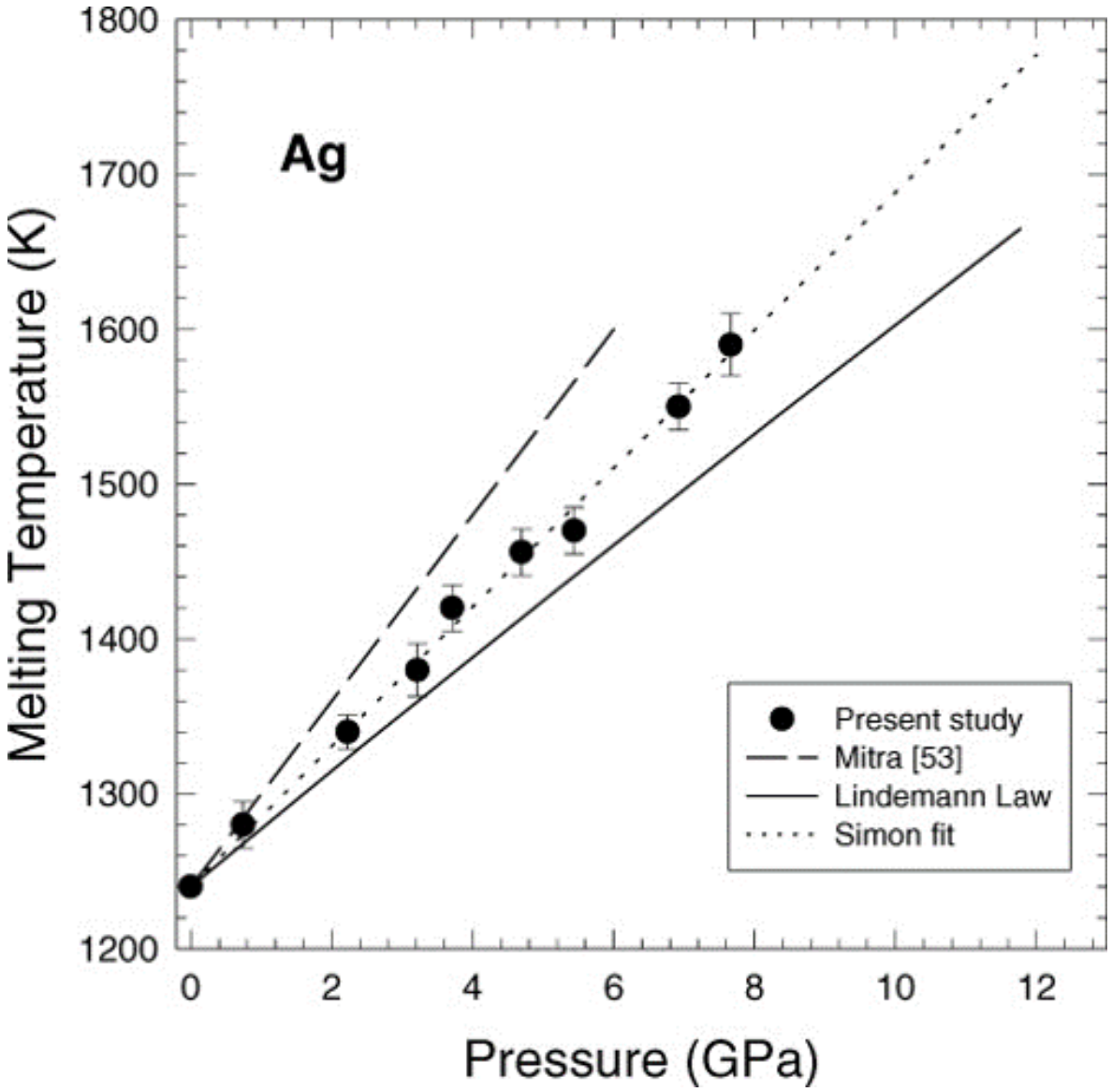

Figure 6.6: Melting temperature of Ag vs pressure. The circles represent experimentally determined melting temperatures based on resistivity measurements by Erradonia (2010). A Simon fit to the data defines the phase boundary. Melting curves are also shown based on the Lindemann law (Lindemann, 1910) and Mitra et al. (1967). Figure reproduced from Errandonea (2010).

Altogether 25 experiments were performed with different sintering parameters and procedures in order to determine the most successful P,T conditions, which were 1100 K and 2.5 to 3.2 GPa. It was also found that success rates were improved for samples that remained at HPHT for extended periods of time so most experiments were maintained at these conditions for > 18 hours. While experiments were generally begun at 1100 K and 2.5 GPa and held at constant

oil pressure, over time the pressure tended to creep higher as a result of thermal pressure generated by the counteraction of the anvils opposition to the tendency for the pressure cell to expand upon heating. This is particularly true for cells with a relatively high level of thermal insulation, which was created by the insertion of the ZrO_2 sleeve and discs surrounding the sample. Therefore, it was important to observe that the temperature, held constant to within +/- 20 K throughout the experiment, was low enough that the increase in pressure did not shift the run conditions into the ahrensite stability field. If this became the case, the temperature would need to be increased to ensure that the sample remained fayalite. Figure 6.7 shows the temperature as a function of time for seven experiments.

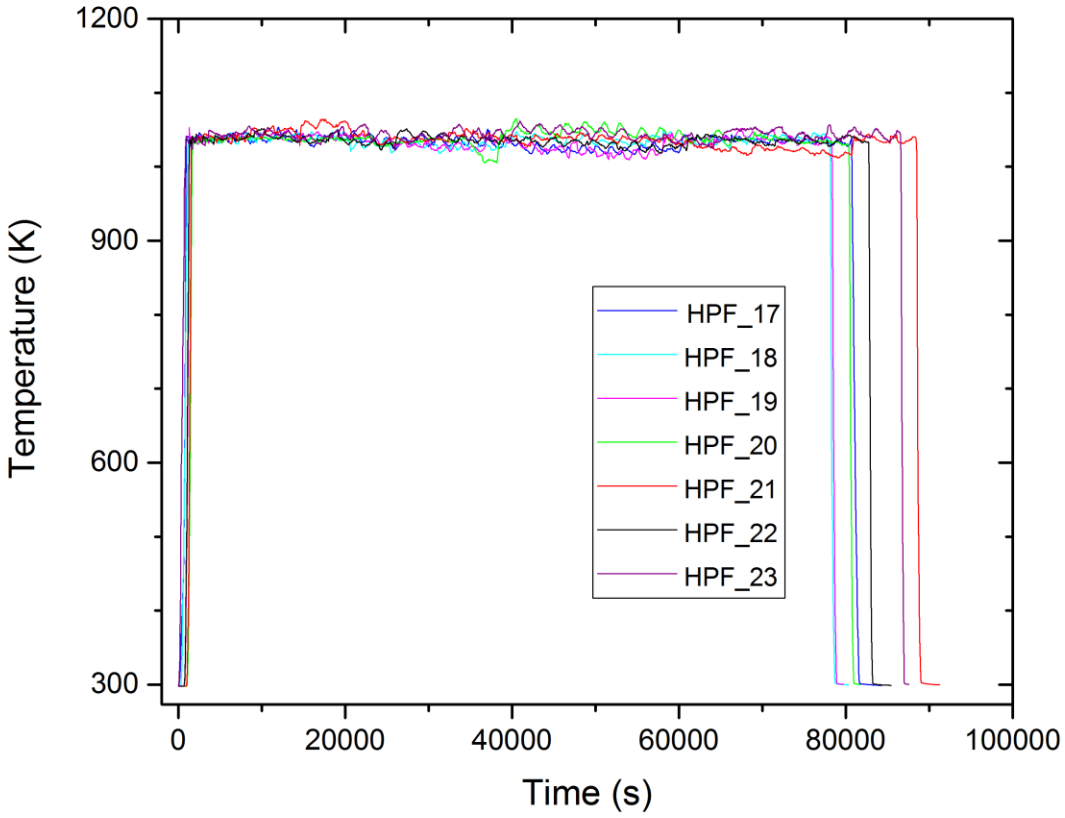

Figure 6.7: Temperature vs. time for 7 sintering experiments. The pressure was initially 2.5 GPa at the beginning of each experiment. However, after > 75000 s the pressure had elevated to ~3.2 GPa as a result of thermal pressure.

Once the sample was sintered the pressure cell had to be returned to ambient conditions and removed from the press while avoiding any possible cracks that may arise in the process. To avoid rapid contraction of the sample upon cooling, instead of quenching, the temperature was lowered at a rate of approximately 2 K/s. Far more importantly, the pressure was lowered very slowly to avoid decompression cracking which can arise when a pressurized material experiences rapid stress release. The result of pressure clamping was especially acute at low pressure. For this reason the cell was depressurized at a rate of approximately 3 MPa/min. until it reached 0.25 GPa of oil pressure. At this point, the release valve was closed to allow for the internal cell pressure to equilibrate with the oil pressure, then brought to ambient conditions over > 4 hrs.

In two experiments the pressure crept up high enough that the P,T conditions approached very near the ahrensite stability field and in one case reached 4.5 GPa and 1175 K surpassing the phase boundary defined by Ono et al. (2013), though not that of Akimoto et al. (1965 and 1967) or Yagi et al. (1987), (see Figure 6.5). However, subsequent XRD patterns of these samples, collected from the top and bottom of their samples where the temperature is expected to be lowest due to thermal gradients, displayed that the no ahrensite was created. An example of one such pattern, collected from the top of the sample that reached 4.5 GPa and 1175 K is shown in Figure 6.8. Note that the blue peaks corresponding to ahrensite do not match any of the peaks on the XRD pattern. Since these data were collected for experimental conditions further into the ahrensite stability field than any other experiment, it is reasonable to assume that ahrensite was not created during any sintering experiment.

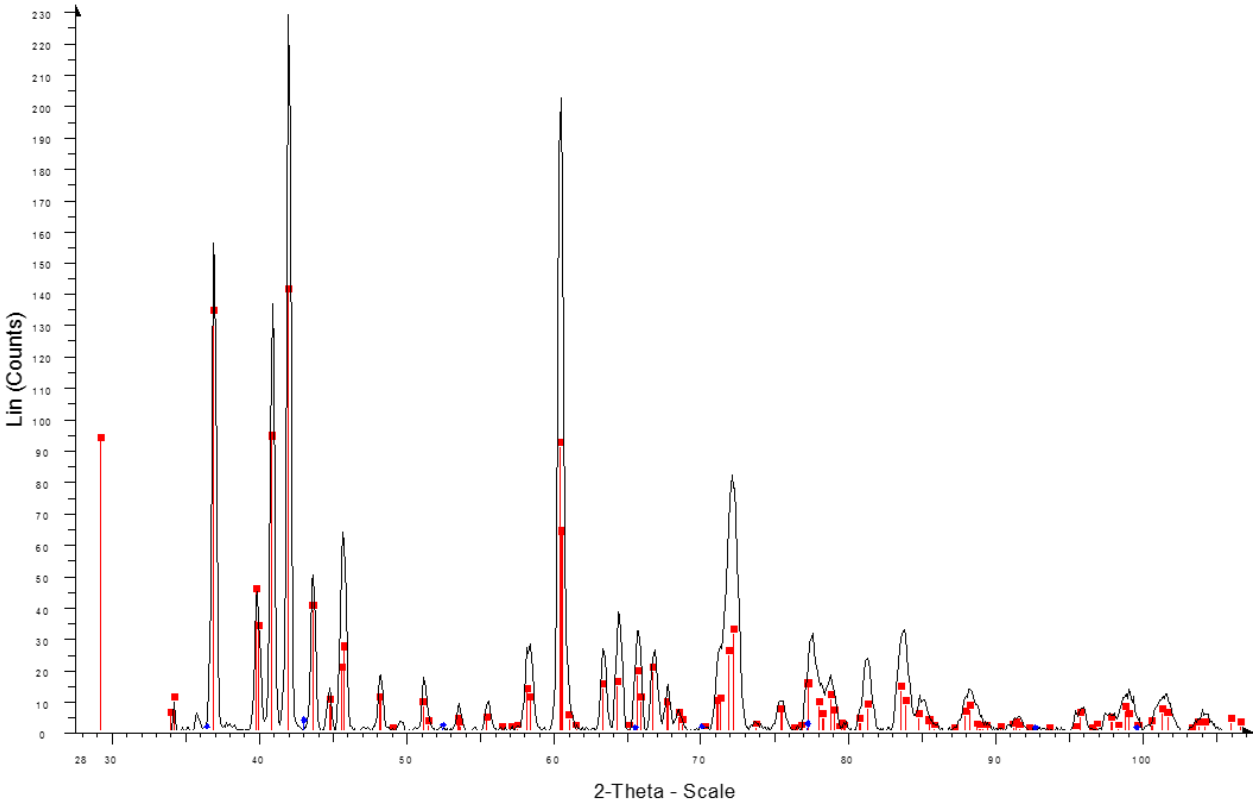

Figure 6.8: XRD pattern collected from the top of a sintered sample where the temperature is lowest due to thermal gradients. The experimental conditions at the highest pressure reached were 4.5 GPa and 1175 K, which according to the phase diagram of Fe_2SiO_4 from Ono et al. (2013), but not that of Akimoto et al. (1967 and 1968) or Yagi et al. (1987), places this sample within the ahrensite stability field. However the sample is dominated by fayalite peaks (red) and does match any of the ahrensite peaks (blue). Since this sample was collected from the experimental conditions closest to the phase boundary it is reasonable to assume that little to no ahrensite was created in any sintering experiments.

6.3.4 Removing the sintered sample

After the sample was sintered and the pressure cell was removed from the press, the sample needed to be extracted. To achieve this, first the pressure cell was broken open with a wedge (Figure 6.9a) and all the cell assembly components were discarded except the Ag sample container (containing the sintered sample) surrounded by the BN sleeve (Figure 6.9b). The BN sleeve was then removed by sanding to reveal the sample container (Figure 6.9c). Next the Ag sample container needed to be removed. This step of the sintering process had the highest potential for fracturing the sample and therefore was performed very carefully. To remove the

base and lid of the sample container a high precision Boley jeweller's lathe was used with a very sharp cutting tool (Figure 6.9d). The base of the sample container was first removed and then the lid (Figure 6.9e). To minimize the amount of tool pressure on the part several passes of the cutting tool were made at 0.05 mm intervals until the Ag was removed and the bottom (or top) of the sample could be seen (Figure 6.9f). In some instances the base and/or the lid was removed by filing. Once the base and the lid were removed the remaining sleeve of Ag surrounding the sample was mounted into a vice and cut away using a scalpel. This was the most delicate part of the sample container removal process with the highest potential of generating micro to macro scale fractures in the sample. For this reason, each pass of the blade typically removed Ag layers with a thickness of < 0.005 mm. Eventually enough Ag was removed that the sample became visible (Figure 6.9g). At this point it was important not to make direct contact between the sample and the scalpel to avoid abrasion. When enough of the Ag was removed what was remaining could be pried open using tweezers. On occasion small amounts of fayalite would remain adhered to the Ag after removal, slightly altering the cylindrical geometry of the sample. However it rarely exceeded 0.1 mm and was considered acceptable. Sintered samples were usually slightly longer than 5 mm along their cylindrical axes after removal from the Ag, but could be polished down to 5 +/- 0.05 mm. The diameter was repeatable to 3 +/- 0.1 mm (Figure 6.9h).

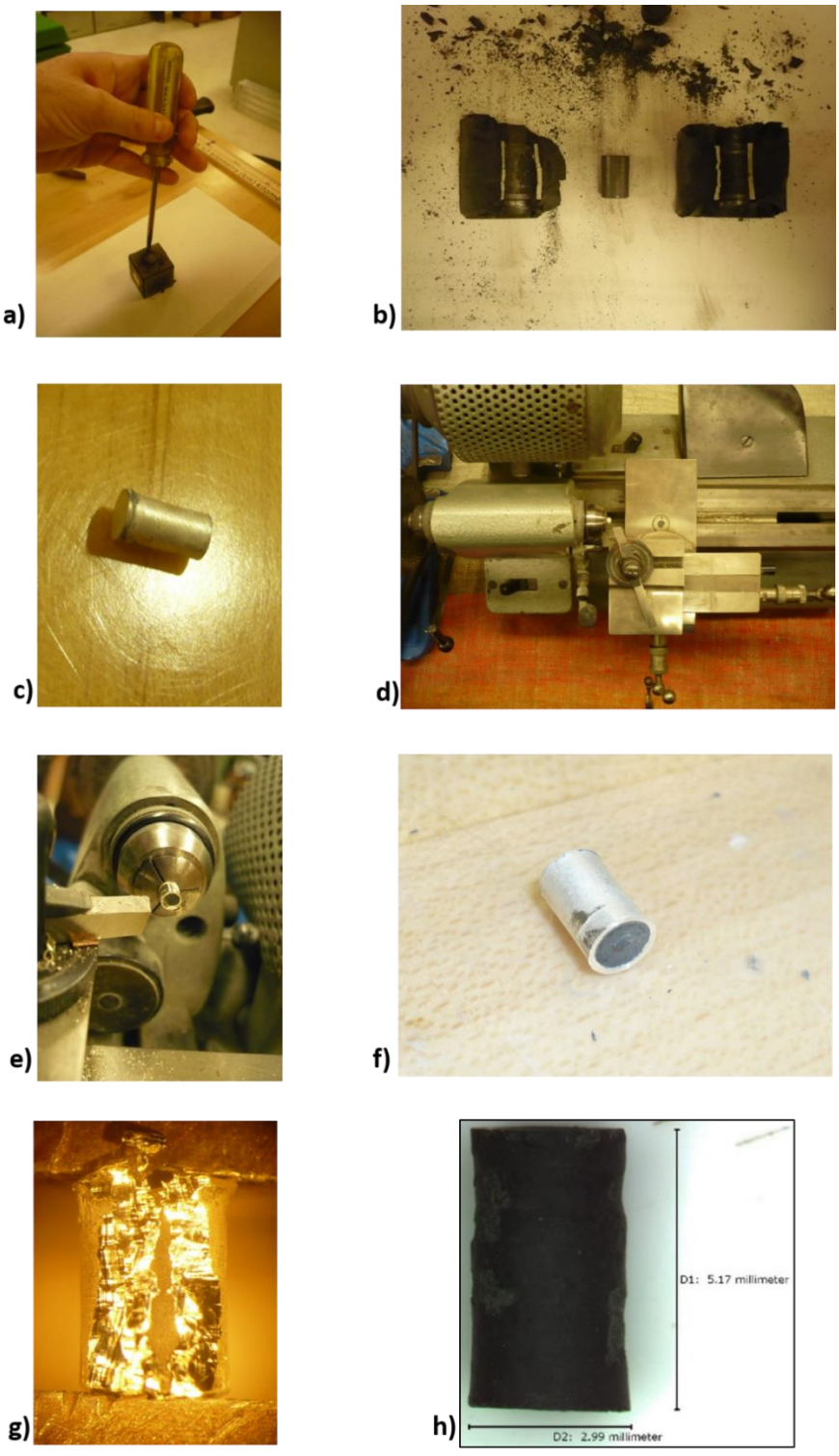

Figure 6.9: The removal process of a sintered sample from the high pressure cell. a) The use of a wedge to break open the high pressure medium. b) The BN material surrounding the sample container and the sample after extraction from the pressure cell. c) The Ag sample container after the BN has been removed. d) The Boley lathe with the sample container mounted in the chuck. e) Removal of the sample container lid using the Boley lathe. f) The sample container with the lid and base removed. g) Removal of the Ag from the sample container to reveal the sample. h) A sintered sample for use in HPHT AE experiments.

Figure 6.10 shows an SEM image of a mirror polished sintered sample. A small percentage (<5 %) of randomly distributed ferrosilite ($FeSiO_3$) appears as dark grey material in this and other SEM images. It is likely this was created during the sintering process since it does not appear in the XRD pattern of the starting material, however the bulk of the sintered material, shown in light grey, remained fayalite and has little very little porosity.

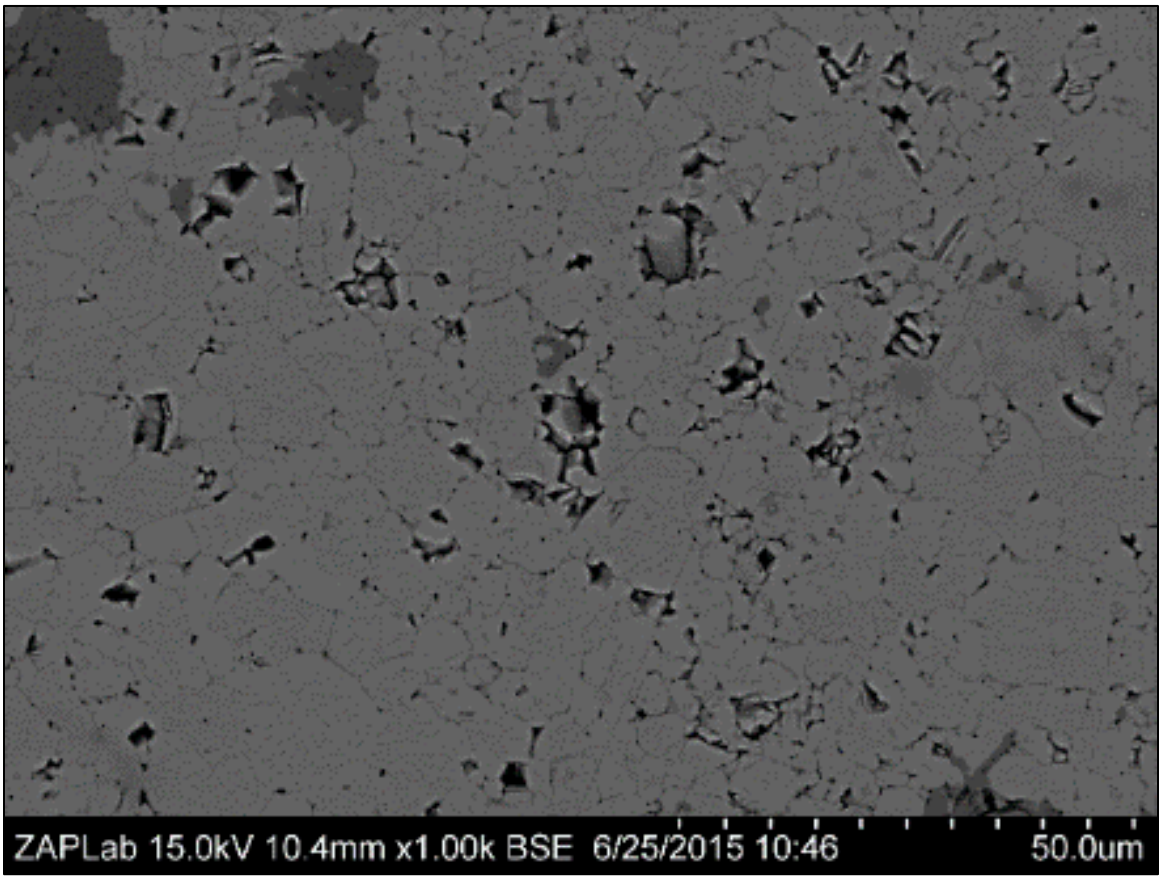

Figure 6.10: SEM image of a sintered fayalite sample. The black areas represent cavities caused by dislodging of grains during polishing. The dark grey areas are grains of ferrosilite ($FeSiO_3$), likely created during the sintering process. The rest of the grains are composed of fayalite (Fe_2SiO_4).

6.4 Coating samples with Ag using evaporation thin-film deposition

In a few cases, the bulk of the sample was well sintered but contained chips or cracks that rendered them unusable as a single monolith. In such cases the samples were mirror polished into discs 1.67 mm in thickness which could be stacked on top of one another to compose a single sample. Each disc was coated in a thin layer of Ag approximately 200 nm thick in the Nanofabrication Lab at Western University by depositing evaporated Ag in a vacuum where it condensed and adhered to the fayalite substrates. This process was performed for experiments HPF_AE_14 and HPF_AE_15. A schematic of the sample is shown in Figure 6.11.

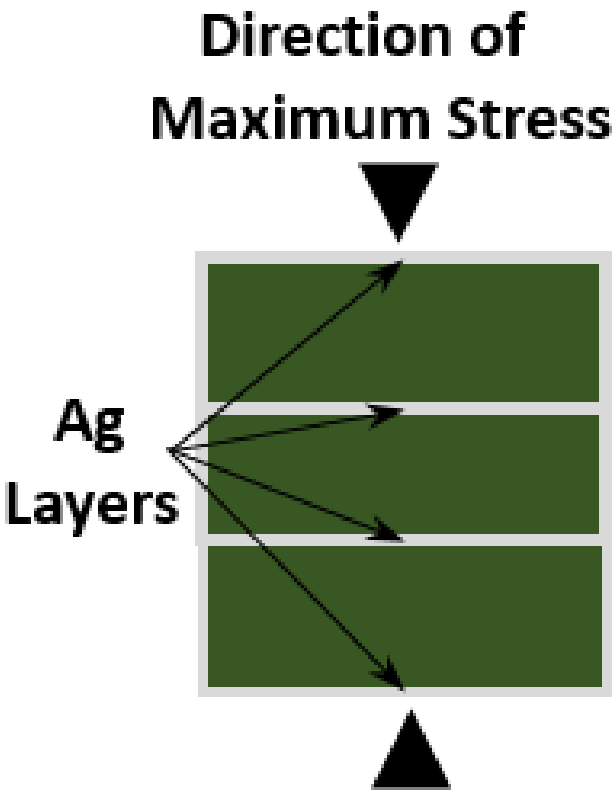

Figure 6.11: Schematic of a sample composed of three fayalite discs (green) coated in thin Ag evaporations (grey).

The purpose of the Ag was to act as a passive marker with a strong visual contrast to that of fayalite/ahrensite so it could easily be distinguished in the recovered samples. In particular, any faults crossing the Ag boundary could be readily detected and their offsets measured. Figure 6.12 shows an image of a sintered fayalite disc coated in Ag. This technique, of coating samples in thin layers of metal, has been successfully used to measure deformation (Karato and Rubie, 1997) and HPHT faulting (Dobson et al., 2004; Jung et al., 2004; Jung et al. 2006; Jung et al., 2009) using Pt and Ni markers respectively.

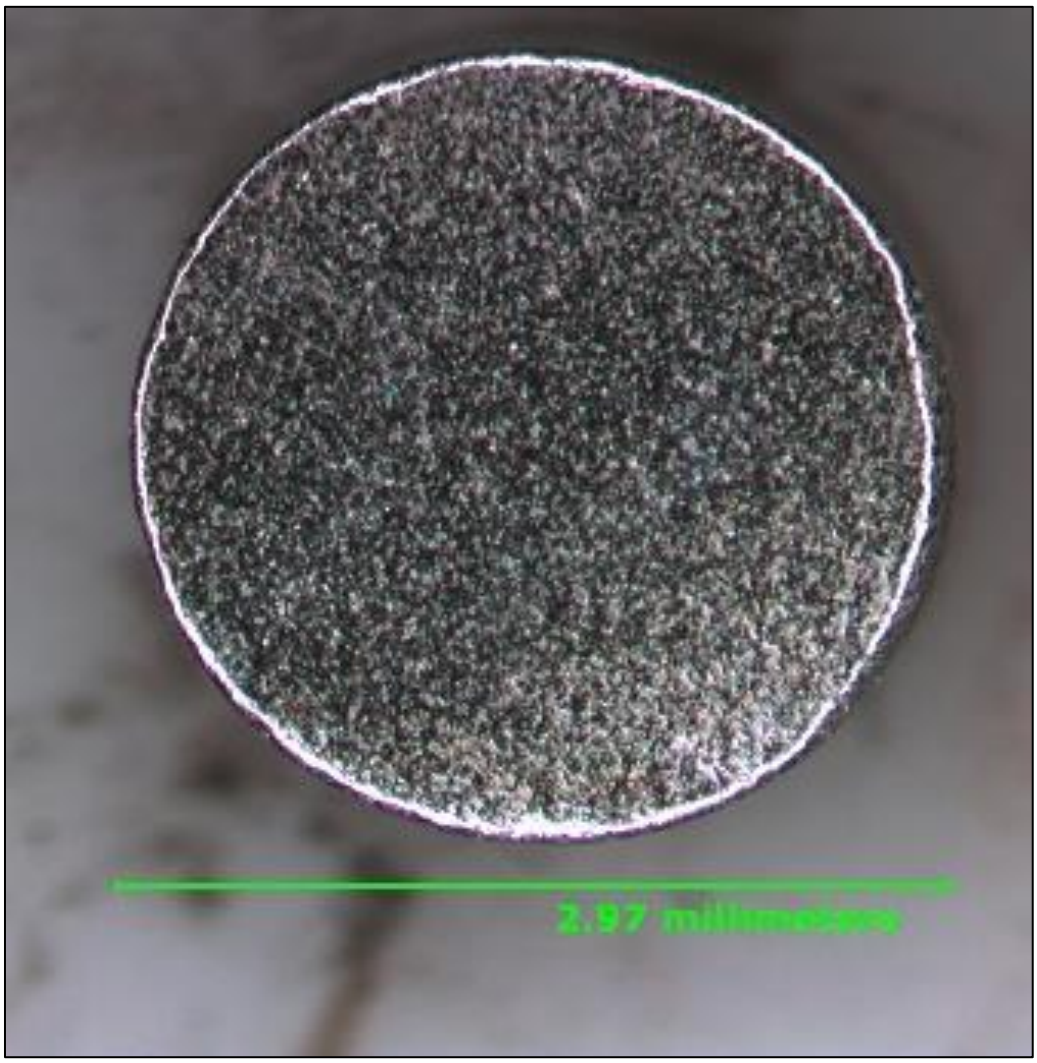

Figure 6.12: Fayalite disc coated entirely in ~200 nm of Ag. The disc is 1.67 mm thick and three such discs were stacked to create a single sample.

6.5 18/11 Cell Assembly for HPHT AE experiments

In order to perform HPHT AE experiments on fayalite, the major requirements were that the sample had to be subjected to high confining pressure, high temperature and a deviatoric component of stress that promoted sample strain while under load. The high pressure assembly was an 18/11 cell which consisted of an octahedron with 18 mm edge lengths compressed by anvils with 11 mm truncations. This configuration is capable of reaching 13 GPa and 2273 K which is well into the stability field of ahrensite. The pressure medium was composed of MgO with ~ 30% porosity for which a 3.3 mm hole was drilled though the center of one triangular face of the octahedron that traversed its entire length along one octahedral axis and exited the center of the opposing triangular face. Within this hole are placed the sample and all other experimental components. Figure 6.13 shows a cross section of the high pressure cell assembly.

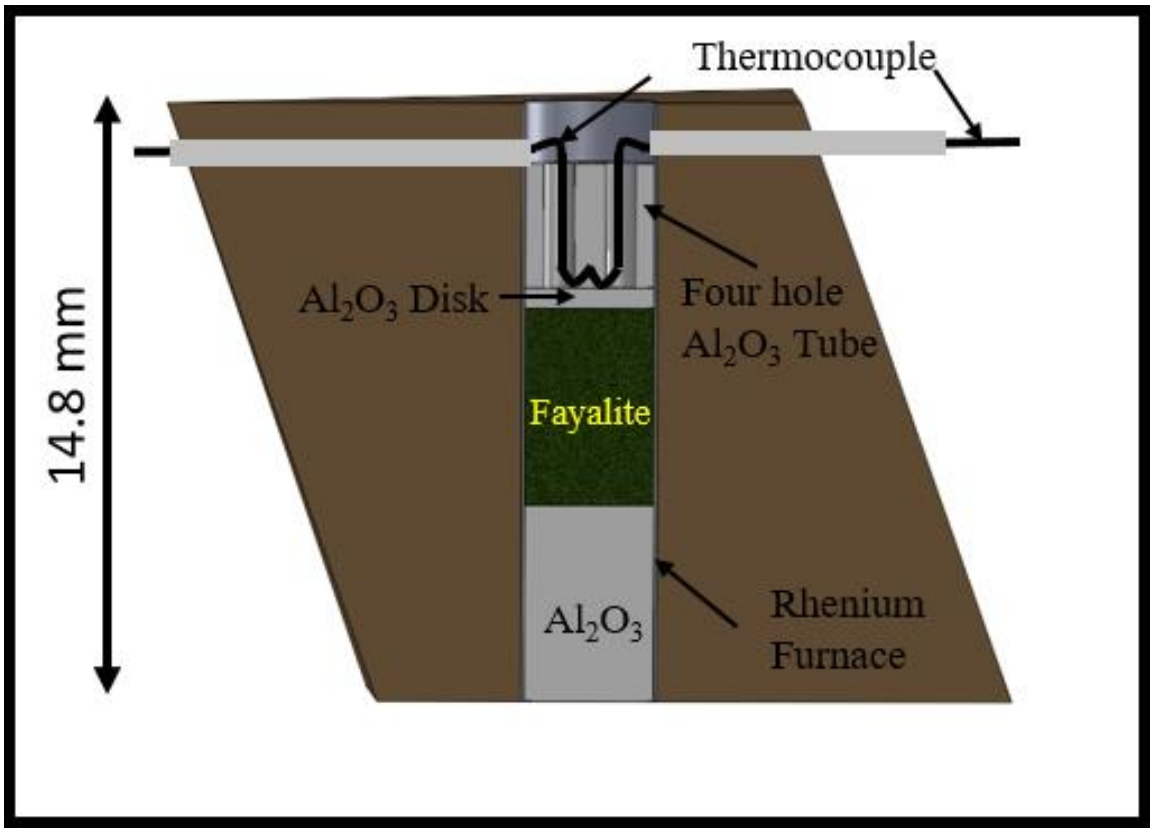

Figure 6.13: Cross section of the 18/11 octahedron with all parts labelled.

A 0.1 mm thick furnace composed of cut and rolled rhenium foil was placed in the hole and traversed the entire length of the cell axisymmetric with the hole. The cylindrical sample, whose dimensions were 3 mm in diameter by 5 mm in length, was placed at the center of the cell assembly such that its centroid was coincident with that of the octahedron. To generate faulting instabilities under load a major requirement was that the sample had to undergo strain at HPHT conditions. This was generated by placing fully dense Al_2O_3 pistons on either side of the sample which have been shown to generate deviatoric stress whose largest component is along the cylindrical axis of the sample (Dobson et al., 2002, 2004; Karato and Rubie, 1997; Jung et al., 2006, 2009). During active pressurization of the cell this translates into active strain compressing the length of the sample along the cylindrical axis and extending the width of the sample with the largest extensions occurring near the center. On one side of the sample a 3 mm diameter, 3.5 mm long fully dense Al_2O_3 piston is placed adjacent to the sample. On the other side of the sample a 0.5 mm fully dense Al_2O_3 disc is placed adjacent to the sample ensuring that the sample rested against a flat surface. Adjacent to the disc is a 3 mm long 4-hole Al_2O_3 tube that houses the thermocouple. The two wires of the thermocouple were threaded through two holes of the tube and contacted one another at the opposite end of the tubes in a cross that was inserted into the remaining two tubes. To ensure that the thermocouple wires did not come in contact with the disc and potentially crack it, a cross is bored out of the end of the 4-hole Al_2O_3 (Figure 6.14a) where the thermocouple wires come into contact (Figure 6.14b). This sets the thermocouple wires back within the tube so they do not contact the disc (Figure 6.14c). The space created from boring the material out is filled in with crushable Al_2O_3 plaster and sanded to create a flat face which contacts the side of the disc opposite the sample (Figure 6.14d).

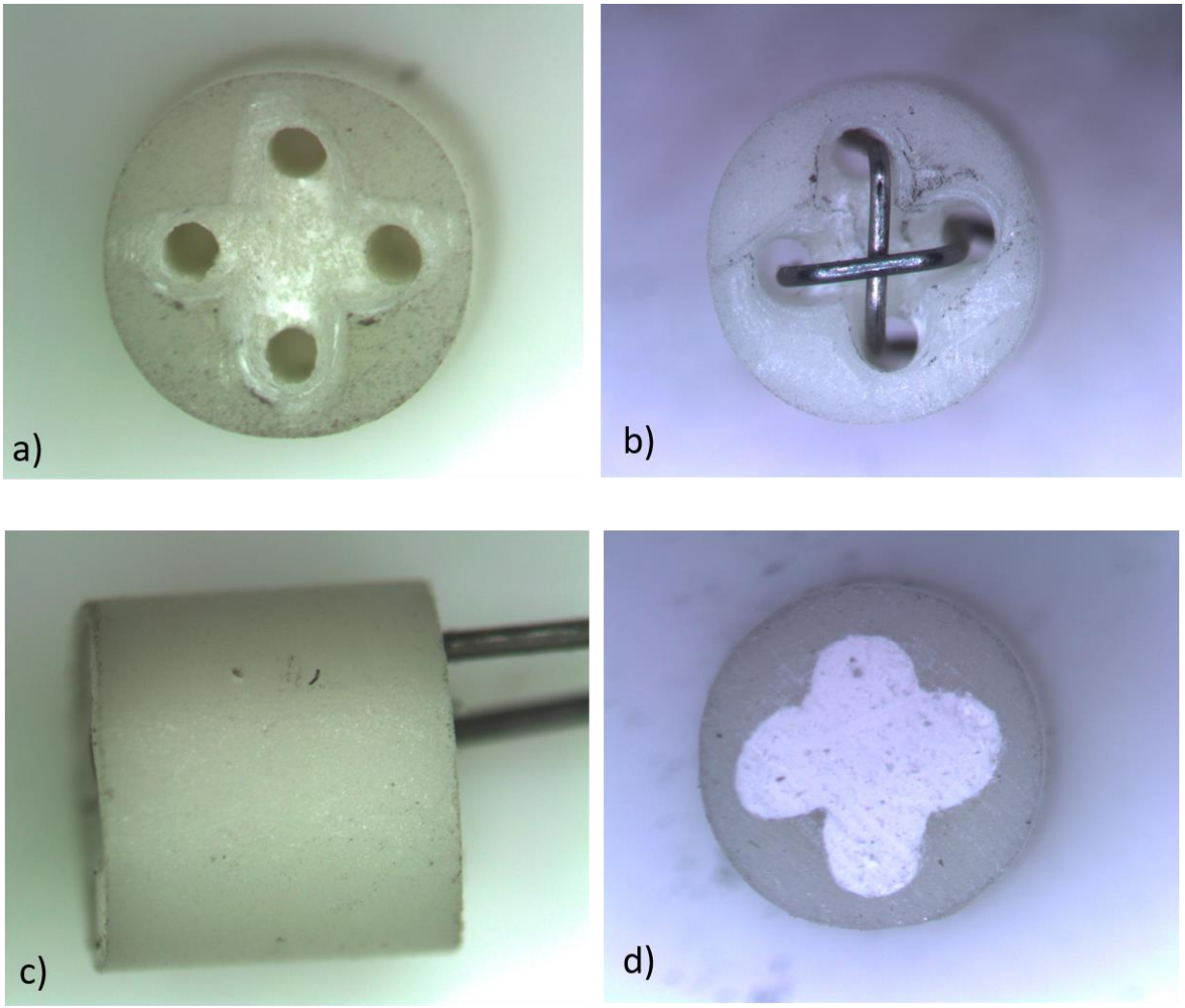

Figure 6.14: 4-hole Al_2O_3 ceramic tube containing the thermocouple. a) a cross of material is bored out of the thermocouple. b) thermocouple wires bent and inserted into the bored out cross to create contact between the $W_{97}Re_3$ and $W_{75}Re_{25}$ wires. c) the thermocouple sitting just below the upper plane of the ceramic tube. d) Al_2O_3 plaster filling the bored out cross and filed to create a flat surface for contact with the Al_2O_3 disk. The diameter Al_2O_3 tube is 3 mm in diameter.

The thermocouple exits the octahedron through an octahedral face through 0.5 mm deep galleries bored out of the octahedron that extend from the central hole to the corners of the octahedron. Within the galleries the thermocouple wires were embedded surrounded by Al_2O_3 tubes to protect them from fracturing upon compression. The wires extended outside of the press where they can be connected to a device which measures the voltage drop at the thermocouple junction and

converts it to a temperature. The galleries and the 0.5 mm space on either side of the sample assembly was filled in with crushable Al_2O_3 plaster to create flat surfaces. During compression at low pressures this material compacted removing its porosity and minimized sample deformation prior to reaching the pressure at which the experiments proper were carried out. Under high pressure, such as those where HPHT AE experiments were run, the Al_2O_3 plaster was compacted until it was fully dense and could contribute to deformation.

6.6 Thermal gradient

During a HPHT deformation experiment the temperature was monitored using a $W_{97}Re_3$-$W_{75}Re_{25}$ thermocouple adjacent to the Al_2O_3 disc and located 3.2 to 3.3 mm from the center of the sample. Due to the large thermogradient within the cell, the temperature at this position was lower than that of the center of the sample. In order to calibrate the temperature as a function of position along the cylindrical axis of the cell assembly an experiment was run to compare the temperature at the center of the sample to the temperature measured at the position of the thermocouple. This was achieved by placing two thermocouples at different positions in the cell: one at the center and the other at its usual position adjacent to the Al_2O_3 disc. The temperature was then raised from ambient to 1273 K, as measured from the thermocouple adjacent to the Al_2O_3 disc where the temperature is relatively cooler, and compared to the temperature at the center of the cell. Figure 6.15 shows the temperature difference between the thermocouple located at the position shown in the cell design of Figure 6.13 and the center of the sample as a function of temperature.

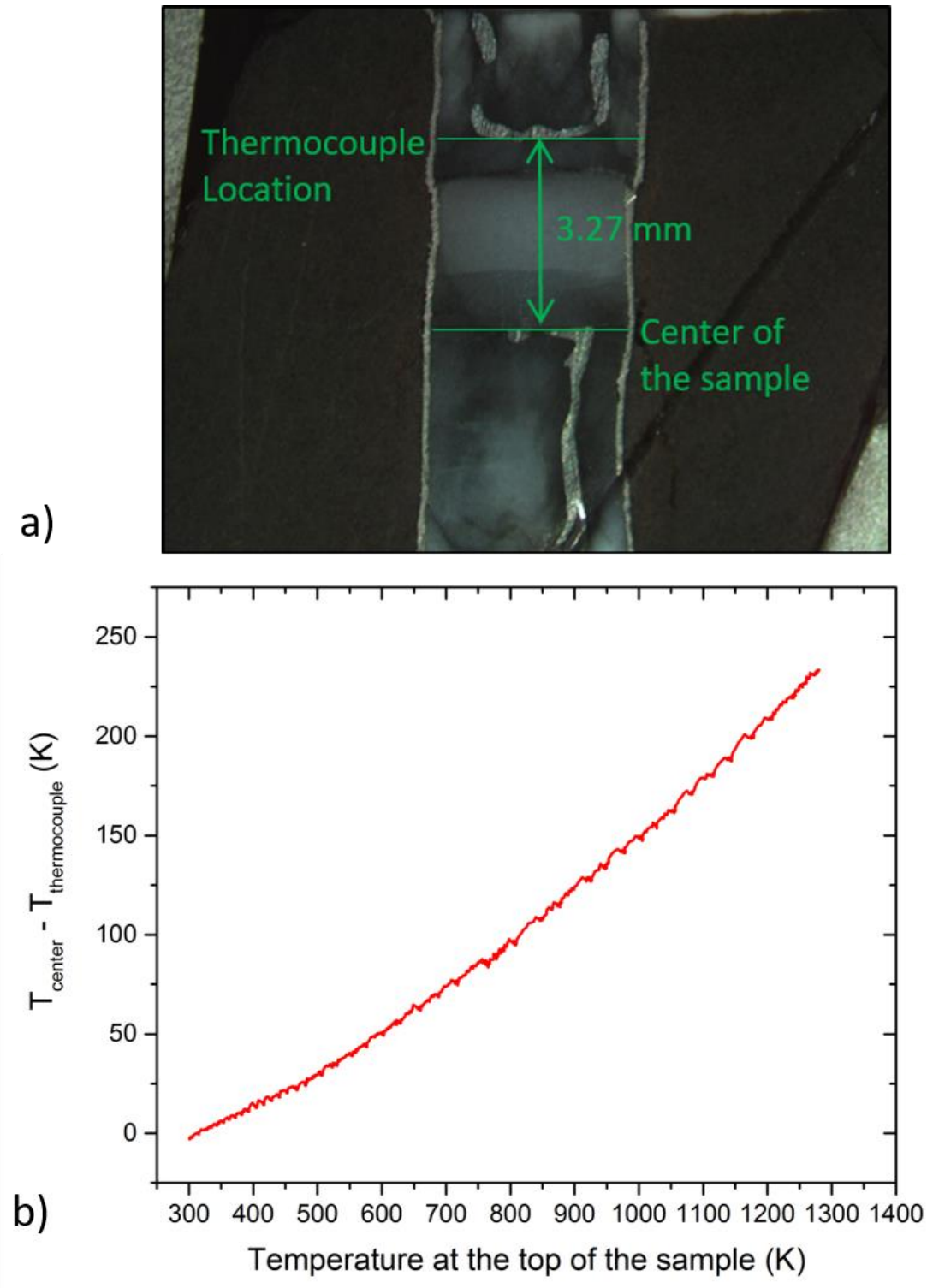

Figure 6.15: Calibration of the thermal gradient. a) A polished section of the recovered high pressure cell showing the positions of the two thermocouples used to measure the thermal gradient. “Thermocouple Location” indicates the position of the thermocouple in HPHT deformation experiments relative to the center of the cell. b) The temperature difference as a function of temperature as measured from the position where the thermocouple is placed in HPHT deformation experiments.

As temperature increased the temperature gradient also increased to an 85 K difference at 773 K to a difference of 230 K when the temperature read 1273 K. Such a large temperature variation along the cylindrical axis of the sample is expected to have an effect on the kinetics of the fayalite/ahrensite transition (Chen et al., 2001; Raterron et al., 2002). In comparison, the lateral variation in temperature is likely to be relatively small though the temperature is expected to get warmer as we move radially out from the cylindrical axis until reaching the furnace past which point the temperature begins to decrease (Leinenweber, 2012).

6.7 HPHT AE experimental Procedure

The purpose of this study was to test the hypothesis that transformational faulting is a viable mechanism for deep focus earthquakes. More specifically, this involved testing whether the analogue material Fe_2SiO_4 was capable of faulting in the HPHT ductile regime, in association with the fayalite to ahrensite transformation, and whether such an instability was seismogenic in nature. Furthermore, it aimed to determine at what conditions of pressure, temperature, strain rate and ahrensite production mechanical instabilities could develop. A total of 15 experiments were performed on sintered fayalite samples under varying conditions of pressure, temperature and strain rate, for differing amounts of time in the ahrensite stability field. These included conditions very near the kinetic boundary of the metastable transition to those of rapid transformation. Each experiment consisted of three stages: 1) cold compression to the starting pressure 2) deformation at HPHT followed by quenching and 3) depressurization at ambient temperature. In all cases the sample was actively pressurized during stage 2 to generate a component of deviatoric stress,

resulting from the presence of the Al_2O_3 pistons, along the sample axis. Acoustic activity was monitored during all three stages.

Stage 1: Cold compression

Initial pressurization from 1 atm to the pressure where the test proper could commence (between 3.8 and 5.8 GPa) was done slowly over ~70,000 s at room temperature to allow the high pressure cell to smoothly adjust and permeate any space between components. The low pressurization rate of ~3.4 MPa/min was carried out with the aim of avoiding fracturing of the sample prior to heating. During this stage of pressurization acoustic data were collected, including full waveforms of hits, so acoustic event location analysis could be carried out. In most cases both the preamp gain and the threshold was set to 40 dB. During the first ~ 0.5 to 1 GPa of pressurization, when cell compaction and gasket formation are most intense, the rotary pump was used. This was necessary since the syringe pump does not have enough travel in the syringes to reach high pressure if gasket formation iss included in a pumping cycle. Above this pressure, when gasket formation was well underway, the rotary pump was turned off and the syringe pump was initiated which provided a slower, smoother pumping rate.

Stage 2: The test proper

The second stage of pressurization was carried out with a much higher pressurization rate and accompanied by heating. Initially the pressure was increased incrementally until the final run temperature of the experiment was reached. This was to avoid any large acoustic events originating in the gaskets or pressure medium associated with jerks to the system caused by rapid increases in the pressurization rate. Reaching the final run temperature typically took around 100 to 200 s depending on the final temperature reached. Controlling the pressurization rate is important since,

in combination with temperature, controls the strain rate of the sample. However, while high strain rates promote faulting the experiment must last long enough for the growth of ahrensite to occur. The phase transformation to ahrensite is a kinetically controlled process dependent upon temperature, over-pressurization and time. Using the germanate olivine (Mg_2GeO_4) as a guide it was expected that faulting would occur when small amounts of spinel were present (Green and Burnley, 1989; Schubnel et al., 2013). Experiments fit into two main categories of pressurization rate which were determined by the type of pump used. When the pumping rate is run at its maximum of 1800 rpm, the rotary pump can achieve a maximum pressurization rate of $6.7x10^{-3}$ GPa/s compared to $2.0x10^{-3}$ GPa/s for the syringe pump. For experiments pressurized from 4 to 9 GPa, this translates to a minimum duration 745 s or 2500 s respectively.

Figure 6.16 shows the P,T paths taken during deformation of all 15 experiments superimposed on the Fe_2SiO_4 phase diagram showing the phase boundary from Ono et al. (2013).

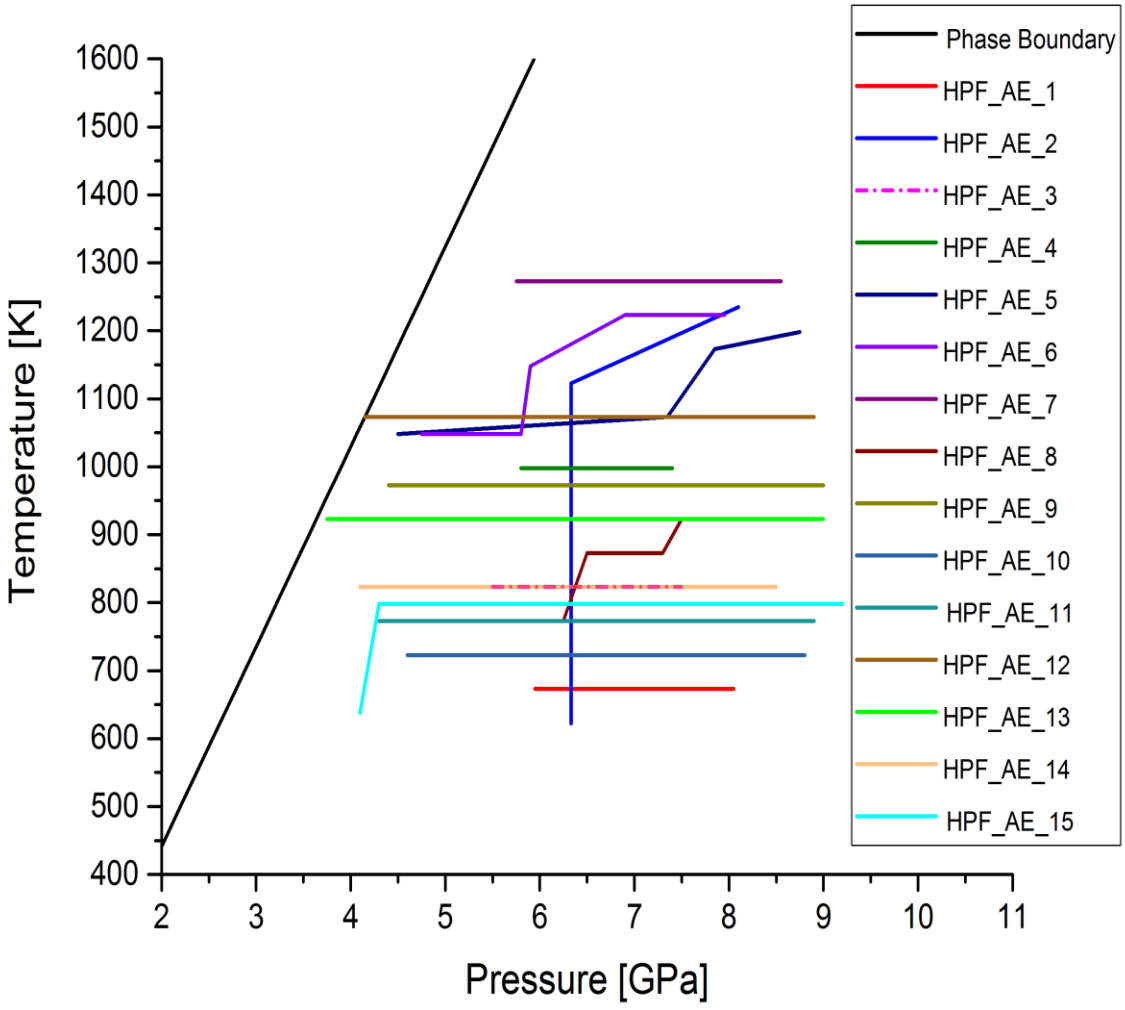

6.16: P,T paths for all 15 HPHT deformation experiments on fayalite showing the phase boundary between fayalite and ahrensite from Ono et al., (2013). HPF_AE_3 is the pink dashed line overlying HPF_AE_14 shown in peach.

Stage 3: Decompression

Depressurization was carried out slowly over the course of > 40,000 s to avoid depressurization fractures forming in the sample. This process is particularly prominent at low pressures where the rapid release of pressure clamping is strongly manifested. Therefore, the final 1 GPa of depressurization was carried out exceptionally slowly to minimize this effect. Acoustic

data were collected including full waveforms of hits during depressurization for every experiment. In most cases both the preamp gain and the threshold were set to 40 dB.

6.8 Conclusions

A process has been developed to fabricate sintered fayalite samples for use in HPHT AE experiments to test the hypothesis that transformational faulting is responsible for deep focus earthquakes. They are produced under HPHT conditions in a 1000 ton press using fayalite powder encased in a Ag sample container contained within a pyrophyllite pressure medium. They are hot pressed in the fayalite stability field and the recovered samples contain >95% fayalite, with small amounts of ferrosilite and no ahrensite. SEM analysis of grains reveal no preferred crystal orientation, are approximately uniform in size and contain very low porosity allowing for faulting to traverse multiple grains and propagate acoustic signals through the sample. Each sample is 3 mm in diameter and > 5 mm in length and can be filed down to 5 mm to produce uniformly sized samples with a very high degree of repeatability. Samples were placed at the center of an 18/11 octahedral cell with Al_2O_3 pistons positioned on either side of the sample to generate an elevated component of deviatoric stress along the sample cylindrical axis. At low pressure the system generates a large amount of acoustic noise due to porosity loss in the pressure medium and formation of the gaskets but settles to tolerable level above ~ 1.5 GPa. A total of 15 experiments was run on pre-sintered fayalite samples to test the hypothesis that deep focus earthquakes result from transformational faulting due to the transition of olivine to spinel structure. In order to achieve this, each sample was rapidly pressurized at HPHT to introduce active strain under varying

conditions of pressure, temperature and strain rate at metastable conditions in the ahrensite stability field. Results of these experiments are given in chapter 7.

6.9 References

Aki, K. and Richards, P.G., 1980. *Quantitative Seismology: Theory and Methods*, W.H. Freeman, San Francisco, USA.

Akimoto S, Fujisawa H, Katsura T, 1965. The olivine–spinel transition in Fe_2SiO_4 and Ni_2SiO_4. *J. Geophys. Res.*, **70**, 1969–1977.

Akimoto S, Komada E, Kushiro I, 1967. Effect of pressure on the melting of olivine and spinel polymorph of Fe2SiO4, *J. Phys. Res.* **72**, 679–686.

Bridgman, P.W., 1938. The resistance of nineteen metals to 30,000 kg/cm3, *Proc. Am. Acad. Arts. Sci.*, **72**, 157–205.

Chen, J., Weidner, D.J., Parsie, J.B., Vaughn, M.T. and Raterron, 2001. Observation of cation reordering during the olivine-spinel transition in fayalite by *in situ* synchrotron X-ray diffraction at high pressure and temperature, *Phys. Rev. Lett.*, **86**, 4072-4075.

Dobson, D.P., Meredith, P.G. and Boon, S.A., 2002. Simulation of subduction zone seismicity by dehydration of serpentine, *Science*, **298**, 1407-1410.

Dobson, D.P., Meredith, P.G. and Boon, S.A., 2004. Detection and analysis of microseismicity in multi anvil experiments. *Phys. Earth Planet In.*, **143-144**, 337-346.

Dorogokupets P.I., Dewaele A., 2007. Equations of state of MgO, Au, Pt, NaCl-B1, and NaCl-B2: internally consistent high-temperature pressure scales, *High. Press. Res.*, **27**, 431–446.

Errandonea, D., 2010. The melting curve of ten metals up to 12 GPa and 1600 K, *J. Appl. Phys.*, **108**, 033517.

Jung, H., Green, H.W., 2004. Intermediate depth earthquake faulting by dehydration embrittlement with negative volume change, *Nature*, **428**, 545-549.

Jung, H., Fei, Y., Silver, P.G. and Green, H.W., 2006. System for detecting acoustic emissions in multianvil experiments: Application to deep seismicity in the Earth, *Rev. Sci. Instrum.*, **77**, 014501.

Jung, H., Fei, Y., Silver, P.G. and Green, H.W., 2009. Frictional sliding in serpentine at very high pressure, *Earth Planet Sci. Lett.*, **277**, 273-279.

Karato, S.-I. and Rubie, D.C., 1997. Toward an experimental study of deep mantle rheology: A new multianvil sample assembly for deformation studies under high pressures and temperatures, *J. Geophys. Res.*, **102**, 20111-20122.

Leinenweber, K.D, Tyburczy, J.A., Sharp, T.G., Soignard, E., Diedrich, T., Petuskey, W.B., Wang, Y. and Mosenfelder, J.L., 2012. Cell assemblies for reproducible multi-anvil experiments (the COMPRES assemblies), *Am. Mineral.*, **97**, 353-368.

Lindemann, F.A., 1910. The calculation of molecular vibration frequencies, *Z. Phys.*, **11**, 609-612.

Mitra, R., Decker, D.L. and Vanfleet, H.B., 1967. Melting curves of copper, silver, gold and platinum, *Phys. Rev.*, **161**, 613.

Officer, T. and Secco, R.A., 2015. Detection of a P-induced liquid ⇌ solid phase-transformation using multiple acoustic transducers in a multi-anvil apparatus, *High. Press. Res.*, **35**, 289–299.

Ono, S., Kikegawa, T. and Higo, Y., 2013. In situ observation of a phase transition in Fe_2SiO_4 at high pressure and high temperature, *Phys. Chem. Minerals*, **40**, 811-816.

Raterron, P., Chen, J. and Weidner, D.J., 2002. A process for low-temperature olivine-spinel transition under quasi-hydrostatic stress, *Geophys. Res. Lett.*, **29**, 36.

Shearer, P.M., 1999. *Introduction to Seismology*, Cambridge University Press, Cambridge, UK.

Schubnel, A., Brunet, B., Hilairet, N., Gasc, J., Wang, Y. and Green, H.W., 2013. Deep-focus earthquake analogs recorded at high pressure and temperature in the laboratory, *Nature*, **341**, 1377-1380.

Yagi, T., Akaogi, M., Shimomura, S., Suzuki, T., Akimoto, S.-I., 1987. In situ observation of the olivine-spinel phase transformation in Fe_2SiO_4 using synchrotron radiation, *J. Geophys. Res.*, **92**, 6207-6213.

Chapter 7: Results and Discussion

7.1 Introduction

A total of 15 experiments were run on sintered fayalite samples in the ahrensite stability field in an attempt to initiate mechanical instabilities in the nominally ductile regime. In all cases samples were actively pressurized under deviatoric stress conditions to induce deformation. Acoustic activity was monitored throughout each experiment including cold compression, the test proper and depressurization. Post-mortem analysis *via* Raman spectroscopy was carried out to delineate the phase assemblages in the recovered samples, and optical and scanning electron microscopy (SEM) was used to investigate textures and macro/microstructures indicative of faulting.

Conclusive evidence that the phase transition is associated with the rupture process should include:

- The presence of the ahresite in the recovered samples. In order to be confident the phase change is linked to the faulting process it is essential that we witness evidence the phase change occurred within the fault zone.

- The occurrence of faulting and microstructures associated with the transformation to ahrensite.

- Acoustic emissions (AE) that accompany the transformation and originate within the sample based on location inversion of arrival times. While it is not possible to determine the exact moment the phase change occurs *in situ*, acoustic emissions appearing while

the sample is in the ahrensite stability field and beyond the brittle/ductile transition would suggest that the acoustic signal is linked to transformational faulting.

7.2 P,T path and associated acoustic activity during pressurization, HPHT deformation, and depressurization

Each experiment consisted of three stages: pressurization, deformation at HPHT in the ahrensite stability field, and depressurization. The acoustic activity associated with each stage displays distinct characteristics that reflect the pressure, temperature, (de)pressurization rate and hysteresis of the pressure cell and gaskets. While the specific details of each experiment will influence acoustic behaviour, a representative description of each stage, given below, satisfactorily pertains to all experiments unless otherwise stated.

7.2.1 *Stage 1: Pressurization at ambient temperature*

The initial 1 atm to 1 GPa stage of pressurization was acoustically noisy due to frictional slipping associated with the compaction of the MgO pressure cell and formation of the gaskets. This was particularly true for the first 0.5 GPa of pressurization when the rotary pump was used, which is far more mechanically noisy than the syringe pump. During this stage > 10,000 hits/min. and several hundred events/min. was typical but exponentially decreased as the compaction of the cell neared completion and the gaskets were close to fully formed. At this point the rotary pump was deactivated and the syringe pump was initialized. This provided a slower, smoother pumping rate and resulted in a dramatic drop in the amount of acoustic activity to < 1000 hits/min. As pressurization persisted, the hit rate continued to exponentially decrease until reaching a

background rate of ~ 1 hit/sec and a few tens of events/min. around 1.5 GPa. This background hit rate remained stable, even if the pressurization rate doubled, until it reached the pressure at which heating could commence. At this point pressurization was stopped and the pressure cell and gaskets were left to sit for several minutes to adjust until the background hit rate settled to zero. Figure 7.1 shows the hit rate, event rate and pressure as a function of time for a typical experiment.

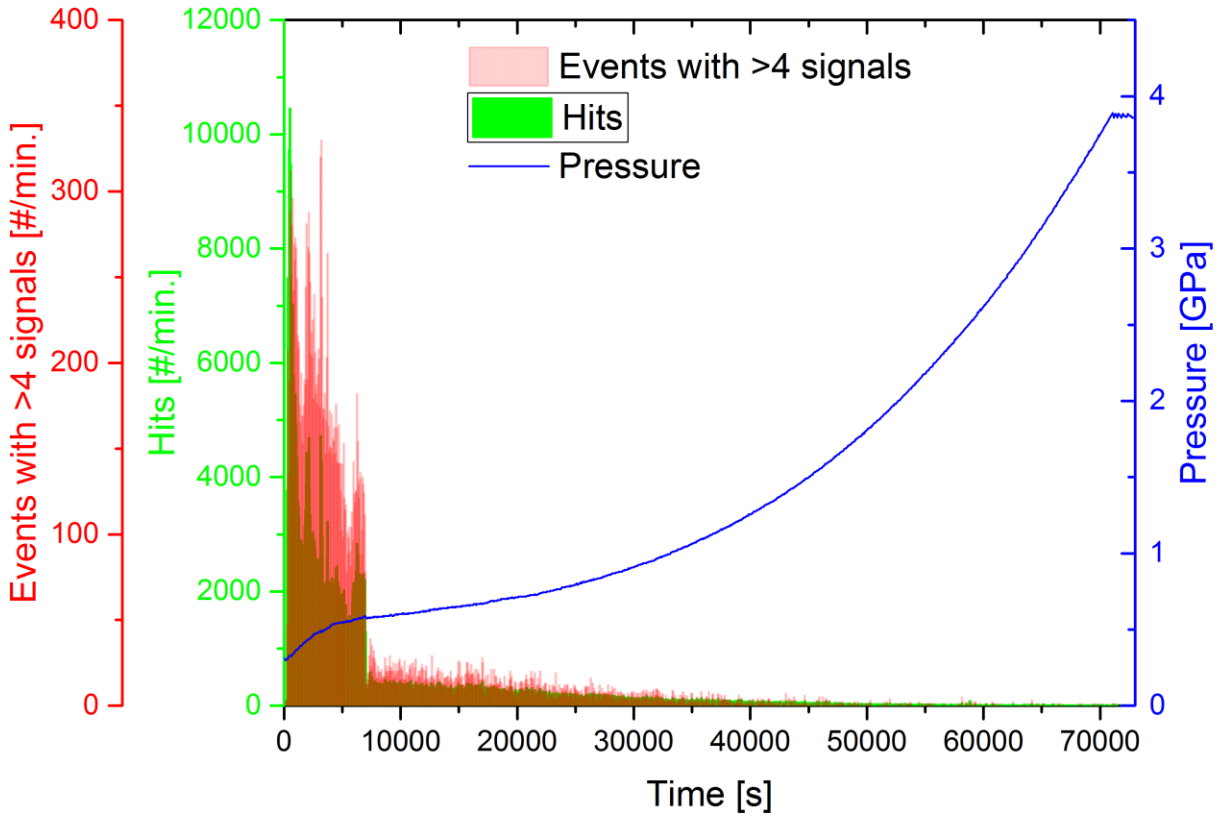

Figure 7.1: Acoustic activity including the hit and event rate plotted alongside pressure as function of time for a typical experiment. Hits/min., shown in green, appear brown when they overlap with events/min. shown in pink.

7.2.2 Stage 2: The test proper

Experiments to initiate transformational faulting were run with high pressurization rates, which translated to high strain rates, at elevated temperature in the ahrensite stability field. As mentioned in the experimental methods section the pressurization rate was increased incrementally during heating to minimize large jerks to the system associated with rapid acceleration. The level of acoustic activity roughly coincided with the degree of pumping and slowly rose alongside the rpm of the pump motor. In most cases the pressurization rate briefly appeared to level off while the temperature increased from ~473 K to 573 K due to softening of the pressure medium. However pumping was maintained and appeared to have little effect on the level of acoustic activity. Therefore, it is possible that active strain of the sample continued under these conditions even though the oil pressure plateaued. Reaching the final run temperature typically lasted approximately 200 s to 300 s and coincided with a relatively rapid increase in the final pressurization rate. As this point the level of acoustic activity began to increase with a much higher ratio of hits to events indicating a high level of low energy signals. The total amount of acoustic activity recorded depended on pre-amplification, the pressurization rate and threshold value, and could differ by approximately an order of magnitude between end member conditions. Figure 7.2 shows the pressure, temperature and, acoustic hit and event rates for an experiment run with a relatively high pre-amplification, rapid pressurization rate and low amplitude threshold (see Table 7.1). As such, it represents one of the highest levels of acoustic activity observed. The histogram of events is broken down into events comprised of 4,5 and 6 hits superimposed over top of the total number of events recorded.

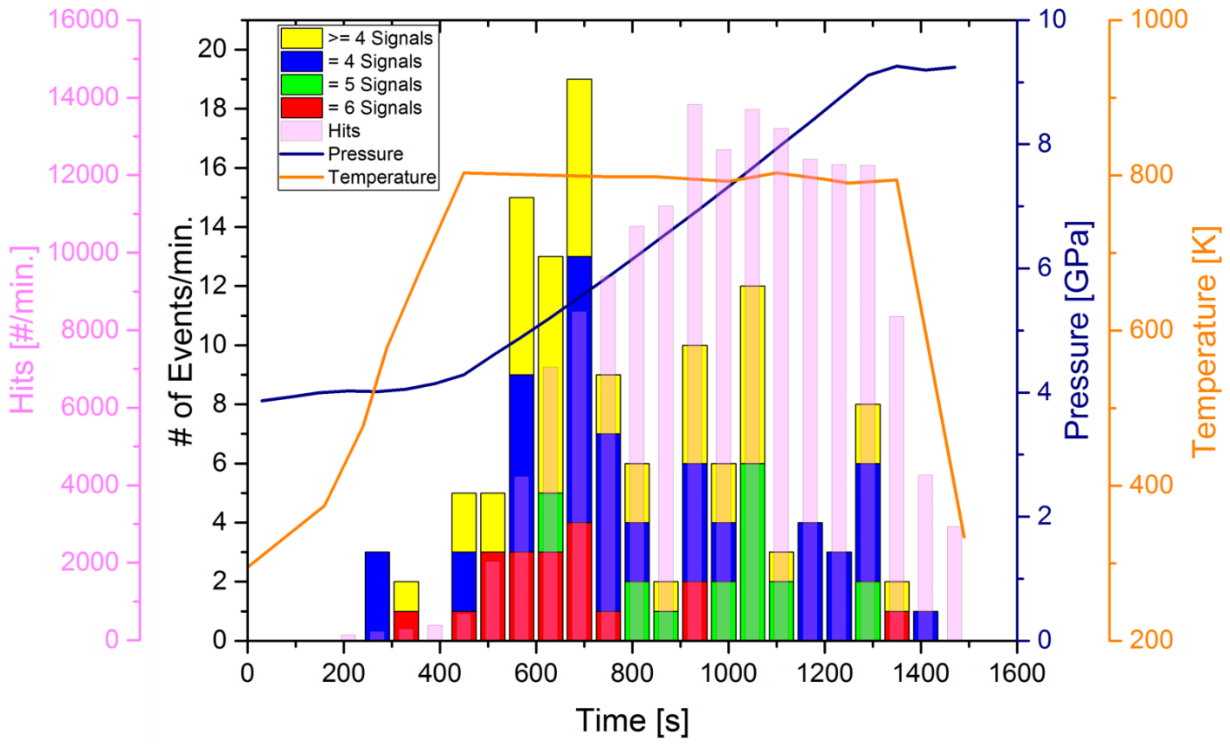

Figure 7.2: Pressure, temperature, and acoustic hit and event rates for HPF_AE_15 which was carried out with a relatively high pre-amplification, rapid pressurization rate and a low threshold. It represents end member conditions for generating and recording the largest numbers of hits and events. The opposite end member conditions with relatively low pre-amplification, low pressurization rates and high thresholds typically recorded more than an order of magnitude fewer hits and events.

7.2.3 Stage 3: Depressurization

Depressurization was done slowly over the course of >40,000 s to avoid depressurization fractures from forming in the sample. In particular, this process was particularly prominent at low pressures where the rapid release of pressure clamping is most strongly manifested. Therefore the final GPa of depressurization is done especially slowly to minimize this effect. However, even at very low depressurization rates the amount of acoustic activity increases in both hit and event rate, and contained several high energy events. It is unlikely that this effect can be completely removed unless depressurization occurred over several days, however depressurization cracks tend to orient

perpendicular to the long axis of the sample and can be distinguished from faulting due to brittle processes that tend to orient at angles of 30^0 to 50^0 to the long axis of the sample (Burnley et al., 1991). Figure 7.3 shows the pressure, and acoustic hit and event rates as a function of time for a typical depressurization cycle. Initial depressurization from 9 to 4 GPa is relatively quiet even though the depressurization rate is relatively high. Below this pressure acoustic activity began to increase as a large amount of elastic strain energy stored in the sample and pressure medium was released.

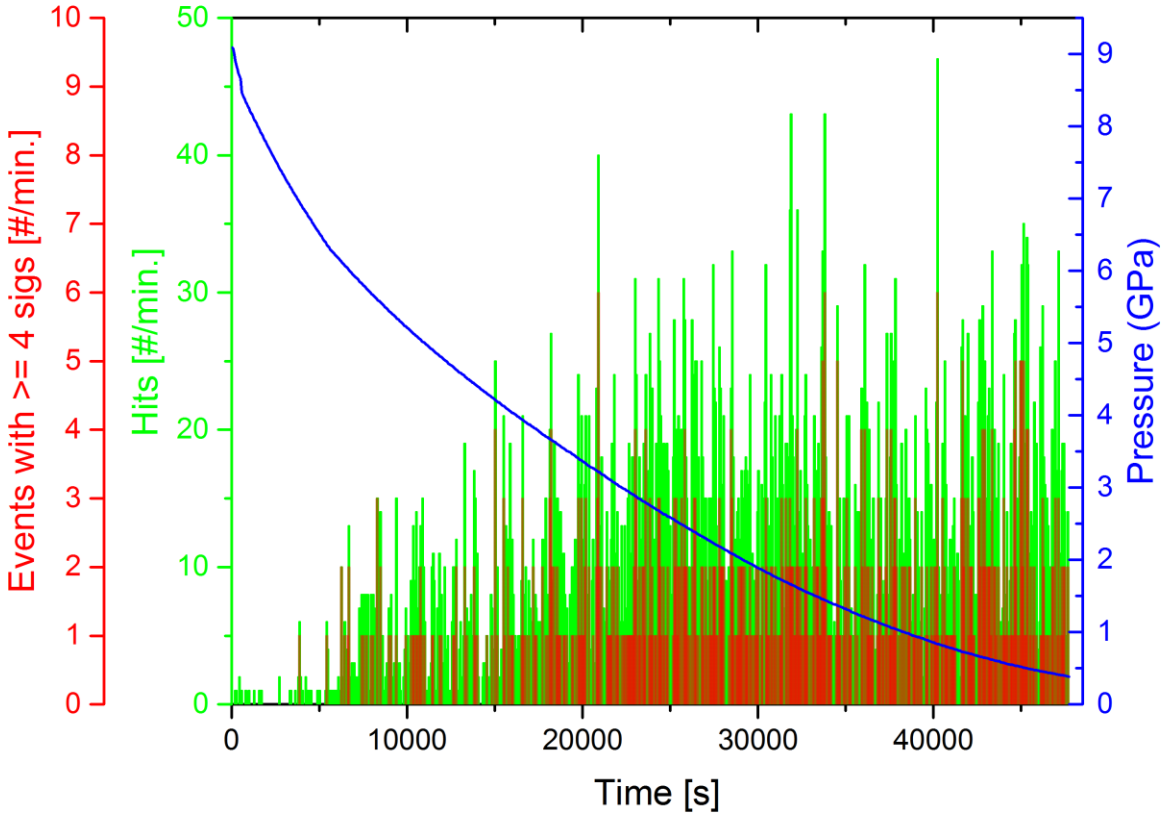

Figure 7.3: Depressurization from 9 GPa to an room temperature and ambient conditions. As pressure decreased the hit and event rates began to increase as elastic strain energy was released. Several of the events recorded at low pressure possessed very high energies.

Figure 7.4 shows the hit rate, event rate and pressurization path as a function of time for the entire duration of a typical experiment.

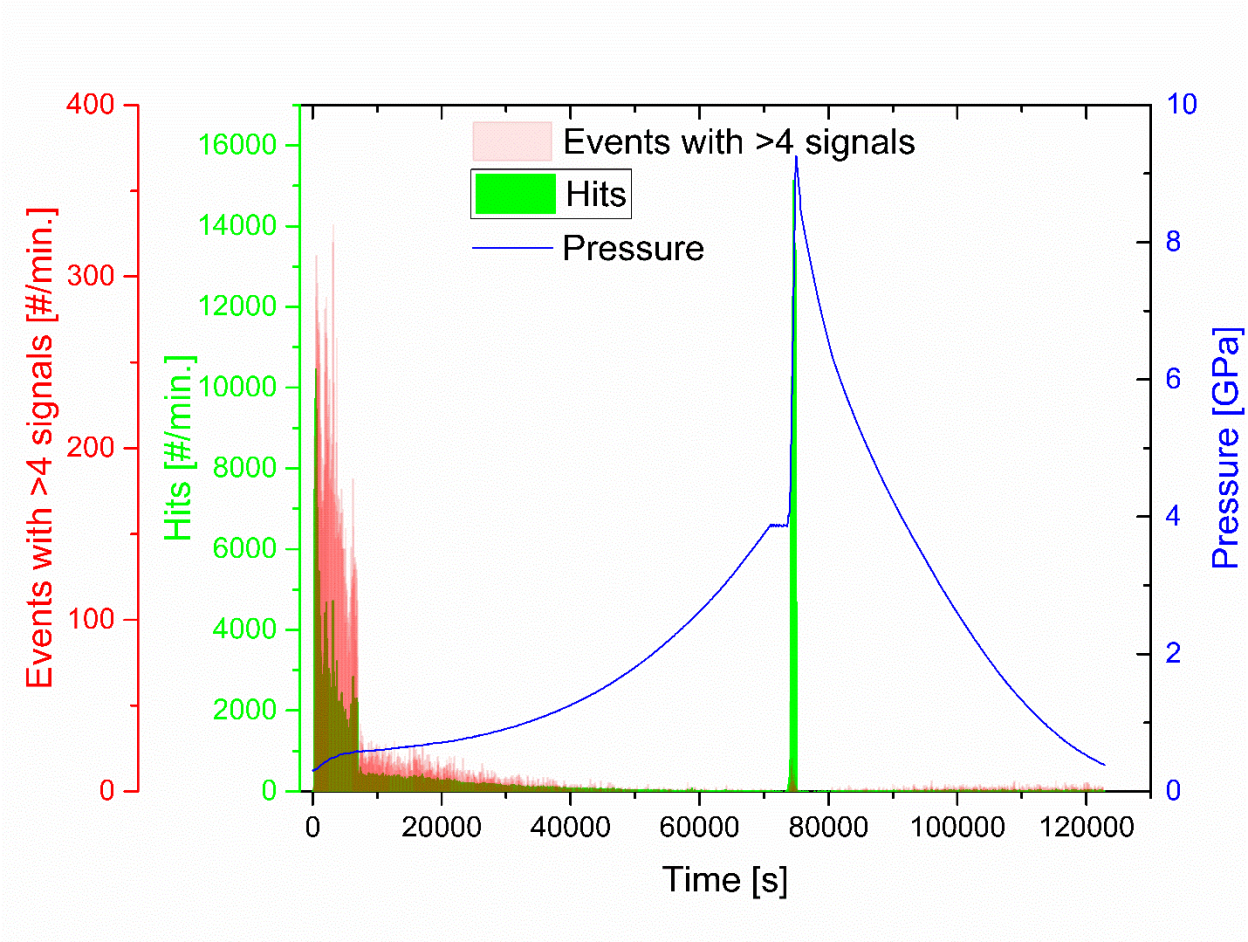

Figure 7.4: The pressure and, acoustic hit and event rates as a function of time for the entire duration of a typical experiment.

7.3 Analysis of bulk recovered samples *via* optical microscopy

Recovered samples were carefully removed from the high pressure cell using a diamond saw to create a small incision in the octahedron. The MgO cell was then pried open using a wedge to extract the furnace which contained the Al_2O_3 pistons and the post mortem sample. The furnace was peeled away using tweezers to reveal the sample, which in most cases could be dislodged from the pistons, so that a pristine sample was extracted. Due to its hardness, Al_2O_3

generates extremely high deviatoric stresses resulting in considerable sample deformation. In all cases the length was reduced and the diameter was extended occasionally leading to “barreling” so that the largest component of extension lay near the center. Figure 7.5 shows a typical recovered sample after removal from the octahedron. Its original dimensions were 5 mm in length by 3 mm in diameter.

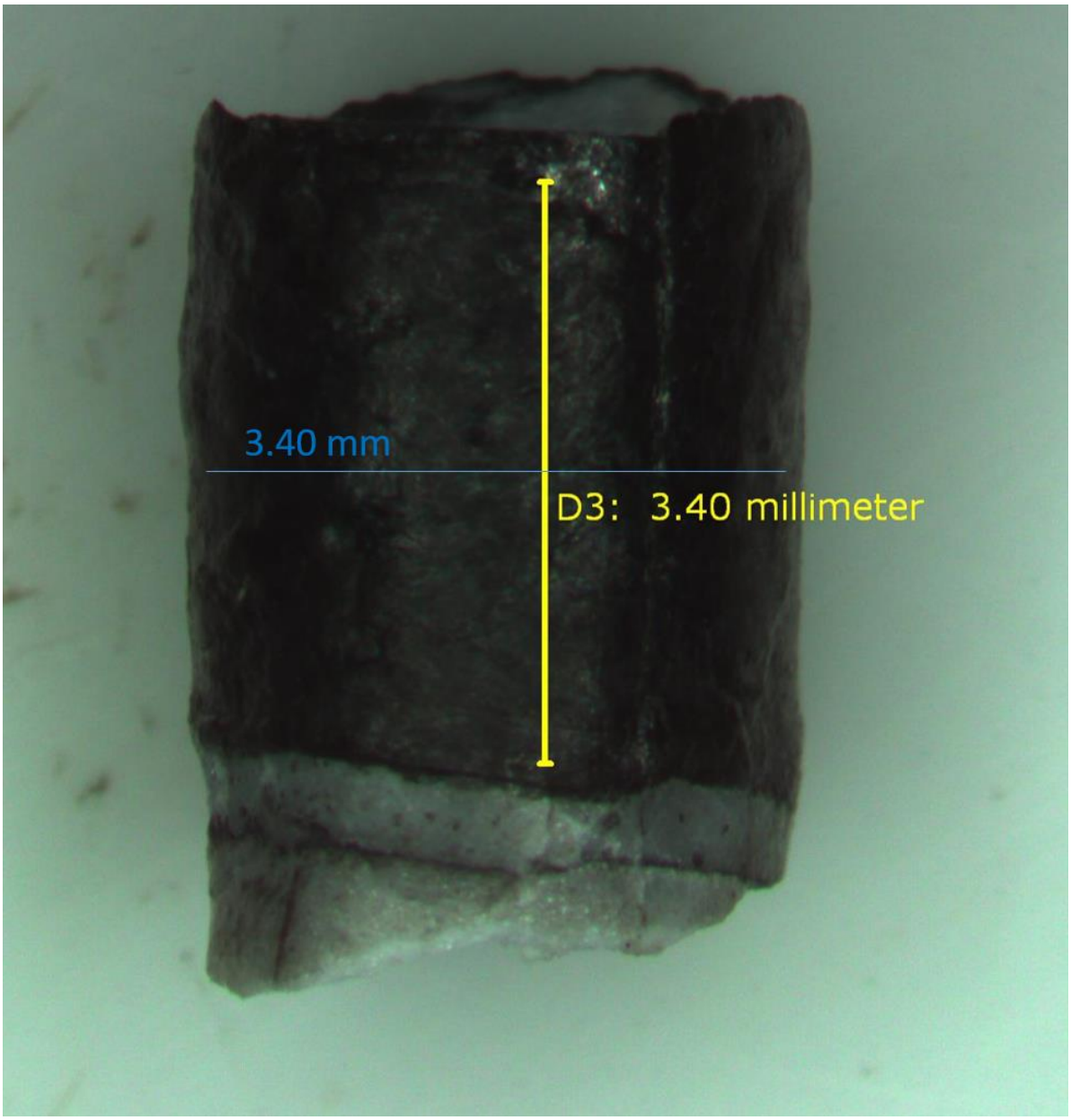

Figure 7.5: A typical sample recovered after an experiment. The samples original dimensions were 5 mm in length by 3 mm in dia. Note the compression along the cylindrical axis and the increase in diameter.

Table 7.1 shows the experimental conditions of each experiment including name, pre-amplification, threshold, pressure range, temperature range, duration, pressurization rate, the maximum strain of the sample, and the strain rate.

Experiment	Pre-amplification	Threshold	Pressure	Temperature	Duration	Pressurization Rate	Maximum Strain	Strain Rate
	(dB)	(dB)	(GPa)	(K)	(s)	(GPa/s)	(%)	(s^{-1})
HPF_AE_1	37	40	5.7 - 8.1	423-623*	2210	1.06E-03	31	1.4E-04
HPF_AE_2	37	40	5.8 - 7.9	776 - 1123	1700	1.24E-03	39	2.3E-04
HPF_AE_3	37	40	5.3 - 7.3	823	1275	1.58E-03	32	2.5E-04
HPF_AE_4	37	40	5.6 - 8.0	998	1185	1.99E-03	41	3.5E-04
HPF_AE_5	37	40	4.6 - 8.7	1048 - 1198	3750	1.10E-03	32	8.5E-05
HPF_AE_6	37	40	4.7 - 8.0	1048 - 1223	1780	1.83E-03	41	2.3E-04
HPF_AE_7	37	40	5.8 - 8.6	1273	1551	1.84E-03	38	2.4E-04
HPF_AE_8	40	40	5.4 - 9.0	773 - 923	1810	1.97E-03	27	1.5E-04
HPF_AE_9	40	40	4.4 - 9.2	973	1150	4.22E-03	32	2.8E-04
HPF_AE_10	49	36.3	4.7 - 8.9	748	900	4.73E-03	29	3.2E-04
HPF_AE_11	49	34	4.2 - 8.8	773	750	6.13E-03	24	3.1E-04
HPF_AE_12	49	32.1	3.8 - 9.1	1073	788	6.70E-03	28	3.6E-04
HPF_AE_13	49	32.1	3.9 - 9.0	923	850	5.98E-03	27	3.2E-04
HPF_AE_14	49	30.6	4.0 - 9.0	823	930	5.41E-03	24	2.5E-04
HPF_AE_15	49	30.6	4.0 - 9.2	798	1030	5.11E-03	30	2.8E-04

Table 7.1: Experimental conditions for HPHT deformation experiments on fayalite.
* This temperature was estimated from the power/temperature relations of proceeding experiments

It should be noted that the strain rates were calculated by dividing the total amount of strain experienced by each sample by the duration of the experiment proper (i.e. the time expended during deformation at elevated P,T). Therefore, this represents an upper limit on the strain rate since any strain accumulated during cold compression is included in this estimate. The amount of deviatoric stress generated is mainly controlled by two factors: 1) the relative hardness of the Al_2O_3 piston with respect to the sample and 2) the ratio of piston length to piston diameter (Dobson et al., 2004). Large components of deviatoric stress were desired under conditions during HPHT deformation since it contributes to faulting (Houseman an England, 1986), but was

an unwanted byproduct during cold compression as it had the potential to initiate brittle failure at low pressure and bias subsequent HPHT behavior (Riggs, 2000). To minimize this, a 1.5 mm plug of crushable alumina was placed on either end of the sample assembly. The purpose of this was to absorb some of the strain during cold compression and minimize stress/strain that could lead to fracturing of the sample at low pressure. At elevated pressure the porosity was removed and behaved like fully dense Al_2O_3 and contributed to the non-hydrostatic component of stress. This is the likely reason for higher strain rates in the first 7 experiments compared to the following 8 when the Al_2O_3 plug was implemented.

7.3.1 Thin Section Preparation

One of the challenges of sectioning the recovered samples was selecting the best azimuthal position and the optimum depth of material removal that would render the most revealing surface(s) for analysis. In order to estimate this, samples were studied under magnification to evaluate any surface features that could point to possible internal structures. Once a suitable position was chosen, the recovered samples were then adhered to a surface using double-sided tape and encased in resin to form a rigid "puck". Both sides of the puck were sanded to create planar surfaces. As material was removed, the samples were monitored under the microscope in an attempt to optimize the appropriate depth that revealed the most significant features. Once satisfied with depth, the samples were further polished using ¼ μm diamond paste to generate a low relief thin section that could be analyzed microscopically. However, this process left a lot to speculation since the exterior features revealed little of the internal structure of the specimens. Therefore, in the case of HPF_AE_15, which was composed of stacked discs coated in Ag, and generated a large acoustic event, special consideration was taken to ensure that the most

revealing surfaces were selected. To facilitate this the sample was CT scanned at the University of Texas High Resolution X-Ray Computed Tomography Facility. This resulted in a 3D volumetric rendering of the internal structure of the specimen with ~ 8 μm voxel resolution. Due to the contrast in density of the Ag markers and the matrix, the presence of what appeared to constitute a fault could be easily identified. Based on the presence and orientation of this feature the sample was sectioned to highlight it. Figure 7.6 illustrates the depth and orientation of sectioning as well as the slices chosen for evaluation.

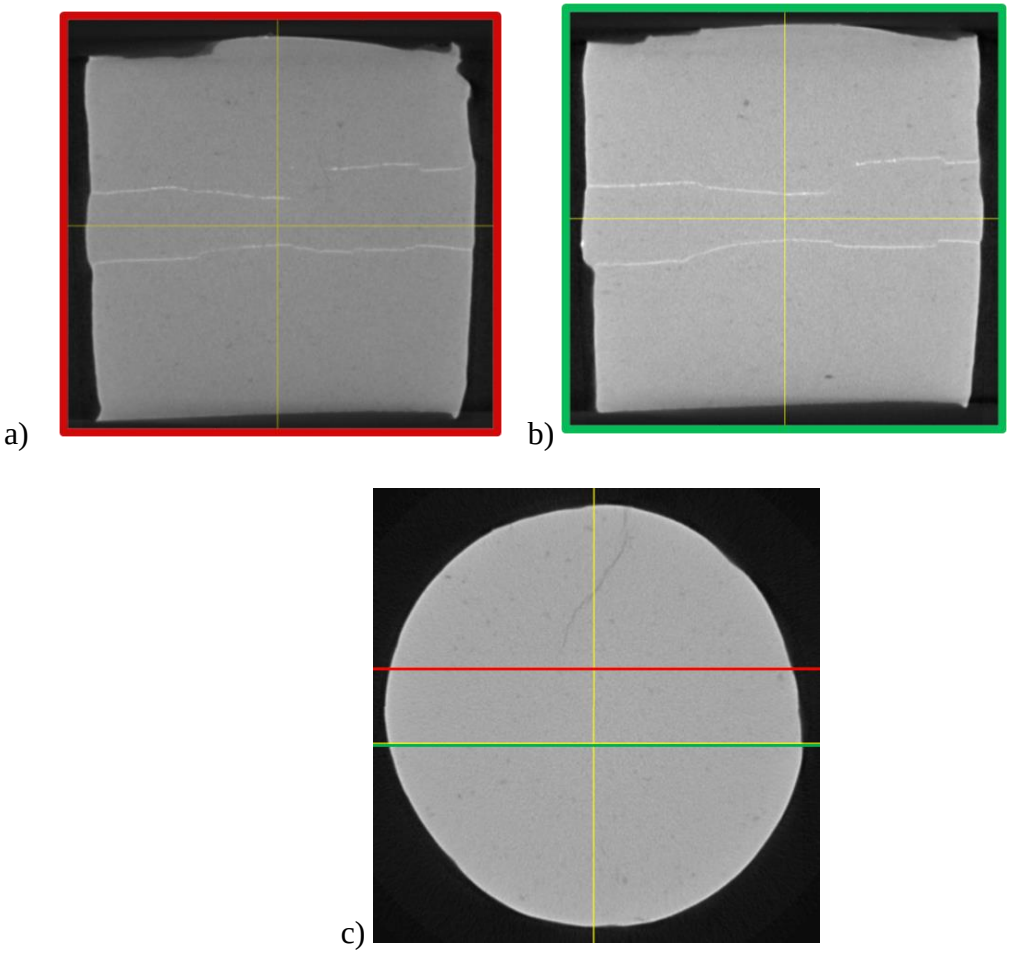

Figure 7.6: a) and b) show the CT slices chosen for post sectioning evaluation for HPF_AE_15. The coloured borders indicate where the slices were taken in c). c) A CT slice taken half way through the sample and perpendicular to the cylindrical axis. Horizontal lines illustrate the depth and orientation of sectioning.

7.3.2 Conjugate faulting

Images of the recovered samples had a tendency to fall into two categories depending on the temperature at which the experiment was run. Samples that were deformed at relatively low temperatures (<950 K) display dark zones superimposed on a lighter background whose appearance and orientation are consistent with the structural manifestation of catastrophic faulting. Namely, the 2D thin sections display conjugate faults running diagonally at approximately 30^0 to 50^0 to the vertical with several smaller narrow faults intersecting these at either parallel or sub-parallel angles. These features show a strong similarity to those witnessed in natural olivine samples that were deformed at HPHT (Green et al., 1990; Dobson et al., 2004). However, while Green et al. (1990) interpreted them to have occurred at HPHT in the wadsleyite stability field, Dobson et al. (2004) inferred they most likely happened during cold compression. Unlike brittle fracture at ambient conditions, adjacent material on either side of the fault is not mechanically separated. Instead, it contains fine grained, highly consolidated material whose composition and structural make-up is higher in ahrensite than the surrounding matrix. This is not surprising since under HPHT conditions adjacent planes in the fault gouge are expected to either, undergo sintering, or possibly nucleate and grow into ahrensite across the boundary. It is, however, unambiguous that these features were generated by faulting since HPF_AE_15, which contains visible Ag markers, clearly illustrates several of these features cross cutting and displacing the Ag film as shown in Figure 7.7. In the upper right of Figure 7.7, a large fault is shown that displaced the Ag marker by 0.25 mm and caused a large portion of the sample to slide diagonally down and to the left where it collided with the furnace wall. This fault is responsible for the sample material jutting out on the left side of the image and the rounded deformation near the top of the right side of the image. It is likely that this fault occurred under low pressure conditions since under high confining pressure it seems doubtful that material

would be able to cause the pressure medium to buckle so dramatically. Such a large fracture is expected to generate a substantial acoustic signal and 3 relatively high energy events locate within the sample during the cold compression stage of the experiment (see section 7.5.1).

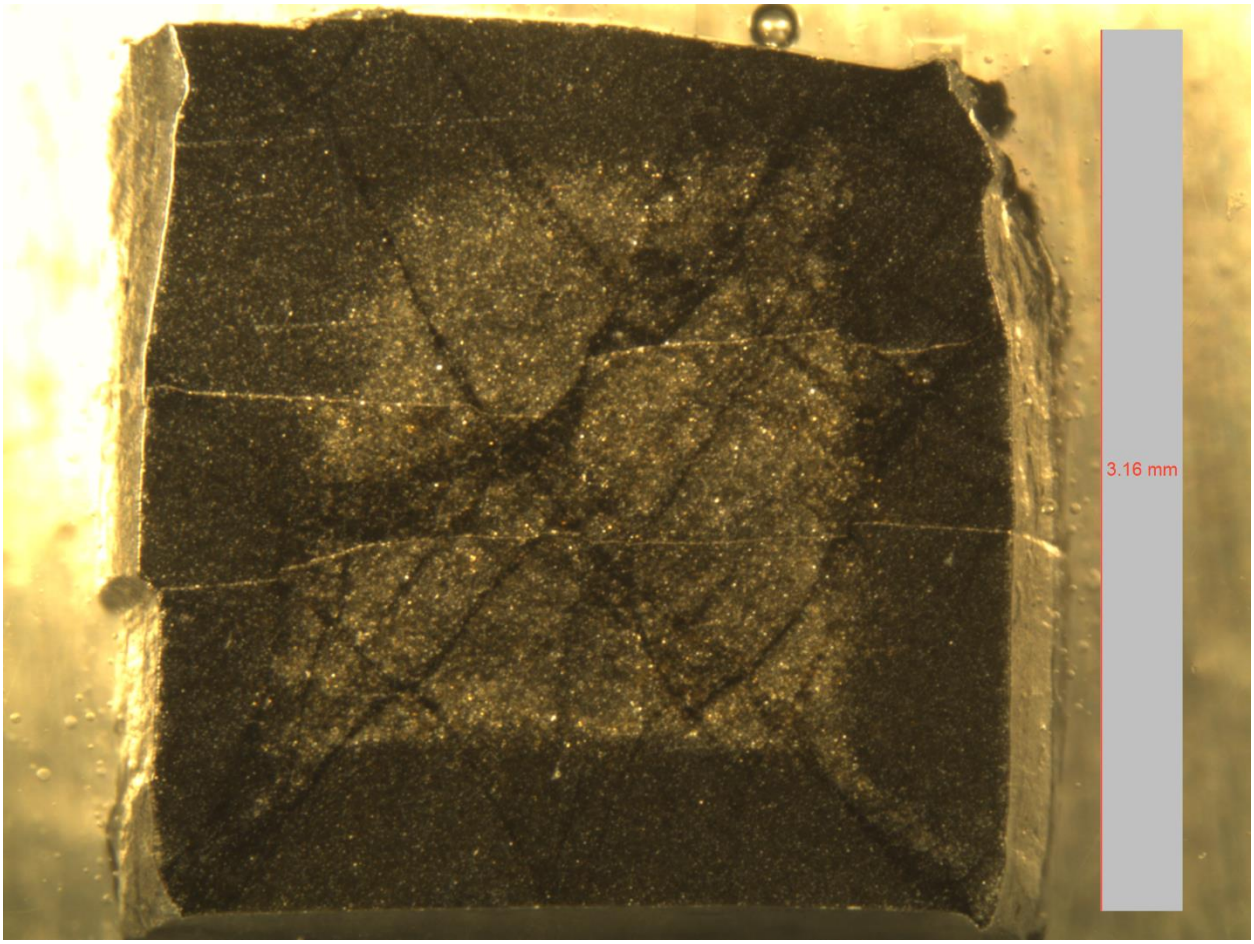

Figure 7.7: Conjugate faulting in HPF_AE_15.

On the other hand, the fault that begins in the upper left of Figure 7.7 and traverses the entire length of the sample, likely happened under HPHT deformation for reasons that will discussed in the section 7.7. Similar to HPF_AE_15, many of the samples display a “rind” of dark material that decorates the sample periphery. Raman analysis confirmed that these areas contain a higher proportion of ahrensite but by no means represent full transformation. The lighter coloured areas are predominantly or entirely fayalite. The features just described for HPF_AE_15 are present to

a greater or lesser degree in all of the experiments with run temperatures of T < 950 K. In contrast, the samples with high run temperatures (T > 950 K) tended to be very dark in colour, relatively uniform in texture and did not display conjugate faulting. In most cases these samples were revealed to be either largely or completely transformed to ahrensite. One such example is HPF_AE_5 (shown in Figure 7.8) which was deformed from 4.6 to 8.7 GPa over 3750 s at a temperature of 1048 - 1198 K. Note the large decompression crack in a plane perpendicular to the sample cylindrical axis near the center of the sample. While a few other experiments also display decompression cracks, this is the only experiment in which the sample broke in two.

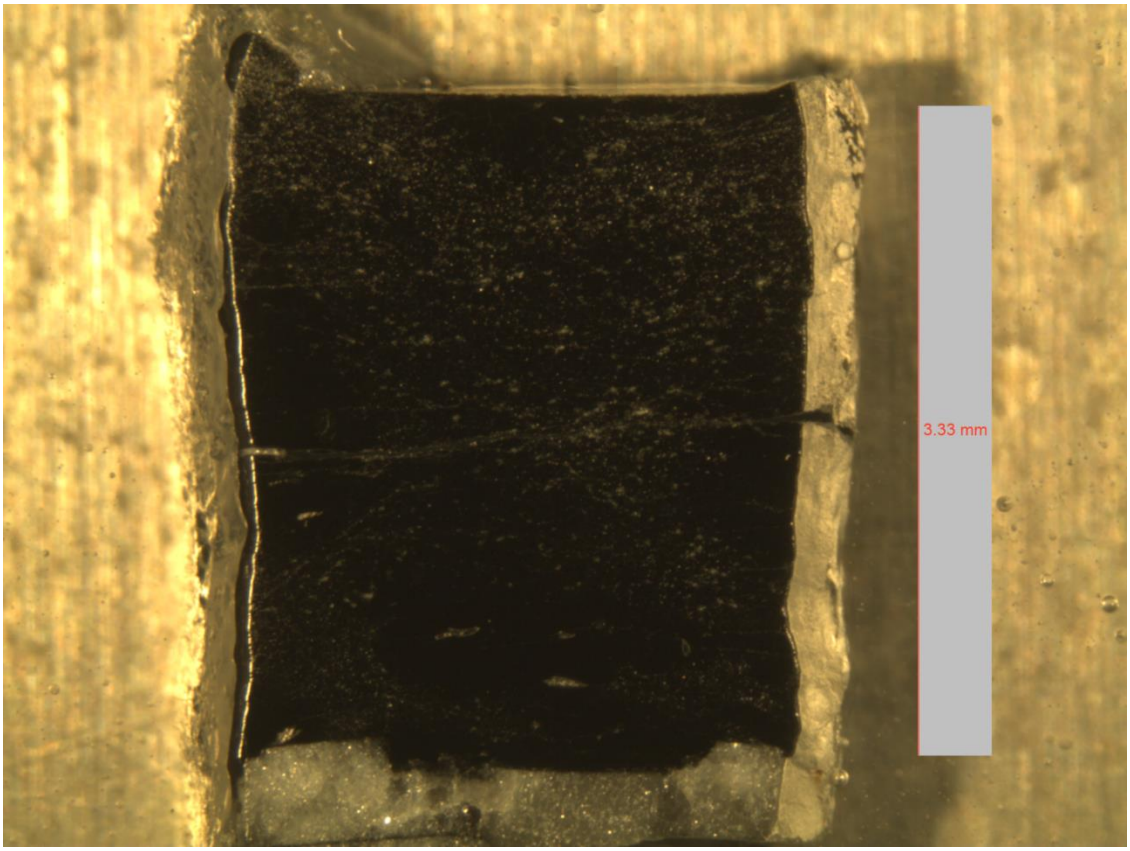

Figure 7.8: Image of HPF_AE_5 post recovery. Note the large decompression crack running horizontally through the center of the sample. The sample fractured into two pieces and had to be fit together before applying epoxy.

7.4 Phase distribution mapping using Raman spectroscopy

7.4.1: Experimental setup of the Raman system

Raman spectra was collected in Dr. Sean Shieh's diamond anvil cell laboratory at Western University. The purpose was to spatially map the phase distribution of fayalite and ahrensite and any other phases present in the post-recovery specimens. The excitation source consisted of an unpolarized Ar ion laser with a wavelength of 514.3 nm and between 300 - 400 mW of power. The polished samples were mounted on stages maneuvered by micrometers with an accuracy of < 1μm normal to the incident beam. Every time data were collected the laser beam was focused on the sample to a spot size of ~3 μm. Scattered photons were collected using lenses and sent to a spectrometer equipped with a liquid nitrogen cooled CCD camera mounted to the output. The spectrograph was calibrated before every run using the 520.5 cm^{-1} peak and spectra were generally accurate to within ±2 cm^{-1}. In order to obtain high quality spectra, data were usually collected for 500 to 800 s and averaged 4 times to reduce signal to noise. Due to the long duration required to accumulate one spectrum (2000 – 3600 s) only a limited number of spectra were acquired. In addition, the long duration introduced the possibility for cosmic rays to be intercepted by the detector which generate high energy spikes in the data. These are unrelated to vibrational modes of the mineral and can be ignored when they appear. In most cases the diffraction grating was angled to disperse light onto the detector with a Raman shift between 200 and 1000 cm^{-1} which includes the strongest stokes-type peaks (i.e. lower energy photons than the laser) of both fayalite and ahrensite. The Raman spectrum of fayalite, has been analyzed by several studies with consistent results (e.g. Chopelas, 1991; Kolesov and Tanskaya, 2004; Mouri and Enami, 2008). Its most salient feature is in the high relative wave-number region where a broad envelope occurs between 800 and 960 cm^{-1} consisting of two lines at 816 cm^{-1} and 840 cm^{-1} that result from SiO_4 stretching vibrations (Kolesov and Geiger 2004a; Kolesov and Geiger 2004b). In contrast, there has been little work done to determine the Raman spectrum of ahrensite. Currently the only

spectrum published is from Ma et al. (2016) who named it after finding the first natural sample of γ-Fe_2SiO_4 in the Tissint Martian meteorite. The spectrum they collected of an unoriented ahrensite sample using a unpolarised 514.3 nm laser beam is shown in Figure 7.9, however, this spectrum can only be used as a very rough guideline for this study since an ahrensite refers to γ-$(Fe,Mg)_2SiO_4$ solid solution with Mg/(Mg + Fe) computed on a molar basis of < 0.5 and their sample contained significant amounts of ringwoodite as well as small amounts of other mixed phases.

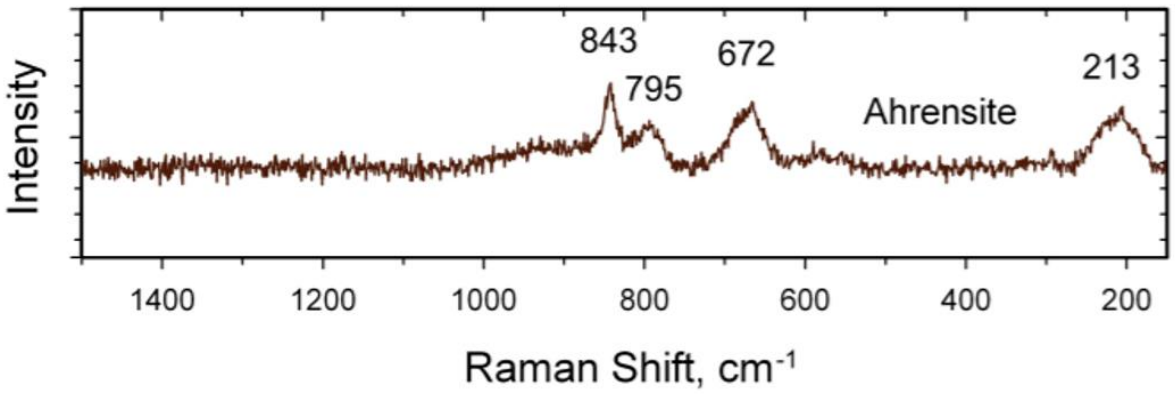

Figure 7.9: The only spectrum currently published for ahrensite from Ma et al., (2016). The spectrum contains a significant amount of ringwoodite as well as a small fraction of other phases.

In order to be confident in the Raman spectrum of ahrensite it was necessary to establish a standard based on a pure ahrensite sample for which subsequent spectra could be referenced against. To verify that a sample was indeed pure ahrensite, X-ray diffraction (XRD) patterns were collected for several positions from the interior and exterior of HPF_AE_5 after recovery from the press. This sample was chosen to serve as a calibrant because it reached a temperature of 1193 K over a duration of 3750 s and was expected to have the largest amount of material that transformed into the γ phase. Figure 7.10 shows the XRD patterns collected from this sample.

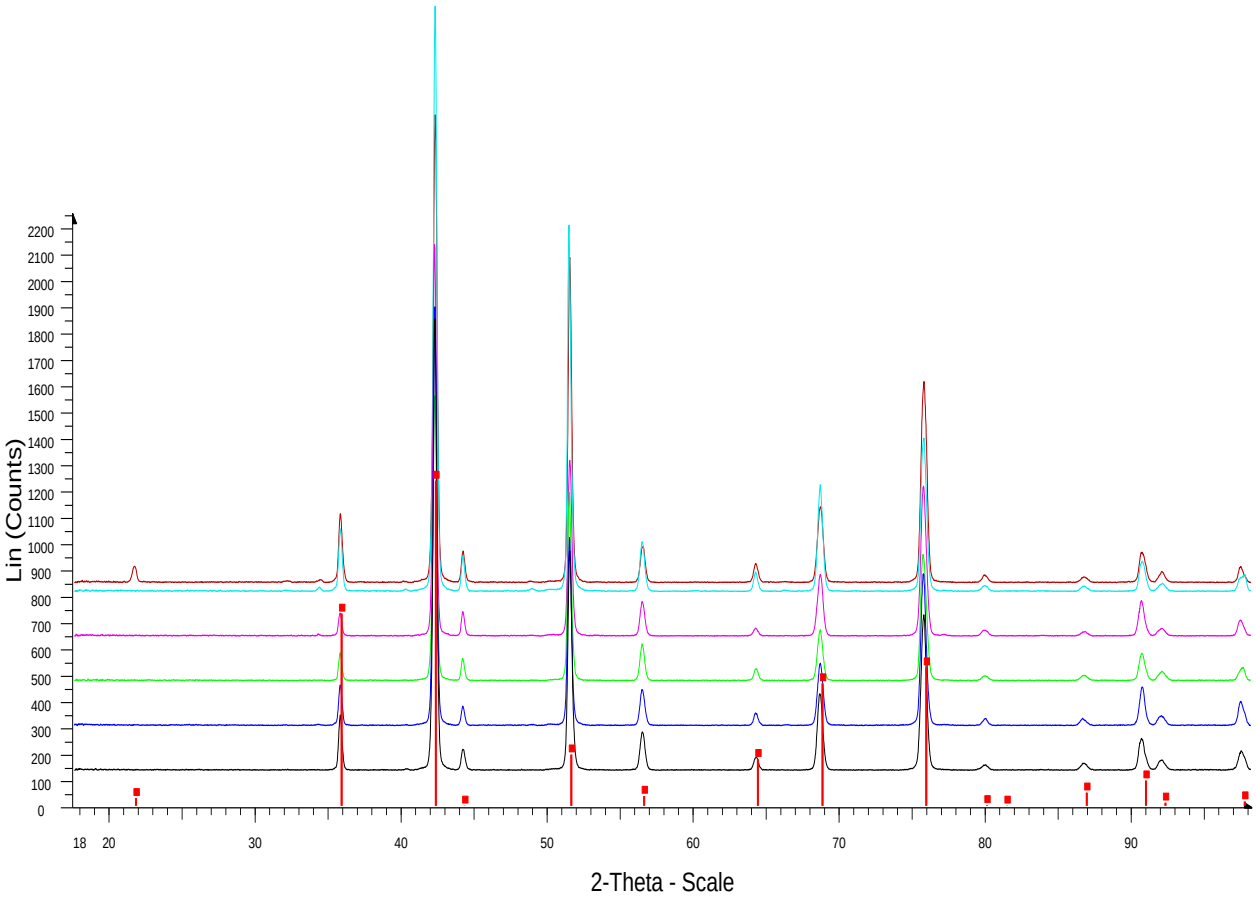

Figure: 7.10: XRD patterns collected from HPF_AE_5. The positions of the ahrensite peaks are shown in red. Note the close match between the diffraction peaks and the ahrensite peaks.

Note that the six spectra shown here nearly perfectly match the ahrensite peaks and do not appear to contain any other peaks corresponding to a different mineral. This indicates that this is likely a nearly pure ahrensite sample and could therefore serve as a high quality standard as the basis of the ahrensite Raman spectrum. Spectra were collected at several different locations along the long axis of the sample showing similar results (see Appendix 2). For the calibration spectrum, data were collected for 3600 s and averaged 4 times to ensure high quality. Figure 7.11 shows a comparison of the Raman spectra for fayalite and ahrensite.

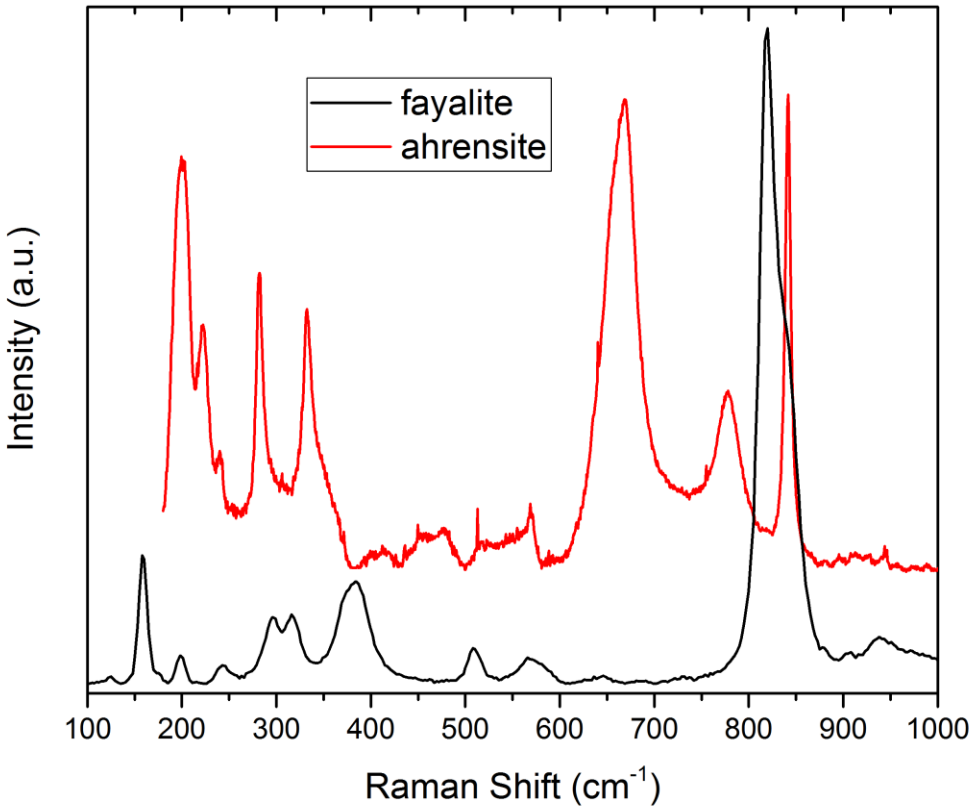

Figure 7.11: Comparison of the Raman spectra for fayalite and ahrensite. The ahrensite spectrum was collected from HPF_AE_5 which had fully transformed to the high pressure phase. The fayalite spectrum is reproduced from a synthetic sample collected with a 514 nm unpolarized laser on an unoriented source (The spectrum was collected by Rossman, G.R. and downloaded from the RUFF database, RUFF I.D. X050077).

The most significant peak in the ahrensite spectrum that served to diagnose the presence of ahrensite is the 666 peak due to its high intensity and the absence of any comparable peaks in the fayalite spectrum at this wavenumber.

7.4.2 Raman analysis of recovered samples

For transformational faulting to occur in fayalite the temperature must be at least high enough to surpass the kinetic boundary of the $\alpha \rightarrow \gamma$ transition under metastable conditions.

Therefore, it was essential to investigate the phase distribution of the recovered samples to detect the presence of ahrensite, particularly within the fault zones.

HPF_AE_1: Raman analysis

The lowest temperature attained in any experiment in this study was that of HPF_AE_1. This is based on the fact that it was run at the lowest furnace power, however the precise run temperature is uncertain since the thermocouple broke during compression. Based on a power temperature relationship of later experiments the temperature of HPF_AE_1 was estimated at 523 - 623 K at the location of the thermocouple which corresponds to a temperature of ~ 563 - 673 K at the center of the sample. It has been shown using synchrotron XRD that the spinel phase can appear at a temperature as low as 638 K at 6.9 GPa and differential stress exceeding 1 GPa by way of a pseudo-martensitic mechanism: a rapid diffusionless anionic rearrangement followed by short range cationic diffusion (Chen et al., 2001). However in another set of experiments the same authors did not witness the transition until 723 K under similar pressure conditions (Ratteron et al., 2002). In both of these studies the stress dependence of the transition was shown to have a significant impact on the transition temperature and how the transition progressed. Under conditions of low differential stress the transition proceeded at a temperature roughly 100 K higher than under high differential stress and advanced by a nucleation and growth mechanism. While it is impossible to accurately measure the differential stress in our samples *in situ* it is expected to be large due the presence of the Al_2O_3 pistons. HPF_AE_1 displays extensive faulting in the recovered sample, however it is not clear whether this arose due to transformational faulting at HPHT or whether they were artifacts of cold compression. Given the uncertainty surrounding both the temperature and differential stress in HPF_AE_1

sections of the sample were analyzed to check for the presence of the high pressure phase. Figure 7.12 shows the Raman spectra collected at several different positions on HPF_AE_1.

a)

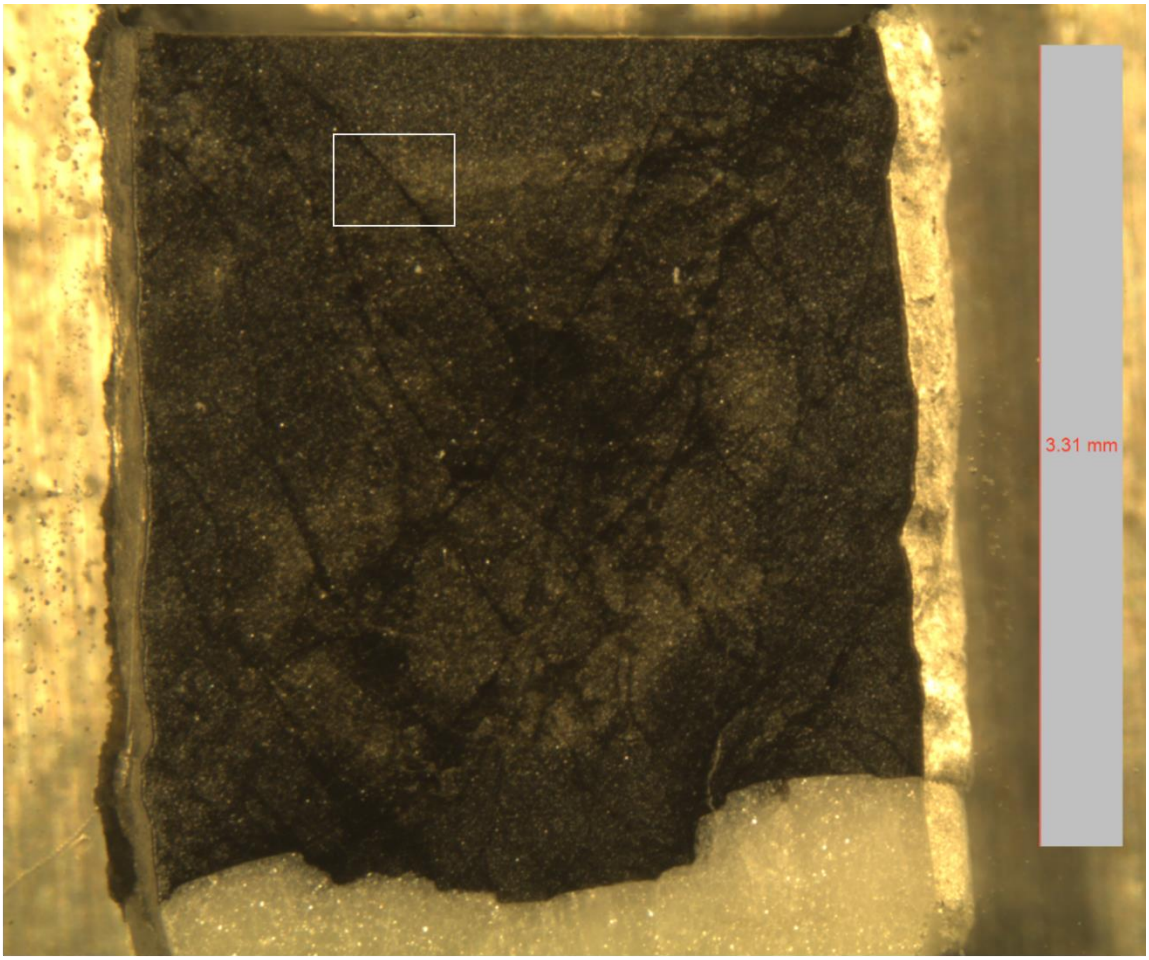

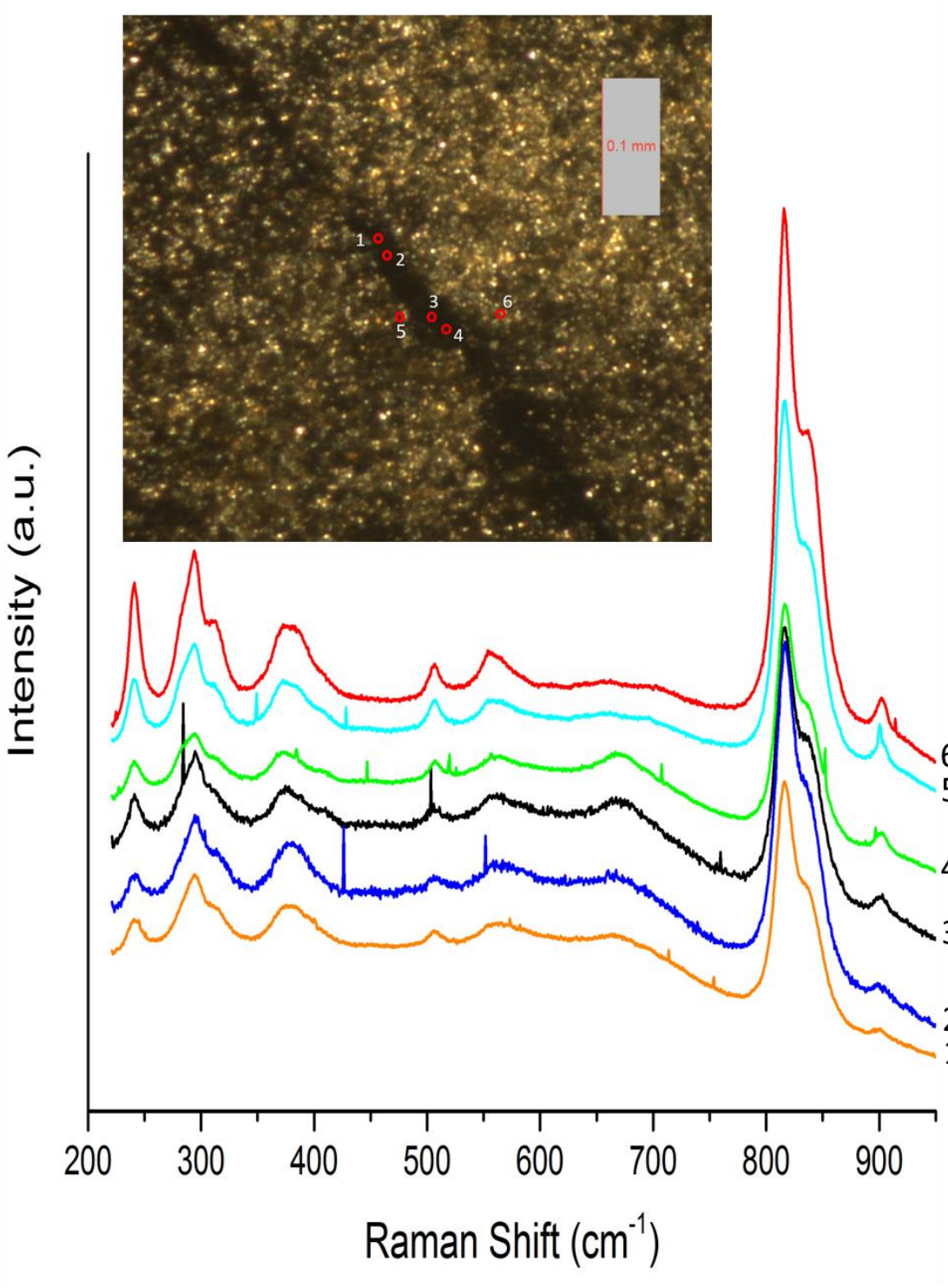

Figure 7.12: Image of HPF_AE_1 indicating the areas where Raman spectra were collected b) Zoom view of the boxes shown in a. Raman spectra collected at several positions indicated in b.

The overall phase assemblage is dominated by fayalite. However, small amounts of ahrensite can be identified within the fault zone as evidenced by the 666 cm^{-1} peak that appears in spectra 1,3, 4 and possibly 2 which did not produce a strong signal and would have benefitted from a longer collection duration. Of particular note is the contrast in the 666 cm^{-1} wavenumber peak between spectra 3, which locates in the fault zone and 5 which locates just adjacent to it. While some of the spectra that were excited within the fault are ambiguous whether or not ahrensite is present spectrum 3 clearly demonstrates that some has been produced.

HPF_AE_11, HPF_AE_15 and HPF_AE_8: Raman Analysis

These samples were run within the intermediate temperature range of 773 K – 923 K. Micrographs of the recovered samples all display conjugate faults that appear dark and are embedded within a lighter matrix. They also contain a "rind" of dark material similar in colour to the faults around their perimeter. Raman spectra were collected for each sample both inside and adjacent to the fault zones and display a higher percentage of ahrensite within the faults as well as the "rind", although the spectra generally reveal mixed phases of fayalite and ahrensite. While the presence of the ahrensite structure within the fault is a necessity of the transformational faulting hypothesis it does not, in and of itself, guarantee these faults were caused by transformational faulting. The presence of ahrensite in the rind indicates that the high pressure phase forms preferentially where there is a boundary condition which is also provided by the faults. Fine grained material within the fault zone may also provide nucleation sites for the transformation. If faulting occurred during cold compression it is possible, at least in theory, that growth of ahrensite was favoured in these sites. Figure 7.13 shows an example of the phase distribution for several locations for HPF_AE_11 which is representative of these intermediate temperature experiments that display conjugate faults. While the 666 cm^{-1} peak appears in all the

spectra it is much more prominent within the fault and drops off dramatically within 10's of microns outside them.

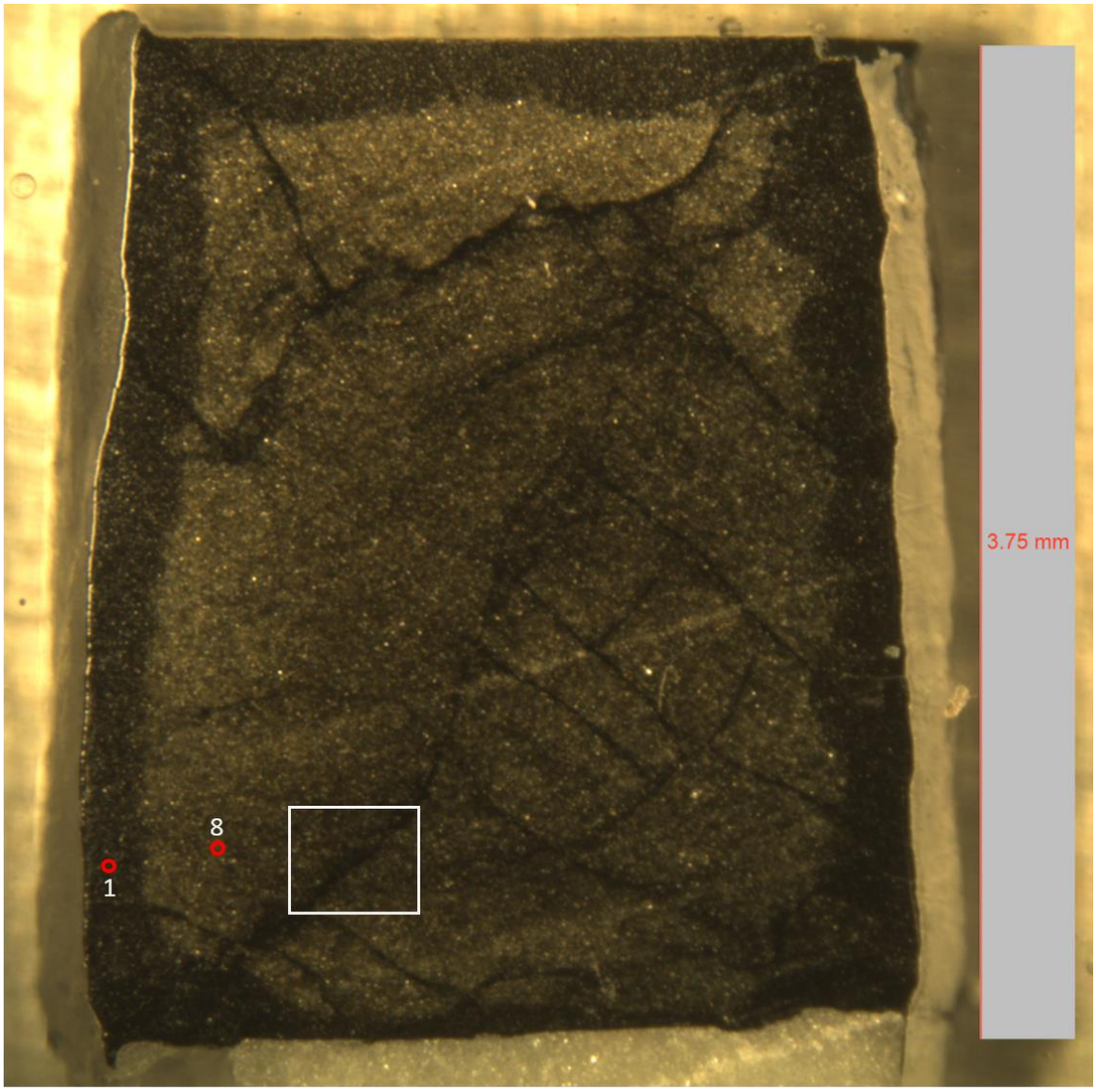

a)

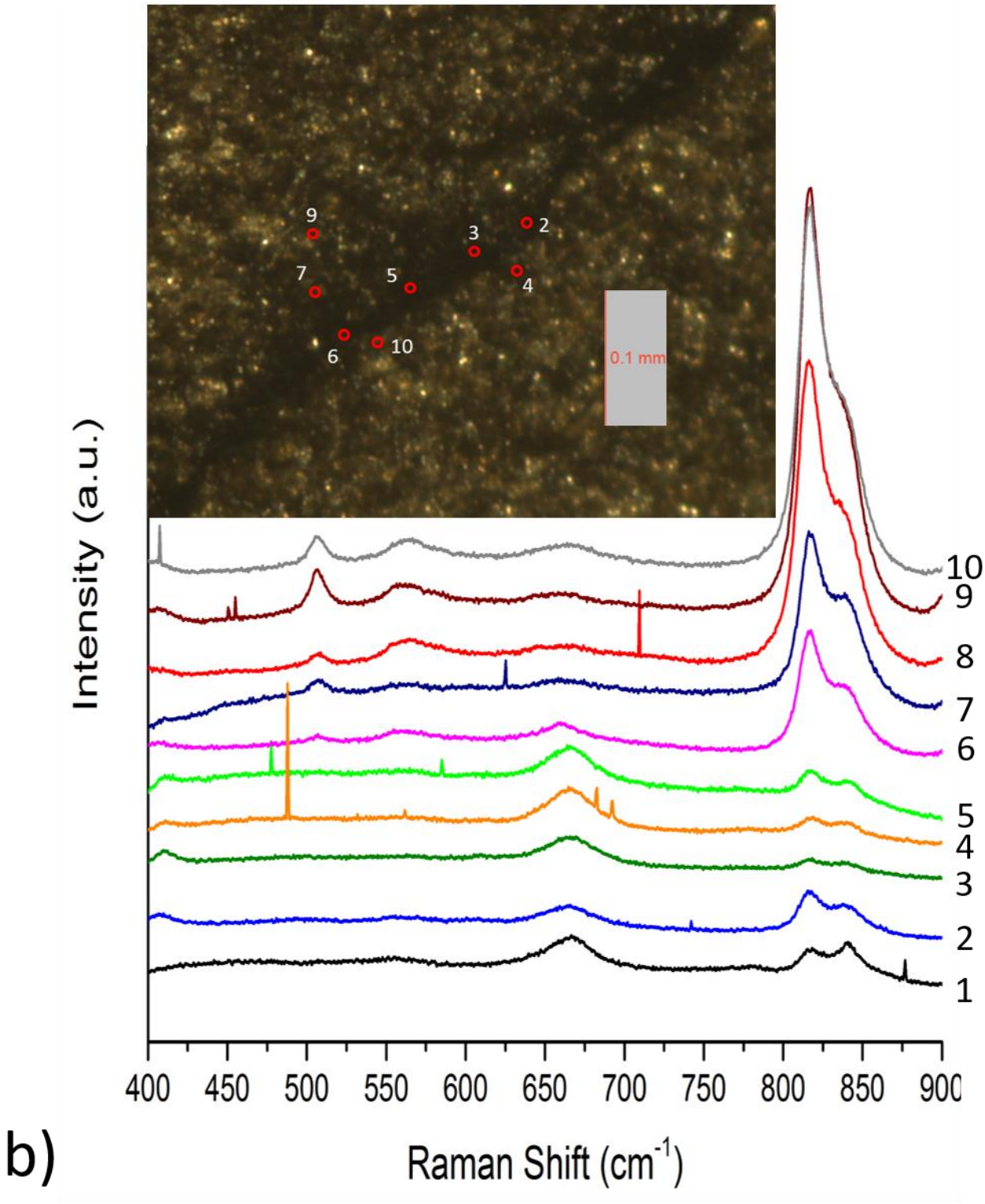

Figure 7.13: Image of HPF_AE_11 indicating the areas where Raman spectra were collected b) Zoom view of the boxes shown in a). Raman spectra collected at several positions indicated in b.

HPF_AE_14: Raman analysis

The recovered sample appears uniformly darker than the other intermediate temperature experiments indicating that a large amount of ahrensite was created during this experiment. It also displays distinct fracturing patterns associated with faulting. In particular, cross cutting faults traverse and offset the Ag markers and appear as a slightly lighter colour than the background and contain extensive cracks within the light coloured bands. Raman spectra were collected in the lower right side of image shown in Figure 7.14a on either side of two conjugate faults that cross the Ag marker (Figure 7.14b). The spectra are shown in Figure 7.14c. The entire sample is dominated by ahrensite particularly in the lighter coloured areas surrounding the faults where the sample has fully transformed. Once outside this region, fayalite appears as indicated by the 816 cm^{-1} line characteristic of the fayalite Raman spectrum. This implies that ahrensite first emerged within the fault zones then grew outward through diffusion controlled nucleation and growth. However, the presence of ahrensite outside the fully transformed bands indicates that nucleation sites existed throughout the sample.

a)

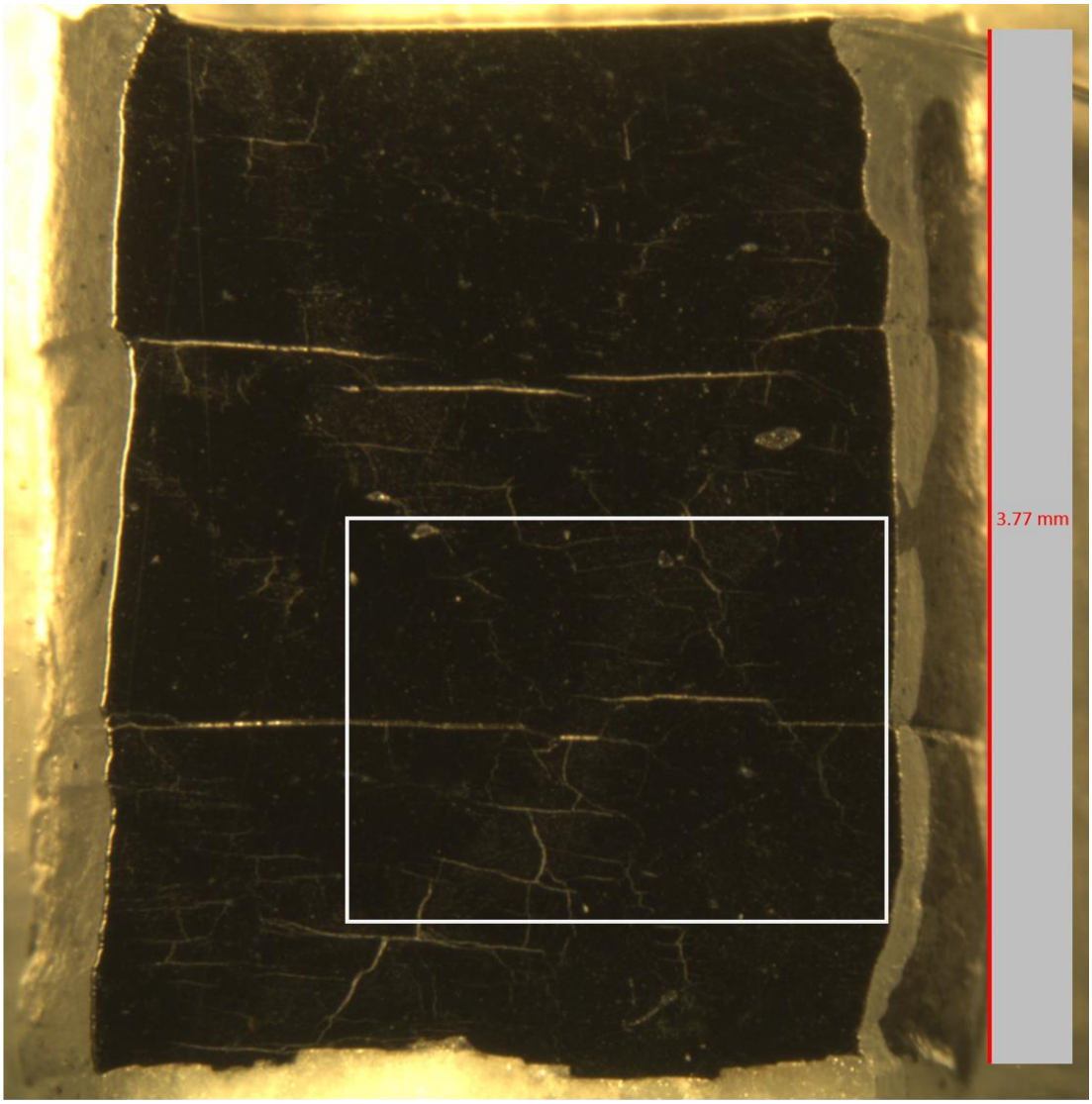

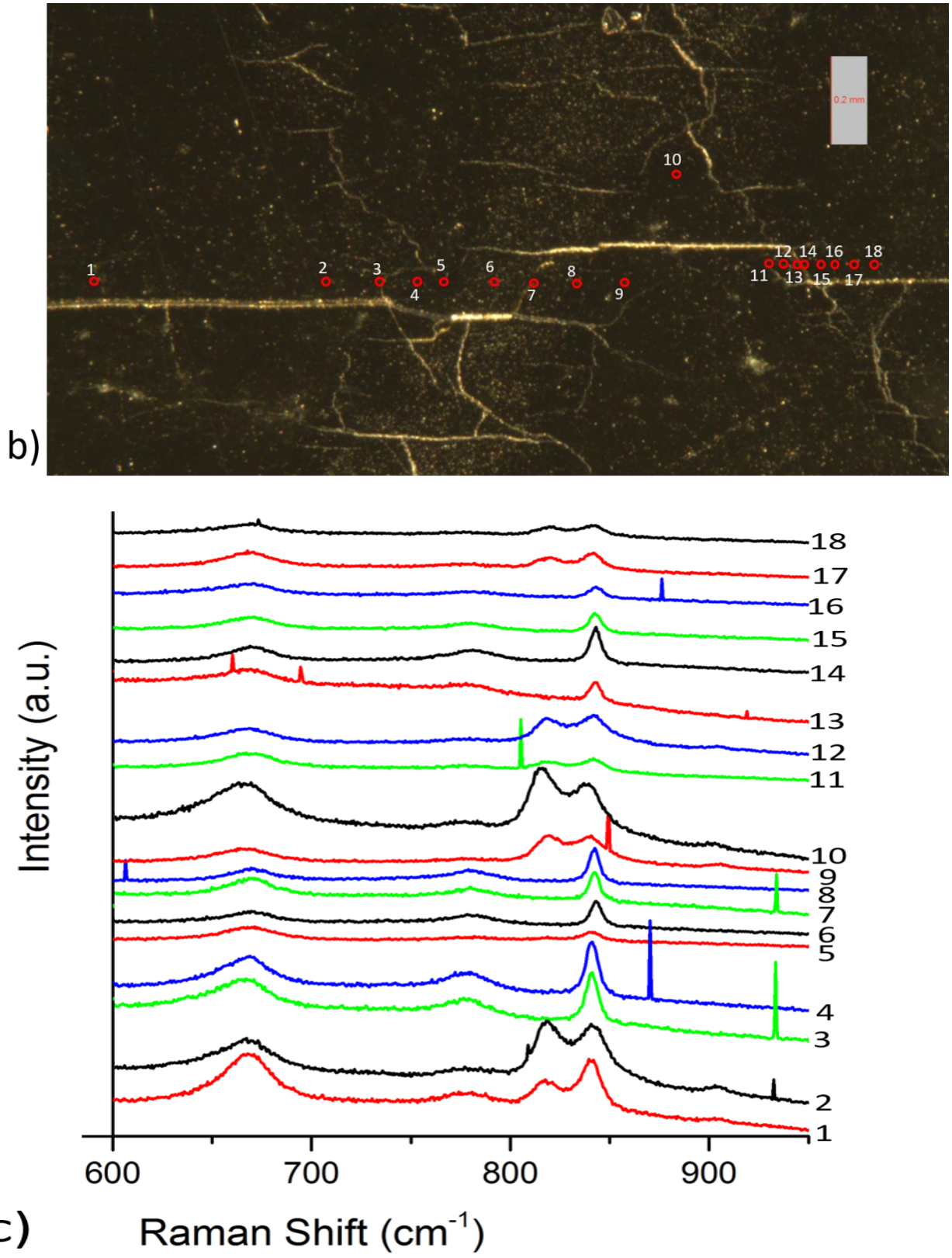

Figure 7.14: a) Image of HPF_AE_14 showing the area where Raman spectra were collected b) zoom view of the box in a. c) Raman spectra going from right to left in the image shown in b.

7.5 Location analysis of AE records

7.5.1 Cold compression

A potential problem that could bias results after sample recovery was the possibility that samples failed by brittle failure during cold compression. Although cold compression was carried out slowly (over > 70,000 s) it was necessary to test whether AE events located within the sample. Because of the large amount of AE events generated at low pressure, only those that located within 10 mm of the origin, based on locations calculated by the Vallen software, were considered for relocation using the inversion algorithm discussed in Chapter 4. This typically resulted in 150 to 650 events whose waveform arrival times were automatically chosen using the AIC algorithm. The vast majority of these originate within the gaskets and pressure medium, however two thirds of experiments recorded between 1 and 5 acoustic events that located within the sample. They tend to consist of high energy events that occurred between 0.25 and 3.25 GPa. Table 7.2 shows the data calculated for each event that located in the sample during pressurization.

Experiment	Sigs	x	y	z	t	E	P	v	σ_x	σ_y	σ_z
(I.D)	#	(mm)	(mm)	(mm)	(s)	(a.u.)	(GPa)	(m/s)	(mm)	(mm)	(mm)
HPF_AE_1	6	0.27	-0.21	-1.38	9481	38565	2.18	6498	0.59	0.59	1.18
	6	-0.21	0.55	-1.55	9551	2095	2.20	6501	0.59	0.59	1.18
	6	-0.27	-0.24	-1.95	9636	5740	2.24	6505	0.59	0.59	1.18
HPF_AE_2	5	0.24	1.19	0.76	1776	337600	0.63	6175	0.79	0.56	1.37
	6	1.05	-0.66	2.26	6862	276333	0.90	6263	0.57	0.57	1.14
	6	0.11	-1.18	2.26	6893	53367	0.91	6265	0.57	0.57	1.14
HPF_AE_4	5	-1.01	-0.17	1.21	1965	1997800	0.25	5983	0.69	0.50	1.20
HPF_AE_5	6	0.52	-0.15	2.42	71214	5920	3.20	6574	0.60	0.60	1.19
HPF_AE_6	5	1.31	-0.53	1.51	1523	3798	0.45	6002	0.60	0.72	1.32
	6	1.32	0.62	2.30	5965	3896667	1.25	6351	0.58	0.58	1.15
	6	-0.46	0.09	2.34	10033	43420	1.91	6466	0.59	0.59	1.17
	6	0.55	0.55	0.57	13564	269	2.59	6536	0.59	0.59	1.18
	6	0.42	0.91	1.90	15797	566	2.77	6549	0.59	0.59	1.19
HPF_AE_7	6	-0.37	-0.96	1.58	2758	213	0.66	6186	0.56	0.56	1.12
	5	0.15	-0.15	0.91	18243	8242	3.12	6570	0.67	0.78	1.46
	6	1.08	0.45	2.30	18277	866	3.14	6571	0.60	0.60	1.19
	6	-0.67	-1.26	-0.67	19315	5761	3.22	6575	0.60	0.60	1.19
HPF_AE_9	6	0.33	1.45	-0.25	4310	1313	0.68	6195	0.56	0.56	1.12
HPF_AE_10	6	1.04	-0.33	1.97	80178	5759	2.46	6525	0.59	0.59	1.18
HPF_AE_13	6	0.18	0.50	2.21	65923	63050	2.57	6534	0.59	0.59	1.19
	6	1.22	0.50	0.48	71250	4716	3.10	6568	0.60	0.60	1.19
	6	0.18	0.71	2.22	71701	210	3.15	6571	0.60	0.60	1.19
	6	0.44	0.45	2.47	72064	89917	3.19	6573	0.60	0.60	1.19
HPF_AE_15	6	-0.35	1.01	1.81	3260	24722	0.71	6203	0.56	0.56	1.13
	6	-0.58	0.24	-0.48	20285	10177	0.93	6269	0.57	0.57	1.14
	6	1.11	0.15	-1.69	60746	18837	2.83	6553	0.59	0.59	1.19

Table 7.2: Events that locate within the sample during cold compression.

It is possible that these events originated outside the sample and were improperly located, particularly since the experiment run with the AgCl sample, which was expected to behave aseismically, indicated a similar number of AEs that were interpreted to be erroneously located (see section 5.9). Indeed, the majority of events were located very near the sample periphery and could have reasonably originated outside it if uncertainty estimates are applied. By the same token, it is conceivable that some of the events that located just outside the sample may have

originated within it. This also leaves open the possibility that the experiments which did not register events within the sample may have fractured and gone undetected or were improperly located. Figure 7.15 shows a representative example of the distribution of event locations during a pressurization cycle. Events that locate within the sample are displayed as closed red dots and those outside the sample are shown as open blue dots.

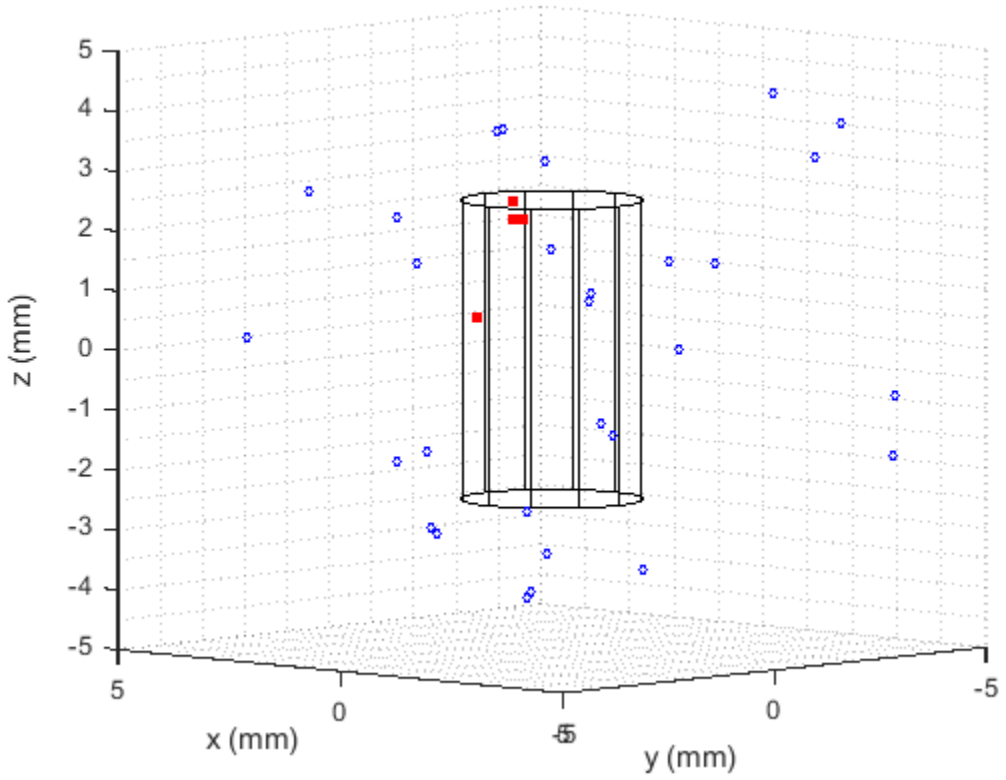

Figure 7.15: The location of events collected for HPF_AE_13 during cold compression. Closed red dots represent events that locate within the sample and open blue dots represent events that locate outside of it. Note that the events that locate within the sample are near the sample extremity and may have originated just adjacent to it but were erroneously located within the sample.

Given the fact that events that lie within the sample could have originated outside it if uncertainty and the well-established low pressure acoustic activity of the pressure medium are taken into account, it is impossible to say with absolute certainty that fracturing occurred during cold compression. However, it is likely that in at least some cases it did since several previous

studies have also witnessed or inferred the fracturing of sintered and natural minerals during cold compression under non-hydrostatic conditions (Dobson et al., 2004; Riggs and Green, 2005; de Ronde et al., 2007 and Gasc et al., 2011).

7.5.2 The test proper

Of the 15 experiments run under HPHT conditions in the ductile regime of Fe_2SiO_4, a total of 5 experiments exhibited acoustic events that located within the sample and one experiment that displayed acoustic events within one standard deviation of the sample. Due to the limited number of AE events (usually < 800) with ≥4 signals within 50 μm during deformation, all arrival times were picked manually to ensure the most accurate location estimates. However, although manual picking is likely to lead to more accurate location estimation it is unreasonable to expect an infinite degree of accuracy. Therefore, location uncertainties are calculated using the procedure discussed in Chapter 4. Table 7.3 shows the information associated with events originating from within the sample dimensions or within 1σ of the sample. It includes: the number of signals associated with each event; its location in terms of its *x*,*y* and *z* coordinates in the coordinate system where the center of the sample is located at [x,y,z] = [0,0,0] and the *z*-axis is coincident with the sample cylindrical axis; the time the event occurred after heating began; the energy of the event averaged by the number of signals recorded; the pressure at which the event occurred; the velocity used to invert for the location; and the standard deviation in the *x*, *y* and *z* directions.

Experiment	Location	Sigs	x	y	z	t	E	P	v	σ_x	σ_y	σ_z
(I.D.)	(w.r.t sample)	#	(mm)	(mm)	(mm)	(s)	(a.u.)	(GPa)	(m/s)	(mm)	(mm)	(mm)
	in	5	0.71	0.62	0.90	339	58	6.33	6687	0.87	0.61	1.49
HPF_AE_2	in	6	0.54	0.15	0.09	392	187	6.33	6687	0.59	0.59	1.18
	in	5	-0.11	0.03	0.63	1621	206	7.91	6734	0.68	0.8	1.48
	1σ	5	-1.47	1.87	0.44	674	12	4.96	6639	0.41	0.48	0.90
HPF_AE_10	1σ	5	-1.35	1.83	0.37	710	14	5.19	6646	0.41	0.48	0.90
	1σ	5	-1.24	1.40	0.22	758	13	5.46	6656	0.41	0.48	0.89
	1σ	5	-1.54	1.81	0.43	792	14	5.67	6663	0.41	0.48	0.90
	in	6	0.10	0.98	-0.37	94	84	4.19	6613	0.47	0.48	0.88
HPF_AE_11	in	4	-0.92	0.13	1.44	765	234	5.69	6664	1.81	0.73	3.46
	1σ	4	-2.01	-0.24	1.20	551	128	4.47	6622	0.52	0.72	0.93
	in	4	-0.60	-1.17	1.46	246	60	3.88	6602	0.52	0.52	1.28
HPF_AE_13	in	4	0.76	-1.06	2.18	987	12	6.53	6694	0.52	0.52	1.25
	1σ	5	1.38	-1.47	-0.29	827	30	5.53	6658	0.5	0.36	0.87
	in	6	0.64	0.07	0.14	1302	38	8.37	6741	0.67	0.71	1.23
HPF_AE_14	1σ	5	-1.05	1.22	0.60	1288	14	8.36	6740	0.86	0.84	1.42
	1σ	4	1.57	0.28	-1.15	670	20	7.21	6714	1.06	0.98	1.92
	in	6	-0.42	-0.73	-1.57	337	5238333	4.14	6611	0.45	0.45	0.91
HPF_AE_15	in	4	-0.57	0.39	1.42	497	289	4.49	6623	0.78	0.87	1.81
	in	4	0.28	0.28	0.57	929	8	6.83	6705	0.80	0.95	1.91

Table 7.3: Event location data and uncertainty for events that locate within the sample or within 1σ of it during HPHT deformation of Fe_2SiO_4. Time is measured from the beginning of heating.

Figure 7.16 shows the location of AE events that occurred during deformation of HPF_AE_11with a cylinder representing the sample (3 mm diameter and 5 mm length). Events that locate within the sample are shown as closed red dots, events within 1σ are shown as open red dots, and events that locate beyond 1σ from the sample are shown as open blue dots.

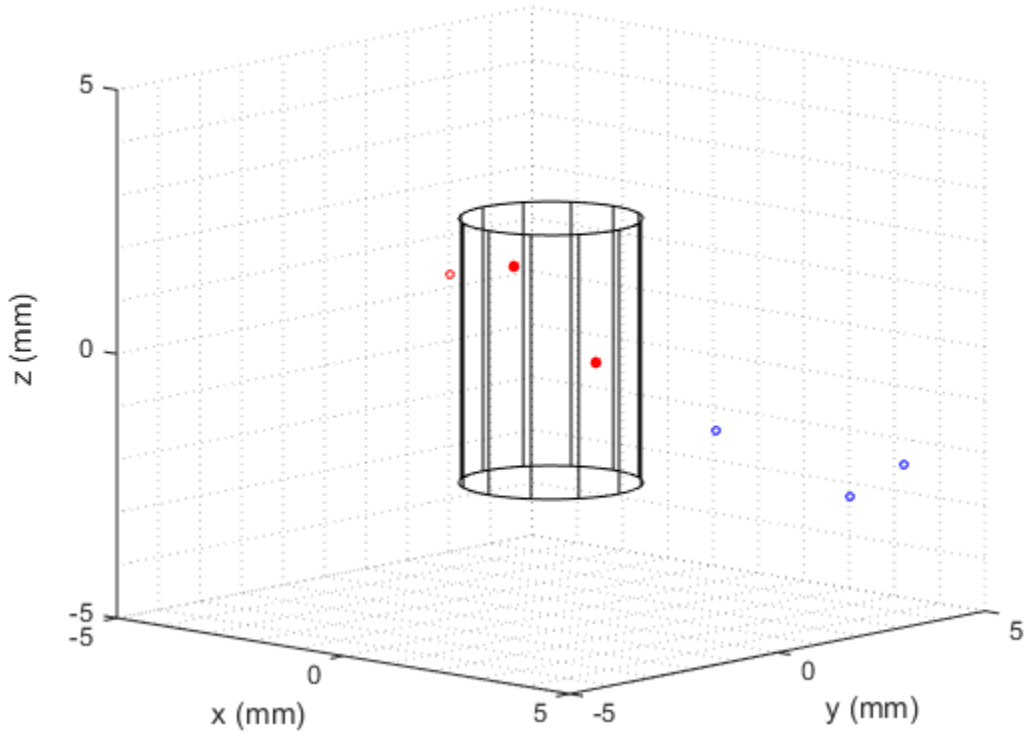

Figure: 7.16: Acoustic event locations during HPHT deformation of HPF_AE_11. Events that locate within the sample are shown as closed red dots, events within 1σ are shown as open red dots, and events that locate beyond 1σ from the sample are shown as open blue dots.

Figure 7.17 shows the P,T coordinates of events that locate within the sample (closed stars) or within one standard deviation of it (open stars). The P,T path of each experiment is superimposed on the Fe_2SiO_4 phase diagram from Ono et al., (2013).

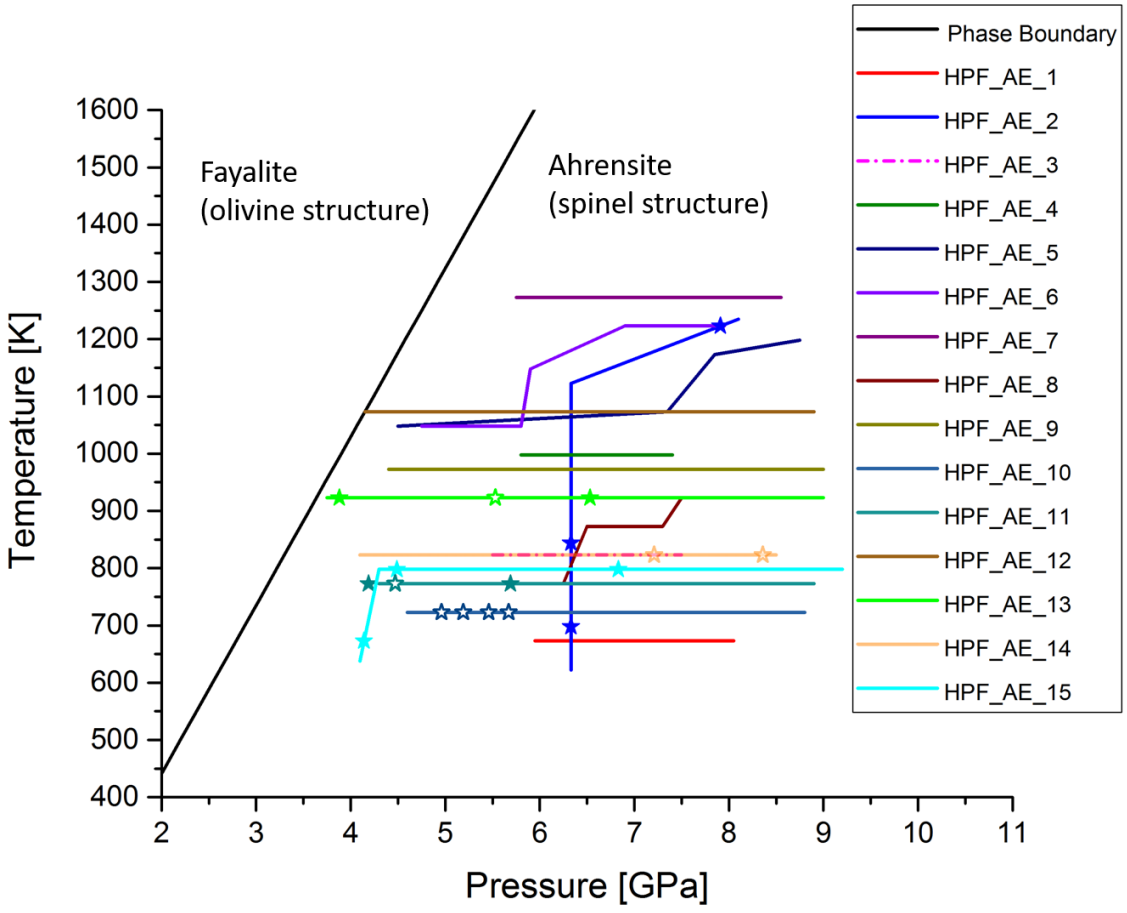

Figure: 7.17: PT paths of HPHT deformation experiments on Fe_2SiO_4. Stars represent the P,T coordinates when AE events occurred. Closed stars represent events that locate within the sample and open stars represent events that locate within 1σ of the sample. The Fe_2SiO_4 phase boundary from Ono et al. (2013) is the solid black line.

Acoustic emissions tend to cluster towards relatively low P,T conditions circumscribed by the envelope P = 3.8 – 8.4 GPa and T = 650 – 950 K. Interestingly, these experiments also display lenticular anticracks and/or planar transformation of ahrensite that strongly resemble those witnessed in deformation experiments on Mg_2GeO_4 (Green and Burnley, 1989; Burnley and Green, 1991; Riggs and Green, 2005). See section 7.6 for examples of microstructures and textures witnessed in the specimens recovered from these experiments. Experiments exceeding 950 K experienced rapid transformation to the high pressure phase. Of the two experiments below 950 K that did not exhibit AE events in the sample, HPF_AE_1 and HPF_AE_8, both

display conjugate faulting and ahrensite in the fault zone. Therefore, it is possible that faulting occurred but the acoustic signals associated with it were below the detection threshold which was set higher than later experiments (see Table 1).

Of all the events that locate within the sample, of particular note is the six signal event generated during HPF_AE_15. The sonic energy and impulsiveness of this event saturated all six transducers and was one of the largest events ever recorded by the system, including those associated with fracturing of the phenolic plates in early experiments. Figure 7.18 shows an example of one of the waveforms captured from channel 6 for this event.

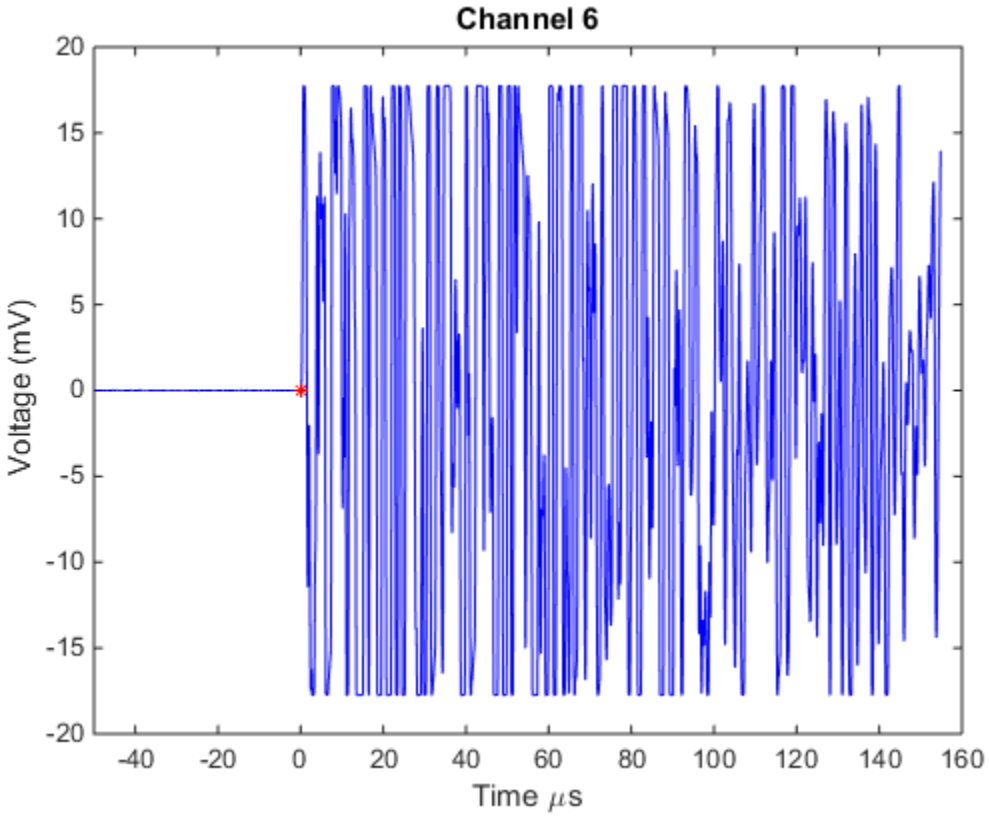

Figure 7.18: Example of the highly impulsive and energetic hit collected during HPHT deformation of HPF_AE_15. Note that the signal generated a very high voltage and saturated the detector.

In addition, because of its impulsiveness, it was possible to accurately pick the proper arrival times to within one data point (25 ns). Figure 7.19 shows a zoomed view of the arrival for the waveform in Figure 7.18. Each point shown represents a sampled datum. The red star represents the arrival point. Therefore, given the accuracy of the arrival time estimates there is reason to be highly confident that it originated from within the sample.

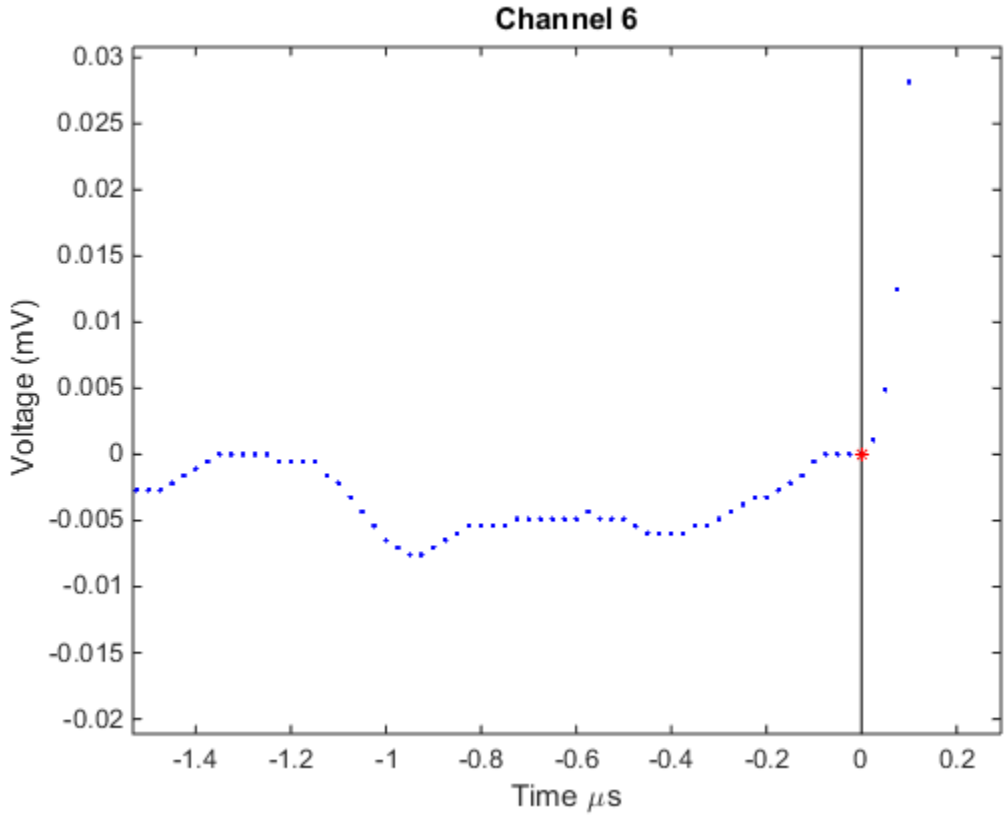

Fig 7.19: A zoomed view of the arrival of the waveform on channel 6. For every waveform connected with this event there was little to no ambiguity picking the waveform arrival times.

Figure 7.20 shows all six waveforms and their arrivals. The compressed vertical axis and the long horizontal axis makes them appear as if the waveforms arrived about 0.3 – 0.5 μs later than the arrival times picked, but zooming in to each waveform displayed results similar to the plot shown in Figure 7.19. Instead, the duration prior to the time the wave reached the most impulsive

part of its rise represents the acceleration of the rupture. For this event, this is approximately 1/3 of a wavelength or about 0.25 μs.

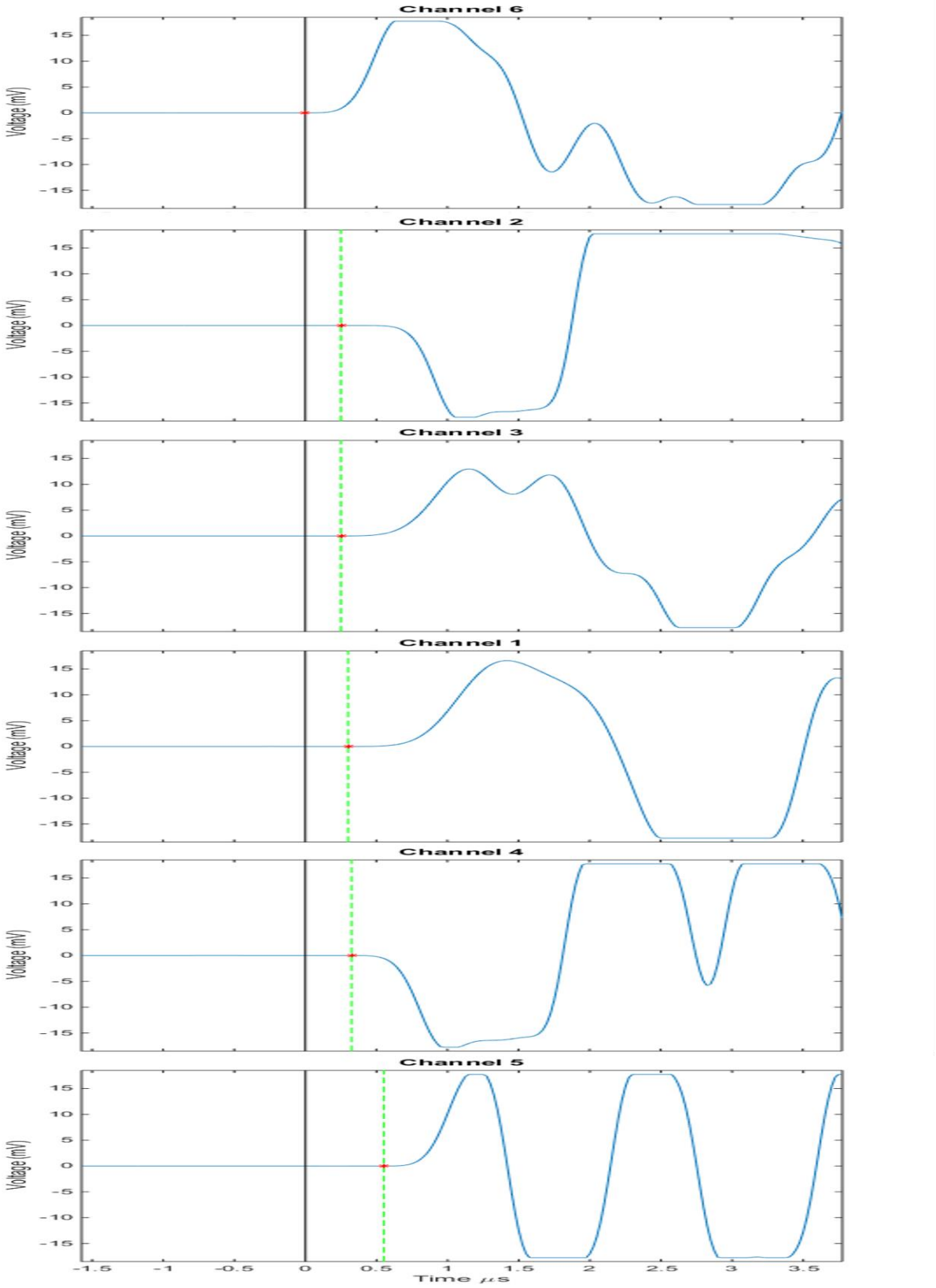

Figure 7.20: All six waveforms collected for the large event measured for HPF_AE_15 at HPHT. The vertical black lines coincide with the time of the first arrival. The red stars are the points of first arrival for each wave and are intersected by the green dashed lines to clarify the offset in time between the first arrival and later arrivals.

Figure 7.21 shows the location of all the events that located in the sample at HPHT for HPF_AE_15 (red dots), plotted alongside the events that located in the sample during cold compression (green dots). The large red dot represents the large event whose waveforms are shown in Figure 7.20. Note that its position coincides well with the initiation of rupture in the upper left corner of Figure 7.7. See Figure A.2.3 for phase analysis of HPF_AE_15 using Raman spectroscopy.

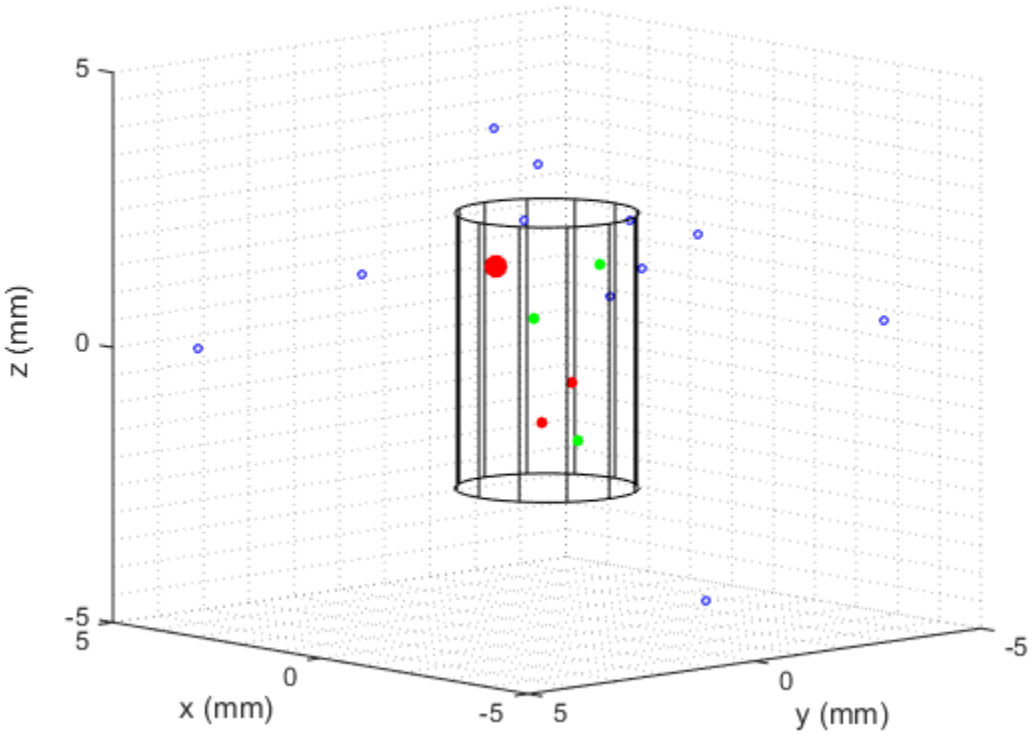

Figure 7.21: Events that locate within the sample for HPF_AE_15 during HPHT deformation (red dots) plotted alongside events that occurred during cold compression (green dots). The large event that saturated all six sensors is the large red dot. Open blue circles are events that occurred within the pressure medium during cold compression.

7.5.3 Decompression

Decompression generated several high energy events due to the release of elastic strain energy as pressure clamping relaxed discontinuously at low pressure. Those that located within the sample are presented in Table 4.

Experiment	Sigs	x	y	z	t	E	P	v	σ_x	σ_y	σ_z
(I.D)	(#)	(mm)	(mm)	(mm)	(s)	(a.u.)	(GPa)	(m/s)	(mm)	(mm)	(mm)
HPF_AE_1	6	0.34	-0.80	-1.51	54761	19633	0.49	6127	0.56	0.56	1.11
	6	0.37	0.10	-1.94	58343	124233	0.79	6229	0.56	0.56	1.13
HPF_AE_4	6	-0.89	1.07	-2.05	80545	335	0.44	6104	0.55	0.55	1.11
HPF_AE_5	6	-0.53	-0.79	0.59	49192	11830	0.40	6087	0.55	0.55	1.10
HPF_AE_6	6	0.63	-0.14	2.23	78845	465333	0.52	6135	0.56	0.56	1.11
HPF_AE_9	4	-1.22	0.31	-0.49	12118	29	3.98	6606	0.69	1.19	1.54
HPF_AE_10	6	-0.07	0.52	1.36	58446	3482	0.40	6089	0.55	0.55	1.10
	4	-0.43	-0.19	-0.99	59676	174	0.38	6083	1.01	0.79	1.43
	4	0.54	0.18	0.61	61098	173	0.37	6078	1.00	0.77	1.41

Table 7.4: Location data and uncertainty for events that located within the sample during decompression. Time is measured from the beginning of depressurization.

Figure 7.22 shows an example of one such event for HPF_AE_5. Not the location of the event coincides well with the position of the large decompression crack shown in Figure 7.7.

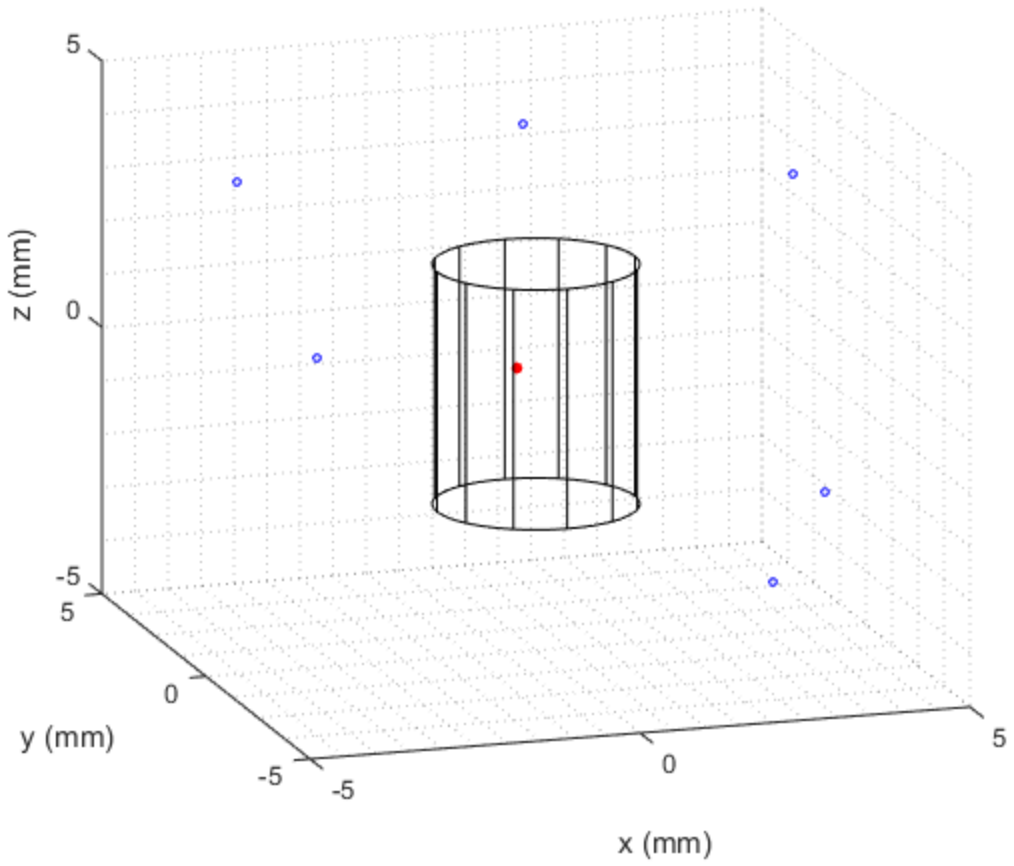

Figure 7.22: Events collected for HPF_AE_5 during decompression. The large event in the center of the image (closed red dot) coincides with the position of the large horizontal decompression fracture shown in Figure 7.7.

7.6 Microstructural analysis of recovered samples

In order to elucidate microstructures in the recovered specimens, thin sections were imaged using optical and scanning electron microscopy (SEM). All optical images were collected with reflected light and SEM images were collected in backscattered electron (BSE) mode. Because fayalite and ahrensite have the same atomic weight they are theoretically indistinguishable in grey scale, however the denser ahrensite phase backscattered electrons slightly more efficiently than fayalite and could be differentiated (Burnley et al., 1991).

HPF_AE_1: Microstructural analysis

HPF_AE_1 was run at the lowest temperature of any experiment and displayed a high degree of conjugate faulting with a small percentage of ahrensite within the faults. However, it registered AEs during cold compression that locate within the sample so it is possible that the faulting was due to fracturing in the brittle regime and not transformationally induced since no AEs located in the sample at HPHT. Figure 7.23 shows an image of the recovered sample taken within the box shown in Figure 7.12.

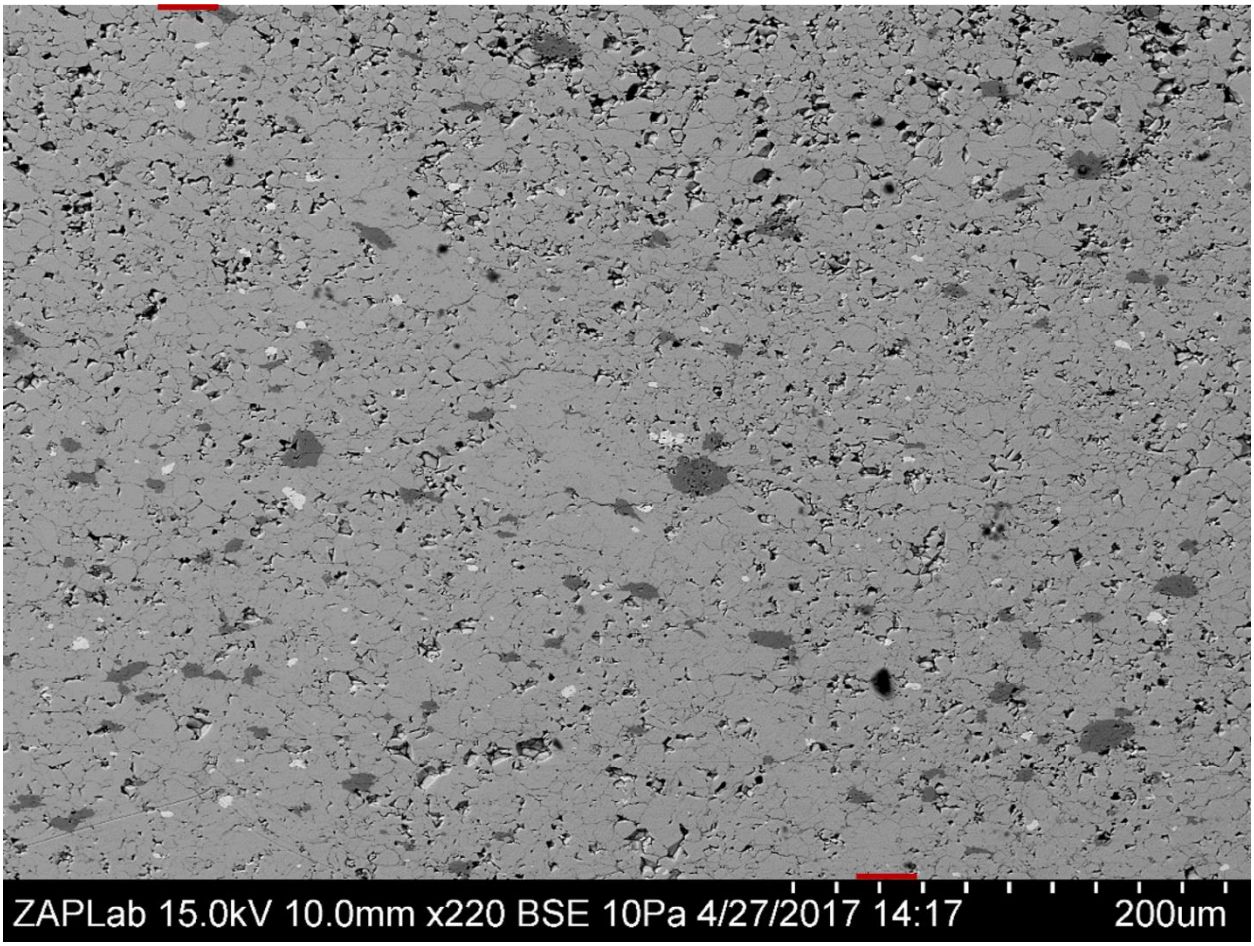

Figure 7.23: Low magnification BSE image of HPF_AE_1 located within the box shown in Figure 7.12. The fault runs from the upper left to the lower right of the image at an angle of ~40^0 and extends beyond the image dimensions. It appears slightly smoother and better consolidated than the surrounding matrix and grain boundaries are more difficult to make out. Red bars indicate where the fault enters and exits the image.

The fault runs diagonally through the entire image at an angle of ~40^0 to the vertical and is highlighted entering and exiting through the red bars. It is distinguished by the presence of fine grained highly consolidated material with much less porosity than the surrounding matrix. Along this feature several ferrosilite grains have been divided and offset as a result of shear fracture with small amounts of ferrosilitic material entrained along these regions. An example of one such grain is shown in Figure 7.24. The image is situated approximately 150 μm SE of where the fault is truncated by Figure 7.23.

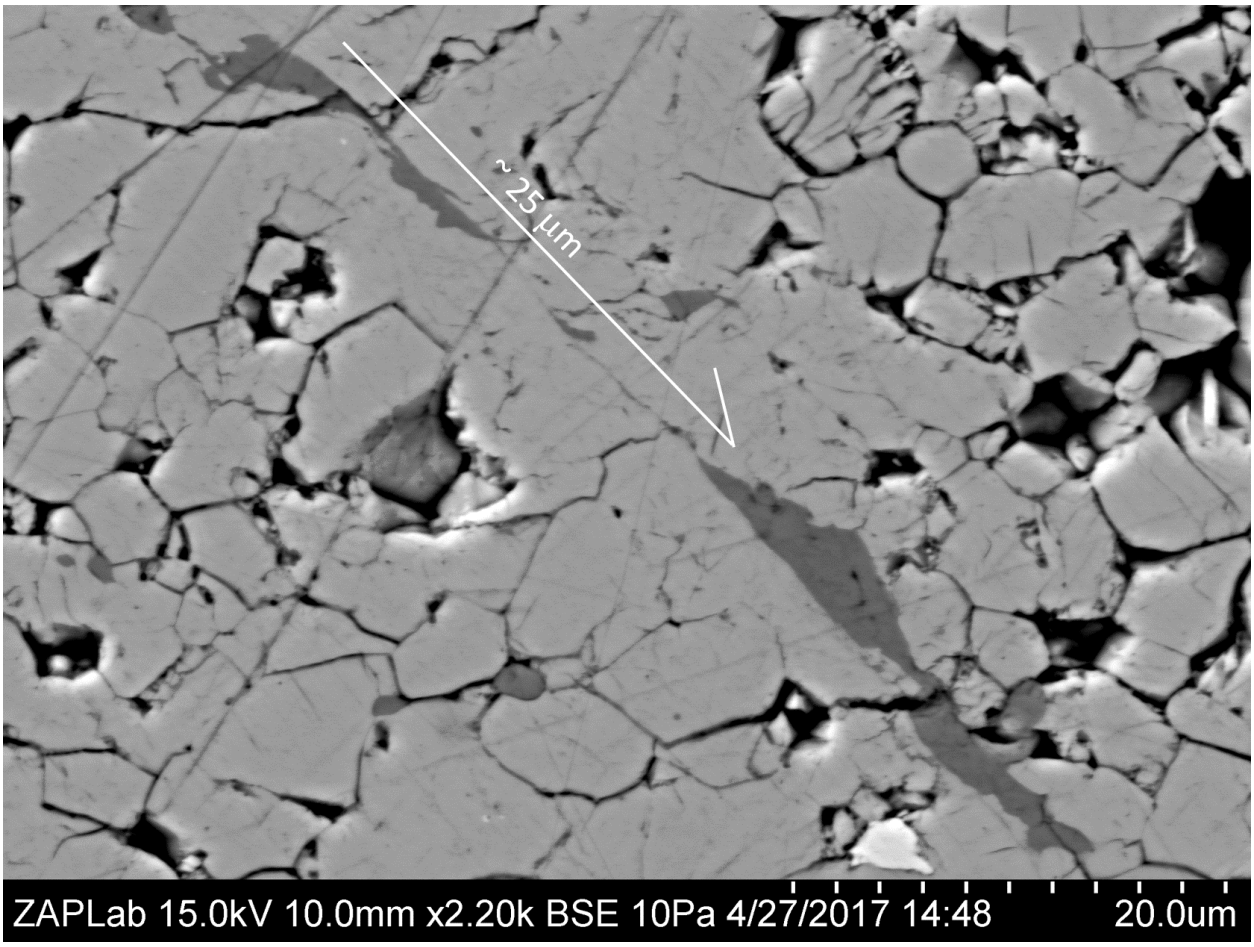

Figure 7.24: BSE image of a ferrosilite grain (dark grey) offset and entrained within the fault gouge.

HPF_AE_5: Microstructural analysis

HPF_AE_5 was run at a relatively high temperature and shown to have completely transformed to ahrensite based on XRD and Raman spectrographic evidence. BSE images of the recovered sample display small amounts of ferrosilite embedded in a homogeneous matrix of highly consolidated ahrensite. In most cases it is difficult to recognize grain boundaries and the sample contains a very low amount of porosity implying that once nucleation and growth of ahrensite had completely consumed fayalite grains, they began to grow together and into one another. A relatively low magnification image of the bulk sample is presented in Figure 7.25, followed by a higher magnification image taken within the same region (Figure 7.26). Note the difficulty in distinguishing grain boundaries compared to the images of HPF_AE_1 shown in Figures 7.23 and 7.24.

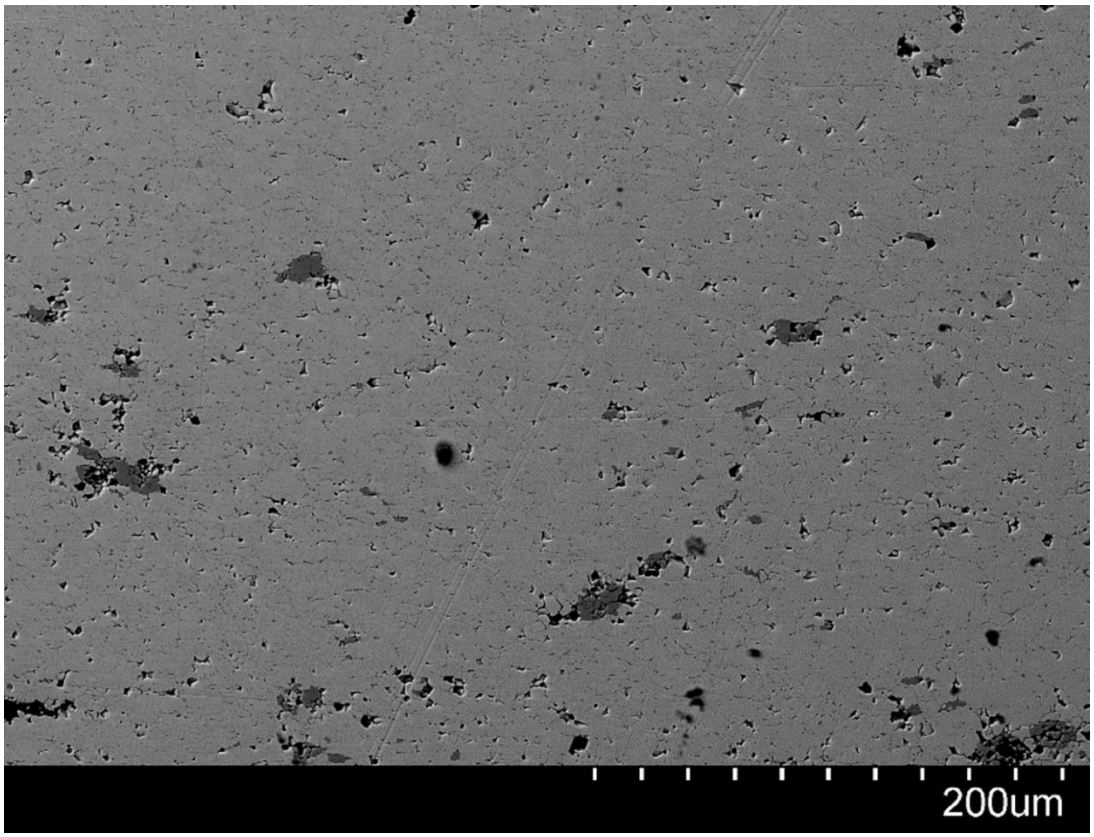

7.25: Low magnification BSE image of HPF_AE_5 after complete transformation to ahrensite.

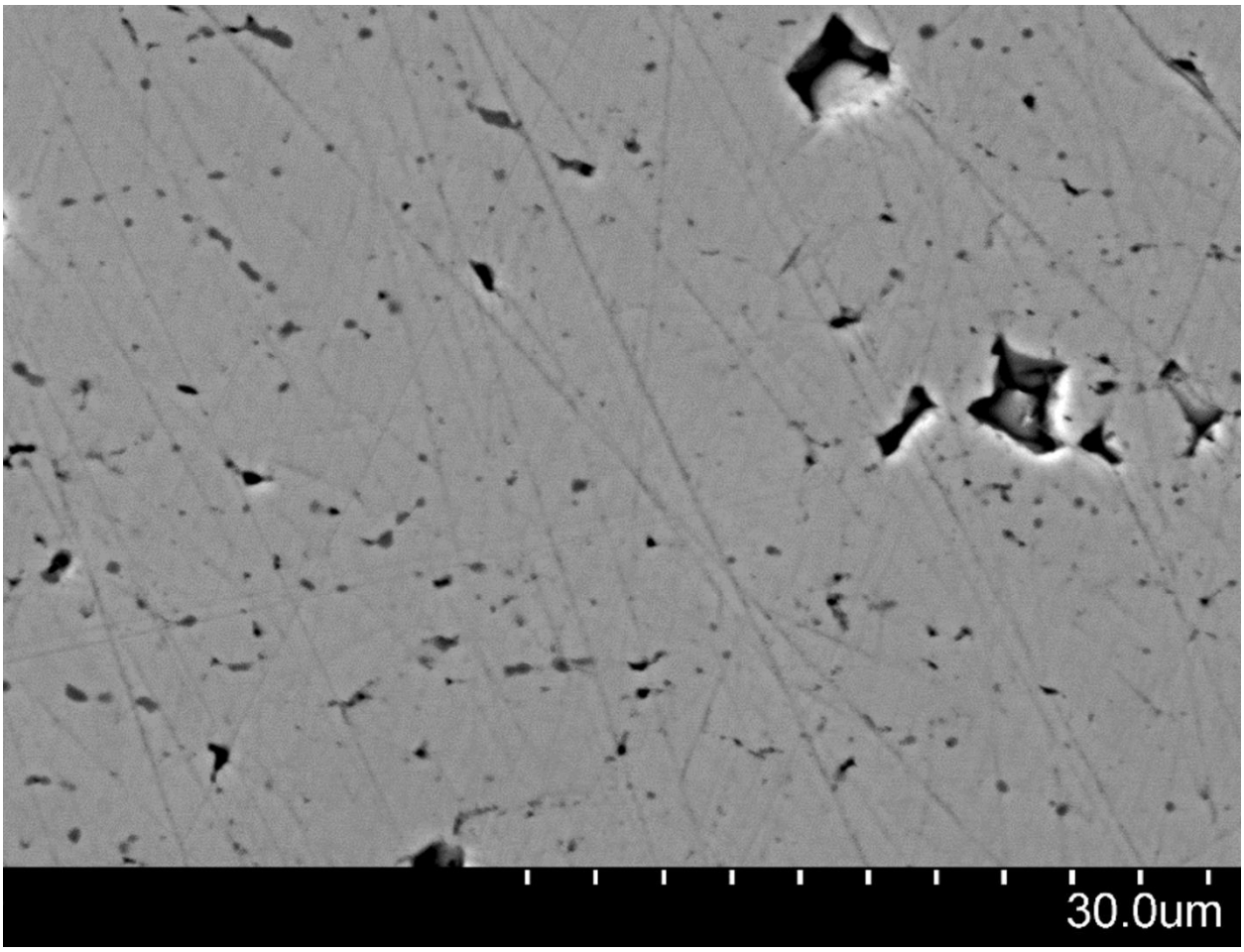

Figure 7.26: Zoomed in image of 7.25. Note the difficulty in distinguishing between the highly consolidated ahrensite grain boundaries. The black features in the upper right were caused by dislodging of grains during polishing.

HPF_AE_11: Microstructural analysis

HPF_AE_11 had a total of three AE events that located within the sample and Raman analysis of the fault zones showed significantly more ahrensite inside them than adjacent to them (see Figure 7.13). Figure 7.27 shows a grey scale optical image of the recovered sample detailing the presence of several conjugate faults which appear bright due the ahrensite contained within them.

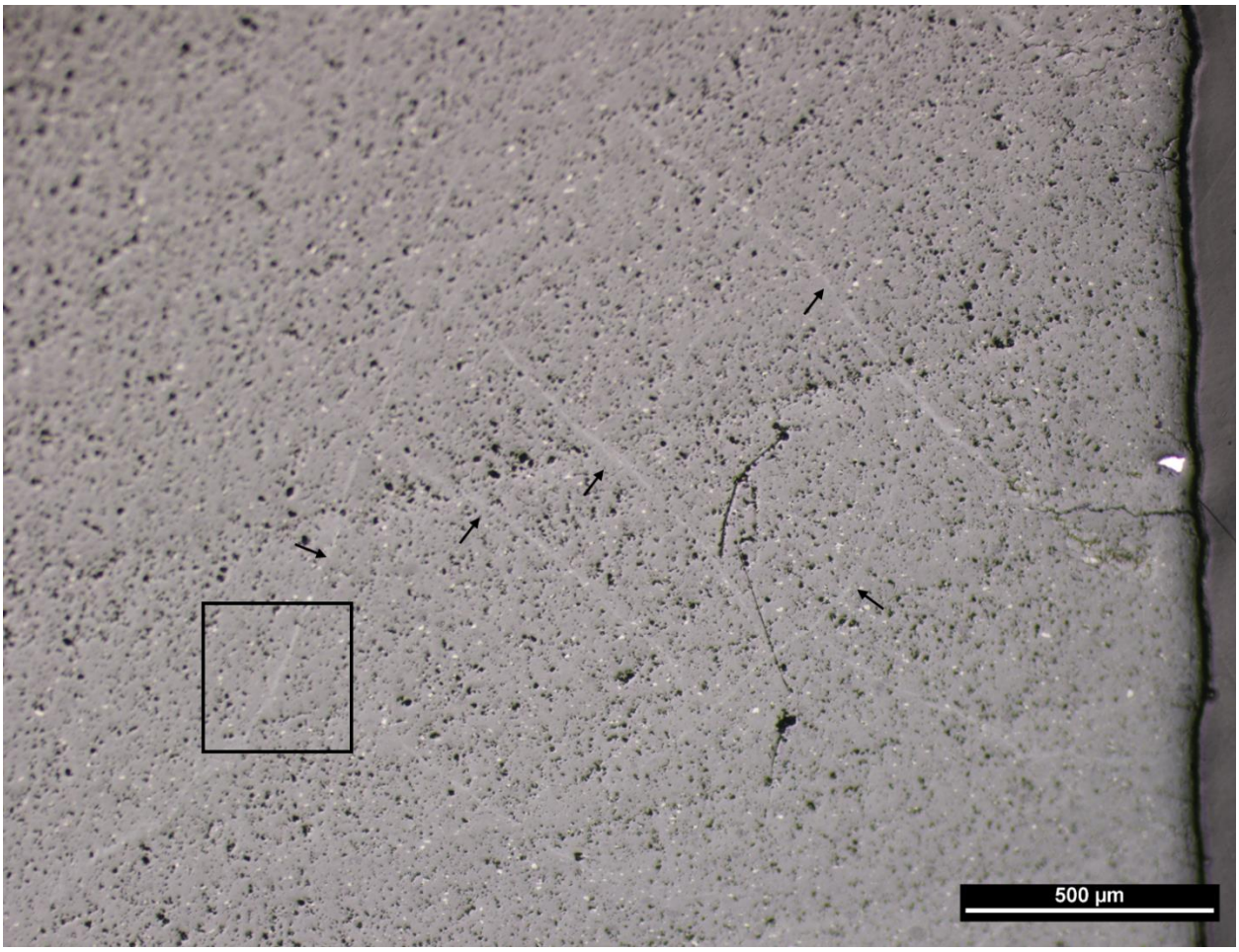

Figure 7.27: Grey scale optical image in reflected light. Ahrensite, which appears lighter, is confined to within the fault zone of several conjugate faults. A few of them are indicated by arrows.

Figure 7.28 shows a BSE image of the box shown in Figure 7.27. The fault can be distinguished from the background matrix by the network of horizontal unloading cracks confined within the fault zone. These features are typical of dislocation pileups that cause stress localization within the faulted regions resulting in fractures perpendicular to the direction of greatest deviatoric stress upon decompression (Christie, 1964). Also, ahrensite is a denser phase which likely concentrated stresses in the fault gouge which caused the horizontal fractures to occur when the sample was unloaded.

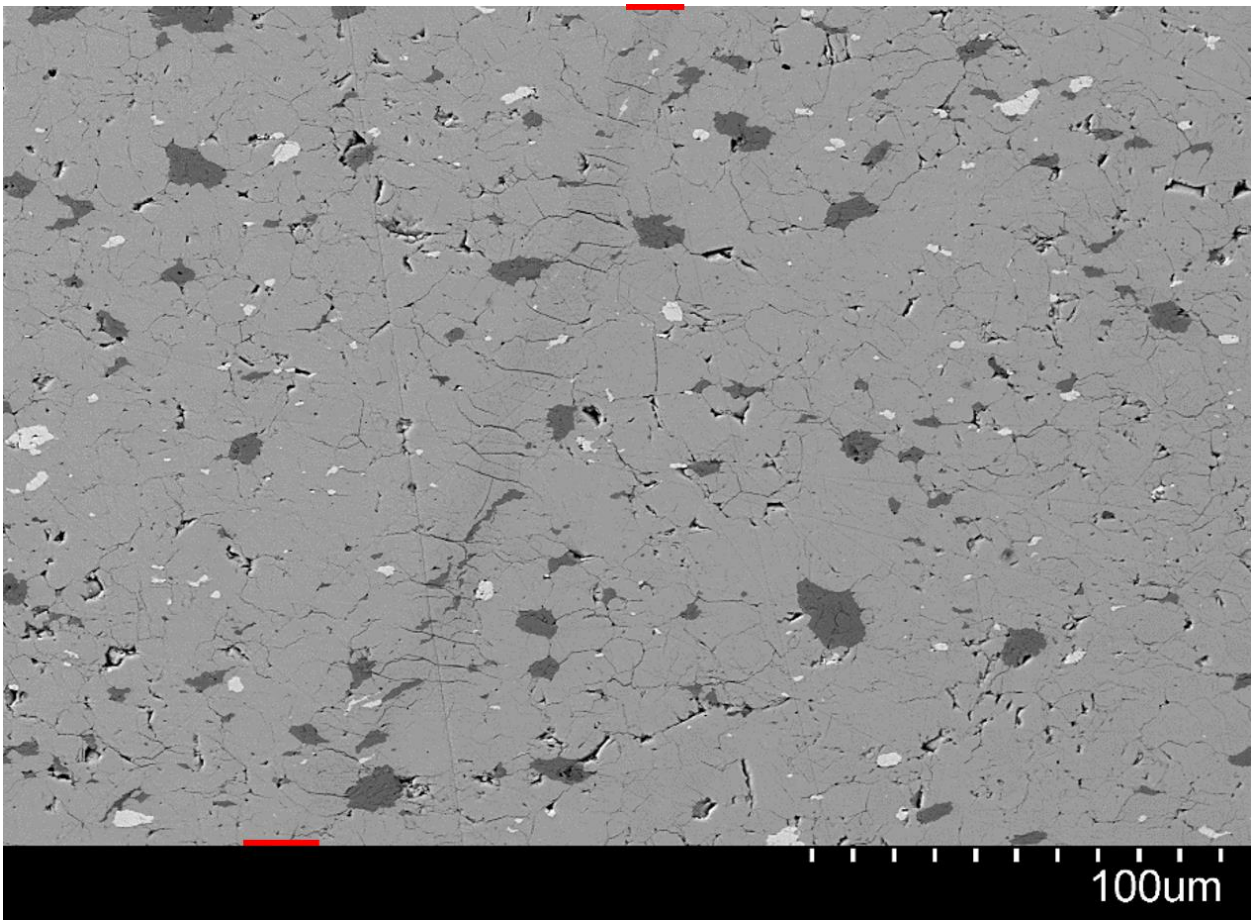

Figure 7.28: BSE image of the fault located in the lower left of Figure 7.13. The fault can be distinguished from the surrounding matrix by the presence of horizontal cracks contained within it.

Closer inspection of the fault gouge revealed anticrack type lenses of ahrensite that are virtually indistinguishable from those seen in HPHT faulting experiments on Mg_2GeO_4 (Green and Burnley, 1989; Burnley et al., 1991). Figure 7.29 shows an example of these features as well as grains that were entrained within the fault gouge during coseismic slip along the fault.

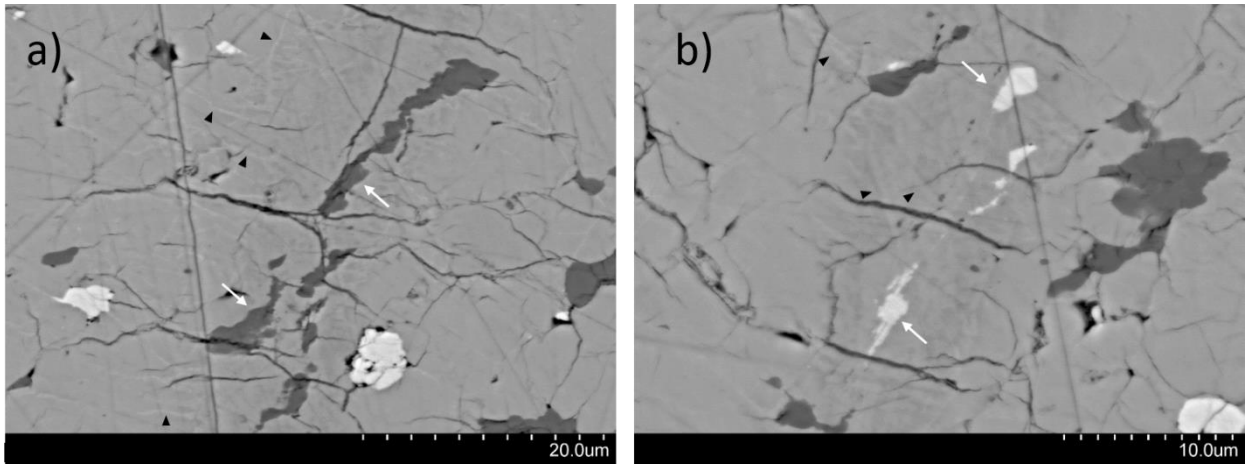

Figure 7.29: BSE images of the fault gouge showing the presence of anticrack lenses of ahrensite growing on grain and subgrain boundaries (black arrowheads). a) A ferrosilite grain, which appears dark grey, being entrained within the fault gouge (white arrows). b) A magnetite grain, which appears white, being entrained within the fault gouge (white arrows). The principal stress is vertical in both images.

The ahrensite has grown as several small lenses a few μm in length on both grain and sub-grain boundaries with some capable of crossing grain boundaries. Similar to the anticracks associated with faulting at HPHT in Mg_2GeO_4, they tend to develop parallel to one another at high angles to the principal stress. They can also be seen linking together along paths roughly parallel to the fault orientation.

HPF_AE_14: Microstructural analysis

HPF_AE_14 was run with a temperature of 823 K which was 50 K higher than HPF_AE_11 and displays many similar features but the degree of transformation was much higher. The regions containing faults, which can easily be delineated by the Ag markers, transformed entirely to ahrensite which shows up as slightly darker than the rest of the image. Figure 7.30 shows an example of a several faults that have transformed into ahrensite.

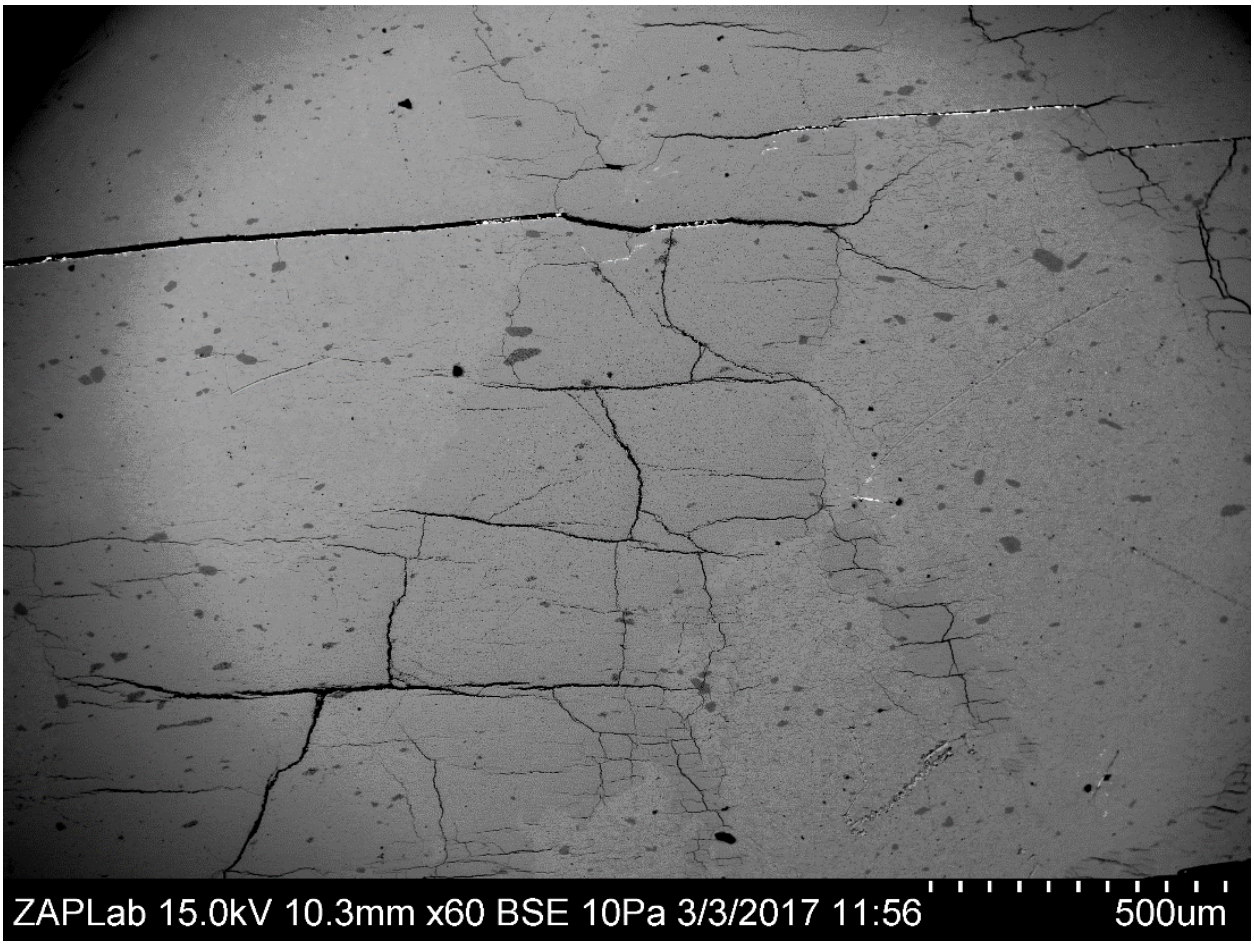

Figure 7.30: BSE image of several faults that have transformed entirely to ahrensite. They appear slightly darker than the partially transformed regions and contain significant amounts of decompression cracks.

The faults zones, possibly generated under HPHT conditions, have subsequently transformed entirely to ahrensite which continued to nucleate and grow horizontally outward from the original fault position. These zones are composed of fully transformed, highly consolidated, low porosity material similar to what was observed in HPF_AE_5 in which the entire sample transformed to ahrensite phase. The difference between the two is that the transformed regions of HPF_AE_14 display several large decompression cracks and fissures that are confined to the transformed areas. The likely reason for this is that the negative volume change associated with the transformation generated large stress concentrations in these areas compared to the surrounding partially transformed material. Upon decompression this stress was released resulting in the network of

fractures confined to the transformed regions. Figure 7.31 shows a view of the boundary of one of these features.

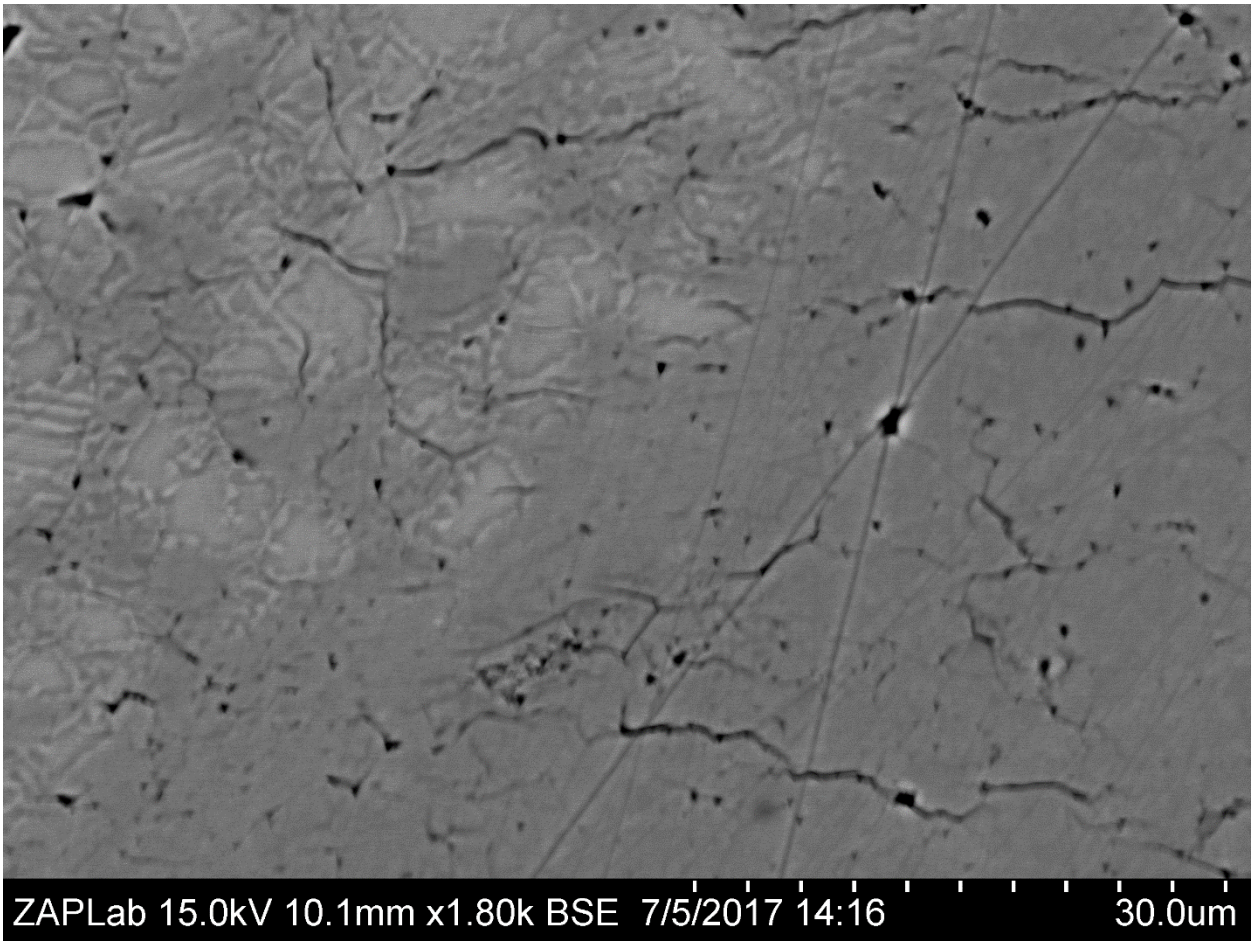

Figure 7.31: The boundary between fully transformed (right side of image) and partially transformed (left side of image) Fe_2SiO_4 in HPF_AE_14.

Adjacent to the fully transformed regions the material is partially transformed with ahrensite decorating grain boundaries as well as growing as lenses and planar transformation features, some of which have been thickened as transformation progressed. Closer inspection of these partially transformed regions display both anticrack lenses and planar transformation features similar to those associated with HPHT faulting in Mg_2GeO_4 (Riggs and Green, 2005). Figure 7.32 shows an example of each.

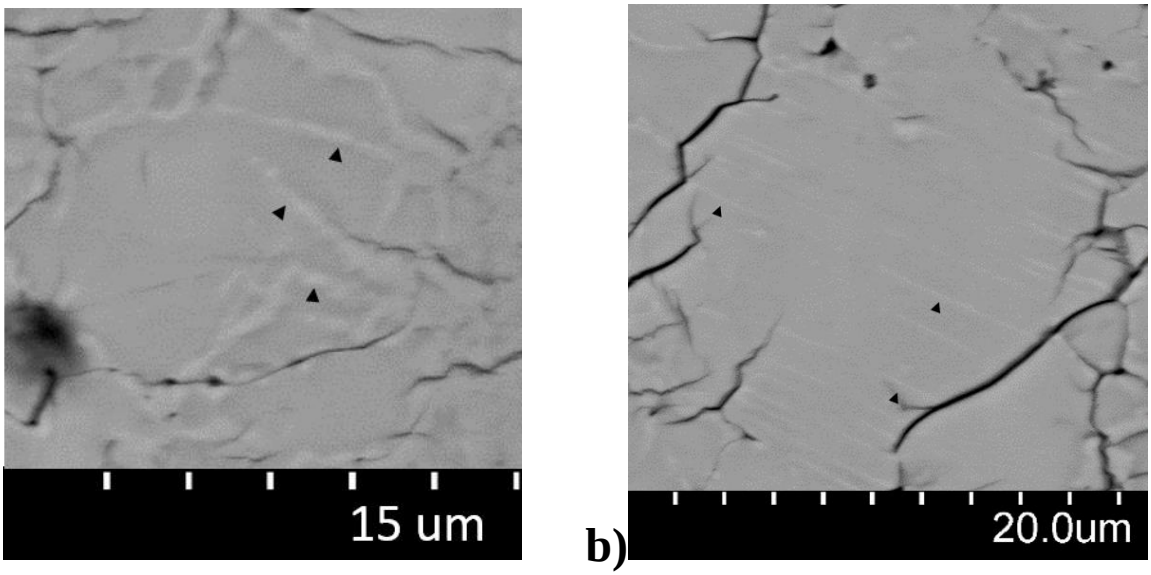

Figure 7.32: HPF_AE_14 sample with black arrowheads indicating a) Anticrack lenses and b) planar transformation features adjacent to the fully transformed faulted regions. Similar features are present throughout most of the sample except in the fully transformed regions which grew outward from the faults.

These features show up throughout most of the sample with a higher density of them near the boundary of the regions that originally started out as faults but transformed to the high pressure phase. It is worth noting that these features are not mutually exclusive which was also observed by Riggs and Green (2005) in Mg_2GeO_4. Therefore, it is likely that the fault zones were initially created by way of transformations of these types, but got entirely consumed by incoherent nucleation and growth of ahrensite over the course of the experiment. HPF_AE_10 also shows similar results (see Appendix 3).

HPF_AE_15: Microstructural analysis

HPF_AE_15 displayed several large faults including one that traversed the entire length of the sample. A composite image of part of the fault is shown below in reflected light (Figure 7.33).

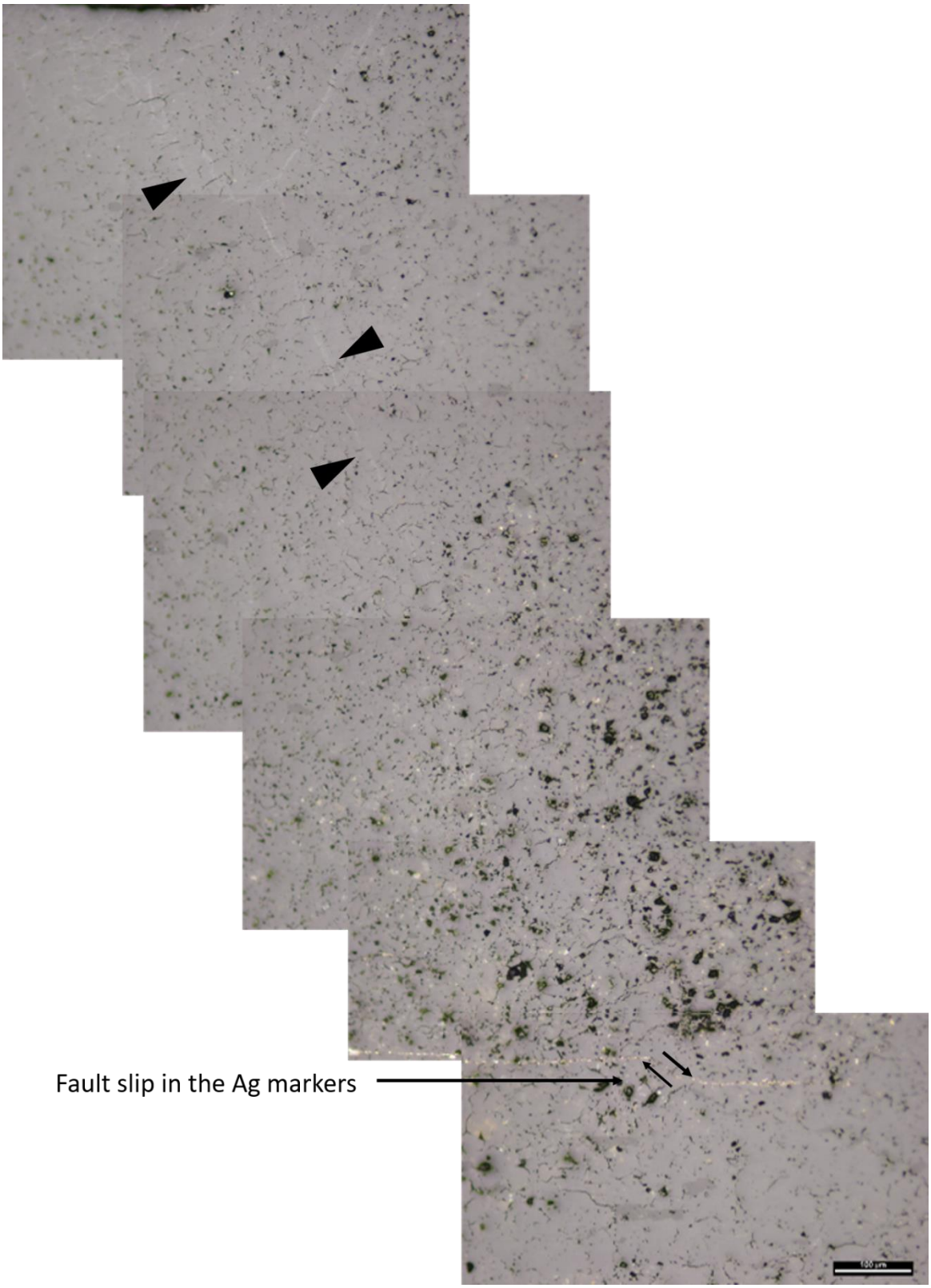

Figure 7.33: Composite micrograph in reflected light of ~1/3 of the length of a fault that traverses the entire length of HPF_AE_15. In the N-W region of the image ahrensite can be seen as thin bright line contained within the fault zone (black arrowheads), but eventually disappears about ¼ of the way along the rupture. Further along the fault in the bottom panel the Ag marker has been displaced as indicated by the black arrows.

Ahrensite can be seen decorating the fault zone for ~1/4 of the rupture length but eventually disappears. The fault, however continues and can be seen offsetting the Ag marker. It even extended through the entire sample offsetting the second Ag marker and continued until it reached the bottom of the sample. SEM imaging of the recovered sample revealed that the ahrensite grew as lenses that are only present in the vicinity of the fault zone, however they do not exist throughout the entire length of the fault. An example of these structures is shown in Figure 7.34.

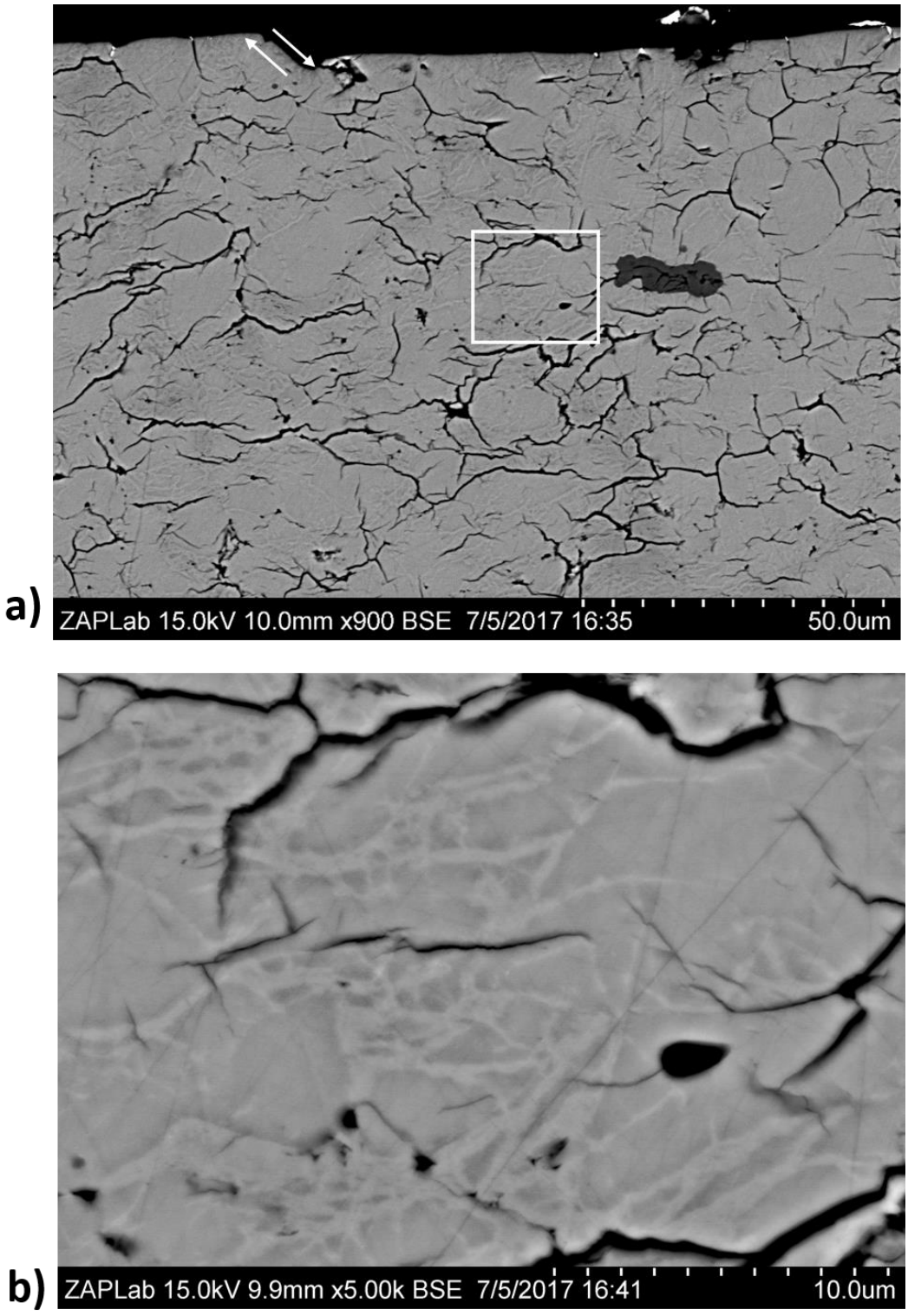

Figure 7.34: Anticrack type lenses nucleating in the vicinity of the fault. a) Low magnification BSE image of the N-W section of the fault. The presence of ahrensite exhibiting the anticrack morphology can be seen within the fault and surrounding material. The fault displacement can be seen at the top of the image (white arrows). b) The boxed region shown in a) under enhanced magnification. The ahrensite lenses are shown growing on grain and subgrain boundaries and linking together to form a network.

7.7 Discussion

In general, acoustic events were initiated near the beginning of deformation at high temperature reflecting Kirby's (1987) hypothesis that faulting occurs when incoherent nucleation and growth of the high pressure phase becomes just kinetically possible. In the presence of shear stress, this initiates runaway transformation along a planar zone leading to macroscopic faulting. This also explains why failure only occurred in a narrow temperature window (~650 – 950 K). Temperatures exceeding this will cause rapid transformation leading to weak and ductile behaviour. Of the six experiments in which AEs were observed to originate within the sample or within 1σ from it, all of them display anticrack type lenses of ahrensite. Of these six experiments, three of them also displayed the same planar transformation features shown to initiate HPHT faulting in Mg_2GeO_4 coexisting with the anticracks. Individual grains of ahrensite in these features are too small to image directly with the SEM, but the fact that the thickness of the lenses are at most ~1μm provides an upper bound on grain size. In reality, individual grains may be much smaller, perhaps even order(s) of magnitude, which would be possible to clarify using transmission electron microscopy (TEM). In most cases these structures tended to develop either inside or in the vicinity of the fault gouges, but could be found throughout a few of the samples that underwent higher degrees of partial transformation. Since AEs were generally recorded near the beginning of deformation it is probable that many of these features were further developed and thickened after faulting occurred since they remained under high P,T and stress conditions for the entire duration of the experiment. This needs to be taken into account when attempting to determine how much ahrensite is required to initiate a mechanical instability and what anticrack density is required for faulting to take place. This may also explain why the faults witnessed in our samples are thicker

than what was observed in some studies on Mg_2GeO_4 when samples were quenched immediately after observing a stress drop (i.e. the moment after faulting initiated) (Green et al., 2015).

The low number of AEs recorded (<5) in this set of experiments is most likely a reflection of the incompatibility of the frequency response of the transducers with respect to the frequency spectrum for events expected from sub mm rupture lengths. In this case only the high end frequency of the transducer response will overlap with the lowest frequencies generated by an AE event and only a small amount of acoustic energy will be collected. Therefore several small events may have been generated but their presence was not detected. This also explains why most of the events that did locate in or near the sample appear to have very low energies. However, one event generated during deformation of HPF_AE_15 possessed one of the largest amounts of energy ever recorded by the system (see section 7.5.2). There is good reason to believe this event resulted in association with the phase transition. Its location in the sample (Figure 7.21) coincides well with the position of the fault beginning in the N-W corner of Figure 7.7a and running S-E for entire length of the sample. This location estimate can be considered accurate since the impulsiveness of the waveforms allowed for precise determination of arrival times. Therefore, the uncertainty of $[\sigma_x, \sigma_y, \sigma_z] = [0.45, 0.45, 0.91]$ mm quoted in Table 7.3 is almost certainly an overestimate. The reason the transducers recorded such high amplitude waveforms is a combination of two factors: the event itself released a lot of seismic radiation and the frequency spectrum of that radiation coincided with the resonant frequency of the transducers. A rough estimate of the period of acoustic waves radiated from a fault can be estimated from the rupture length, L_R, multiplied by the rupture velocity which is typically on the order of half the shear wave velocity, V_s. The shear wave velocity of fayalite at the HPHT conditions where the event occurred is ~4 km/s (Liu et al., 2008; Liu et al., 2010), therefore, for the 4 mm fault in HP_AE_15 this translates to a frequency

of $\nu = (V_s/2)(1/L_{rupture}) = 500kHz$. This is very close to most prominent frequency contained in the waveforms from this event as show in Figure 7.35.

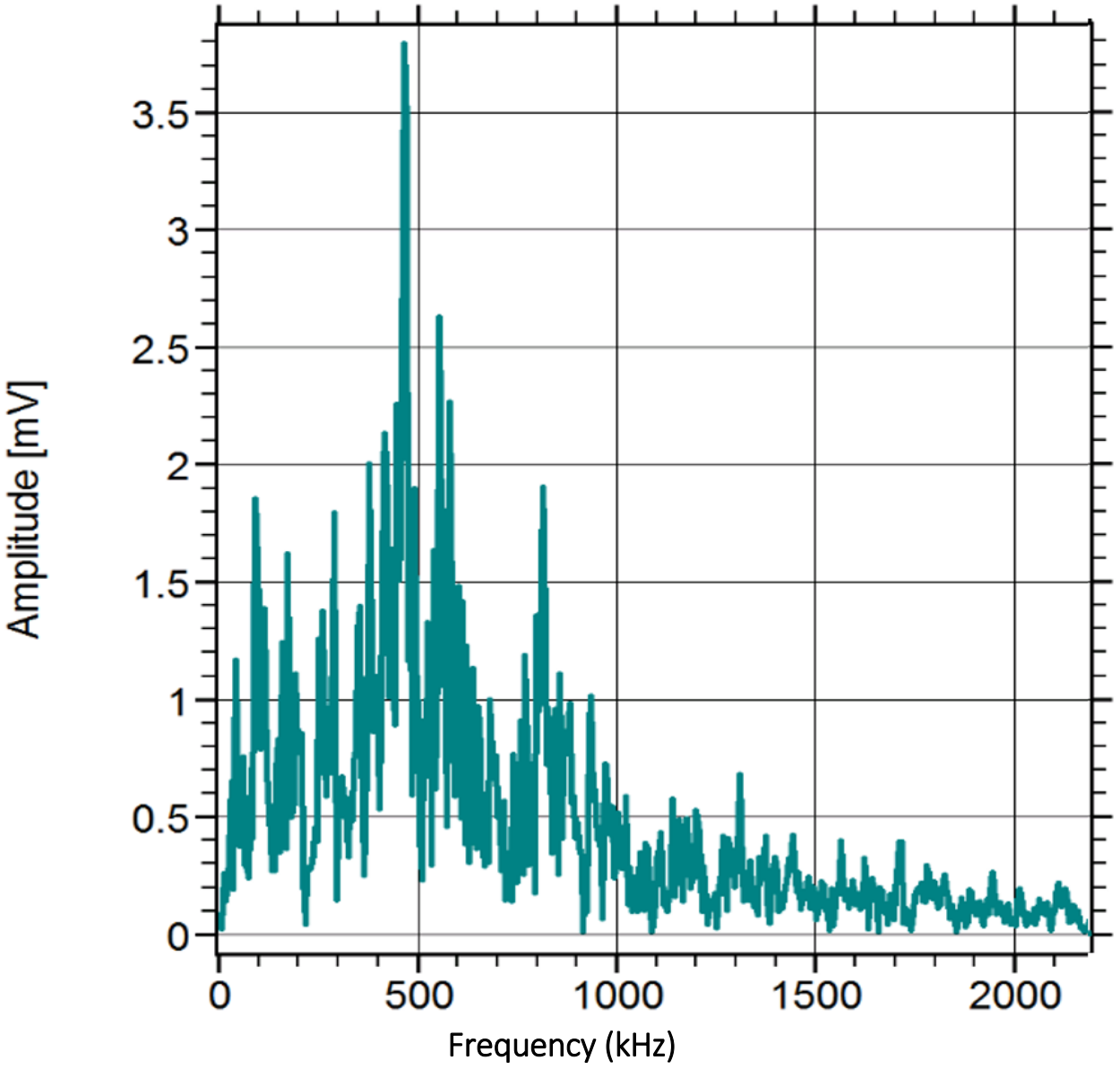

Figure 7.35: Frequency spectrum for a signal making up the large seismic event in HPF_AE_15.

While this is only an approximate estimate it explains why an event of such magnitude was recorded and adds credibility to the hypothesis that the acoustic signal collected arose from that fault.

7.7.1 Application to mantle slabs

Given the fact that anticracks were found contained within the fault that occurred in HPF_AE_15, there is very strong evidence supporting this event was associated with transformational faulting. However, the apparent paucity of ahrensite throughout the entire length of the fault gouge is worth discussing. It appears that ahrensite nucleated in the form of anticracks on grain and subgrain boundaries near the site of fault initiation but did not continue to develop beyond about 1/3 of the way through rupture. Nonetheless, the fault managed to extend the entire length of the sample. One possibility is that nanometric ahrensite is contained throughout the fault but is too fine to distinguish using the SEM. The other is that instability was initiated by the phase transformation but was sustained by way of a different process. Assuming adiabatic conditions, the temperature increase ΔT caused by frictional sliding, can be expressed as $\Delta T = \mu(\sigma_n D/h\rho C)$ (Rice, 2006) where μ is the coefficient of friction, σ_n the normal stress, *D* the coseismic slip, *h* the thickness of the shear band and ρ*c* the specific heat capacity per unit volume. This calculation neglects heat dissipation and the exothermic nature of the transformation, which have opposite effects and tend to cancel each other to some degree. From the AE record we know that σ_n = 4.14 ×10^9 Pa and the specific heat capacity of fayalite at the P,T conditions of the event is 4×10^6 Pa/K (Benisek et al., 2012). The coseismic slip was measured directly from the offset of the Ag film and the width of the fault gouge is ~ 1.5×10^{-6} m (Figure 7.36).

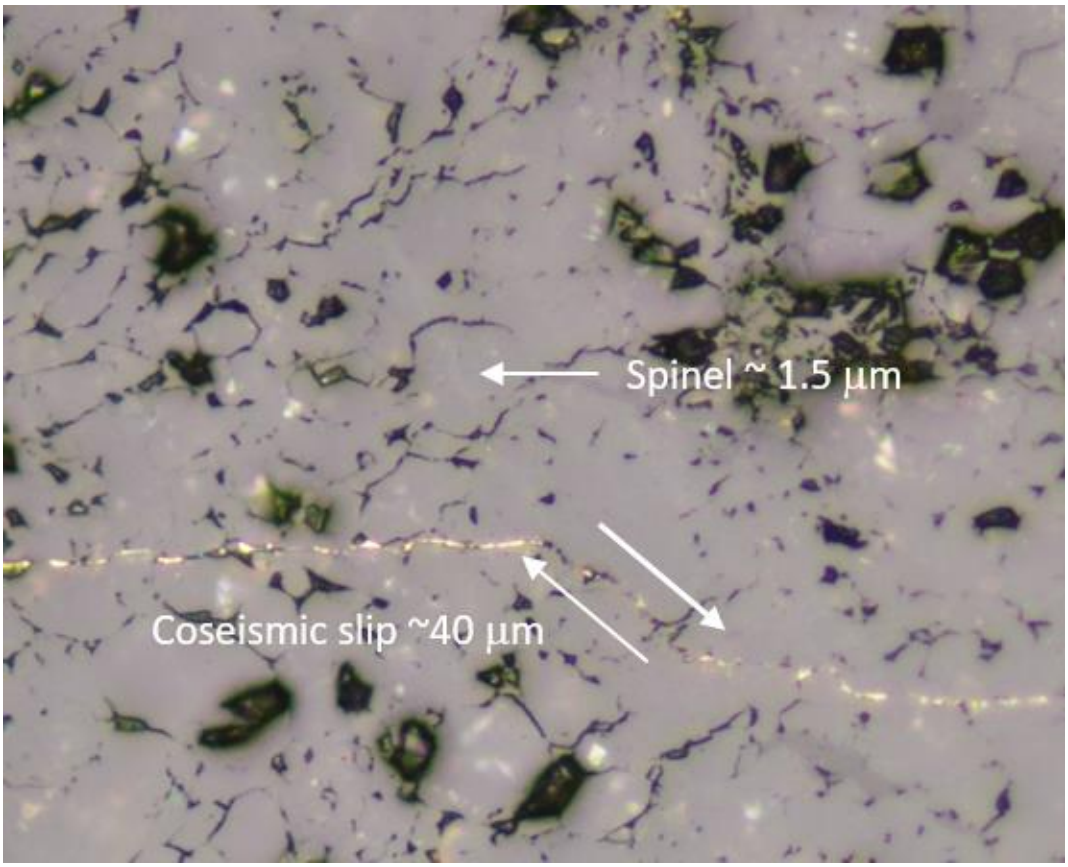

Figure 7.36: The fault, based on the width of ahrensite, and coseismic slip of the fault generated in HPF_AE_15.

Assuming μ ~0.1, a typical value for the steady state frictional coefficient on lubricated faults (Di Toro, 2011), suggests that ΔT generated during sliding would be about 2760 K. Coupled with the experimental run temperature this equates to a temperature of >3400 K which is enough to melt portions of the fault zone (Ohtani, 1979; Akimoto, 1967). This would even be the case if a value of D = $3x10^{-6}$ m is used which is the width of the ahrensite present in the widest regions of the fault zone. If on the other hand frictional melting did not occur, this implies the temperature remained below T_{Melt} = 1710 K and sets an upper bound on the frictional coefficient of ~0.037 which is approximately a factor of 4 higher than that inferred from HPHT in Mg_2GeO_4 (Schubnel et al., 2013; Green et al., 2015) but much lower than those exhibited in high speed friction studies (Di Toro, 2011). In this case the fault surfaces would act as a lubricated interface unable to support shear stress. If the temperature increase placed ΔT between 395 and 1035 K it implies the fault zone was in the stability field of fayalite and the frictional coefficient was even lower, between 0.014 and

0.037. Furthermore, the viscosity of Fe_2SiO_4 melt decreases significantly with pressure which would further lower the coefficient of friction (Spice et al., 2010). Perhaps this could even lead to a superplastic flow scenario if the increase in strain rate caused by the initiation of brittle failure was large (Hobbs and Ord, 1988; Karato, 2001). If so, this would explain why the fault was able to progress without the generation of ahrensite. For a subducting slab, this is equivalent to a rupture initiating due to transformational faulting in the olivine wedge but progressing as a plastic instability. Perhaps this provides an explanation why a few DFEQs appear to have rupture dimensions larger than the olivine wedge confined to the interior of subducting slabs (Tibi et al., 1999; Estabrook and Bock, 1995). If transformational faulting initiates rupture in the cold slab core, this could trigger superplastic flow allowing the rupture to grow outside of the metastable olivine wedge (Ogawa, 1987). This is the conclusion drawn by Zhan et al., (2014) for the 1994 Bolivia earthquake based on analysis of the sequence of subevents associated with it. Given the thermal gradient in the sample, perhaps once the rupture reached the warmer central region thermal runaway occurred. If so, this would help reconcile conflicting observations that lend support to either transformational faulting or shear heating/super plastic flow since this result would indicate that they are not mutually exclusive and can act in concert with one another.

7.8 References

Akimoto S., Komada E. and Kushiro I., 1967. Effect of pressure on the melting of olivine and spinel polymorph of Fe_2SiO_4, *J. Geophys. Res.*, **72**, 679–686.

Benisek, K., Kroll, H. and Dachs E, 2012. The heat capacity of fayalite at high temperatures, *American Mineralogist*, **97**, 657-660.

Burnley, P.C., Green, H.W. and Prior, D.J., 1991. Faulting associated with the olivine to spinel transformation in Mg_2GeO_4 and its implication for deep-focus earthquakes, *J. Geophys. Res.*, **96**, 425-443.

Chen, J., Weidner, D.J., Parsie, J.B., Vaughn, M.T. and Ratteron, P., 2001. Observation of cation reordering during the olivine spinel transition in fayalite by *in situ* synchrotron X-ray diffraction at high pressure and temperature, *Phys. Rev. Lett.*, **86**, 4072-4075.

Chopelas, A. 1991. Single crystal Raman spectra of forsterite, fayalite, and monticellite, *Am. Mineral.*, **76**, 1101-1109.

Christie, J.M., Griggs, D.T. and Carter, N.L., 1964. Experimental evidence of basal slip in quartz, *J. Geol.*, **102**, 734-756

Di Toro, G., Han, R., Hirose, T., De Paola, N., Nielsen, S., Mizoguchi, K., Ferri1, F. Cocco, M. and Shimamoto, T., 2011. Fault lubrication during earthquakes, *Nature*, **471**, 494-498.

Dobson, D.P., Meredith, P.G. and Boon, S.A., 2004. Detection and analysis of microseismicity in multi anvil experiments. *Phys. Earth Planet In.*, **143-144**, 337-346.

Estabrook, C.H. and Bock, G., 1995. Rupture history of the great Bolivian earthquake: slab interaction with 660 km discontinuity?, *Geophys., Res., Lett.*, **22**, 2277-2280.

Green, H.W. and Burnley, P.C., 1989. A new self-organizing mechanism for deep-focus earthquakes, *Nature*, **341**, 733-737.

Green, H.W., Young, T.E, Walker, D. and Scholz, C.H., 1990. Anticrack-associated faulting at very high pressure in natural olivine, *Nature*, **348**, 720-722.

Green, H.W., Shi, F., Bozhilov, K. and Reches, Z., 2015.Phase transformation and nanometric flow cause extreme weakening during fault slip, *Nature Geoscience*, **8**, 484-489.

Gasc, J., Schubnel, A., Brunet, F., Guilln, S., Mueller, H.-J. and Lathe, C., 2011. Simultaneous acoustic emissions monitoring and synchrotron X-ray diffraction at high pressure and temperature: Calibration and application to serpentinite dehydration, *Phys Earth Planet Inter.*, **189**, 121-133.

Hobbs, B.E. and Ord, A., 1988. Plastic instabilities: implications for the origin of intermediate and deep focus earthquakes, *J. Geophys. Res.*, **93**, 10521-10549.

Houseman, G. and England, P., 1986. A dynamical model of lithospheric extension and sedimentary basin formation, *J. Geophys. Res.*, **91**, 719-729.

Karato, S.-I., Riedel, M.R. and Yuen, D.A., 2001. Rheological structure and deformation of subducted slabs in the mantle transition zone: implications for mantle circulation and deep earthquakes, *Phys. Earth. Planet Int.*, **127**, 83-108.

Kirby, S.H., 1987. Localized Polymorphic Phase Transformations in High-Pressure Faults and Applications to the Physical Mechanism of Deep Earthquakes, *J. Geophy. Res.*, **92**, 13789-13800.

Kolesov B. A., Tanskaya, J. V., 1996. Raman spectra and cation distribution in the lattice of olivines, *Materials Research Bulletin*, **31**, 1035-1044.

Kolesov B. A., Geiger, C. A., 2004a. A Raman spectroscopic study of Fe-Mg olivines, *Physics and Chemistry of Minerals,* **31**, 142-154.

Kolesov B. A., Geiger, C. A., 2004b. A temperature dependent single-crystal Raman spectroscopic study of fayalite:evidence for phonon-magnetic excitation coupling, *Physics and Chemistry of Minerals*, **31**, 155-161.

Liu, Q., Liu, W., Whitaker, M.L., Wang, L.P., and Li, B.S., 2008. Compressional and shear wave velocities of Fe_2SiO_4 spinel at high pressure and high temperature. *High Press. Res.*, **28**, 405–413.

Liu, Q., Liu, W., Whitaker, M.L., Wang, L.P., and Li, B.S., 2010. In situ ultrasonic velocity measurements across the olivine-spinel transformation in Fe_2SiO_4. *American Mineralogist*, **90**, 1000–1005.

Ma, C., Tschauner, O., Beckett, J.R., Liu, Y., Rossman, G.R., Sinogeikin, S.V., Smith, J.S., Taylor, L.A., 2016. Ahrensite, γ-Fe2SiO4, a new shock-metamorphic mineral from the Tissint meteorite: implications for the Tissint shock event on Mars, *Geochimica et Cosmochimica Acta*, doi: http://dx.doi.org/10.1016/j.gca.2016.04.042

Mouri, T., Enami, M., 2008. Raman spectroscopic study of olivine-group minerals, *Journal of Mineralogical and Petrological Sciences*, **103**, 100-104.

Nasdala, L., Smith, D.C., Kainl, R. and Zieman, M.A., 2004. Raman Spectroscopy: Analytical perspectives in mineralogical research, **6**, Chapter 7, 281-343.

Ogawa, M., 1987. Shear instability in a viscoelastic material as the cause of deep earthquakes, *J. Geophys. Res.*, **92**, 13801-13810.

Ohtani, E, 1979. Melting relation of Fe_2SiO_4 to about 200 kbar, *J. Phys. Earth*, **27**, 189-208.

Ono, S., Kikegawa, T. and Higo, Y., 2013. In situ observation of a phase transition in Fe_2SiO_4 at high pressure and high temperature, *Phys. Chem. Minerals*, **40**, 811-816.

Ratterron, P., Chen, J. and Weidner, D.J., 2002. A process for low-temperature olivine-spinel transition under quasi-hydrostatic stress, *Geophys. Res. Lett.*, **29**, 36.

J. R. Rice, J.R., 2006. Heating and weakening of faults during earthquake slip. *Journal of Geophysical Research: Solid Earth* **111**, B05311.

Riggs, E.M. and Green, H.W., 2001. Shear localization in transformation-induced faulting: first-order similarities to brittle shear failure, *Tectonophysics*, **340**, 95-107.

Riggs, E.M. and Green, H.W., 2005. A new class of microstructures which lead to transformation-induced faulting in magnesium germanate, *J. Geophy. Res.*, **110**, B03202.

de Ronde, A.A., Dobson, D.P., Meredith, P.G. and Boon, S.A., 2007. Three-dimensional location and waveform analysis of microseismicity in multi-anvil experiments, *Geophys. J. Int.*, **171**, 1282-1294.

Rossman, G.R., ruff.info/fayalite, RUFF I.D. X05007.

Schubnel, A., Brunet, B., Hilairet, N., Gasc, J., Wang, Y. and Green, H.W., 2013. Deep-focus earthquake analogs recorded at high pressure and temperature in the laboratory, *Nature*, **341**, 1377-1380.

Spice, H., Sanloup, C., Cochain, B., de Grouchy, C. and Kono, Y., 2010. Viscosity of fayalite up to 9 GPa, *Geochimica et Cosmochimica Acta*, **148**, 219-227.

Tibi, R., Bock, G. and Wiens, W.A., 1999. The 1996 June 17 Flores Sea and 1994 March 9 Fiji-Tonga earthquakes: constraint on the faulting mechanism at great depths, *J. Geophy. Res.*, **138**, 625-642.

Zhan, Z., Kanamori, H., Tsai, V.C., Helmberger, D.V. and Wei, S., 2014. Rupture complexity of the 1994 Bolivia and 2013 Sea of Okhotsk deep earthquakes, *Earth Planet. Sci. Lett.*, **385**, 89-96.

Chapter 8: Conclusions and Future Work

8.1 General conclusions

A system has been developed capable of monitoring *in situ* microseismicity under conditions of HPHT while samples were actively strained. This was achieved by integrating the AE system by Vallen Systemes with the 3000 ton multi-anvil apparatus in the High-Pressure/High Temperature Mineral Physics Laboratory at Western University. To measure acoustic activity sensors containing piezoelectric transducers are mounted on the rear truncations of six of the eight anvils which were polished to a mirror-finish to optimize acoustic transfer. The sensors are capable of measuring p-waves with frequencies between 100 – 1000 kHz which are fed into a pre-amplifier then sent to the Vallen analog-to-digital boards for signal processing and digitization with a sampling frequency of up to 40 MHz. Due to the large amount of data collected during a typical experiment, the system works on a triggered basis such that only signals energetic enough to surpass a user defined threshold are stored to memory. In order to ensure that the entire waveform is collected, data buffers continuously record and remove data to guarantee that data is captured prior to the onset of the waveform.

Using this system a technique for detecting and measuring phase transitions in the multi-anvil apparatus was developed. As a proof of concept several experiments were run on Hg samples in order to detect the phase change from liquid to solid (and *vice versa*). This was achieved by measuring the change in travel time for pulsed ultrasonic p-waves along three independent acoustic paths simultaneously. Upon phase change from liquid to solid, the travel

time showed an abrupt decrease due to the intrinsic increase in velocity in the sample and a reduced delay between the triggering of the amplitude threshold and the arrival of the waveform (Officer and Secco, 2015).

In order to measure acoustic signals generated by samples a few mm in size at the center of the pressure assembly required overcoming several technical challenges. These included characterizing acoustic and electrical noise generated by the system so that it could either be removed or neglected. The electrical noise, generated through induction of the anvils by the press pump was drastically reduced by placing Diamonite^{TM} discs between the sensors and the anvils to provide electrical isolation. Due to the large amount of spurious acoustic signals generated in the gaskets and pressure medium, it was critical that acoustic events originating within the sample could be distinguished from those generated outside of it. The most direct way of achieving this was by uniquely pinpointing the hypocenter of seismogenic events. Event location was achieved by inputting the arrival times of acoustic signals into a non-linear least squares inversion program written in Matlab. Arrival times could be estimated either by manual selection or automatic picking. The sensitivity of the system was tested by measuring the acoustic activity generated by materials with contrasting mechanical properties. During cold compression of quartz beads, which are brittle, hundreds of events located within the sample. Comparatively, only 4 events located near the periphery of a soft AgCl sample under identical experimental conditions. For each event, uncertainty is estimated based on similar inversion techniques and is ~1mm. During rapid pressurization at HPHT neither experiment generated events either in or near the sample suggesting that the system is acoustically quiet under the conditions of deformation experiments.

An investigation on Fe_2SiO_4 undergoing the olivine → spinel phase transformation during HPHT deformation was conducted to elucidate whether transformational faulting is a viable mechanism for DFEQs. In order to do this, fayalite, which is not a naturally occurring mineral, had to be synthesized. Synthesis was carried out using a stoichiometric mixture of hematite and quartz in a gas mixing furnace and proved to be pure fayalite within the detection limits of X-ray diffraction (XRD) characterization. Sintering of samples was achieved in the 1000 ton cubic press at Western University. Sintered samples displayed uniformly sized grains, no preferred crystal orientation, and contained very low porosity. In some instances, samples were assembled from stacked discs that were coated in a thin layer of Ag. This acted as a passive marker that was used to illustrate the presence of faulting in recovered samples. A total of 15 experiments were performed on sintered fayalite samples under varying conditions of pressure, temperature, stress, strain, strain rate and time (P,T,σ,ε,$\dot{\varepsilon}$, t), in the spinel stability field. These experiments included conditions very near the kinetic boundary of the metastable transition to those of rapid transformation. Results revealed AE events in half a dozen experiments that located either within, or within 1 standard deviation of the sample. Recovered samples displayed both spinel lenses and planer transformation features identical to those found in Mg_2GeO_4 (Green and Burnley, 1989; Burnley and Green, 1991; Riggs and Green, 2005; Schubnel et al., 2013; Green et al., 2015). In most cases these features were restricted to either fault zones or within their immediate vicinity. Evidence of faulting (both AE and visual) was restricted to the P,T window defined by P = 3.8 – 8.4 GPa and T = 650 – 950 K where the transformation becomes just kinetically possible, also resembling the behaviour of Mg_2GeO_4. Up to this point, only one experiment on a silicate mineral undergoing the olivine→spinel transition has demonstrated transformational faulting at HPHT (Green, H.W. et al., 1990) and some dispute

their results (Rubie, 1996; Dupas-Bruzek et al., 1998). Furthermore, this experiment did not connect an acoustic signal with the transformation. This set of experiments performed in this study demonstrate that the iron end-member of olivine is capable of transformational faulting and provide a first step in determining under what conditions Fe_2SiO_4 can generate mechanical instabilities under HPHT conditions. In particular, experiment HPF_AE_15 displays a fault running the entire length of the sample, contains anticrack lenses associated with HPHT faulting which are restricted to the fault zone, and a very large acoustic event whose location coincides with the position of the start of the rupture. Interestingly, the spinel microstructures are only evident for ~1/3 of the way along the fault suggesting that it was initiated by the phase transition but continued to progress by another mechanism, perhaps superplastic flow or shear melting. If this is the case, it may explain why a few earthquakes appear to have rupture dimensions larger than the predicted size of the olivine wedge (Tibi et al., 1999; Estabrook and Bock, 1995). If DFEQs are triggered by phase transitions in olivine, but can continue to proceed by another mechanism(s), this result could help dispel some of the controversy over some of the competing theories of DFEQ mechanisms.

8.2 Future work

The goal of this research and future work in this area is to 1) generate and detect HPHT faults in olivine structured minerals, undergoing transformations to their high pressure polymorphs, and 2) test whether this process is seismogenic in nature. This information can then be assessed to determine if this is a viable mechanism for DFEQ generation. However, it should be emphasized

that the intention of these investigations should not be to simply confirm the transformational faulting hypothesis, but instead should attempt to answer the following questions:

- What is the (P,T,σ,ε ,$\dot{\varepsilon}$, t) envelope in which HPHT faulting can occur?
- What role does the phase transformation play in generating mechanical instabilities?
- What conditions favour either the anticrack model or the planar transformation model?
- Under what conditions is it possible for multiple mechanisms to act in concert with each other?
- Do different faulting mechanisms have different seismic signatures?
- How do source properties for seismic events measured in the lab (e.g. moment tensor, after shock statistics, b-values, stress drop, rupture duration, dimension and velocity, etc.) compare to those observed for DFEQs?

To answer the questions posed above several technical considerations need to be addressed and many experiments need to be run. Below are a few of the challenges that involved and a proposed methodology to overcome them.

8.2.1 Increase the capability of transducers

The likely reason for the low numbers of acoustic events that located within the sample under HPHT conditions was the inability of the transducers to record events from sub mm ruptures. Ideally, a transducer would have a flat frequency response to both p- and s-waves and be able to detect signals from sample length ruptures down to the μm scale. For the mm sized silicate samples in this study, this translates to ~0.1-20 MHz. However, in practise this is

unachievable and instead requires optimizing trade-offs between signal amplitude and frequency response. The primary factors are crystal thickness, oscillator damping and cut orientation. Steps should also be taken to ensure the transducer is electronically isolated from the press and maximizes acoustic transmission from the anvils. Due to the volume confinement in high pressure applications, the selection of commercially available transducers is severely limited. The other option is to acquire piezoelectric crystals and fabricate transducers from them in house. While this option is likely cheaper it precipitates its own host of challenges such as broadening the sharp response of the crystals and ensuring sure they are sensitive enough for HPHT applications since the higher the resonant frequency of the crystal, the lower the overall sensitivity. Another challenge in implementing such transducers would be to calibrate the response functions. However, a methodology could be developed using a function generator to test the transducers. With the transducer attached to the end of an anvil, the waveform propagates from the transducer through the anvil to the anvil tip and bounces back to the transducer. Measuring the interference pattern of the input wave, the transducer response to the input wave and measuring the reflected wave, Fourier transforms of the interferogram could retrieve the transducer response.

8.2.2 Measuring moment tensors of acoustic events

Moment tensor inversion can be used to obtain the source mechanism of an event. DFEQs are believed to result from shear deformation (or double couples), similar to the majority of shallow earthquakes (Frohlich, 2006). To retrieve moment tensors for seismic events requires inverting the first motion polarity and amplitude of unsaturated waveforms. While this could be done for some of the events collected in this study it is unlikely to yield high quality results since it requires waveforms representative of the seismic radiation generated from the source and unsaturated

events. In practise this requires deconvolving the transfer function of the transmitting media and the response function of the transducers, but would not work for the large event generated in HPF_AE_15 since it saturated all six transducers. For these reasons it was considered beyond the scope of this study but, in theory, could provide value information of the source mechanisms of HPHT faults.

8.2.3 Proposed experimentation on Mg_2GeO_4 and the $(Mg,Fe)_2SiO_4$ system

The following is a preliminary outline of the methodology that could be used to address the questions posed at the beginning of this section. First, precisely constrain the (P,T,σ,ε ,ε̇, t) envelope where faulting occurs in Mg_2GeO_4. While several studies have already confirmed the presence of HPHT faulting in Mg_2GeO_4, there are still many outstanding questions regarding how faulting occurs under these conditions in this mineral. In particular, special attention should be paid to distinguish what conditions favour one faulting mechanism over another. Using the information gained on Mg_2GeO_4 and described in this manuscript, experimentation on the $(Mg,Fe)_2SiO_4$ system in the stability field of its high pressure polymorphs would continue. Beginning with Fe_2SiO_4, several more experiments would be needed to more completely constrain the (P,T,σ,ε,ε̇,t) envelop where HPHT faulting occurs and determine what mechanisms operate. Next, increasing molar ratios of Mg would be added to determine what role the intermediate transformation to wadsleyite has on mechanical instability. This would require using a smaller truncation size than the 18/11 cell so it would be worthwhile to run a few experiments on quartz beads in the smaller cell to test if the system is capable of measuring HPHT fracturing on smaller sample sizes. This would likely require the next generation of transducers discussed in section 8.3. Eventually experiments would concentrate on samples with a molar ratio of $(Mg_{0.9}Fe_{0.1})_2SiO_4$ which is representative of natural olivine. Finally, it would also be useful to run deformation

experiments on ringwoodite in the ringwoodite stability field to test if HPHT mechanical instabilities can occur without the incidence of the phase change. Throughout this process results would be continually interpreted within the context of how they relate to the geophysical and seismological observations of DFEQs.

8.3 References

Burnley, P.C., Green, H.W. and Prior, D.J., 1991. Faulting associated with the olivine to spinel transformation in Mg_2GeO_4 and its implication for deep-focus earthquakes, *J. Geophys. Res.*, **96**, 425-443.

Dupas-Bruzek, C., Sharp, T.G., Rubie, D.C. and Durham, W.B., 1998. Mechanisms of transformation and deformation in $Mg_{1.8}Fe_{0.2}SiO_4$ olivine and wasleyite under non-hydrostatic stress, *Phys. Earth Planet, Int.*, **108**, 33-48.

Estabrook, C.H. and Bock, G., 1995. Rupture history of the great Bolivian earthquake: slab interaction with 660 km discontinuity?, *Geophys., Res., Lett.*, **22**, 2277-2280.

Frohlich, C., 2006. *Deep Earthquakes*, Cambridge Univ. Press. Cambridge, England.

Green, H.W. and Burnley, P.C., 1989. A new self-organizing mechanism for deep-focus earthquakes, *Nature*, **341**, 733-737.

Green, H.W., Young, T.E, Walker, D. and Scholz, C.H., 1990. Anticrack-associated faulting at very high pressure in natural olivine, *Nature*, **348**, 720-722.

Green, H.W., Shi, F., Bozhilov, K. and Reches, Z., 2015.Phase transformation and nanometric flow cause extreme weakening during fault slip, *Nature Geoscience*, **8**, 484-489.

Officer, T. and Secco, R.A., 2015. Detection of a P-induced liquid ⇌ solid phase transformation using multiple acoustic transducers in a multi-anvil apparatus, *High Pres. Res.*, **35**, 289-299.

Riggs, E.M. and Green, H.W., 2005. A new class of microstructures which lead to transformation-induced faulting in magnesium germanate, *J. Geophy. Res.*, **110**, B03202.

Rubie, D.C., 1996. Phase transformation in the Earth's mantle. In *High Pressure and High Temperature Research on Mantle Materials*, eds. Mellini, M., Ranalli, G., Ricci, C.A. and Trommsdorff, V., Proceedings of the International School of Earth and Planetary Sciences, Siena, Italy, 41-66.

Schubnel, A., Brunet, B., Hilairet, N., Gasc, J., Wang, Y. and Green, H.W., 2013. Deep-focus earthquake analogs recorded at high pressure and temperature in the laboratory, *Nature*, **341**, 1377-1380.

Tibi, R., Bock, G. and Wiens, W.A., 1999. The 1996 June 17 Flores Sea and 1994 March 9 Fiji-Tonga earthquakes: constraint on the faulting mechanism at great depths, *J. Geophy. Res.*, **138**, 625-642.

Appendix 1: Non-linear least squares inversion algorithm for hypocentral location

The computer code below inverts events comprised of acoustic signals registered on six transducers. To invert for events on 4 or 5 transducers slight modifications are required the number of iterations in some of the loops. The inputs required are excel files of the waveforms and hit data recorded by the Vallen system.

```
tic

clear all
close all
waveforms = xlsread('HPF_AE_1_expt_wf_6he_all_evts.xlsx');      %Imports
Waveform points and Header (as String Matrix)
hit_data = xlsread('HPF_AE_1_expt_hit_data_all_evts.xlsx');

%the following loop changes the channel number from channel 7 to channel 4
for u = 1:length(hit_data(:,5))
    if hit_data(u,5) == 7
        hit_data(u,5) = 4;
    end
end

nsamp=8192;     %number of points in waveform
samp_rate=40e6;   %sample rate (Hz)
tbtp=1/samp_rate; %time between samples (in seconds)
tcp=2001;       %threshold cross point
tcp_vec = [tcp tcp tcp tcp tcp tcp];%1x6 vector of threshold crossing point



event_number = 1;
waveform_index = 1;


for n = 1:length(hit_data(:,15))

    if hit_data(n,15) == 6

        first_motion(event_number,:) = {'', '', '', '', '', ''};
        first_motion_num(event_number,:) = [0 0 0 0 0 0];

        chan_order_mtx_fm(event_number,:) = hit_data(n:n+5,5);
```

```
        AIC_vec = [0, 0, 0, 0, 0, 0]; %1x6 vector of threshold crossing
points. It starts with a matrix of zeros and changes to the AIC pick each
loop

        for q = 1:6 %for each of the six signals in an event


%%%%%%%%%%%%%%%%%%%%%%%%%%%%%%%%%%%%%%%%%%%%%%%%%%%%%%%%%%%%%%%%%%%%%%%%%%%%
            %AIC

            AIC_loop = waveforms((tcp-1000):(tcp+2000),waveform_index);
            AIC_samp = length(AIC_loop);


            for k = 1:AIC_samp      %looping through each sample

                AIC(k)=k*log(var(AIC_loop(1:k)))+(AIC_samp-k-
1)*log(var(AIC_loop(k+1:AIC_samp)));     %computing AIC for each point in the
entire sample

                if AIC(k) == -Inf         %if AIC = -Inf, corresponding to
zero variance, set to second term in loop
                    if k <= tcp
                        AIC(k)=(AIC_samp-k-
1).*log(var(AIC_loop(k+1:AIC_samp)));       %if the index is less than the
threshold cross point set to first term in AIC
                    else
                        AIC(k) = k*log(var(AIC_loop(1:k)));   %if the index
is greater than the threshold cross point set to first term in AIC
                    end
                end
            end

            AIC_vec(q) = find(AIC==min(AIC))+1000;     %finding the arrival
sample in the series that corresponds to the arrival

            fm_check_diff = zeros(1,10);
            for pt = 1:10
                fm_check_diff(pt) = waveforms(AIC_vec(q)+pt,waveform_index) -
waveforms(AIC_vec(q)+pt-1,waveform_index);
            end
            fm_check = sum(fm_check_diff);
            if fm_check >= 0
                first_motion(event_number,chan_order_mtx_fm(event_number,q))
= {'up'};

first_motion_num(event_number,chan_order_mtx_fm(event_number,q)) = 1;
            end
            if fm_check <= 0
                first_motion(event_number,chan_order_mtx_fm(event_number,q))
= {'down'};

first_motion_num(event_number,chan_order_mtx_fm(event_number,q)) = -1;
            end
```

```
%%%%%%%%%%%%%%%%%%%%%%%%%%%%%%%%%%%%%%%%%%%%%%%%%%%%%%%%%%%%%%%%%%%%%%%%%%%%%%%

            waveform_index = waveform_index + 1;
        end

        AIC_ap(event_number,:) = AIC_vec;  %creating a large matrix of all
the AIC picks for every waveform
        apb4th = tcp_vec - AIC_vec; %number of points waveform arrives before
the threshold cross point
        diff_ar = apb4th*tbtp; %difference in arrival time (i.e actual
waveform is early by this much)
        tct = hit_data(n:n+5,4)/1000;  %getting the threshold crossing time
and dividing by 1000 to get it isn sec.
        tct = tct';
        AIC_arrival_times(event_number,:) = tct-diff_ar;   %finding the
actual arrival time
        event_number = event_number + 1;

    end


end

event_number = event_number - 1;

%creating a file of arrival points
fid1 = fopen('HPF_AE_1_6_hits_expt_all_events_AIC_Chosen Arrival
Times.txt','w');
fprintf(fid1,'%12.9f  %12.9f  %12.9f  %12.9f  %12.9f
%12.9f\r\n',AIC_arrival_times');
fclose(fid1);

fid2 =
fopen('HPF_AE_1_6_hits_expt_all_events_Waveform_arrival_points.txt','w');
fprintf(fid2,'%6.0f  %6.0f  %6.0f %6.0f  %6.0f  %6.0f\r\n',AIC_ap');
fclose(fid2);

fid3 = fopen('HPF_AE_1_6_hits_expt_all_events__First motions.txt','w');
fprintf(fid3,'%3.0f  %3.0f  %3.0f %3.0f  %3.0f
%3.0f\r\n',first_motion_num');
fclose(fid3);



nsamp=8192;    %number of points in waveform
samp_rate=40e6;   %sample rate (Hz)
tbtp=1/samp_rate; %time between samples (in seconds)
tcp=2001;      %threshold cross point
tcp_vec = [tcp tcp tcp tcp tcp tcp];%1x6 vector of threshold crossing point



%Vectors of channel positions  (m)
ch1_cube = [29.5 29.5 29.5]/1000;
```

```
ch2_cube = [-29.5 -29.5 -29.5]/1000;
ch3_cube = [-29.5 -29.5 29.5]/1000;
ch4_cube = [29.5 29.5 -29.5]/1000;
ch5_cube = [29.5 -29.5 29.5]/1000;
ch6_cube = [-29.5 29.5 -29.5]/1000;

%TRANSFORMING THE CUBE COORDINATES TO THE SAMPLE COORDINATES

%transformation cosines for x_cube to x_sample
x1 = cos(35.3*pi/180);
x2 = cos(65.9*pi/180);
x3 = cos(65.9*pi/180);

%%transformation cosines for y_cube to y_sample
y1 = cos(90*pi/180);
y2 = cos((180-45)*pi/180);
y3 = cos(45*pi/180);

%transformation cosines for z_cube to z_sample
z1 = cos(54.7*pi/180);
z2 = cos((180-54.7)*pi/180);
z3 = cos((180-54.7)*pi/180);


%Transformation to sample coordinate system for all 6 transducers

ch1x = (x1*29.5)+(x2*29.5)+(x3*29.5);
ch1y = (y1*29.5)+(y2*29.5)+(y3*29.5);
ch1z = (z1*29.5)+(z2*29.5)+(z3*29.5);

ch1 = [ch1x ch1y ch1z]/1000;

%%%%%%%%%%%%%%%%%%%%%%%%%%%%%%%%%%%%%%%%%%%%%%%%%%%%%%%%%%%
ch2x = (x1*(-29.5))+(x2*(-29.5))+(x3*(-29.5));
ch2y = (y1*(-29.5))+(y2*(-29.5))+(y3*(-29.5));
ch2z = (z1*(-29.5))+(z2*(-29.5))+(z3*(-29.5));

ch2 = [ch2x ch2y ch2z]/1000;

%%%%%%%%%%%%%%%%%%%%%%%%%%%%%%%%%%%%%%%%%%%%%%%%%%%%%%%%%%%
ch3x = (x1*(-29.5))+(x2*(-29.5))+(x3*29.5);
ch3y = (y1*(-29.5))+(y2*(-29.5))+(y3*29.5);
ch3z = (z1*(-29.5))+(z2*(-29.5))+(z3*29.5);

ch3 = [ch3x ch3y ch3z]/1000;

%%%%%%%%%%%%%%%%%%%%%%%%%%%%%%%%%%%%%%%%%%%%%%%%%%%%%%%%%%%
ch4x = (x1*29.5)+(x2*29.5)+(x3*(-29.5));
ch4y = (y1*29.5)+(y2*29.5)+(y3*(-29.5));
ch4z = (z1*29.5)+(z2*29.5)+(z3*(-29.5));

ch4 = [ch4x ch4y ch4z]/1000;

%%%%%%%%%%%%%%%%%%%%%%%%%%%%%%%%%%%%%%%%%%%%%%%%%%%%%%%%%%%
```

```
ch5x = (x1*29.5)+(x2*(-29.5))+(x3*29.5);
ch5y = (y1*29.5)+(y2*(-29.5))+(y3*29.5);
ch5z = (z1*29.5)+(z2*(-29.5))+(z3*29.5);

ch5 = [ch5x ch5y ch5z]/1000;

%%%%%%%%%%%%%%%%%%%%%%%%%%%%%%%%%%%%%%%%%%%%%%%%%%%%%%%%
ch6x = (x1*(-29.5))+(x2*29.5)+(x3*(-29.5));
ch6y = (y1*(-29.5))+(y2*29.5)+(y3*(-29.5));
ch6z = (z1*(-29.5))+(z2*29.5)+(z3*(-29.5));

ch6 = [ch6x ch6y ch6z]/1000;

gpm = [ch1; ch2; ch3; ch4; ch5; ch6]'; %grand position vector - each row
contains the position of a sensor
X = gpm(1,:);  % X positions of sensors 1-6
Y = gpm(2,:);  % Y positions of sensors 1-6
Z = gpm(3,:);  % Z positions of sensors 1-6

vel = 5000;
sigma_d = 0.148e-6;
event_number = 1;
waveform_index = 1;


%Loop for picking arrival times from each waveform, measuring first motions
and inverting fot the event location based on chosen arrival times
for n = 1:length(hit_data(:,15))

    if hit_data(n,15) == 6

        p(event_number) = (0.00844*(2*hit_data(n,9)))-
(0.000000529765*(2*(hit_data(n,9))^2));   %pressure when event occured in GPa
        v(event_number) = (0.06069*(p(event_number)^5))-
(2.09316*(p(event_number)^4))+(27.13761*(p(event_number)^3))-
(167.43937*(p(event_number)^2))+(529.98332*p(event_number))+5902.27813;
%velocity when event occured

        chan_order_mtx=hit_data(n:n+5,5);


        max_diff = max(AIC_arrival_times) - min(AIC_arrival_times); %
%maximum difference in arrival time

        data = [X(chan_order_mtx);
            Y(chan_order_mtx);
            Z(chan_order_mtx);
            AIC_arrival_times(event_number,:)]';

        %Inversion

        mk = [0,0,0,(29.5/1000)/vel]';    %initial guess for model vector
        G = zeros(6,4);   %creating a matrix of zeros for G, partial
derivitive matrix i.e. 2nd term in Taylor expansion
```

```
        for k = 1:100

            dk = mk(4)+(1/vel)*((mk(1)-data(:,1)).^2 + (mk(2)-data(:,2)).^2 +
(mk(3)-data(:,3)).^2).^(1/2);   %finding data (predicted arrival times) for
model mk, where k is the iteration index based on travel time equation
            delta_dk = data(:,4)-dk;
            sum2_delta_dk = sum((data(:,4)-dk).^2);

            %finding matrix of partial derivitives
            G(:,1) = ((mk(1)-data(:,1))./vel).*((mk(1)-data(:,1)).^2 +
(mk(2)-data(:,2)).^2 + (mk(3)-data(:,3)).^2).^(-1/2);
            G(:,2) = ((mk(2)-data(:,2))./vel).*((mk(1)-data(:,1)).^2 +
(mk(2)-data(:,2)).^2 + (mk(3)-data(:,3)).^2).^(-1/2);
            G(:,3) = ((mk(3)-data(:,3))./vel).*((mk(1)-data(:,1)).^2 +
(mk(2)-data(:,2)).^2 + (mk(3)-data(:,3)).^2).^(-1/2);
            G(:,4) = 1;

            delta_mk = (G'*G)^(-1)*G'*delta_dk;    %finding delta_mk using
matrix of total inversion
            mk = mk + delta_mk;
            %calculating uncertainty in the model
            Gsig(:,1) = ((mk(1)-data(:,1))/v(event_number)).*((mk(1)-
data(:,1)).^2 + (mk(2)-data(:,2)).^2 + (mk(3)-data(:,3)).^2).^(-1/2);
            Gsig(:,2) = ((mk(2)-data(:,2))/v(event_number)).*((mk(1)-
data(:,1)).^2 + (mk(2)-data(:,2)).^2 + (mk(3)-data(:,3)).^2).^(-1/2);
            Gsig(:,3) = ((mk(3)-data(:,3))/v(event_number)).*((mk(1)-
data(:,1)).^2 + (mk(2)-data(:,2)).^2 + (mk(3)-data(:,3)).^2).^(-1/2);
            Gsig(:,4) = 1;
            var_m = (sigma_d^2)*((Gsig'*Gsig)^(-1));
            sigma_xx = sqrt(var_m(1,1));
            sigma_yy = sqrt(var_m(2,2));
            sigma_zz = sqrt(var_m(3,3));
            sigma_tt = sqrt(var_m(4,4));

            %the next set of nested if statements breaks me out of the loop
if my model has reached a high level of accuracy
            if delta_mk(1) < 0.0000001
                if delta_mk(2) < 0.0000001
                    if delta_mk(3) < 0.0000001
                        if delta_mk(4) < 0.0000001/vel

                            break
                        end
                    end
                end
            end

        end

        %computing eigen values and eigen vectors to get the error ellipse
        xy_submat = [var_m(1,1), var_m(1,2);
            var_m(2,1),var_m(2,2)];
```

```
xz_submat = [var_m(1,1), var_m(1,3);
    var_m(3,1),var_m(3,3)];
yz_submat = [var_m(2,2), var_m(2,3);
    var_m(3,2),var_m(3,3)];

nan_check = isnan(sigma_xx);

if nan_check == 0
    if sigma_xx ~= Inf
        if sigma_xx ~= -Inf
            [e_vec_xy, e_val_xy] = eig(xy_submat);
            [e_vec_xz, e_val_xz] = eig(xz_submat);
            [e_vec_yz, e_val_yz] = eig(yz_submat);

            ee_smaj_xy_mm = sqrt(e_val_xy(1,1))*1000;
            ee_smin_xy_mm = sqrt(e_val_xy(2,2))*1000;
            ee_xy_or = atan(e_vec_xy(1,1)/e_vec_xy(2,2))*180/pi;
            ee_smaj_xz_mm = sqrt(e_val_xz(1,1))*1000;
            ee_smin_xz_mm = sqrt(e_val_xz(2,2))*1000;
            ee_xz_or = atan(e_vec_xz(1,1)/e_vec_xz(2,2))*180/pi;
            ee_smaj_yz_mm = sqrt(e_val_yz(1,1))*1000;
            ee_smin_yz_mm = sqrt(e_val_yz(2,2))*1000;
            ee_yz_or = atan(e_vec_yz(1,1)/e_vec_yz(2,2))*180/pi;

        end
    end
end

if nan_check == 1
    ee_smaj_xy_mm = NaN;
    ee_smin_xy_mm = NaN;
    ee_xy_or = NaN;
    ee_smaj_xz_mm = NaN;
    ee_smin_xz_mm = NaN;
    ee_xz_or = NaN;
    ee_smaj_yz_mm = NaN;
    ee_smin_yz_mm = NaN;
    ee_yz_or = NaN;
end


if sigma_xx == Inf
    ee_smaj_xy_mm = Inf;
    ee_smin_xy_mm = Inf;
    ee_xy_or = Inf;
    ee_smaj_xz_mm = Inf;
    ee_smin_xz_mm = Inf;
    ee_xz_or = Inf;
    ee_smaj_yz_mm = Inf;
    ee_smin_yz_mm = Inf;
    ee_yz_or = Inf;
end

num_it_vec(event_number) = k;
event_location(event_number,1:3) = mk(1:3)*1000;
```

```
        event_location(event_number,4) = hit_data(n,2)*86400;
%+mk(4)/1000;
        Val_Loc(event_number,:)=hit_data(n,11:13);
        diff_Val_In(event_number,:) = event_location(event_number,1:3)-
hit_data(n,11:13);
        energy(event_number) = sum(hit_data(n:n+5,8)/6);
        sigma(event_number,:) = [sigma_xx*1000, sigma_yy*1000, sigma_zz*1000,
sigma_tt*1000000];
        ee_xy(event_number,:) = [ee_smaj_xy_mm, ee_smin_xy_mm, ee_xy_or];
        ee_xz(event_number,:) = [ee_smaj_xz_mm, ee_smin_xz_mm, ee_xz_or];
        ee_yz(event_number,:) = [ee_smaj_yz_mm, ee_smin_yz_mm, ee_yz_or];


        event_number = event_number +1;

    end

end

nole = event_number-1;  %number of located events

t = event_location(:,4);
energy = energy';
p = p';
v = v';

col6 = repmat(6,length(event_location(:,1)),1);

sig6_xyztEPv_sigma_error_ellipses = [col6 event_location(:,1)
event_location(:,2) event_location(:,3) t energy p v sigma(:,1) sigma(:,2)
sigma(:,3) sigma(:,4) ee_xy(:,1) ee_xy(:,2) ee_xy(:,3) ee_xz(:,1) ee_xz(:,2)
ee_xz(:,3) ee_yz(:,1) ee_yz(:,2) ee_yz(:,3)]; %making a matrix with the
energy and the model

fid4 = fopen('HPF_AE_1_6_hits_expt_all_events_Located event data.txt','w');
fprintf(fid4,'%0s %5s %6s %6s %8s %10s %6s %6s %13s %10s %10s %10s %14s %12s
%12s %12s %12s %12s %12s %12s %12s\r\n','Sigs', 'x', 'y', 'z', 't', 'E', 'P',
'v', 'sigma_x', 'sigma_y', 'sigma_z', 'sigma_t', 'ee_smaj_xy', 'ee_smin_xy',
'ee_xy_or', 'ee_smaj_xz', 'ee_smin_xz', 'ee_xz_or', 'ee_smaj_yz',
'ee_smin_yz', 'ee_yz_or');
fprintf(fid4,'%3s %8s %6s %6s %7s %11s %6s %6s %10s %10s %10s %13s %9s %12s
%15s %9s %12s %15s %9s %12s %15s\r\n','#', '(mm)', '(mm)', '(mm)', '(s)',
'(a.u.)', '(GPa)', '(m/s)', '(mm)', '(mm)', '(mm)', '(microsec)', '(mm)',
'(mm)', '(degrees)', '(mm)', '(mm)', '(degrees)', '(mm)', '(mm)',
'(degrees)');
fprintf(fid4,'%3.0f %8.2f %6.2f %6.2f %8.0f %10.0f %6.2f %6.0f %10.2f %10.2f
%10.2f %10.2f %12.2f %12.2f %12.0f %12.2f %12.2f %12.0f %12.2f %12.2f
%12.0f\r\n',sig6_xyztEPv_sigma_error_ellipses');
fclose(fid4);

toc
```

The following program takes .txt files created by the previous program and plots the locations of acoustic events in 3-dimensional space with respect to a representation of the sample.

```
tic

clear all
close all

four_sig_file = 'HPF_AE_1_4_hits_expt_all_events_Located event data.txt';
five_sig_file = 'HPF_AE_1_5_hits_expt_all_events_Located event data.txt';
six_sig_file = 'HPF_AE_1_6_hits_expt_all_events_Located event data.txt';
delimiterIn = ' ';
headerlinesIn = 2;
four_sigs = importdata('HPF_AE_1_4_hits_expt_all_events_Located event
data.txt',delimiterIn,headerlinesIn);
five_sigs = importdata('HPF_AE_1_5_hits_expt_all_events_Located event
data.txt',delimiterIn,headerlinesIn);
six_sigs = importdata('HPF_AE_1_6_hits_expt_all_events_Located event
data.txt',delimiterIn,headerlinesIn);

four_sigs_xyztEvp_sigma_error_ellipses = four_sigs.data;
five_sigs_xyztEvp_sigma_error_ellipses = five_sigs.data;
six_sigs_xyztEvp_sigma_error_ellipses = six_sigs.data;

all_sigs_xyztEvp_sigma_error_ellipses =
[four_sigs_xyztEvp_sigma_error_ellipses;
five_sigs_xyztEvp_sigma_error_ellipses;
six_sigs_xyztEvp_sigma_error_ellipses];
[time_order,event_order_index] =
sort(all_sigs_xyztEvp_sigma_error_ellipses(:,5));
all_sigs_xyztEvp_sigma_error_ellipses_in_order =
[all_sigs_xyztEvp_sigma_error_ellipses(event_order_index,:)];

%creating a file of data on all events in order of ascending time
fid1 = fopen('HPF_AE_1_expt_all_events_AIC_Located event
data_order.txt','w');
fprintf(fid1,'%0s %5s %6s %6s %8s %10s %6s %6s %13s %10s %10s %10s %14s %12s
%12s %12s %12s %12s %12s %12s %12s\r\n','Sigs', 'x', 'y', 'z', 't', 'E', 'P',
'v', 'sigma_x', 'sigma_y', 'sigma_z', 'sigma_t', 'ee_smaj_xy', 'ee_smin_xy',
'ee_xy_or', 'ee_smaj_xz', 'ee_smin_xz', 'ee_xz_or', 'ee_smaj_yz',
'ee_smin_yz', 'ee_yz_or');
fprintf(fid1,'%3s %8s %6s %6s %7s %11s %6s %6s %10s %10s %10s %13s %9s %12s
%15s %9s %12s %15s %9s %12s %15s\r\n','#', '(mm)', '(mm)', '(mm)', '(s)',
'(a.u.)', '(GPa)', '(m/s)', '(mm)', '(mm)', '(mm)', '(microsec)', '(mm)',
'(mm)', '(degrees)', '(mm)', '(mm)', '(degrees)', '(mm)', '(mm)',
'(degrees)');
fprintf(fid1,'%3.0f %8.2f %6.2f %6.2f %8.0f %10.0f %6.2f %6.0f %10.2f %10.2f
%10.2f %10.2f %12.2f %12.2f %12.0f %12.2f %12.2f %12.0f %12.2f %12.2f
%12.0f\r\n',all_sigs_xyztEvp_sigma_error_ellipses_in_order');
fclose(fid1);
```

```
%finding the events that locate within the sample
aed =all_sigs_xyztEvp_sigma_error_ellipses_in_order;

fid2 = fopen('HPF_AE_1_expt_all_events_AIC_Located in
sample_in_order.txt','w');
fprintf(fid2,'%0s %5s %6s %6s %8s %10s %6s %6s %13s %10s %10s %10s %14s %12s
%12s %12s %12s %12s %12s %12s %12s\r\n','Sigs', 'x', 'y', 'z', 't', 'E', 'P',
'v', 'sigma_x', 'sigma_y', 'sigma_z', 'sigma_t', 'ee_smaj_xy', 'ee_smin_xy',
'ee_xy_or', 'ee_smaj_xz', 'ee_smin_xz', 'ee_xz_or', 'ee_smaj_yz',
'ee_smin_yz', 'ee_yz_or');
fprintf(fid2,'%3s %8s %6s %6s %7s %11s %6s %6s %10s %10s %10s %13s %9s %12s
%15s %9s %12s %15s %9s %12s %15s\r\n','#', '(mm)', '(mm)', '(mm)', '(s)',
'(a.u.)', '(GPa)', '(m/s)', '(mm)', '(mm)', '(mm)', '(microsec)', '(mm)',
'(mm)', '(degrees)', '(mm)', '(mm)', '(degrees)', '(mm)', '(mm)',
'(degrees)');


u = 1;
for k = 1:length(aed(:,1))
    if sqrt(aed(k,2)^2+aed(k,3)^2) <= 1.5
        if aed(k,4) <= 2.5
            if aed(k,4) >= -2.5
                lo_in(u,:) = aed(k,:);
                fprintf(fid2,'%3.0f %8.2f %6.2f %6.2f %8.0f %10.0f %6.2f
%6.0f %10.2f %10.2f %10.2f %10.2f %12.2f %12.2f %12.0f %12.2f %12.2f %12.0f
%12.2f %12.2f %12.0f\r\n',lo_in(u,:)');
                u = u + 1;
            end
        end
    end
end
u = u-1;

fclose(fid2);



fid3 = fopen('HPF_AE_1_expt_all_events_AIC_Located 1sigma from
sample_in_order.txt','w');
fprintf(fid3,'%0s %5s %6s %6s %8s %10s %6s %6s %13s %10s %10s %10s %14s %12s
%12s %12s %12s %12s %12s %12s %12s\r\n','Sigs', 'x', 'y', 'z', 't', 'E', 'P',
'v', 'sigma_x', 'sigma_y', 'sigma_z', 'sigma_t', 'ee_smaj_xy', 'ee_smin_xy',
'ee_xy_or', 'ee_smaj_xz', 'ee_smin_xz', 'ee_xz_or', 'ee_smaj_yz',
'ee_smin_yz', 'ee_yz_or');
fprintf(fid3,'%3s %8s %6s %6s %7s %11s %6s %6s %10s %10s %10s %13s %9s %12s
%15s %9s %12s %15s %9s %12s %15s\r\n','#', '(mm)', '(mm)', '(mm)', '(s)',
'(a.u.)', '(GPa)', '(m/s)', '(mm)', '(mm)', '(mm)', '(microsec)', '(mm)',
'(mm)', '(degrees)', '(mm)', '(mm)', '(degrees)', '(mm)', '(mm)',
'(degrees)');


q = 1;
for s = 1:length(aed(:,1))
    if abs(aed(s,2)) ~= Inf
        if sqrt(aed(s,2)^2+aed(s,3)^2) > 1.5
```

```
            if abs(aed(s,2)) <= 1.5+aed(s,9)
                if abs(aed(s,3)) <= 1.5+aed(s,10)
                    if abs(aed(s,4)) <= 2.5+aed(s,11)
                        lo_1sig(q,:) = aed(s,:);
                        fprintf(fid3,'%3.0f %8.2f %6.2f %6.2f %8.0f %10.0f
%6.2f %6.0f %10.2f %10.2f %10.2f %10.2f %12.2f %12.2f %12.0f %12.2f %12.2f
%12.0f %12.2f %12.2f %12.0f\r\n',lo_1sig(q,:)');
                        q = q + 1;
                    end
                end
            end
        end
    end
end

q = q-1;

fclose(fid3);




%PLOTTING THE POSITIONS OF LOCATED EVENTS

plot3(six_sigs_xyztEvp_sigma_error_ellipses(:,2),
six_sigs_xyztEvp_sigma_error_ellipses(:,3),
six_sigs_xyztEvp_sigma_error_ellipses(:,4), 'bo','MarkerSize',3)
hold on
plot3(five_sigs_xyztEvp_sigma_error_ellipses(:,2),
five_sigs_xyztEvp_sigma_error_ellipses(:,3),
five_sigs_xyztEvp_sigma_error_ellipses(:,4), 'bo','MarkerSize',3)
plot3(four_sigs_xyztEvp_sigma_error_ellipses(:,2),
four_sigs_xyztEvp_sigma_error_ellipses(:,3),
four_sigs_xyztEvp_sigma_error_ellipses(:,4), 'bo','MarkerSize',3)
xlabel('x (mm)')
ylabel('y (mm)')
zlabel('z (mm)')
axis([-5, 5, -5, 5, -5, 5])
grid MINOR


if u > 0
    for w = 1:u
        if lo_in(w,1) == 6
            plot3(lo_in(w,2), lo_in(w,3), lo_in(w,4), 'r.', 'Markersize', 15)
        end
        if lo_in(w,1) == 5
            plot3(lo_in(w,2), lo_in(w,3), lo_in(w,4), 'r.', 'Markersize', 15)
        end
        if lo_in(w,1) == 4
            plot3(lo_in(w,2), lo_in(w,3), lo_in(w,4), 'r.', 'Markersize', 15)
        end
    end
end
```

```
if q > 0
    for c = 1:q
        if lo_1sig(c,1) == 6
            plot3(lo_1sig(c,2), lo_1sig(c,3), lo_1sig(c,4), 'ro',
'Markersize', 3)
        end
        if lo_1sig(c,1) == 5
            plot3(lo_1sig(c,2), lo_1sig(c,3), lo_1sig(c,4), 'ro',
'Markersize', 3)
        end
        if lo_1sig(c,1) == 4
            plot3(lo_1sig(c,2), lo_1sig(c,3), lo_1sig(c,4), 'ro',
'Markersize', 3)
        end
    end
end



%plotting the sample
circ_points = linspace(0, 2*pi, 1000);
x_circ = 1.5*cos(circ_points);
y_circ = 1.5*sin(circ_points);

z_samp_top = zeros(1, 1000)+ 2.5;
z_samp_bot = zeros(1, 1000)- 2.5;


plot3(x_circ, y_circ, z_samp_top, '-k')
plot3(x_circ, y_circ, z_samp_bot, '-k')



%adding lines to sample
%plotting lines for sample
%making lines for sample

samp_line = [-2.5, 2.5];

theta1 = 0*(pi/180);
theta2 = 30*(pi/180);
theta3 = 60*(pi/180);
theta4 = 90*(pi/180);
theta5 = 120*(pi/180);
theta6 = 150*(pi/180);
theta7 = 180*(pi/180);
theta8 = 210*(pi/180);
theta9 = 240*(pi/180);
theta10 = 270*(pi/180);
theta11 = 300*(pi/180);
theta12 = 330*(pi/180);

line1x = [1.5*cos(theta1), 1.5*cos(theta1)];
```

```
line1y = [1.5*sin(theta1), 1.5*sin(theta1)];
line2x = [1.5*cos(theta2), 1.5*cos(theta2)];
line2y = [1.5*sin(theta2), 1.5*sin(theta2)];
line3x = [1.5*cos(theta3), 1.5*cos(theta3)];
line3y = [1.5*sin(theta3), 1.5*sin(theta3)];
line4x = [1.5*cos(theta4), 1.5*cos(theta4)];
line4y = [1.5*sin(theta4), 1.5*sin(theta4)];
line5x = [1.5*cos(theta5), 1.5*cos(theta5)];
line5y = [1.5*sin(theta5), 1.5*sin(theta5)];
line6x = [1.5*cos(theta6), 1.5*cos(theta6)];
line6y = [1.5*sin(theta6), 1.5*sin(theta6)];
line7x = [1.5*cos(theta7), 1.5*cos(theta7)];
line7y = [1.5*sin(theta7), 1.5*sin(theta7)];
line8x = [1.5*cos(theta8), 1.5*cos(theta8)];
line8y = [1.5*sin(theta8), 1.5*sin(theta8)];
line9x = [1.5*cos(theta9), 1.5*cos(theta9)];
line9y = [1.5*sin(theta9), 1.5*sin(theta9)];
line10x = [1.5*cos(theta10), 1.5*cos(theta10)];
line10y = [1.5*sin(theta10), 1.5*sin(theta10)];
line11x = [1.5*cos(theta11), 1.5*cos(theta11)];
line11y = [1.5*sin(theta11), 1.5*sin(theta11)];
line12x = [1.5*cos(theta12), 1.5*cos(theta12)];
line12y = [1.5*sin(theta12), 1.5*sin(theta12)];


plot3(line1x, line1y, samp_line, 'k-')
plot3(line2x, line2y, samp_line, 'k-')
plot3(line3x, line3y, samp_line, 'k-')
plot3(line4x, line4y, samp_line, 'k-')
plot3(line5x, line5y, samp_line, 'k-')
plot3(line6x, line6y, samp_line, 'k-')
plot3(line7x, line7y, samp_line, 'k-')
plot3(line8x, line8y, samp_line, 'k-')
plot3(line9x, line9y, samp_line, 'k-')
plot3(line10x, line10y, samp_line, 'k-')
plot3(line11x, line11y, samp_line, 'k-')
plot3(line12x, line12y, samp_line, 'k-')


toc
```

Appendix 2: Images and spectra of phase distribution maps for HPF_AE_5, HPF_AE_8 and HPF_AE_15 using Raman spectroscopy

Raman spectra collected from HPF_AE_5

Raman spectra were collected for several positions along the cylindrical axis of HPF_AE_5 which reached a temperature of 1193 K over a duration of 3750 s. All spectra indicate the sample was fully transformed to ahrensite (see Figure A.2.1). Data were collected for varying amounts of time and vary in signal to noise. The calibration spectrum was collected for 1800 s and averaged over 6 collections.

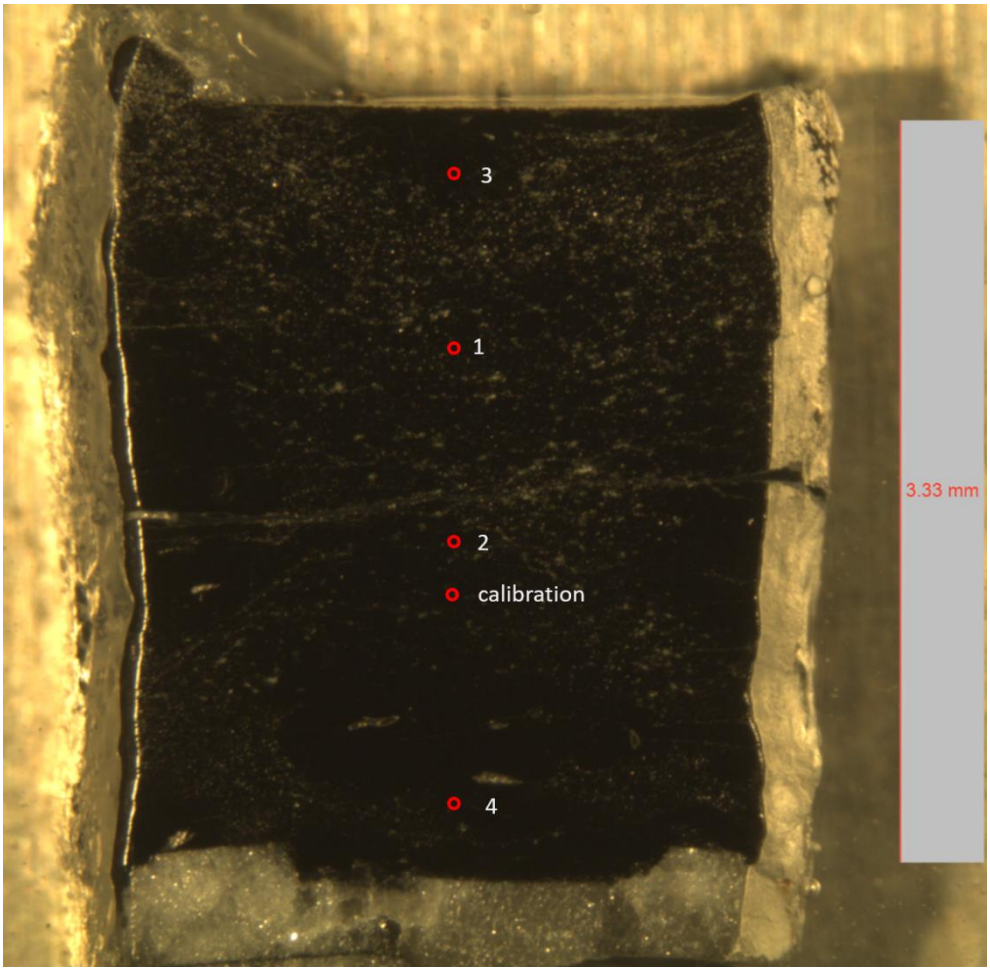

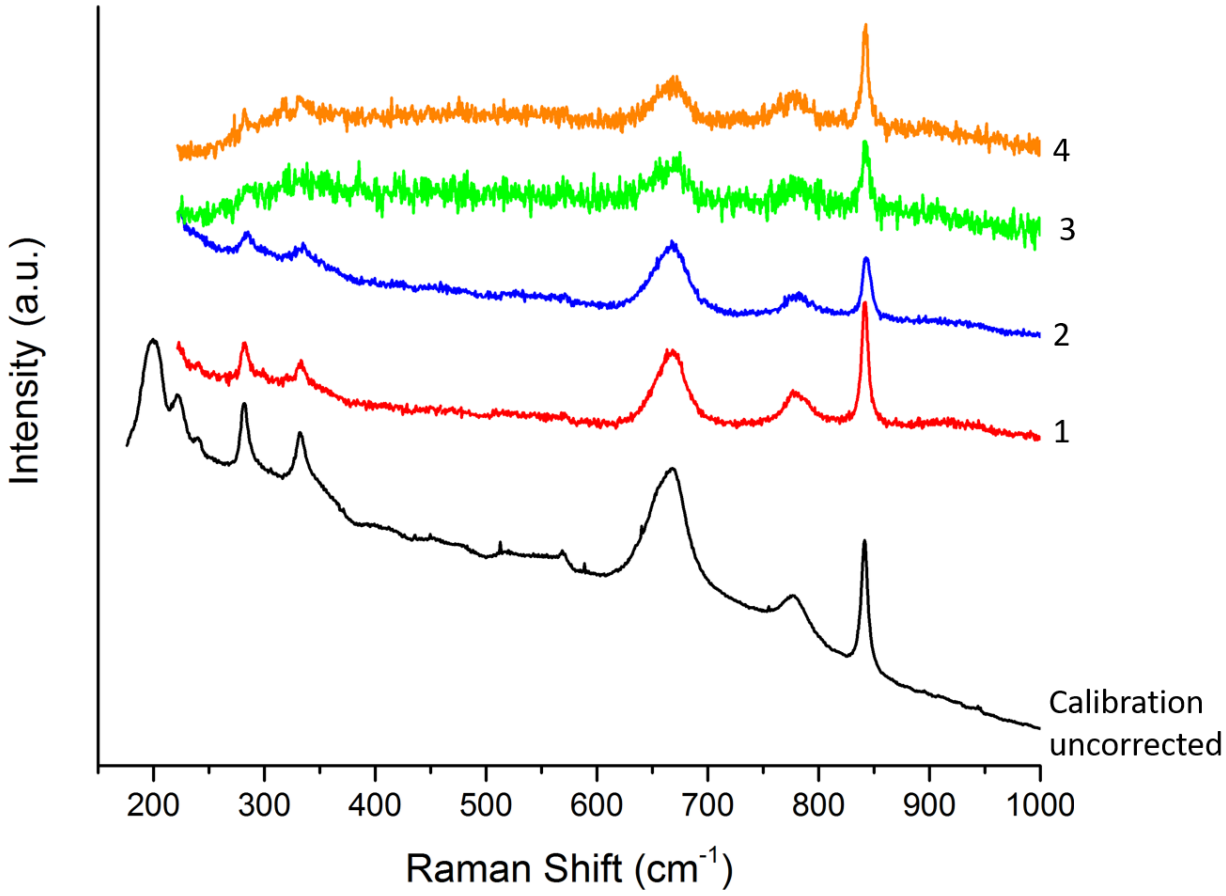

Figure A.2.1: Raman spectra collected from 4 positions along the sample cylindrical axis from the bottom to the top of HPF_AE_5. The entire sample was transformed to ahrensite and used to calibrate the Raman spectrum. The calibration spectrum which was 20x more intense than the others was scaled to fit on the same plot.

Raman spectra collected from HPF_AE_8

Raman spectra were collected at several positions for HPF_AE_8 both inside and outside the fault zones indicated in Figure A.2.2. The sample is generally dominated by fayalite but contains small amounts of ahrensite throughout the sample with a higher percentage inside the fault zones than outside. There also appears to be another peak with of a Raman shift of 611 cm^{-1} in the spectra collected within the fault zones attributed to an unknown mineral. It may have

been introduced as a result of the oxygen fugacity in experiments but does not correspond to magnetite nor ferrosilite.

a)

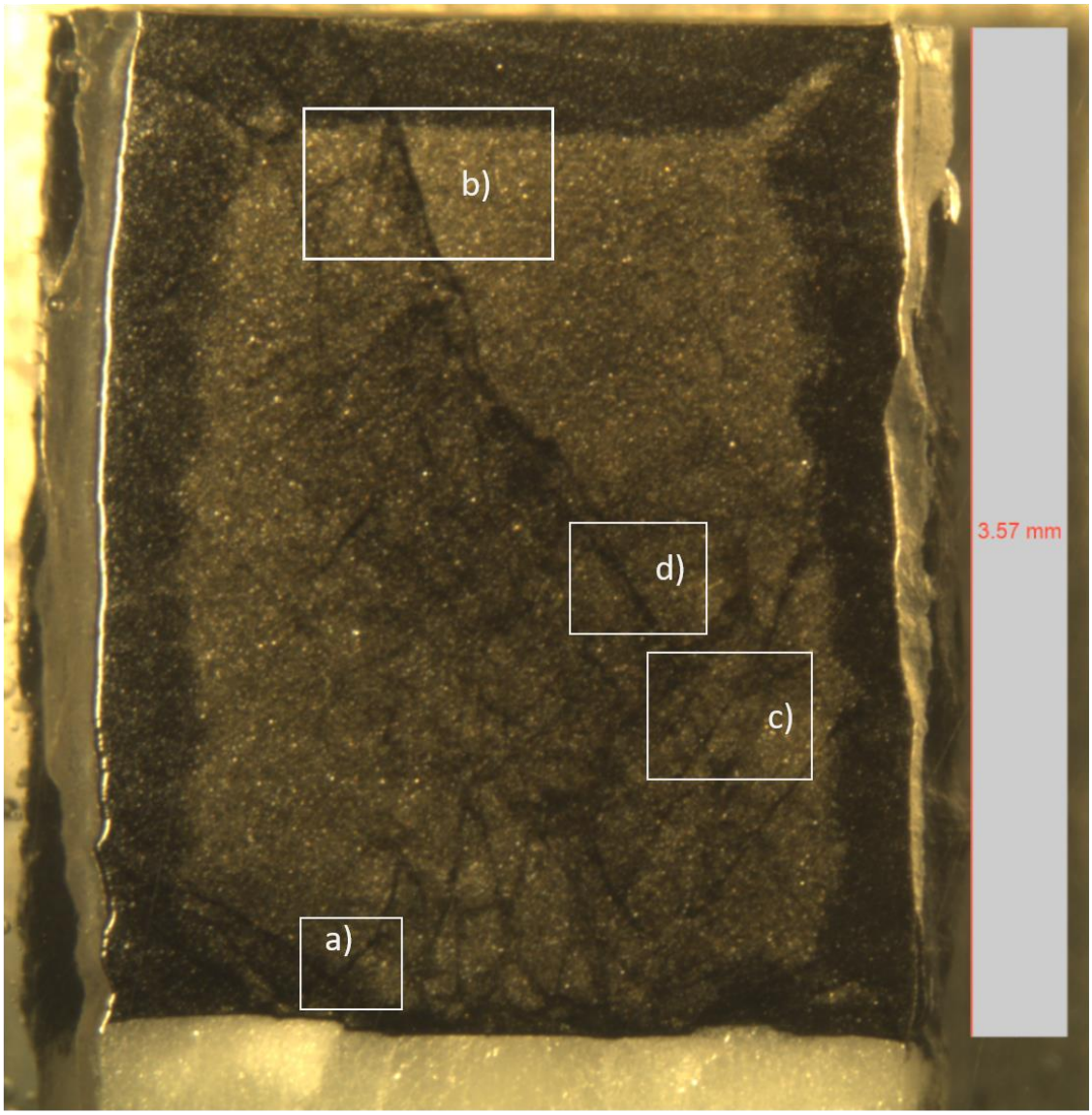

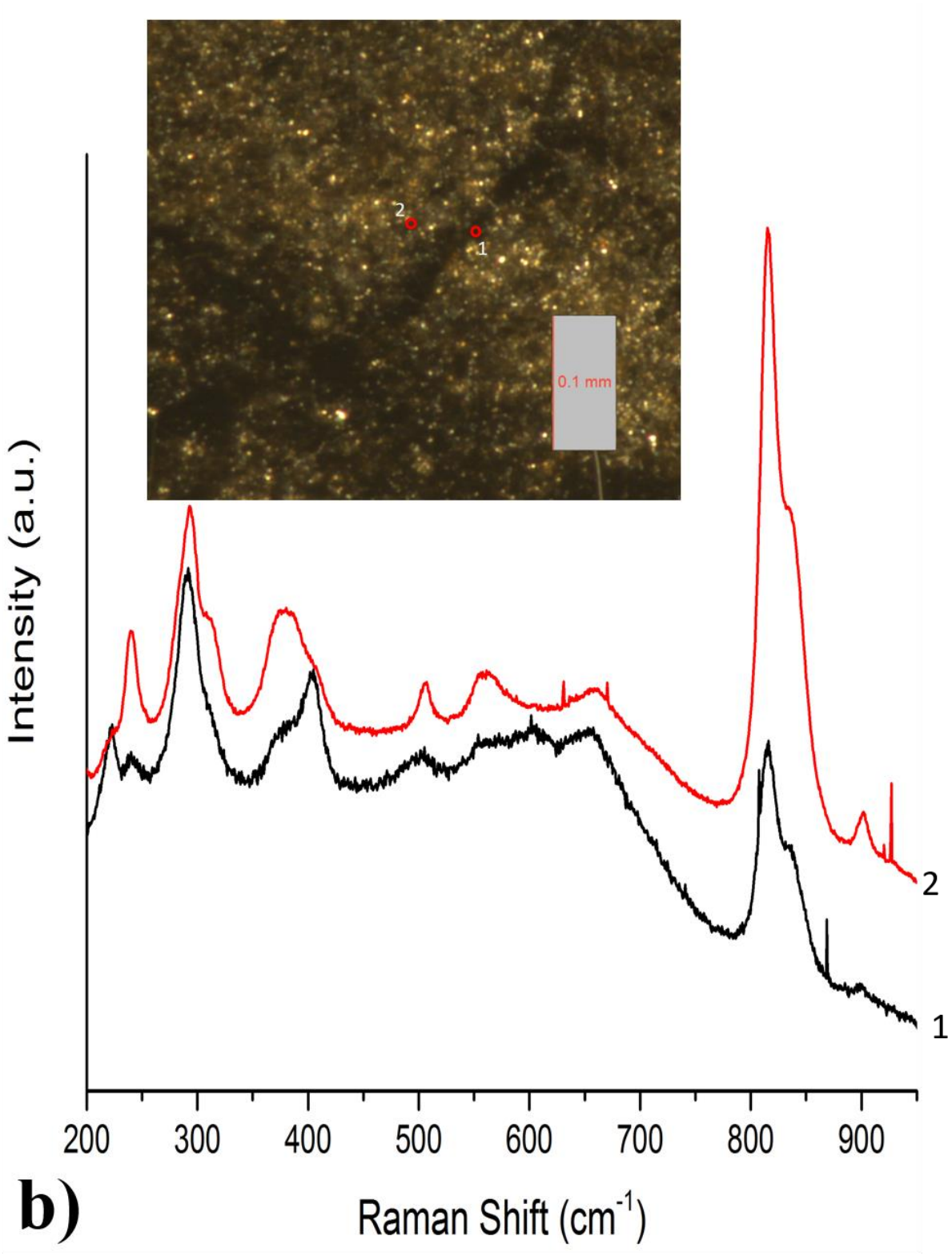
2
1
0.1 mm
Intensity (a.u.)
2
1
200
300
400
500
600
700
800
900
b)
Raman Shift (cm-1)

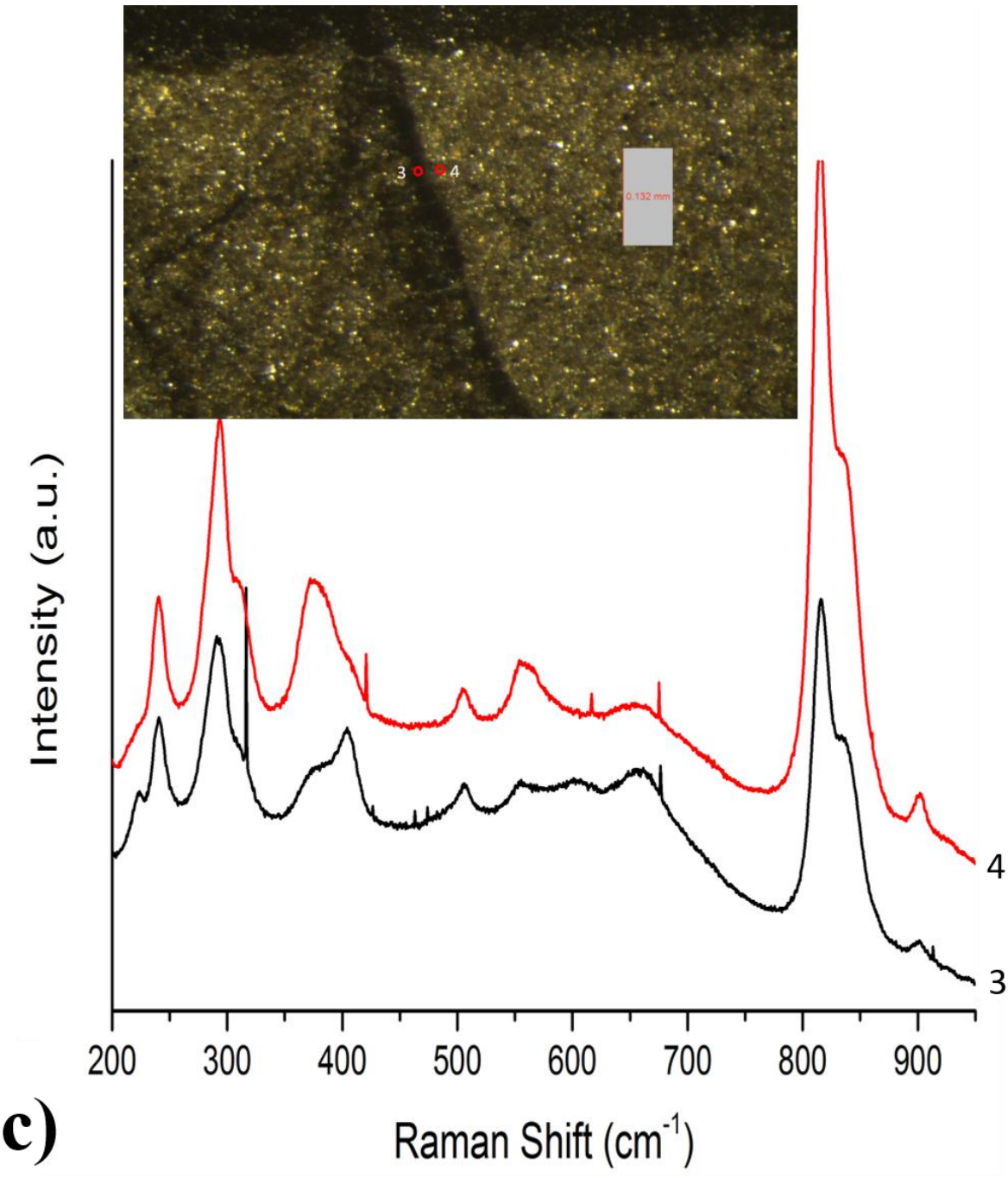
3
4
0.132 mm
Intensity (a.u.)
4
3
200
300
400
500
600
700
800
900
Raman Shift (cm-1)

c)

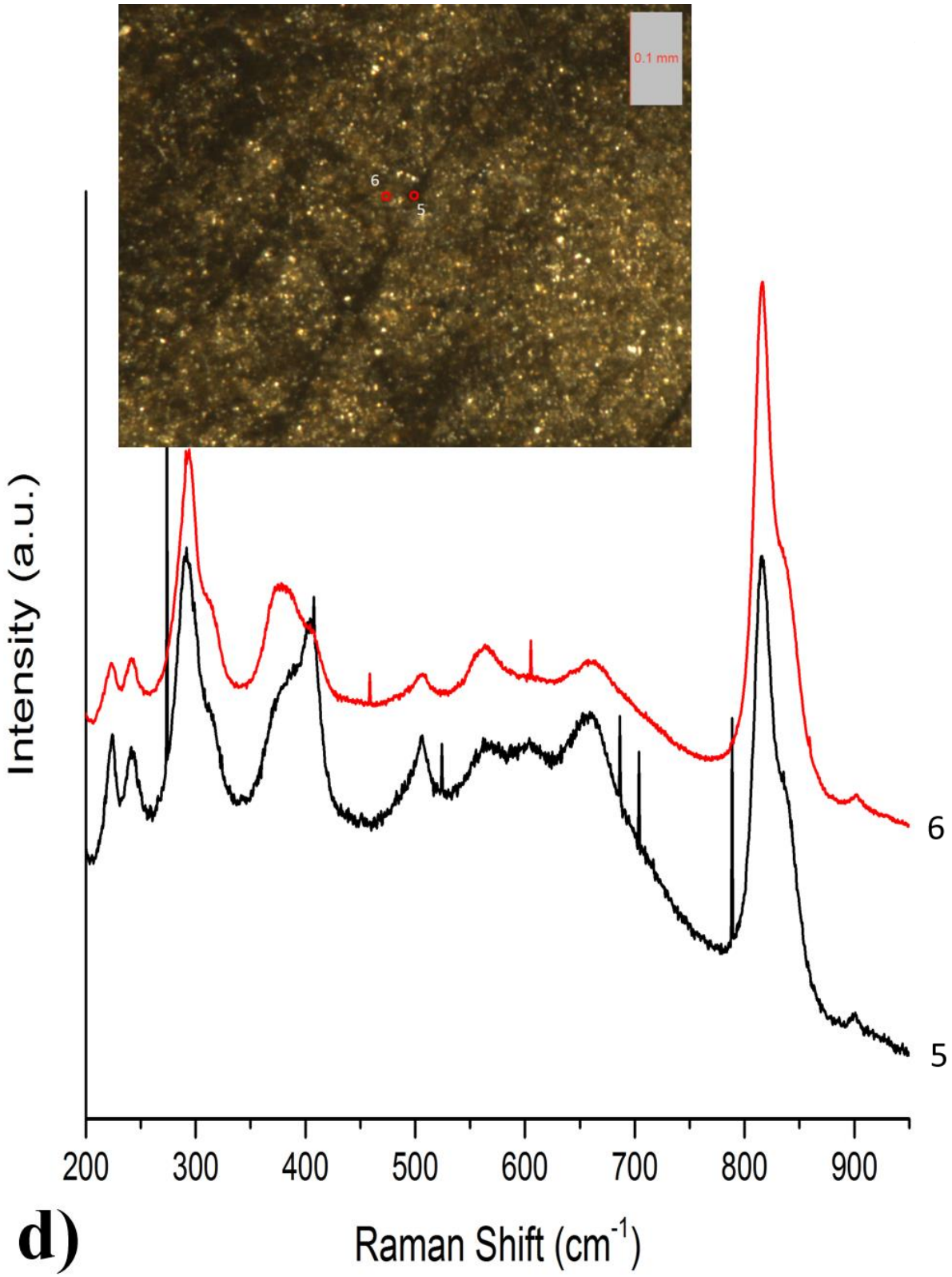
0.1 mm
6
5
Intensity (a.u.)
6
5
200
300
400
500
600
700
800
900
Raman Shift (cm-1)

d)

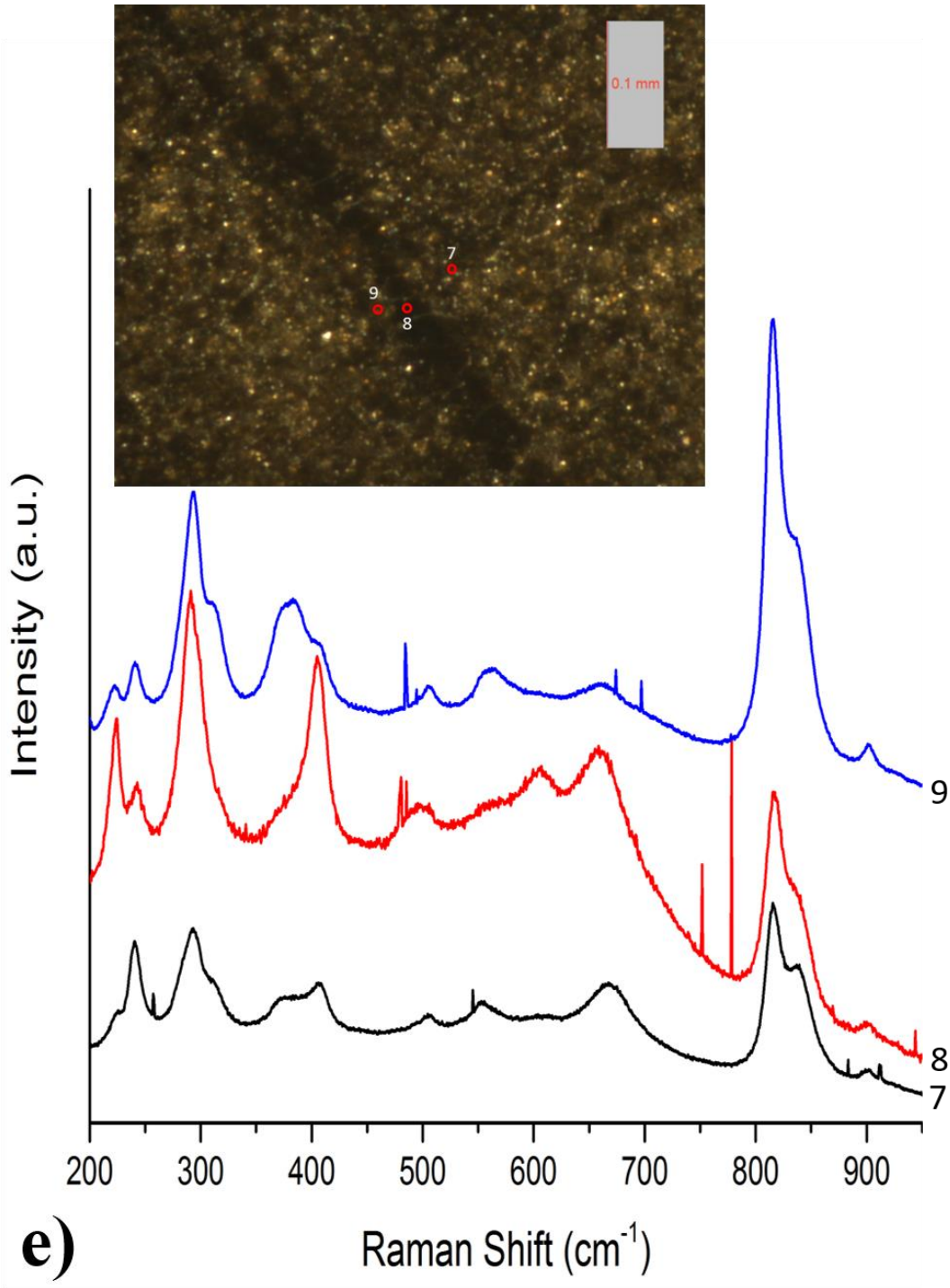

Figure A.2.2: Raman spectra collected from several positions on HPF_AE_8. **a)** Polished sample showing boxes within which Raman spectra were collected. **b)** A zoom view of the positions where Raman spectra were collected from box a). The spectra corresponding to each position are given below. **c)** A zoom view of the positions where Raman spectra were collected from box b). The spectra corresponding to each position are given below. **d)** A zoom view of the positions where Raman spectra were collected from box c). The spectra corresponding to each position are given below. **e)** A zoom view of the positions where Raman spectra were collected from box d). The spectra corresponding to each position are given below.

Raman spectra collected from HPF_AE_15

HPF_AE_15 shows similar results to that of HPF_AE_8 and HPF_AE_11. The sample is dominated by fayalite but contains a small amount of ahrensite in the fault zones and in the dark rind surrounding the sample indicating that ahrensite likely nucleated at the boundary between the sample and the furnace, or the Al_2O_3 pistons, and grew inward. Figure A.2.3 shows the Raman spectra collected for HPF_AE_15 and the positions they were collected.

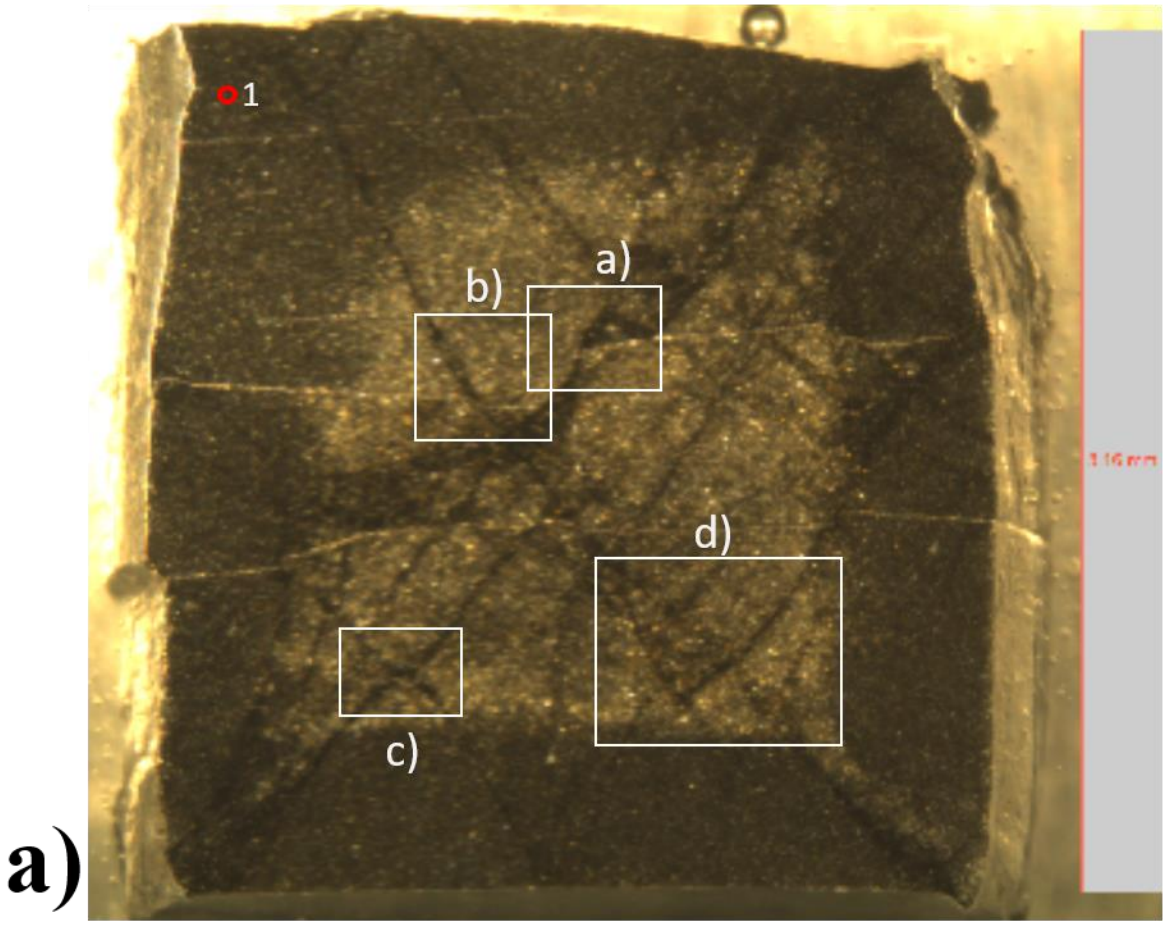

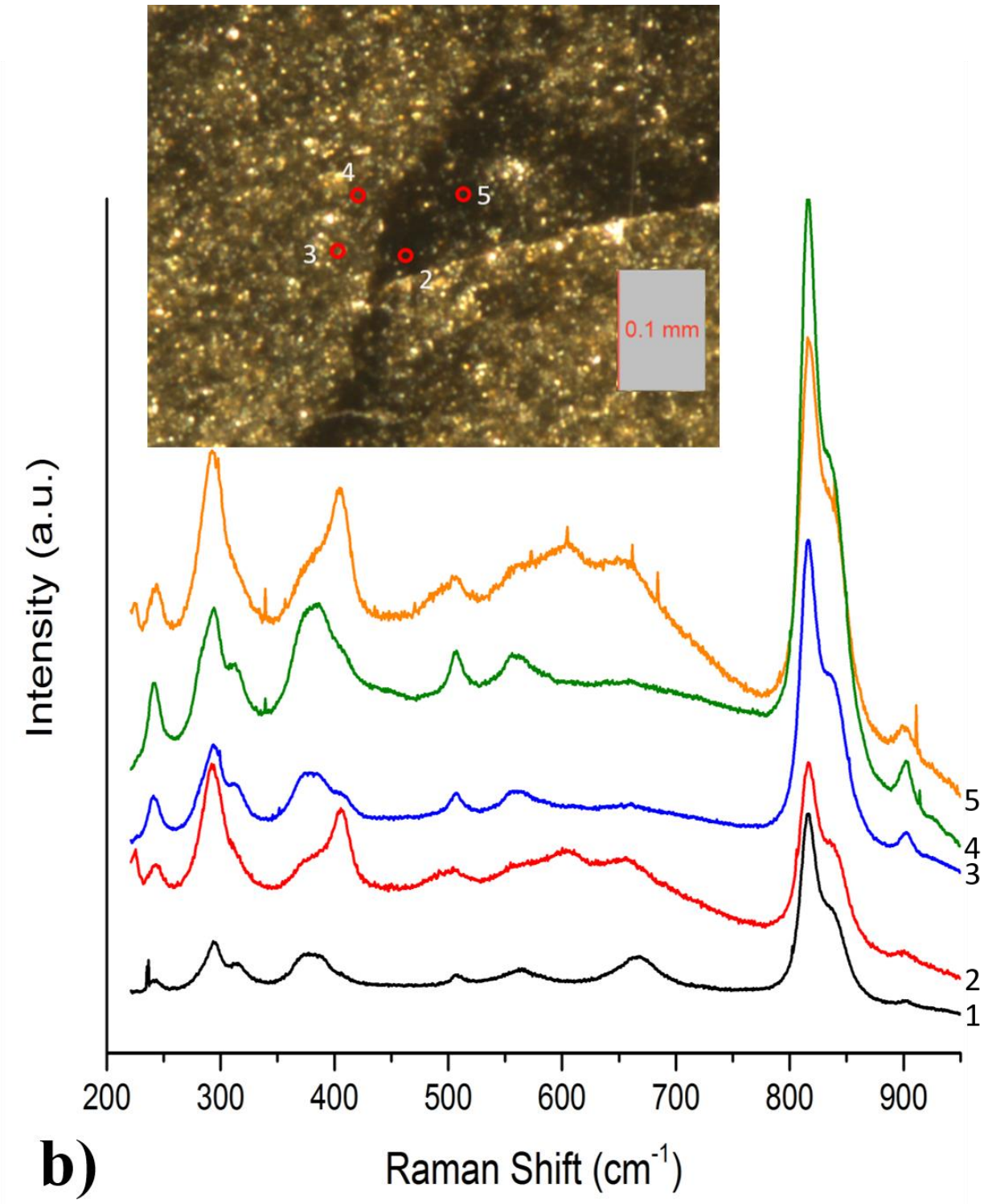
4
5
3
2
0.1 mm
Intensity (a.u.)
5
4
3
2
1
200
300
400
500
600
700
800
900
Raman Shift (cm-1)

b)

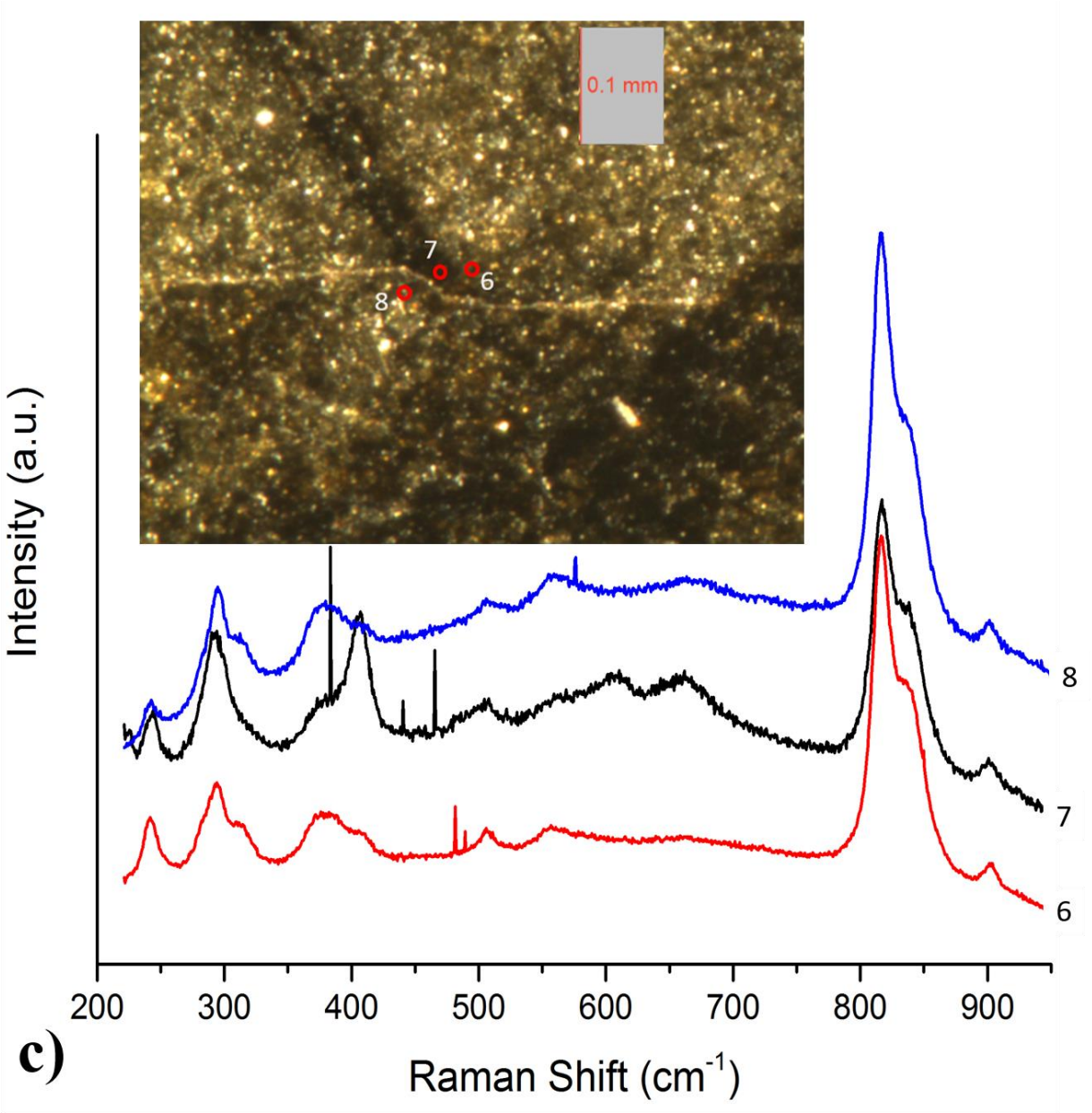
0.1 mm
7
6
8
Intensity (a.u.)
8
7
6
200
300
400
500
600
700
800
900
Raman Shift (cm-1)
c)

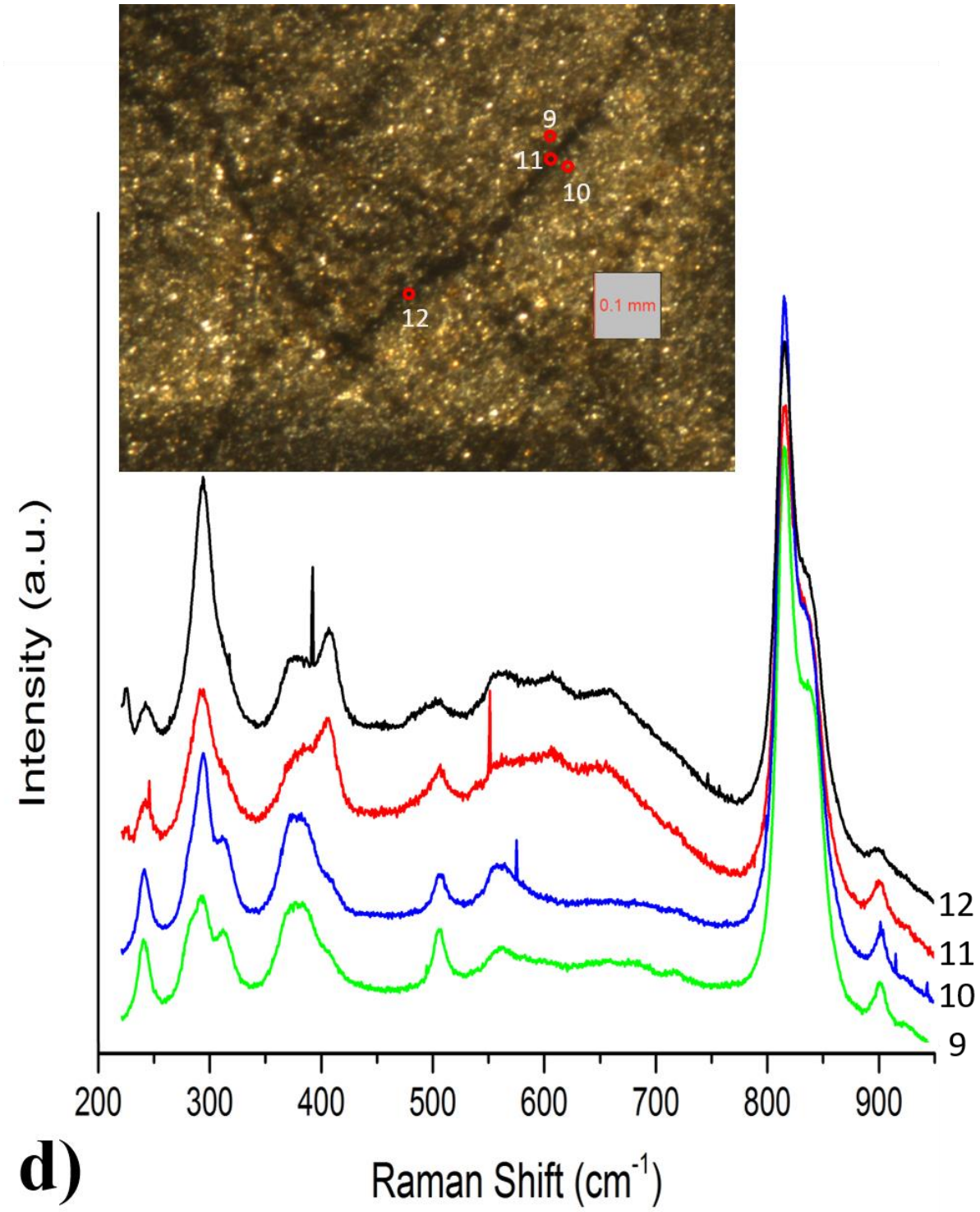
9
11
10
12
0.1 mm
Intensity (a.u.)
12
11
10
9
200
300
400
500
600
700
800
900
Raman Shift (cm-1)

d)

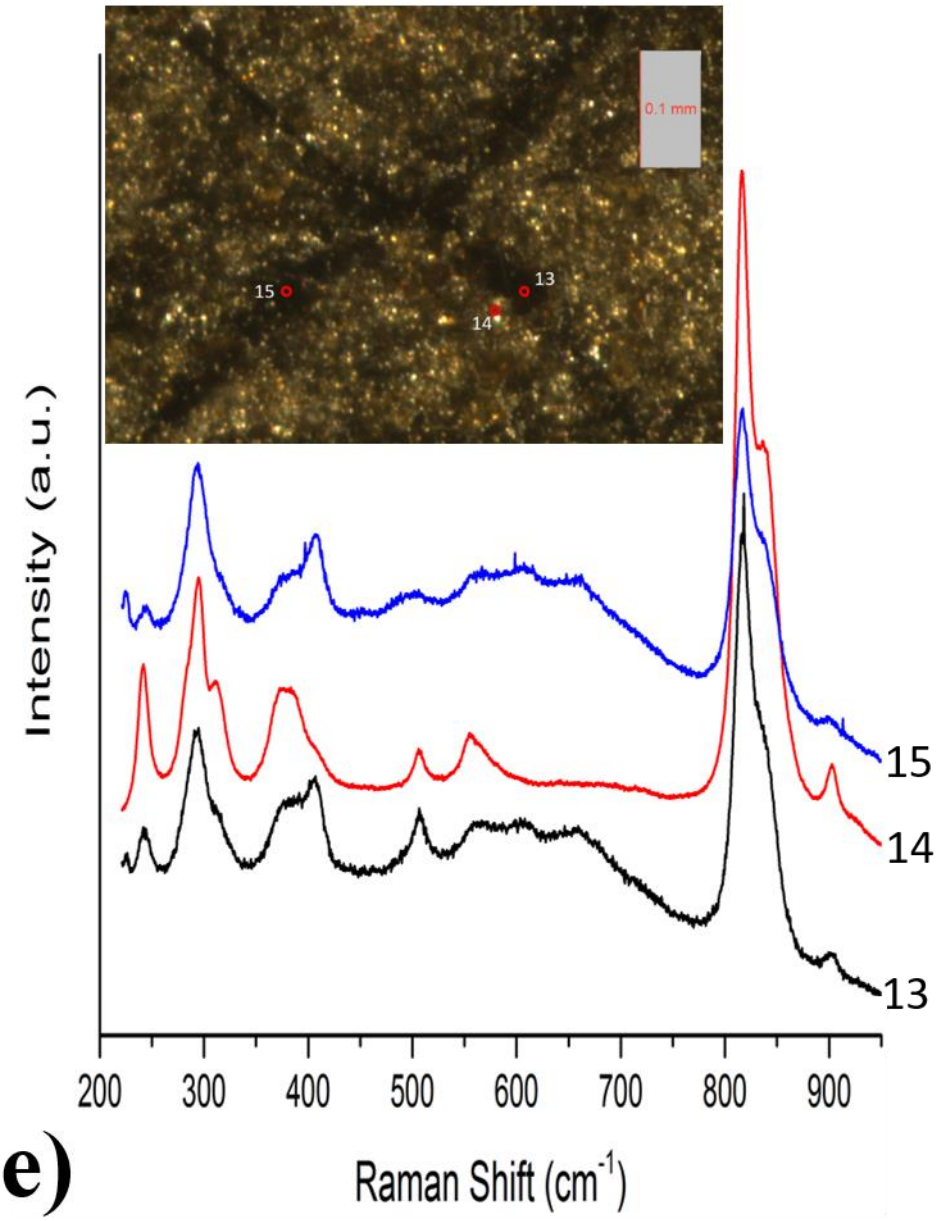

Figure A.2.3: Raman spectra collected from several positions on HPF_AE_15. **a)** Polished sample showing boxes within which Raman spectra were collected. **b)** A zoom view of the positions where Raman spectra were collected from box **a**. The spectra corresponding to each position are given below. The position of spectrum 1 is indicated in **a**. **c)** A zoom view of the positions where Raman spectra were collected from box **b**. The spectra corresponding to each position are given below. **d)** A zoom view of the positions where Raman spectra were collected from box **c**. The spectra corresponding to each position are given below. **e)** A zoom view of the positions where Raman spectra were collected from box **d**. The spectra corresponding to each position are given below.

Appendix 3: Microstructural analysis of recovered samples from HPHT deformation experiments on Fe_2SiO_4

Microstructural analysis: HPF_AE_13

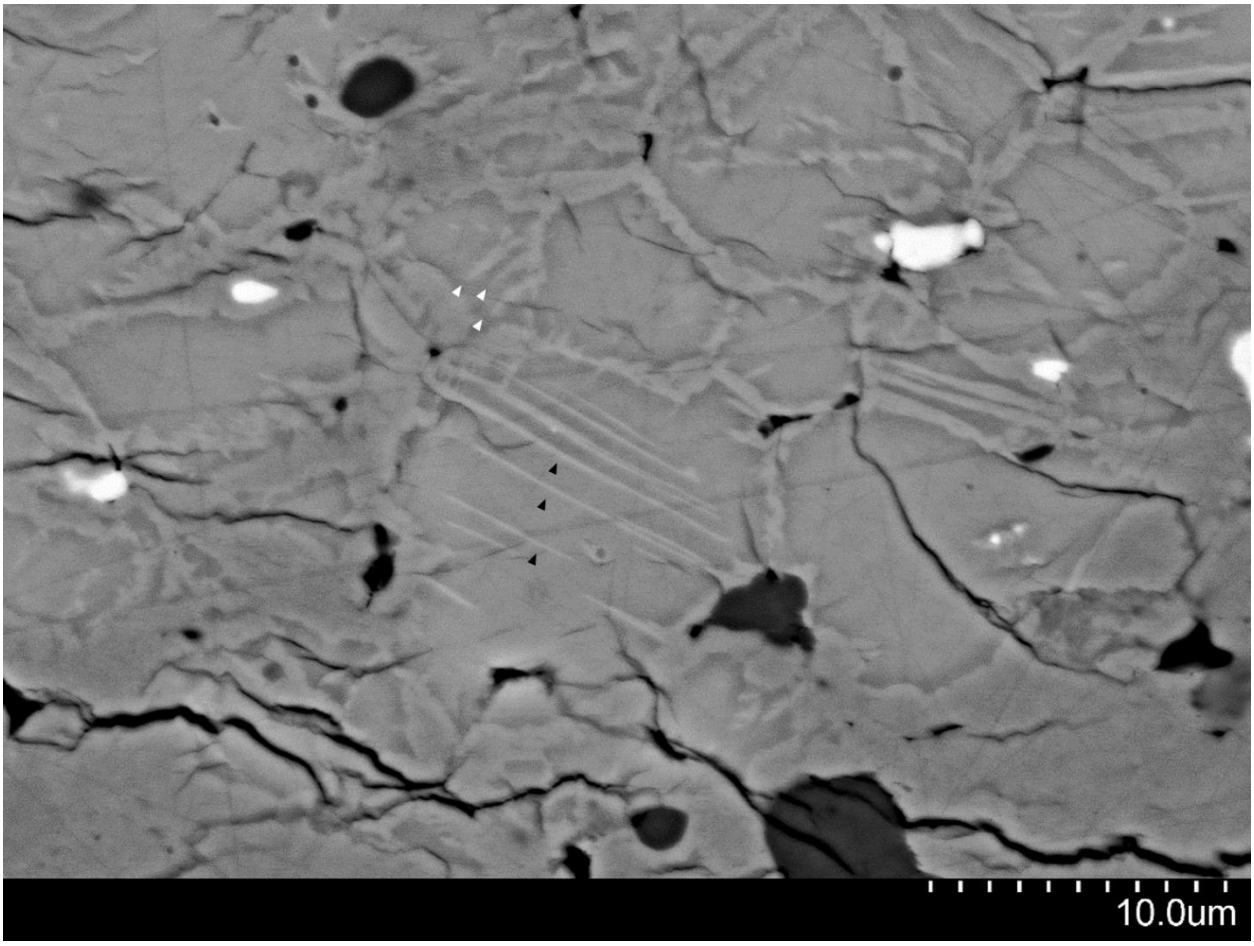

Figure A.3.1: BSE image showing partially developed planar transformation features (black arrowheads) and anticrack lenses (white arrowheads) coexisting in HPF_AE_13.

Microstructural analysis: HPF_AE_10

HPF_AE_10 shows similar features to HPF_AE_14, namely there is a large fault running from the S-W to the N-E in Figure A.3.2 that has full transformed to spinel and appears darker than the surrounding material. Several large decompression cracks also developed in this region.

The rest of the sample also experienced a high degree of partial transformation. Figure A.3.3 shows the boundary between the fully and partially transformed material. Note the presence of anticracks adjacent to the fully transformed region. Several areas also display planar transformation features as shown in Figure A.3.4. This sample was run at 748 K and displayed more transformation to the high pressure phase than HPF_AE_11 and HPF_AE_15 which were run at 773 and 798 K respectively. The likely reason for this is that, judging by the large amount of magnetite grains, which appear white in the BSE images, this sample experienced slightly different sintering conditions which led to a larger number of dislocations than other experiments and provided more sites for transformation.

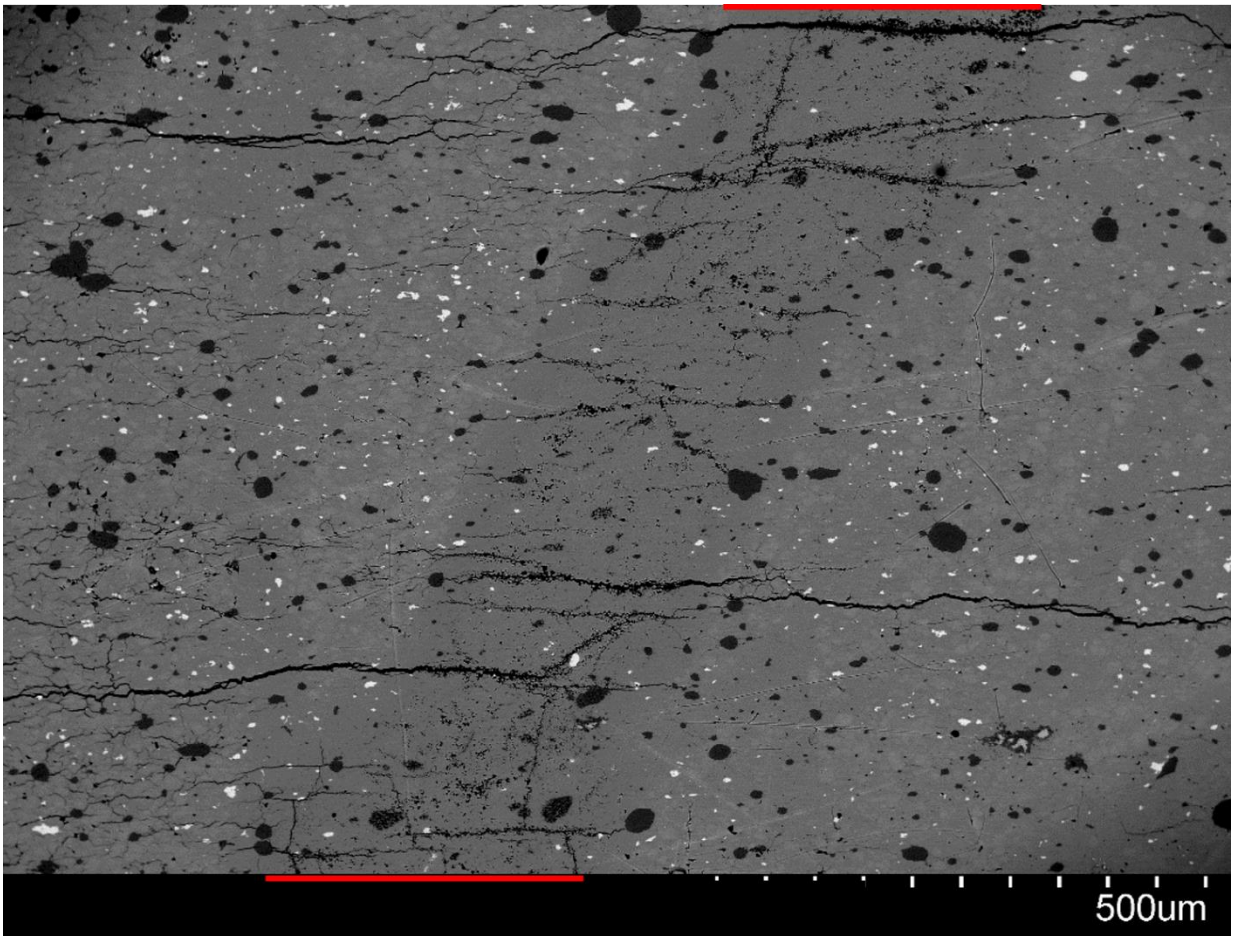

Figure A.3.2: A large fault entering and exiting through the red bars that has fully transformed to spinel and displays several decompression cracks.

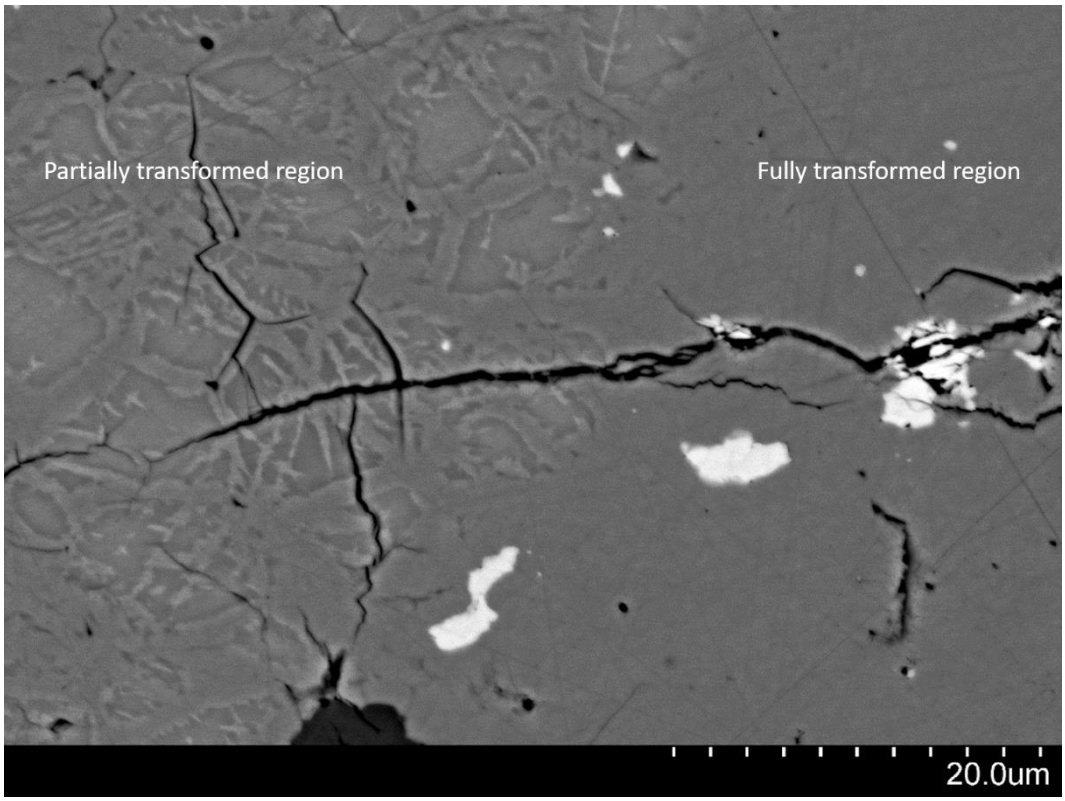

Figure A.3.3: Anticrack lenses adjacent to the fully transformed region.

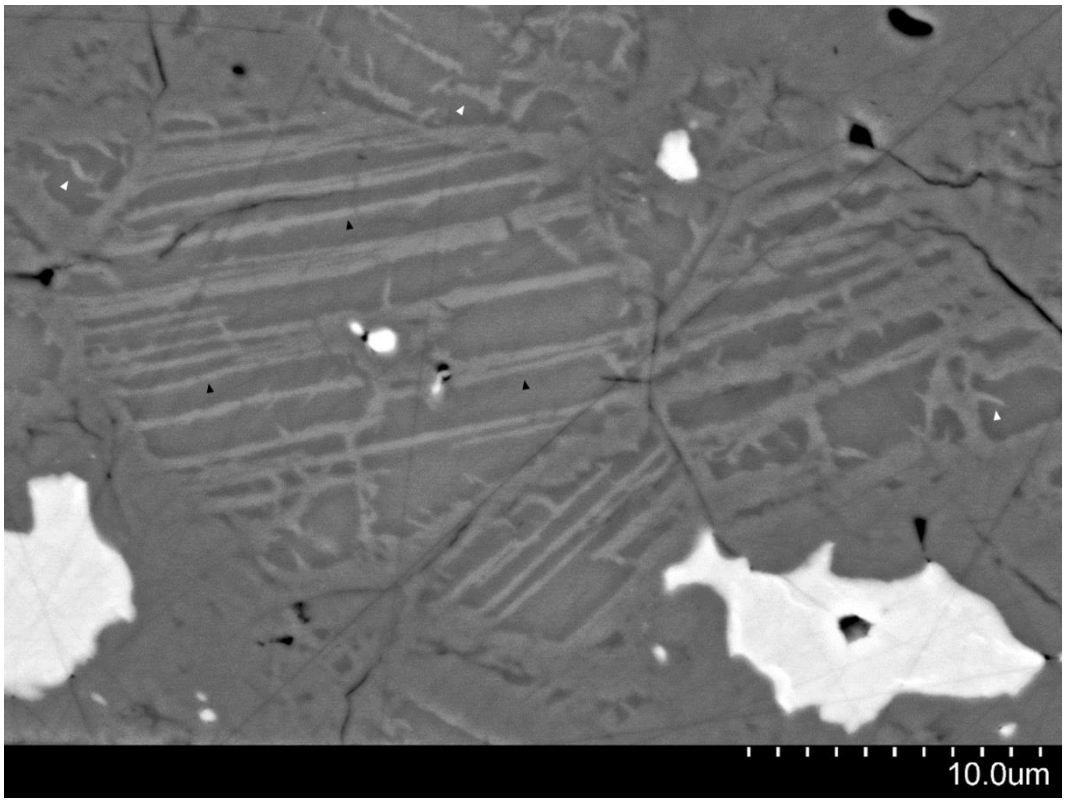

Figure A.3.4: Planar transformation features and anticrack lenses coexisting in the recovered sample.

Microstructural Analysis: HPF_AE_3

HPF_AE_3 was run under P,T conditions that lay within the P,T window where faulting occurred in other samples. The likely reason it did not register any AEs is because the pre-amplification was lower and the threshold was higher than later experiments that did register AEs. Therefore, any acoustic signals it may have generated may have been too low to detect. It does however show a fault containing spinel in an optical micrograph as shown in Figure A.3.5.

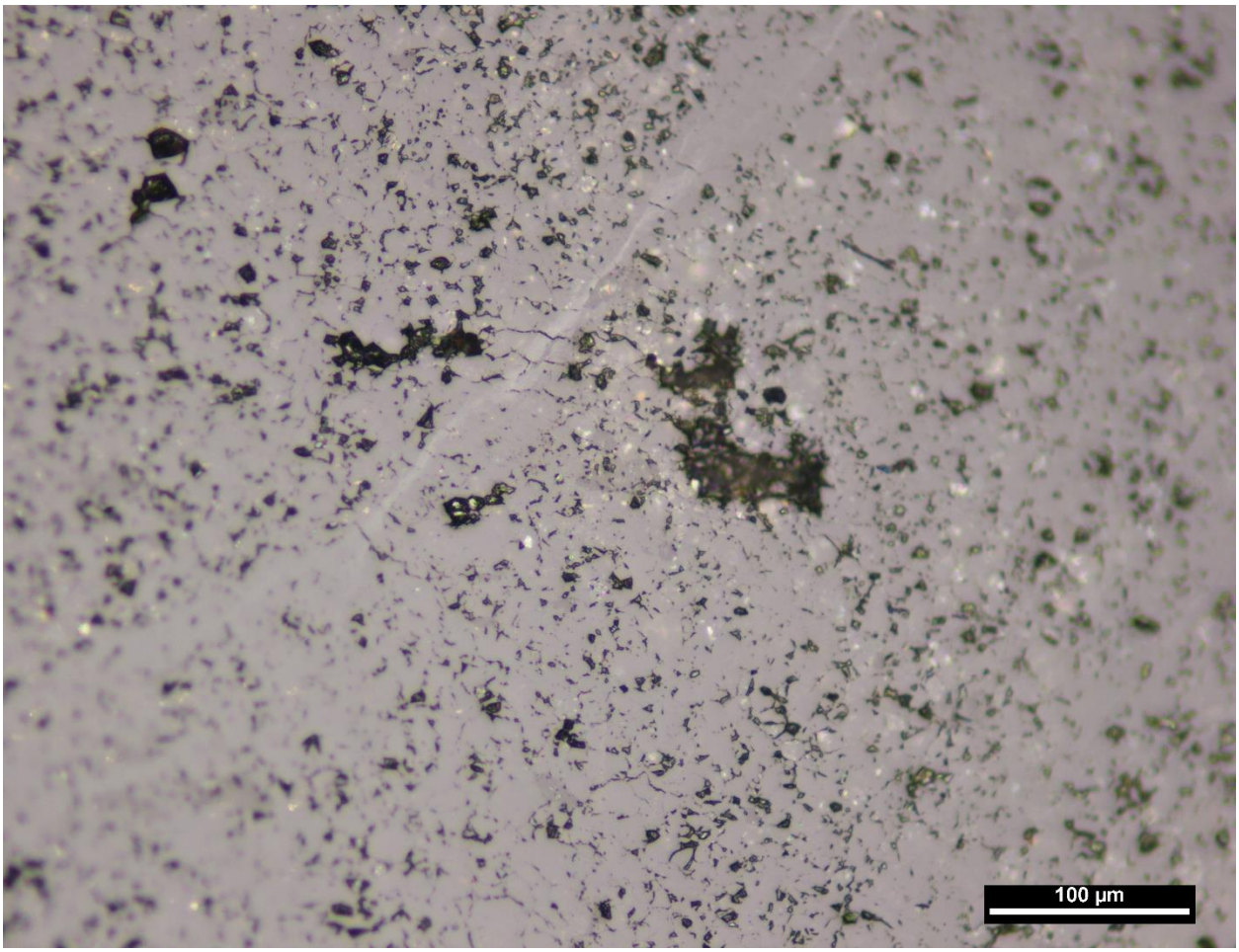

Figure A.3.5: A fault gouge containing ahrensite in HPF_AE_3.

Curriculum Vitae

Education

PhD: Geophysics, University of Western Ontario - to be defended Oct., 2017
Thesis: "*Investigating the mechanism of deep-focus earthquakes via in-situ acoustic emission experiments on Fe_2SiO_4 at high temperature and pressure*"

Highlights of my PhD include:
- Independently conceiving of a novel thesis project to test experimentally the hypothesis that deep-focus earthquakes are caused by mineral phase transitions in the mantle.
- Securing funding though two successful grant applications, of which I was the primary contributor, to purchase acoustic emission equipment currently in operation in the Mineral Physics Laboratory at UWO.
- Development of a HPHT AE monitoring system including characterizing and discriminating between/removing spurious signals generated by acoustic and electrical sources.
- Writing a computer code that locates the position of acoustic events in a micro-seismic array to sub-mm accuracy using non-linear least squares inversion techniques.
- Being the first to measure acoustic activity and observing microstructures associated with faulting due to phase changes in fayalite under mantle conditions.

Master of Science: Astronomy, University of Western Ontario, 2008
Thesis: "*Scattering of electromagnetic waves by a grid of elliptic dielectric ribbons*"
Sub Projects included:
- Writing a computer program to compute the ideal shape of a curved mirror to focus an arbitrarily incident Gaussian beam without distortion.
- Writing a computer simulation of Gaussian beam propagation through the optics of the Caltech Submillimetre Observatory (CSO).
- Participated in observations of star forming regions within molecular gas clouds at the (CSO).

Bachelor of Science: Honours Specialization in Physics, University of Western Ontario, 2005

Ontario Secondary School Graduation Diploma: Clarke Road Secondary School, 2000

Publications

Officer, T. and Secco, R.A., 2017, Microseismic monitoring of the olivine → spinel transition in fayalite under non-hydrostatic stress. (*in prep*)
Officer, T. and Secco, R.A., 2015, Detection of a P-induced liquid ⇌ solid-phase transformation using multiple acoustic transducers in a multi-anvil apparatus, *High Pressure Research,* 35, 289-299, DOI: 10.1080/08957959.2015.1035715.
Officer, T. and Secco, R.A., 2013, Acoustic emission experiments at high pressures, *International Innovations*, June, 38 – 40. (*non-refereed*)

Landstreet, J.D., Kupka, F., Ford, H.A., **Officer, T.**, Sigut, T.A.A., Silaj, J., Strasser, S., Townshend, A., 2009, Atmospheric velocity fields in tepid main sequence stars, *Astronomy and Astrophysics*, 503, 973 – 986, DOI:10.1051/0004-6361/200912083.

Conference Proceedings

Officer, T. and Secco, Deep earthquakes in the lab: Microseismic monitoring of the olivine → spinel transition in fayalite under non-hydrostatic stress, AESRC, London, Canada, Mar. 31-Apr. 2, 2017. (*talk*)
Officer, T. and Secco, R.A., AE development at Western University: Microseismic monitoring of the olivine → spinel transition in fayalite under non-hydrostatic stress, Acoustic Emission Workshop, GSECARS, The Advanced Photon Source, Jan. 29-31, 2016. (*talk*)
Officer, T. and Secco, R.A., Deep Earthquakes in the lab: AE development at Western University, Special session on multi-anvil techniques, Joint Assembly, AGU-GAC-MAC-CGU, Montreal, Canada, May 3-7, 2015. (*talk*)
Officer, T. and Secco, Are deep earthquakes generated by phase transitions in the mantle? Acoustic monitoring of the olivine → spinel transition at high pressure and temperature, Geo-Diversity, AESRC, Ottawa, Canada, Mar. 28-30, 2014. (*talk*)
Officer, T. and Secco, R.A., Micro-seismicity at high pressure and temperature: Developing a system for generating and detecting deep earthquakes in the lab, Meeting of the Americas, AGU, Cancun, Mexico, 14-17 May, 2013. (*talk*)
Officer, T. and Secco, R.A, Microseismic monitoring of the olivine → Spinel Transition in Fayalite Under Non-Hydrostatic Stress, Fall Meeting, AGU, San Francisco, USA, 12-16, Dec., 2016. (*poster*)
Officer, T. and Secco, R.A., Detection of a pressure-induced liquid ⇌ solid phase transformation using multiple acoustic transducers in a multi-anvil apparatus, COMPRES Annual Meeting, Colorado Springs, USA, 6-9, Jul., 2015. (*poster*)
Officer, T. and Secco, R.A., Microseismicity at high pressure and temperature: Developing a system for generating and measuring deep earthquakes in the Lab, COMPRES Annual Meeting, Colorado Springs, USA, 6-9, Jul., 2015. (*poster*)
Officer, T. and Secco, R.A., Detection of a pressure-induced liquid ⇌ solid phase transformation using multiple acoustic transducers in a multi-anvil apparatus, Joint Assembly, AGU-GAC-MAC-CGU, Montreal, Canada, May 3-7, 2015. (*poster*)
Officer, T. and Secco, Microseismicity at High Pressure and Temperature: Developing a system for generating and measuring deep earthquakes in the lab, Fall Meeting, AGU, San Francisco, USA, Dec. 9-13, 2013. (*poster*)

Awards and Honours:

- National Sciences and Engineering Research Council (NSERC) Post-Graduate Scholarship recipient (Sept. 2012 - Aug. 2014). Awarded to top 2% of applicants.
- Ontario Graduate Scholarship (OGS) recipient (Sept. 2011 – Aug. 2012). Awarded to top 10% of applicants.
- Two-time winner: Best Geophysics talk, ASERC conference (2014, 2017). Presented by the Canadian Society of Exploration Geophysicists.
-Winner: Best Talk overall, ASERC conference (2017).

Teaching Experience

Instructor - Department of Earth Science, University of Western Ontario (UWO)
- Physics of the Earth (upper year/grad) – (Jan. – Apr., 2012)
- Earth Shaken and Stirred/The Dynamic Earth (1st and 2nd year) - (Sept. – Dec., 2013)
- Advanced Physics of the Earth (upper year/grad) - (Jan. – Apr., 2014)
I was the full instructor for *Physics of the Earth* and the co-instructor (50% duty) for *Earth Shaken and Stirred/The Dynamic Earth* and *Advanced Physics of the Earth*. The focus of these courses is on the physics of the Earth with emphasis on Earth's formation, seismology, heat transfer, magnetic field, earthquakes, volcanoes, gravity, radioactive dating, mantle rheology and the physics of minerals. This required preparing and delivering 3 lecture hours per week, overseeing weekly seminars/laboratories, as well as creating and grading exams and assignments.

Teaching Assistantships (TA) – University of Western Ontario
During my graduate studies I have had the opportunity to be a teaching assistant in a wide range of disciplines including physics, astronomy, math and earth science. This involved instruction via several different teaching styles including lecturing, one-on-one tutoring, facilitating computer and experimentally based lab exercises, leading discussion groups, assisting in astronomical observations, maintaining an online learning course, as well as grading and providing feedback.
Courses TAed include:
- Modern Physics Laboratory
- Intermediate Physics Laboratory
- Introduction to Astronomy
- Calculus for Engineers
- Physics of the Earth's Interior
- Resources, Environment and Sustainability in a Material Society
- Catastrophic Events in Earth History

Technical Skills and Training

- Extensive knowledge of HPHT experimentation using multi-anvil apparatuses
- Abundant experience applying microseismic monitoring and analysis to HPHT applications
- Extensive experience with CAD design to create 3D models of HPHT assemblies
- Proficient in the use of both manual and CNC lathes and mills
- Extensive experience in the fabrication and assembly of HPHT experimental components
- Programming and scientific computing expertise using Matlab and C++

Relevant Work Experience

Sciencetech Inc.
May 2007 - Aug. 2009
Title: Project Leader

Job Description:
I was in charge of handling projects, primarily those associated with research and development. Our typical customers were university researchers looking for high precision optical equipment to

be used in laboratory environments. From an organizational standpoint, I was responsible for making sure the parts were ordered, machined and assembled within a definite time frame. As a physicist I designed optical systems to the customer's specifications and integrated the different components together so the system could be used to perform precise measurements. This involved aligning each individual piece of optical equipment, then amalgamating them into a functioning system. The final phase of a project was to test the equipment to make sure it performed its specified function within the constraints of rigid accuracies.

Sciencetech Inc. Career Highlights:

- Led a project that pioneered a new technique for the fabrication of beam splitting polarizers for THz frequencies in conjunction with the National Research Council of Canada and the University of Western Ontario. This was accomplished using lithographic nanofabrication techniques under cleanroom conditions.
- Designed and built a Raman spectroscopy system.
- Designed the optical layout for Sciencetech Inc.'s Fourier transform infrared spectrometers.
- Specialized in the design and production of quantum efficiency systems.

Summer Research Assistantships, University of Western Ontario

May 1 – Aug. 31, 2005
Research area: **Polarimetric Astronomy**

-Wrote a computer program to simulate beam propagation in a Martin-Puplett polarimeter, allowing for quantitative analysis of instrumental polarization.

May 1 – Aug. 31, 2004
Research area: **Atmospheric Physics**

-Prepared and launched weather balloons equipped with radio- and ozonesondes.
-Wrote computer algorithms to analyze the transport of ozone across the tropopause.

May 1 – Aug. 31, 2003 and 2002
Research area: **Stellar Astronomy**

- Processed observational data from the Canada-France-Hawaii telescope.
- Organized a computer database of photometric and spectral data for stars.